-7316 ANL-7316

-7316 ANL-7316

-7316 ANL-7316

-7316 ANL-7316

-7316 ANL-7316

-7316 ANL-7316

-7316 ANL-7316

-7316 ANL-7316

-7316 ANL-7316

-7316 ANL-7316

-7316 ANL-7316

The facilities of Argonne National Laboratory are owned by the United States Government. Under the terms of a contract (W-31-109-Eng-38) between the U. S. Atomic Energy Commission, Argonne Universities Association and The University of Chicago, the University employs the staff and operates the Laboratory in accordance with policies and programs formulated, approved and reviewed by the Association.

MEMBERS OF ARGONNE UNIVERSITIES ASSOCIATION

The University of Arizona
Carnegie Institute of Technology
Case Institute of Technology
The University of Chicago
University of Cincinnati
Illinois Institute of Technology
University of Illinois
Indiana University
Iowa State University
The University of Iowa
Kansas State University
The University of Kansas
Loyola University
Marquette University
Michigan State University
The University of Michigan
University of Minnesota
University of Missouri
Northwestern University
University of Notre Dame
The Ohio State University
Purdue University
Saint Louis University
Washington University
Wayne State University
The University of Wisconsin

LEGAL NOTICE

This report was prepared as an account of Government sponsored work. Neither the United States, nor the Commission, nor any person acting on behalf of the Commission:

A. Makes any warranty or representation, expressed or implied, with respect to the accuracy, completeness, or usefulness of the information contained in this report, or that the use of any information, apparatus, method, or process disclosed in this report may not infringe privately owned rights; or

B. Assumes any liabilities with respect to the use of, or for damages resulting from the use of any information, apparatus, method, or process disclosed in this report.

As used in the above, "person acting on behalf of the Commission" includes any employee or contractor of the Commission, or employee of such contractor, to the extent that such employee or contractor of the Commission, or employee of such contractor prepares, disseminates, or provides access to, any information pursuant to his employment or contract with the Commission, or his employment with such contractor.

Printed in the United States of America
Available from
Clearinghouse for Federal Scientific and Technical Information
National Bureau of Standards, U. S. Department of Commerce
Springfield, Virginia 22151
Price: Printed Copy $3.00; Microfiche $0.65

ANL-7316
Propulsion Systems and
Energy Conversion
(TID-4500)
AEC Research and
Development Report

ARGONNE NATIONAL LABORATORY
9700 South Cass Avenue
Argonne, Illinois 60439

GALVANIC CELLS WITH FUSED-SALT ELECTROLYTES

by

E. J. Cairns, C. E. Crouthamel, A. K. Fischer,
M. S. Foster, J. C. Hesson, C. E. Johnson,
H. Shimotake, and A. D. Tevebaugh

Chemical Engineering Division

November 1967

TABLE OF CONTENTS

	Page
NOMENCLATURE	16
I. SUMMARY AND CONCLUSIONS	17
A. Cells with Sodium Anodes	18
B. Cells with Lithium Anodes	20
C. Materials Stability	23
D. Conclusions	23
II. INTRODUCTION	25
III. GALVANIC CELLS--GENERAL CONSIDERATIONS	27
A. Thermally Regenerative Cells	27
1. Carnot-cycle Efficiency (Eff_C)	28
2. Current Efficiency (Eff_I)	31
3. Voltage Efficiency (Eff_E)	31
4. Gibbs Free-energy Efficiency (Eff_G)	32
5. Overall Efficiency (Eff_S)	32
6. Cell and Regenerator Requirements	33
B. Secondary Cells--The Storage of Electricity	35
IV. CELLS WITH SODIUM ANODES	38
A. Thermodynamics of Sodium-containing Systems	38
1. Thermodynamic Measurements by the Emf Method	38
2. Thermodynamic Measurements by the Liquid-Vapor Equilibrium Method	42
3. Thermodynamic Analysis of the Results for the Sodium-Bismuth System	49
4. Thermodynamic Analysis of the Results for the Sodium-Lead System	56
5. Implications of Thermodynamic Results for Sodium-Bismuth and Sodium-Lead Regenerative Cells	58
B. Physicochemical Properties of Sodium-containing Systems	61
1. Determination of Density, Viscosity, and Surface Tension of Alloys and Electrolytes	61
2. Current-efficiency Studies in Sodium Halide Electrolytes	64
3. Sodium-transfer Studies	65
4. Solubility of Intermetallic Compounds in Fused Salts	73

TABLE OF CONTENTS

Page

C. Phase Relationships for Sodium Halide Electrolytes 75
1. Experimental Method. 76
2. Thermal-analysis Results 77

D. Studies of Cells, Regenerators, and Systems 80
1. Sodium-Bismuth Experimental Cells 80
2. Regenerator and Condenser Studies 87
3. Systems Based on Cells with Sodium Anodes 98

V. CELLS WITH LITHIUM ANODES. 105

A. Thermodynamics of Lithium-containing Systems. 105
1. Emf Studies of Lithium Hydride-containing Systems . . . 105
2. Emf Studies of Lithium-containing Bimetallic Systems . 108
3. Liquid-Vapor Equilibrium Measurements on the Lithium-Tin System 111
4. Thermodynamic Analysis of Results for Lithium-containing Systems 112

B. Physicochemical Properties of Lithium-containing Systems. 116
1. Conductivity of Lithium Hydride-Lithium Halide Mixtures 116
2. Density of Lithium Hydride-Lithium Halide Mixtures . . 117
3. Solubilities of Lithium-containing Intermetallic Compounds in Fused Salts 119
4. Raman Spectral Studies of Fused Salts 120
5. Visible Absorption Spectra 125

C. Phase Relationships for Lithium Halide-containing Electrolytes 128
1. Lithium Halide Systems 128
2. Lithium Hydride-containing Systems 132

D. The Hydrogen Electrode in Lithium Hydride-containing Systems. 139
1. Hydrogen-permeation Studies 139
2. Kinetics of the Hydrogen Electrode 142

E. Studies of Cells, Regenerators, and Systems 150
1. Lithium Hydride Galvanic Cells. 150
2. Bimetallic Cells with Lithium Anodes. 154

VI. MATERIALS STABILITY 168

A. Introduction 168

TABLE OF CONTENTS

Page

B. Heavy-metals Compatibility 168
1. Literature Survey 168
2. Static-corrosion Tests Using Heavy Metals 168
3. Dynamic-corrosion Tests. 173

C. Electrolyte Compatibility Studies 177
1. Literature Survey 177
2. Experimental Results of Fused-salt Corrosion Tests . . 179

D. Alkali-metal Compatibility Studies 180
1. Literature Survey 180
2. Results of Alkali-metal Corrosion Tests. 180

E. Insulators for Bimetallic Cells 180

F. Guidelines for the Selection of Cell and Regenerator Materials. 185

APPENDIXES

A. Purification of Gases for Inert-atmosphere Enclosures . . . 187

B. Quasi-thermodynamic Analysis of Self-discharge Sodium Transfer in Cells with Electrolytes Having Electronic and Ionic Conductivity 191
1. Assumptions 191
2. Derivation 192

C. Methods for the Study of Liquid-Vapor Equilibria 196
1. Total Vapor-pressure Measurements 196
2. Vapor Density and Composition by the Transpiration Method 198

D. Description of Laser-excited Raman Spectrophotometer. . . 201

ACKNOWLEDGMENTS 204

REFERENCES 205

LIST OF FIGURES

No.	Title	Page
1.	Some Schemes for Converting Thermal Energy into Electricity	25
2.	Schematic Diagram of a Thermally Regenerative Galvanic-cell System	27
3.	Temperature-Entropy Diagram for a Thermally Regenerative Galvanic-cell System	28
4.	Periodic Chart Showing Location of Anode and Cathode Materials Suitable for Use in Galvanic Cells	35
5.	Schematic Diagram of the Helium-purification System	39
6.	Schematic Diagram of a Sodium-Bismuth Cell with a Solid Sodium Chloride Electrolyte	40
7.	Current-Voltage Characteristics for the Cell $Na(\ell)/NaCl(s)/40$ a/o Na in $Bi(\ell)$	40
8.	Corrected Potentials for the Cell $Na(\ell)/NaCl(s)/Na$ in Bismuth as a Function of Temperature and Composition	41
9.	Total Vapor Pressures in the Sodium-Bismuth System	44
10.	Diagram of Log Pressure vs. Log Composition for the Sodium-Bismuth System at 1173°K	46
11.	Total Pressure as a Function of Composition for the Sodium-Bismuth System at 1173°K	46
12.	Calculated Emfs for the Cell $Na(\ell)/Na^+$ Electrolyte/Na in $Bi(\ell)$, as a Function of Cathode Alloy Composition for Four Temperatures	47
13.	Diagram of Log Pressure vs. Log Composition for the Sodium-Lead System at 1126°K	48
14.	Total Pressure for the Sodium-Lead System at 1126°K, as a Function of Composition	48
15.	Activity Coefficients of Sodium in Sodium-Bismuth Alloys Calculated from Cell-potential Measurements	49
16.	Comparison of Saturation Concentrations Obtained from Emf Data with the Published Phase Diagram for the Sodium-Bismuth System	50
17.	Standard Free Energy of Formation of NaBi(s) and $Na_3Bi(s)$ as a Function of Temperature from Cell-potential Measurements	50

LIST OF FIGURES

No.	Title	Page
18.	Log of Activity Coefficients as a Function of Composition for the Sodium-Bismuth System	52
19.	Log of Activity Coefficients as a Function of Composition for the Sodium-Lead System at 1126°K	57
20.	Sequence of Schematic Temperature-Composition Phase Diagrams for Sodium-Bismuth System at Decreasing Pressures	59
21.	Experimental Apparatus for Surface-tension Measurements	62
22.	Densities of Several Sodium-Bismuth Alloys as a Function of Temperature	63
23.	Surface Tension of Some Sodium-Bismuth Alloys as a Function of Temperature	63
24.	Densities of Several Sodium-Lead Alloys as a Function of Temperature	64
25.	Density, Viscosity, and Surface Tension for the 15.2 m/o NaF-31.6 m/o NaCl-53.2 m/o NaI System	64
26.	Schematic Diagram of Types 1 and 3 Sodium-Bismuth Cells Used in the Study of Self-discharge Sodium Transfer	66
27.	Schematic Diagram of Type 2 Sodium-Bismuth Cell Used in the Study of Self-discharge Sodium Transfer	67
28.	Schematic Diagram of Type 4 Sodium-Bismuth Cell Used in the Study of Self-discharge Sodium Transfer	67
29.	Self-discharge Sodium-transfer Rate and Conductance at Open Circuit for a Type 1 Sodium-Bismuth Cell as a Function of Temperature	68
30.	Self-discharge Sodium-transfer Rate and Conductance at Open Circuit for a Type 1 Sodium-Bismuth Cell as a Function of Temperature	68
31.	Self-discharge Sodium-transfer Rate of Type 3 Sodium-Bismuth Cells as a Function of Current Density	69
32.	Self-discharge Sodium-transfer Rate in Types 3 and 4 Sodium-Bismuth Cells as a Function of Interelectrode Distance	70
33.	Solution of Eq. 59 for $K_eX_A/\kappa_i = 0.4$, $K_e/\kappa_i = 100$, $K_eX_A = 0.4$, $\kappa_i = 1$	73
34.	Solubility of Sodium-containing Intermetallic Species in Molten Salts	74

LIST OF FIGURES

No.	Title	Page
35.	Thermal-analysis Sample Assembly	76
36.	Crystallization Temperatures for the Binary Systems NaF-NaCl, NaCl-NaI, NaI-NaF	78
37.	Crystallization Temperatures for the Ternary System NaF-NaCl-NaI	79
38.	Open-circuit Potential of a Sodium-Bismuth Cell at 859°K as a Function of Cathode Composition; 38 m/o NaCl-NaI Electrolyte	81
39.	Experimental Sodium-Bismuth Cell	82
40.	Voltage-Current Density Curve for a Sodium-Bismuth Cell at 823°K as a Function of Current Density; 20 a/o Sodium in Bismuth Cathode; Interelectrode Distance = 2.5 cm; Electrolyte Composition = 15.2 m/o NaF-31.6 m/o NaCl-53.2 m/o NaI	82
41.	Improved Sodium-Bismuth Cell with Liquid Electrolyte	82
42.	Voltage of the Sodium-Bismuth Cell as a Function of Current Density	83
43.	Interfacial Sodium Concentration during Charge and Discharge of a Sodium-Bismuth Cell	84
44.	Terminal Voltage during Constant-current Discharge of a Sodium-Bismuth Cell	85
45.	Three-cell Bimetallic Battery Designed to Utilize Liquid Electrodes and a Liquid Electrolyte	86
46.	Bimetallic Battery Designed to Utilize an Immobilized Electrolyte	87
47.	Heat and Mass Balance around a Regenerator and a Condenser	88
48.	Cathode-metal Flow Diagram for a Thermally Regenerative Galvanic Cell	90
49.	Schematic Representation of Density-Temperature-Composition Relationships for Natural Convection Circulation of Cathode Alloys	90
50.	Schematic Representation of Procedure for Graphical Solution of Eq. 89	91
51.	Concentration Distribution in the Liquid-film Model for a Regenerator	93

LIST OF FIGURES

No.	Title	Page
52.	Thermal Regenerator No. 1 for the Sodium-Lead System.	96
53.	Thermal Regenerator No. 2 for the Sodium-Lead System.	98
54.	Flow Diagram of Thermally Regenerative Bimetallic Cell System	98
55.	Heat, Mass, and Momentum Boundary-layer Thicknesses in Gases, Liquids, and Liquid Metals.	101
56.	Thermally Regenerative System Based on a Linear-combination Design.	101
57.	Thermally Regenerative System Based on a Composite Design	102
58.	Composite Thermally Regenerative System Designed for Use with Immobilized Electrolyte	103
59.	Composite Thermally Regenerative System Designed for Use with Immobilized Electrolyte	103
60.	Sodium-Lead Thermally Regenerative System.	104
61.	Voltage of a Sodium-Lead Thermally Regenerative Cell at 848°K as a Function of Current Density	104
62.	Lithium Hydride Cell Assembly	105
63.	Emf of Lithium Hydride Saturated Cell as a Function of Temperature	107
64.	Schematic Diagram of a Lithium-containing Bimetallic Cell with a Reference Electrode of $Li_3Bi(s)$ in Bi	108
65.	Emf for the Cells $Li(\ell)/LiCl\text{-}LiF$ or $LiCl\text{-}KCl/Bi(\ell)$ Saturated with Li_3Bi, as a Function of Temperature.	109
66.	Emf-Temperature-Composition Characteristics of the Cell $Li(\ell)/LiCl\text{-}LiF(\ell)/Li$ in $Bi(\ell)$.	109
67.	Emf-Temperature-Composition Characteristics of the Cell $Li(\ell)/LiCl\text{-}LiF(\ell)/Li$ in $Sn(\ell)$.	109
68.	Emf of a Lithium-Bismuth Cell as a Function of Cathode Composition at T = 750 and 900°K.	110
69.	Emf of a Lithium-Tin Cell as a Function of Cathode Composition at T = 750 and 900°K	110
70.	Emf of the Cell $Li(\ell)/LiCl\text{-}LiF(\ell)/Li$ in $Te(\ell)$, as a Function of Cathode Composition at T = 798°K.	111

LIST OF FIGURES

No.	Title	Page
71.	Schematic Diagram of High-temperature Transpiration Apparatus	112
72.	All-metal Parallel-electrode Assembly for Measuring the Electrolytic Conductivity of Molten Salts	116
73.	Circuit Diagram for the Low-impedance AC Bridge	117
74.	Conductivity of the LiH-LiCl System at 700°K	118
75.	Solubilities of Some Intermetallic Compounds in Fused Salts, as a Function of Temperature	119
76.	Schematic Diagram of Laser-excited Raman Spectrophotometer	122
77.	The Anti-Stokes 459-cm^{-1} Raman Band of Carbon Tetrachloride at 295°K	122
78.	Fused-salt Sample Cell and Its Peripheral Apparatus	124
79.	Raman Spectrum of the $NaNO_3$-KNO_3 Eutectic Mixture at 523°K	125
80.	Absorption Spectrum of Li_2Te in LiCl-LiF (Curve A) and Li_2Te in LiCl (Curve B) at 923°K	126
81.	Absorption Spectrum of Cs_2Te in CsCl at 948°K	127
82.	Absorption Spectrum of Tellurium in CsCl at 948°K	127
83.	Crystallization Temperatures for the Binary Systems LiF-LiBr,[127] LiCl-LiBr,[127] and LiF-LiCl[128]	129
84.	Crystallization Temperatures for the Ternary System LiF-LiCl-LiBr[129]	129
85.	Crystallization Temperatures for the Binary Systems LiF-LiI and LiCl-LiI	130
86.	Crystallization Temperatures for the Ternary System LiF-LiCl-LiI	131
87.	Crystallization Temperatures for the Binary Systems LiH-LiF and LiH-LiCl	133
88.	Crystallization Temperatures for the Binary System LiH-LiBr	133
89.	Crystallization Temperatures for the Binary System LiH-LiI	134
90.	Comparison of Experimental Data for $\Delta\mu^{E}_{LiH}$ with Values Calculated Assuming LiX_2^-, Li^+, and H^-	136

LIST OF FIGURES

No.	Title	Page
91.	Crystallization Temperatures for the Ternary System LiH-LiF-LiCl	137
92.	Crystallization Temperatures for the Ternary System LiH-LiCl-LiI	138
93.	Gas Measuring Apparatus for Hydrogen Permeation Studies	140
94.	Permeation Isobars for Hydrogen through Vanadium and Armco Iron	141
95.	Schematic Diagram of the Electrochemical Cell	143
96.	Voltametric Data for the Lithium Hydride Cell, LiCl-KCl Eutectic, 648°K, Iron Microelectrode	145
97.	Voltametric Data for the Lithium Hydride Cell, LiCl-KCl Eutectic, 648°K, Iron Microelectrode; Hydrogen Atmosphere, 1 atm	146
98.	Effect of Lithium Hydride Concentration on Anodic Limiting Current, LiCl-KCl Eutectic, 648°K, Iron Microelectrode; Hydrogen Atmosphere, 1 atm	146
99.	Heyrovsky-Ilkovic Analysis of Voltametric Curve, LiCl-KCl Eutectic, 648°K, Iron Microelectrode, 8 x 10^{-2} m/o LiH; Hydrogen Atmosphere, 1 atm	147
100.	Overpotential Analysis of Cathodic Voltametric Curve, LiCl-KCl Eutectic, 648°K, Iron Microelectrode, 8 x 10^{-2} m/o LiH; Hydrogen Atmosphere, 1 atm	148
101.	Chronopotentiogram with Tungsten Electrode, LiCl-KCl Eutectic, 648°K; Electrode Area, 0.345 cm^2; Current, 129.7 mA; 25.68 m/o LiH	148
102.	Lithium Hydride Cell with a Vanadium-diaphragm Cathode	151
103.	Current Density-Voltage Curve for a Lithium Hydride Cell with a 0.025-cm Vanadium-diaphragm Cathode at 808°K	152
104.	Current Density-Voltage Curve for a Lithium Hydride Cell with a 0.005-cm Vanadium-diaphragm Cathode at 698°K	152
105.	Calculated Equilibrium Hydrogen Pressure for LiH-LiCl Mixtures	153
106.	Schematic Diagram of the Lithium-containing Bimetallic Cell Used in Voltage-Current Density Measurements	156
107.	Voltage of Lithium-containing Bimetallic Cells as a Function of Current Density; Electrolyte: LiCl-KCl	157

LIST OF FIGURES

No.	Title	Page
108.	Experimental Lithium-Tellurium Cell (Schematic Representation)	158
109.	Steady-state Voltage-Current Density Curves for a Lithium-Tellurium Cell at 743°K	158
110.	Short-time Voltage-Current Density Curve for a Lithium-Tellurium Cell at 748°K	159
111.	Constant-current Voltage-Capacity Curves for a Lithium-Tellurium Cell at 753°K	160
112.	Cross Section of Lithium-Tellurium Cell	160
113.	Current Density-Voltage Characteristics of Lithium-Selenium Cells with and without Iron Additives in the Cathode	161
114.	Estimated Vapor-Liquid Equilibrium Relationships for the Lithium-Tin System	163
115.	Thermal-convection Loop (Schematic Representation) for Dynamic-corrosion Studies	173
116.	Dynamic Corrosion of 1020 Steel and Type 316 Stainless Steel by Liquid Bismuth and Sodium-Bismuth Alloy (1123°K Hot-leg Temperature, 723°K Cold-leg Temperature)	174
117.	Dynamic Corrosion of 1020 Steel and Type 316 Stainless Steel by Sodium-Bismuth Alloys (923°K Hot-leg Temperature, 823°K Cold-leg Temperature)	175
118.	Summary of Published Data for the Static-corrosion Resistance of Materials to Liquid Bismuth, Lead, and Tin	186
A.1.	Schematic Diagram of Helium-purification System	188
C.1.	Schematic Diagram of the Classical Form of the Quasi-static Method for Measuring Vapor Pressures	196
C.2.	Schematic Diagram of the Apparatus Used in an Adaptation of the Rodebush-Dixon (Quasi-static) Technique for Measuring Vapor Pressures	197
C.3.	Transpiration Apparatus (Schematic Diagram)	199
D.1.	Laser-excited Raman Spectrophotometer (Schematic Diagram)	201

LIST OF TABLES

No.	Title	Page
I.	Efficiencies for Thermally Regenerative Bimetallic Cells	32
II.	Total Vapor Pressure for the Sodium-Bismuth System	43
III.	Transpiration Results for the Sodium-Bismuth System at 1173°K	45
IV.	Total Vapor Pressures for the Sodium-Lead System as Measured by Quasi-static Method	47
V.	Transpiration Results for the Sodium-Lead System at 1126°K	48
VI.	C_{ij} Coefficients Derived for Eq. 33	49
VII.	Activities and Activity Coefficients for the Liquid Sodium-Bismuth System at 1173°K	52
VIII.	Activities and Activity Coefficients for the Sodium-Lead System at 1126°K	56
IX.	Characteristics of Sodium-Bismuth Cells Used in Study of Self-discharge Sodium Transfer	66
X.	Self-discharge Sodium Transfer Rate in Type 4 Sodium-Bismuth Cells Operating at 250 mA/cm^2 and 842°K	69
XI.	Crystallization Temperatures for Sodium Systems	77
XII.	Crystallization Temperatures for NaF-NaCl-NaI Ternary	79
XIII.	Calculated Characteristics of Bimetallic Cells with Sodium Anodes	80
XIV.	Emf-Temperature Data for Lithium Hydride Cells Using Indicated Electrolytes	107
XV.	Calculated Values and Literature Values for the Enthalpy, Free Energy, and Entropy of Lithium Hydride	113
XVI.	Coefficients, C_{ij}, Used in Calculating $\Delta\mu^E_{Li}$ in Lithium-Bismuth Alloys	114
XVII.	Coefficients, C_{ij}, Used in Calculating $\Delta\mu^E_{Li}$ in Lithium-Tin Alloys	114
XVIII.	Comparison of Standard Free Energies of Formation for Solid Intermetallic Compounds of Lithium	115
XIX.	Density of LiH-LiCl Mixtures	118
XX.	Molar Volumes of LiH-LiCl Mixtures at 973°K	119

LIST OF TABLES

No.	Title	Page
XXI.	Solid-Liquid Equilibrium Characteristics of Lithium Halide Mixtures	128
XXII.	Crystallization Temperatures for the Systems LiF-LiI and LiCl-LiI	130
XXIII.	Crystallization Temperatures for the System LiF-LiCl-LiI	131
XXIV.	Solid-Liquid Equilibrium Characteristics of Lithium Hydride-Lithium Halide Mixtures	133
XXV.	Crystallization Temperatures for the Binary Systems LiH-LiF, LiH-LiCl, LiH-LiBr, and LiH-LiI	133
XXVI.	Thermodynamic Properties of the System LiH-LiCl	135
XXVII.	Thermodynamic Properties of the System LiH-LiBr	135
XXVIII.	Thermodynamic Properties of the System LiH-LiI	136
XXIX.	Crystallization Temperatures for the System LiH-LiCl-LiF	137
XXX.	Crystallization Temperatures for the System LiH-LiCl-LiI	138
XXXI.	Chronopotentiometric Data, Tungsten Electrode	149
XXXII.	Calculated Characteristics of Bimetallic Cells with Lithium Anodes	154
XXXIII.	Discharge Voltage-Current Characteristics of Lithium-anode Bimetallic Cells	155
XXXIV.	Pressure and Temperature Changes of the Vapor Flow in a Straight Regenerator Tube	164
XXXV.	Summary of Experimental Data in Literature (1950-1965) on Corrosion of Container Materials by Heavy Metals	169
XXXVI.	Static Corrosion of Nonrefractory Metals and Alumina by Bismuth, Tin, and Lead	170
XXXVII.	Static Corrosion of Refractory Metals by Bismuth, Tin, and Lead at 1273°K	171
XXXVIII.	Dynamic Corrosion of Various Materials by Bismuth, Lead, and Sodium-Bismuth and Sodium-Lead Alloys	177
XXXIX.	Relative Stabilities of Some Metal Oxides at 1000°K	182
XL.	Properties of Some Double Oxides with Li_2O	183

NOMENCLATURE ➡

NOMENCLATURE

A	area, cm^2
a	activity, dimensionless
B	constant, variable dimensions, depending on use
b	correction factor
C	molar concentration, $moles/cm^3$
C_{Ab}	molar concentration of component A in the bulk, $moles/cm^3$
C_{Ae}	molar concentration of component A in equilibrium with component B, $moles/cm^3$
C_{Ai}	interfacial molar concentration of component A, $moles/cm^3$
C_{A0}	equilibrium molar concentration of component A, $moles/cm^3$
C_i	molar concentration of component i, $moles/cm^3$
C_{ij}	constant, variable dimensions (see Sections IV.A.3.a and V.A.4.b)
C_p	specific heat at constant pressure, cal/deg-g
$\tilde{C}_p$	molar heat capacity at constant pressure, cal/(mole-deg)
C_v	specific heat at constant volume, cal/deg-g
D	diameter, cm
$\mathcal{D}$	diffusion coefficient, cm^2/sec
$\mathcal{D}_{A-B}$	binary diffusion coefficient, cm^2/sec
$\mathcal{D}_{i-m}$	effective diffusion coefficient, cm^2/sec
d	depth or thickness, cm
$\mathcal{E}$	electromotive force, V
E	cell voltage, V
$E_{1/2}$	half-wave potential, V
E_{a-c}	IR free-cell voltage, V
E_{a-r}	anode vs reference potent
E_{oc}	open-circuit potential, V
Eff_C	Carnot-cycle efficiency (se
Eff_{C-D}	charge-discharge efficienc (see Eq. 25)
Eff_E	voltage efficiency (see Eq.
Eff_G	Gibbs free-energy efficienc (see Eq. 22)
Eff_h	heat-exchange efficiency
Eff_I	current efficiency (see Eq. 20)
Eff_S	system efficiency (see Eq. 23)
$\mathcal{F}$	Faraday constant;
g	acceleration due to gravity, 980 cm/sec^2
g_c	gravitational conversion factor, dimensionless
H	enthalpy, cal
$\Delta H^\dagger$	enthalpy of activation, cal/(g-atom)
$\tilde{H}_A$	molar enthalpy of anode metal, cal/mole
$\tilde{H}_C$	molar enthalpy of cathode metal, cal/mole
ΔH_f	enthalpy of formation, cal
$\Delta \tilde{H}_f$	molar enthalpy of formation, cal/mole
$\Delta \tilde{H}_i$	molar enthalpy of component i, cal/mole
ΔH_0	constant of integration, cal/mole (see Eq. 121)
$\Delta \tilde{H}_v$	molar enthalpy of vaporization, cal/mole
ΔH_v	enthalpy of vaporization, cal
h	film heat-transfer coefficient, $cal/(cm^2\text{-}sec)$
I	current, Amp
I_L	limiting current, Amp
$I_{L,a}$	anodic limiting current, Amp
$I_{L,c}$	cathodic limiting current, Amp
I_0	exchange current, Amp
i	current density, Amp/cm^2
i_C	charging current density, Amp/cm^2
i_D	discharging current density, Amp/cm^2
i_e	partial electrical current density of electrons, Amp/cm^2
i_i	equivalent current density for component i, Amp/cm^2
$i_{i,oc}$	equivalent current density for component i at open circuit, Amp/cm^2
i_L	limiting current density, Amp/cm^2
J	molar flux with respect to fixed coordinates, $moles/(cm^2\text{-}sec)$
J_i	molar flux of component i with respect to fixed coordinates, $moles/(cm^2\text{-}sec)$
j	mass flux with respect to fixed coordinates, $g/(cm^2\text{-}sec)$
j_i	mass flux of component i with respect to fixed coordinates, $g/(cm^2\text{-}sec)$
K	equilibrium constant,
k_c	mass-transfer coefficient, cm/sec
L	length, cm
$l\bar{w}$	lost work, erg
M	molecular weight, g/mole; or atomic weight, g/(g-atom)
M_a	Mach number, dimensionless
M_m	atomic weight of monatomic species, g/mole
m	mass, g
N	number of equivalents per mole, equiv/mole
Nu	Nusselt number for heat transfer, hL/k, dimensionless
n	number of moles
n	number of electrons transferred in the rate-determining step
P	total pressure, atm, dynes/cm
Pr	Prandtl number, $C_p\rho\nu/k$, dimensionless
p_i	partial pressure of component i, atm, $dynes/cm^2$
p_m	partial pressure of monatomic species, atm
Q	heat, cal
q	heat flow rate, cal/sec
$\mathcal{R}$	universal gas constant; 8.3143 joules/(deg-mole), 1.9872 cal/(deg-mole)
R	electrical resistance, ohms
Ra	Rayleigh number, $L^3\rho\beta g\,\Delta T\,C_p/\nu k$, dimensionless
Re	Reynolds number, vD/ν, dimensionless
r	radial distance, cm
S	entropy, cal/deg
ΔS_f	entropy of formation, cal/(mole-deg)
S	conductance per unit depth of immersion of electrodes in electrolyte, mhos/cm
Sc	Schmidt number, $\nu/\mathcal{D}$, dimensionless
T	absolute temperature, °K
T_e	equilibrium temperature, °K
T_m	temperature at the melting point, °K
T_w	temperature at the wall, °K
T_v	temperature of the vapor, °K
V	volume, cm^3
$\tilde{V}$	molar volume, cm^3/mole
$\tilde{V}_i$	molar volume of component i, cm^3/mole
w_C	molar flow rate of cathode metal, moles/sec
w	weight, g (see Section IV.B.1.a)
w	work, erg (see Section III.A.1)
ω	mass flow rate, g/sec
X_i	mole fraction of component i, dimensionless
X_A	mole fraction of anode metal, dimensionless
X_C	mole fraction of cathode metal, dimensionless
x,y,z	coordinate distance, cm

Greek Symbols

α	fraction of the overvoltage aiding the forward reaction, dimensionless
β	thermal coefficient of volumetric expansion, deg^{-1}
γ	activity coefficient, dimensionless
γ_i	activity coefficient of component i, dimensionless
δ	boundary-layer thickness, cm
δ_C	concentration boundary-layer thickness, cm
δ_v	momentum boundary-layer thickness, cm
δ_T	thermal boundary-layer thickness, cm
ζ	ratio of specific heats, C_p/C_v, dimensionless
η	overvoltage, V
θ	time, sec
κ_e	partial electronic conductance, mhos/cm
κ_i	partial ionic conductance, mhos/cm
μ	chemical potential, cal/mole
μ_e	chemical potential of the electrons, cal/mole
μ_i	chemical potential of component i, cal/mole
$\Delta\mu_i^E$	excess chemical potential of component i, cal/mole
$\Delta\mu_i^M$	chemical potential on mixing for component i, cal/mole
ν	kinematic viscosity, cm^2/sec
ρ	density, g/cm^3
σ	standard deviation
τ	transition time (length of plateau), sec
τ_a	anodic transition time, sec
τ_c	cathodic transition time, sec
φ	local electrical potential, V

Subscripts

A	refers to the anode metal
a	refers to the anode
an	refers to the anolyte
C	refers to the cathode meta
c	refers to the cathode
ca	refers to the catholyte
(g)	refers to gas
i	refers to species i
(ℓ)	refers to liquid

GALVANIC CELLS WITH FUSED-SALT ELECTROLYTES

by

E. J. Cairns, C. E. Crouthamel, A. K. Fischer,
M. S. Foster, J. C. Hesson, C. E. Johnson,
H. Shimotake, and A. D. Tevebaugh

I. SUMMARY AND CONCLUSIONS

The rapidly developing technology of today needs a spectrum of electrical power sources, energy converters, and energy storage devices. Much of the energy demand involves the conversion of thermal energy to electrical energy; hence much of the energy-conversion research effort is in this area. The thermally regenerative galvanic cell occupies an important position in energy conversion for specialty applications where silence, simplicity, and unattended operation are important. Such a system is compatible with high-temperature nuclear reactors and radioisotope heat sources. In the area of energy storage, bimetallic cells with fused-salt electrolytes can be operated as secondary cells, which can be charged and discharged at high rates. This makes them attractive in many applications.

The thermally regenerative bimetallic galvanic cells discussed in this report use a relatively volatile liquid-alkali metal having a low electronegativity for the anode, and a relatively nonvolatile liquid metal of high electronegativity for the cathode. In the cell portion of the system, the anode metal is oxidized to form a cation which migrates through the fused-salt electrolyte to the cathode, where it is electrochemically reduced, forming an alloy with the cathode metal. The electrons released at the anode travel through the electrical circuit to the cathode, doing work as they go, finally arriving at the cathode to complete the circuit. The cathode alloy circulates from the cell to a high-temperature regenerator (1050-1600°K), where the anode metal is vaporized away from the cathode metal. The anode metal vapor passes to a relatively cool condensation zone, and the condensate is returned to the anode compartment of the cell, completing the cycle.

The process described above is Carnot-cycle limited, and the maximum theoretical efficiency of the overall conversion process is determined by the temperature of the regenerator and the condenser. Any inefficiencies in the system reduce the overall efficiency to a value below that for the ideal Carnot cycle.

In selecting suitable anode metal-cathode metal pairs, the proper electronegativity differences must be chosen so that the alloy can be separated at reasonable regenerator conditions while still maintaining an appropriate cell voltage (0.5-0.7 V). Furthermore, the electrode materials and the electrolyte should melt at low temperatures to provide a low heat-rejection temperature (and a high Carnot-cycle efficiency). The solubilities of the metal phases in the electrolyte should be minimized to prevent excessive transfer of material by diffusion. Of course, corrosion must be avoided. These considerations indicate the important research areas in the development of a practical galvanic cell system.

Significant differences exist in the properties of the cells and systems, depending on the alkali metal used as the anode. Of the alkali metals, lithium and sodium exhibit the highest cell emf values and have the best physicochemical properties for use in galvanic cell systems. Therefore only lithium and sodium have been investigated in detail. The work is thus classified under the headings: cells with sodium anodes and cells with lithium anodes.

A. Cells with Sodium Anodes

A knowledge of the thermodynamics of the binary alloys comprising the systems of interest for bimetallic cells is important in predicting the ideal behavior of practical cells. The thermodynamic functions of the alloy are used in the calculations of the cell emf, the regenerator temperature and pressure, the purity of the anode metal condensate returned to the cell, and the conditions under which solid formation can be avoided.

Thermodynamic properties of binary sodium-containing alloys have been determined by means of emf and vapor-liquid equilibrium techniques. The free-energy behavior of the sodium-bismuth and sodium-lead systems can be accurately accounted for by means of the quasi-ideal solution theory. This theory allows for the formation of intermetallic compounds in the liquid phase and reflects the thermodynamic behavior of the system in terms of the equilibrium constants of formation for the intermetallic compounds. The sodium-bismuth and sodium-lead systems have been successfully treated by the quasi-ideal solution method.

The results of the thermodynamic studies of binary alloys are important in determining the efficiency of system operation. The sodium-bismuth and sodium-lead systems would not be high-efficiency systems because the regeneration process requires more than one equilibrium stage for an acceptable separation of sodium from the bismuth or lead. For the sodium-bismuth system, the conditions of regenerator operation must be selected so as to avoid the deposition of solid Na_3Bi from the vapor phase. This requires a minimum pressure of 240 Torr (corresponding to a minimum temperature of 1040°K). The sodium-lead system does not suffer from this problem.

The emf of the sodium-lead cell is not high enough (0.3-0.5 V) to make it attractive as a practical device. However, the emf of the sodium-bismuth cell (0.55-0.75 V) does not by itself eliminate this system from further consideration.

To design cells and systems, such physicochemical property data as densities, viscosities, surface tensions, electrolytic conductivities, and solubilities must be available. The following properties were determined for some of the systems: the density of sodium-lead alloys, as a function of temperature and composition; the density and surface tension of sodium-bismuth alloys, as a function of temperature and composition; the density, surface tension, and viscosity of the ternary NaF-NaCl-NaI eutectic, as a function of temperature.

The transfer of electrode material from one electrode to the other in a manner that does not produce electricity in the external circuit is called self-discharge. Under certain conditions, the rate of self-discharge in cells with sodium anodes (transfer of sodium from anode to cathode) is high enough to be of concern as a loss of efficiency. The self-discharge process in sodium-anode cells has been studied as a function of several operating parameters. The rate of self-discharge increases with increasing solubility of the electrode materials in the electrolyte, increases with decreasing electrolyte thickness, and increases with increasing cell voltage.

In connection with the self-discharge process, the solubilities of metals and sodium-containing intermetallic compounds (formed at the cathode) have been determined for several combinations of cathode alloys and electrolytes at several temperatures. As expected, lower temperatures favor lower solubilities. Some intermetallic compounds have surprisingly high solubilities in alkali halide melts and yielded intensely colored solutions, usually some shade of red.

The search for low-melting sodium-cation electrolytes for use with cells having sodium anodes was restricted to halide systems because all the other anions considered are either unstable with respect to liquid sodium or form very high-melting compounds with sodium. The lowest-melting ternary sodium halide electrolyte was 15.2 m/o NaF-31.6 m/o NaCl-53.2 m/o NaI, melting at 802.6°K. This was the electrolyte in most of the cell studies using sodium anodes. The phase diagrams for several other binary and ternary sodium halide systems have also been determined.

Engineering studies of cells, regenerators, and systems with sodium anodes have included the sodium-bismuth cell and the sodium-lead system (cell plus regenerator). The sodium-bismuth cell was operated as an electrically rechargeable (secondary) cell for about 18 months with no performance decline and only minimal corrosion. Subsequent experiments

using the same cell (with some improvements) showed that the sodium-bismuth cell can be operated at current densities in excess of 1 Amp/cm^2 in both the charge and discharge modes. This was the first proof of the fast-charge, high-power density discharge capabilities of bimetallic cells.

The first sodium-lead regenerative system operated reasonably well for a cumulative time of more than 100 hr. The erratic circulation of the cathode alloy first noted in the experiments with the complete system was subsequently investigated using a separate regenerator. These experiments resulted in the design and construction of an improved regenerator which operated smoothly for more than 1000 hr before being shut down. The improved regenerator design has been incorporated into a system, which has been constructed and is currently being prepared for operation.

B. Cells with Lithium Anodes

The thermodynamic properties of those lithium-containing binary systems expected to be suitable for use in thermally regenerative galvanic cells and secondary cells have been studied by means of emf and vapor-liquid equilibrium methods. The results of these thermodynamic studies have been used in choosing the best systems for specified applications and in determining the appropriate conditions for the operation of the cell and the regenerator.

The lithium-hydrogen system (forming lithium hydride) has been studied by means of the emf method. The cell emf as a function of temperature and lithium hydride content (of the electrolyte) has been determined. These data yielded values for the free energy of formation of lithium hydride as a function of temperature.

The emf as a function of cathode alloy composition and temperature has been measured for the lithium-bismuth, lithium-tin, and lithium-tellurium systems. These data have been used to calculate the excess chemical potentials of lithium in the cathode alloys, thereby providing a thermodynamic description of the alloys. The emf data pointed out that the lithium-tin system might be appropriate as a thermally regenerative system, and that the lithium-tellurium system with its relatively high voltages (1.6-1.8 V) should be of interest in secondary cells. In connection with the lithium-tin system, the appropriate vapor-liquid equilibrium measurements are now in progress.

The specific conductances and densities of some of the fused lithium halide electrolyte systems are being determined as an adjunct to the thermodynamic studies. The conductances and densities are expected to aid in the choice among the various thermodynamic models for interpreting the phase-diagram results.

The Raman spectra of fused salts and solutions of intermetallic compounds in fused salts are being determined to obtain information on the structure of the dissolved species. The results are expected to aid in minimizing the rate of self-discharge of bimetallic cells. In addition, the Raman spectra will be of theoretical importance for the determination of the structure of fused salts and solutions of intermetallic compounds in fused salts. A highly sensitive laser-excited Raman spectrophotometer has been constructed, and preliminary experiments with fused nitrates have proved the instrument's capability.

Some visible absorption spectra of intermetallic compounds dissolved in fused-alkali halides have been recorded and have been interpreted in terms of possible structures of the dissolved intermetallics. The compound Li_2Te may exist in solution as $LiTe^-$. This point will be investigated further using Raman spectrometry.

A program of phase-diagram determinations for lithium halide-containing systems has been carried out for the purpose of selecting the most useful electrolytes for the various lithium-anode cells. Several binary and ternary lithium halide systems have been determined for use with lithium-anode bimetallic cells. Various ternary lithium halide systems currently under investigation include LiF-LiCl-LiI, with a minimum melting point of 614.2°K. Comparison of the minimum melting points obtainable with lithium halide systems and the corresponding sodium halide systems show that the lithium halide systems have lower melting points by about 200°K. This is important in two ways: (a) The lower cell-operating temperatures provide for higher Carnot-cycle efficiencies, and (b) lower cell temperatures provide for lower solubilities of the electrode materials in the electrolyte.

Several binary and ternary lithium hydride-containing systems have been investigated for use with the lithium-hydrogen cell. The most suitable electrolyte for this cell was found to be the lithium hydride-lithium chloride-lithium iodide eutectic (14.5 m/o LiH-27.5 m/o LiCl-58.0 m/o LiI) which melts at 606.1°K, providing for a low cell operating temperature and maximizing the Carnot-cycle efficiency.

A thermodynamic analysis of the binary lithium hydride-lithium halide systems has indicated the possibility of the presence of polyatomic ions such as LiX_2^- in the fused-salt mixture. The existence of such species cannot be proved except by some relatively direct method of observation such as spectroscopy. The existence of polyatomic species will be investigated further by spectroscopic techniques.

The hydrogen cathode of the lithium-hydrogen cell is the seat of the rate-determining processes for this cell. Consequently, we have studied both the kinetics of hydrogen permeation through thin metal foils (which serve as hydrogen diffusion cathodes) and the kinetics of hydrogen reduction.

The most suitable material for the rapid diffusion of hydrogen in the cell environment was vanadium; iron and iron-molybdenum alloys showed lower permeation rates by about an order of magnitude.

The rate of the cathodic reduction of hydrogen on pure iron in a fused alkali halide electrolyte was studied using chronopotentiometric and voltametric techniques. The mechanism of hydrogen reduction involves a one-electron rate-determining step, and the rate corresponds to an exchange current density of 1 mA/cm^2. This exchange current density indicates that it is desirable to have an electrode of high surface roughness to provide for an increased geometric current density at low overvoltages.

Complete lithium-hydrogen cells have been studied using 0.005-cm-thick vanadium diaphragm cathodes. Current densities in the range of 100 mA/cm^2 have been obtained at cell voltages as high as 0.35 V, with low concentrations (<2 m/o LiH) of LiH in the electrolyte. Higher performances would probably be obtained with thinner vanadium diaphragms.

A number of bimetallic cells with lithium anodes have been investigated. These have included the Li-Sn, Li-Te, Li-Bi, Li-Cd, Li-Pb, and Li-Zn cells. All these systems showed current densities in excess of 300 mA/cm^2.

Further work on the lithium-tellurium cell has shown that current densities in excess of 5 Amp/cm^2 can be obtained on both charge and discharge. The corresponding power densities (~ 2.5 W/cm^2) and charge rates (less than 15 min for full charge) are higher than those for commercially available secondary cells. This opens up the possibility for many applications of lithium-tellurium secondary cells.

The lithium-tin system is currently under investigation as a thermally regenerative galvanic cell. Because of the very low vapor pressure of tin relative to that of lithium, an excellent separation of lithium from tin can probably be accomplished in a simple, single-stage regenerator with no reflux. Furthermore, the regenerator should operate above 1300°K, while the cell should operate near 600°K, providing for an overall system efficiency near 30%. This is not possible with any presently known sodium system. Engineering studies of the lithium-tin thermally regenerative cell have begun.

The transformation of laboratory cells to more practical configurations is greatly simplified when one or more of the liquid phases are immobilized. Currently, advances are being made in the area of electrolyte immobilization by addition of a high specific-area ceramic filler material to form a rigid paste electrolyte.

C. Materials Stability

To perform experiments and build cells in which liquid alloys and fused salts are used at elevated temperatures, corrosion-resistant metals, alloys, and ceramics must be available. Both static and dynamic materials-stability studies have been performed by exposing various metals of construction to liquid metals and alloys of the group tin, bismuth, lead, sodium, lithium, and tellurium. These experiments led to the conclusion that for cells operating below 600°C and using bismuth, lead, and alloys of these with sodium, ferritic and austenitic stainless steels, low carbon steel, and pure iron are all suitable. For higher temperatures, liquid bismuth, lead, and alloys of these with sodium, and also liquid tin require the use of refractory metals such as tungsten, molybdenum-tungsten alloys, etc. For tellurium and lithium-tellurium alloys below 600°C, pure iron seems suitable based on preliminary tests.

The ceramic material which has been found to be most appropriate for use with cells having sodium anodes is Al_2O_3. Cells with lithium anodes cannot contain Al_2O_3 because of a reaction between alumina and lithium. Double-oxides containing lithium are being investigated as suitable ceramics for use in lithium-anode cells. Other materials of interest include nitrides and phosphides.

D. Conclusions

In addition to the specific conclusions at the end of each section of this report, the following general conclusions can be reached:

1. Both the emf and the vapor-liquid equilibrium techniques are useful in determining thermodynamic properties of liquid alloys containing alkali metals and metals of higher electronegativity. The emf technique is more useful at the lower temperatures, where vapor pressures are below a few Torr; the vapor-liquid equilibrium methods are more useful at higher temperatures, where the solubility of the alloy (or its constituents) in the electrolyte interferes with the emf method. In the intermediate-temperature region, the two methods are in close agreement.

2. The use of the quasi-ideal solution theory in the treatment of the thermodynamic data for the sodium-bismuth and sodium-lead systems is consistent with the idea of compound formation in the liquid phase. Further investigation is warranted.

3. Phase-diagram determinations by the thermal-analysis method have pointed out several ternary alkali halide electrolyte systems that are useful for thermally regenerative and secondary galvanic cells. Lithium halide-containing systems have particularly low melting points.

4. Spectroscopic studies and liquid-solid equilibrium studies of solutions of intermetallic compounds in fused alkali halides have indicated that at least some intermetallic compounds dissolve as polyatomic species, yielding highly colored solutions.

5. Studies of lithium-hydrogen cells indicate that their performance is limited by the hydrogen cathode to values below 100 mW/cm^2. The relatively modest cell voltages and current densities (compared to bimetallic cells) cause this cell to be of limited interest.

6. Studies have indicated that some bimetallic cells are capable of very high power densities (3.5 W/cm^2 for lithium-tellurium and lithium-selenium cells) and very high recharge rates (less than 15 min for full charge). These characteristics open up the possibility of many applications for bimetallic cells as energy storage devices.

7. Studies of thermally regenerative systems have shown that sodium-anode systems can be regenerated continuously for extended periods of time (in excess of 1000 hr) to prove the feasibility of continuous thermal regeneration. Further work on systems of potentially higher efficiency, such as lithium-tin, is warranted.

8. Materials-compatibility investigations have indicated that stainless steels and some other ferrous alloys are suitable for use with bimetallic systems below 600°C. For higher temperatures (as in regenerators), refractory metals and their alloys are necessary. Ceramic materials, such as alumina, and double metal oxides, such as $LiAlO_2$, are presently the best choices as insulators and fillers.

II. INTRODUCTION

One of the chief requirements of our rapidly developing technology is a versatile array of electrical power sources, energy converters, and energy storage devices. The most ubiquitous form of energy is probably heat, while the most useful form is electricity. The efficient, economical conversion of heat to electricity is the objective of much of the present technological effort in energy conversion.

Some of the devices for the conversion of thermal energy to electrical energy are indicated schematically in Fig. 1. The piston engine includes various types of internal-combustion engines. These devices have the advantages of being relatively inexpensive (less than $100/kW) and having high power-to-weight ratios, in the range of 10 W/lb for the size range 1-10 kW.[1,2] Internal-combustion engines have the disadvantages of being noisy, not being very reliable (1000-1500 hr of operation between major overhauls),[1] and having only moderate thermal efficiency (10 to 13%).[1,2] Gas turbines are more reliable than piston engines and have a higher power-to-weight ratio but are more expensive (up to $1000/kW) and less efficient (8-10%).[1] Both of these devices contribute significantly to air pollution.

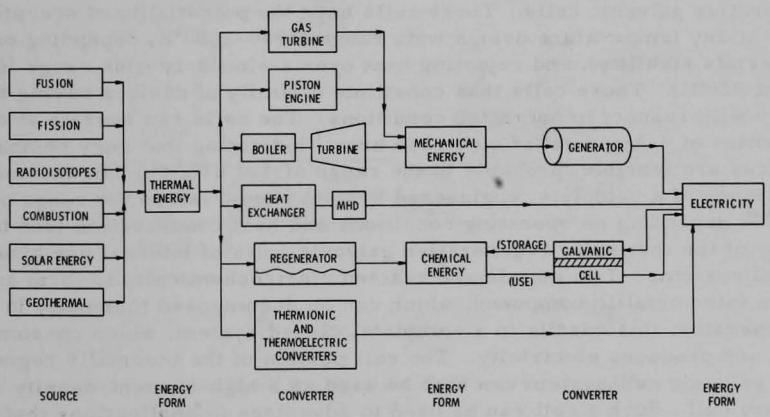

308-511

Fig. 1. Some Schemes for Converting Thermal Energy into Electricity

Of the direct energy-conversion devices, which in general are not yet well developed, the thermionic converter has demonstrated the highest efficiency (12-16%),[3,4] power densities of 4 to 5 W/cm^2 having been achieved in small engineered converters (100-200 W total power).[4] To obtain these high efficiences, high cathode temperatures (1750°K) are necessary.[4] A typical value for power per unit volume for a thermionic converter system with heat source would be about 1 kW/ft^3. Thermoelectric converters

operate at lower temperatures (1200°K and below), lower efficiences (3-5%),[5,6] and lower power densities, and result in bulkier systems which have a power per unit volume of about 100 W/cu ft.[6] Thermionic and thermoelectric devices have an advantage over internal-combustion engines and gas turbines in that they have no moving parts. Therefore, they can be made relatively silent and maintenance-free, and are long-lived, an advantage for military and remote applications.

A disadvantage of thermionic and thermoelectric devices is their very high capital cost. In thermionic converters, the high cost is necessitated partly by the close spacing of emitter and collector, and partly by the expensive materials and technology required by the high temperatures and heat flux densities necessary for efficient operation. Because of the high materials costs for the thermoelectric couples, the thermoelectric devices are expensive, and, because of their inefficiency, they require a large amount of material for a given power output.

A system is needed that can (1) convert heat to electricity, at efficiencies at least as high as those presently available with the above systems (10-15%), (2) have a long life, (3) have no moving parts, and (4) have a reasonable cost. These needs may eventually be fulfilled by thermally regenerative galvanic cells. These cells have the potentiality of accepting heat at any temperature over a wide range (1050-1600°K, depending on materials stability), and rejecting heat over a similarly wide range (600 to about 925°K). These cells thus constitute a family of devices having flexibility with respect to operating conditions. The cells can operate at current densities of 1 Amp/cm^2 of electrode area,[7] indicating that very compact devices are feasible, probably in the range of 1-2 kW/ft^3. The thermal efficiency of a complete, engineered system should fall in the range of 9-30%, depending on operating conditions and heat conservation (see below). Many of the thermally regenerative galvanic cells of interest use binary metal systems. Two metals are reacted electrochemically to form an alloy or an intermetallic compound, which can be decomposed thermally in a regenerator; this results in a complete, closed system, which consumes heat and produces electricity. The cell portion of the thermally regenerative galvanic cell system can also be used as a high-current-density secondary cell. Such a cell can be used to advantage in applications that demand both rapid charge and rapid discharge.

Both thermally regenerative galvanic cells and secondary bimetallic cells have been studied at Argonne National Laboratory for several years.[8-23] Argonne's research and development work on these systems will be discussed in detail in this report.

III. GALVANIC CELLS--GENERAL CONSIDERATIONS

A. Thermally Regenerative Cells

A typical thermally regenerative galvanic-cell system is shown schematically in Fig. 2. The system consists primarily of a galvanic cell to produce electricity, a regenerator to thermally decompose the product of the cell reaction into the original reactants, and a heat exchanger to conserve heat. Energy from the heat source is used in the regenerator to vaporize the relatively volatile anode metal A away from the liquid cathode alloy at temperature T_2. The vapor (pure A) passes over to the condensation zone, where it rejects its heat of vaporization at temperature T_1 and returns to the galvanic cell (also at T_1). Concurrently, the cathode alloy, depleted of metal A, returns to the cell after passing through a heat exchanger, where it is cooled to temperature T_1 by the cathode alloy leaving the cell. In the cell, the following electrode reactions take place:

$$\text{Anode:} \quad A \rightarrow A^+ + e^- \tag{1}$$

$$\text{Cathode:} \quad A^+ + e^- + C \rightarrow AC \text{ (in C)}. \tag{2}$$

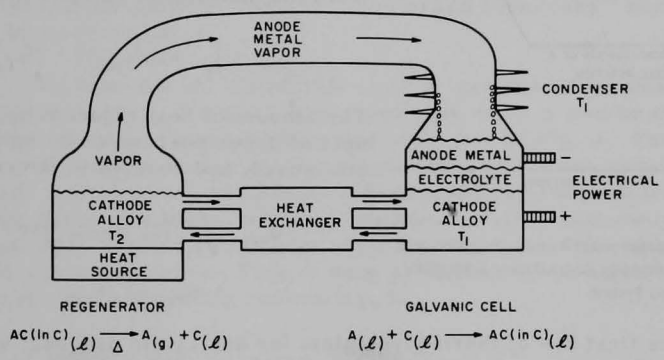

308-512

Fig.2. Schematic Diagram of a Thermally Regenerative Galvanic-cell System

The anode metal A is electrochemically oxidized to form the ion A^+, which migrates through the electrolyte to the cathode. At the cathode, metal A is reduced to the zero-valent state and dissolved in the cathode metal C, where it may form an intermetallic compound such as AC. The electrons flow through an external electrical circuit, doing work as they go. The driving force for the electrons is the tendency of metal A to form an alloy and/or an intermetallic compound with metal C. This tendency is measured by the Gibbs free-energy change for the reaction, which is directly related to the electromotive force for the cell reaction:

$$\Delta \underset{\sim}{G} = -NF\underset{\sim}{E}. \tag{3}$$

The electrolyte should contain a reasonable concentration of A^+ ions so that the electrode reactions can take place rapidly with no diffusion limitation due to a shortage of A^+ ions at the cathode surface.

1. Carnot-cycle Efficiency (Eff_C)

The maximum efficiency at which this closed-cycle system and the other systems discussed above can operate is the Carnot-cycle efficiency, given by

$$Eff_C = \frac{T_2 - T_1}{T_2}. \tag{4}$$

This can be verified by considering the reversible cycle on a temperature-entropy diagram, as shown in Fig. 3. The amount of heat supplied to the system is the amount required for heating from T_1 to T_2 the quantity of cathode alloy containing one gram-atom of A, plus the amount of heat required to vaporize one gram-atom of the volatile metal A away from the nonvolatile cathode metal C,

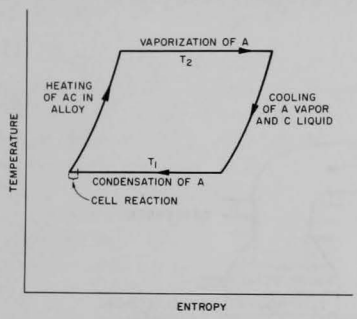

308-514

Fig. 3. Temperature-Entropy Diagram for a Thermally Regenerative Galvanic-cell System

$$Q_{in} = \int_{T_1}^{T_2} n_{AC}\tilde{C}_{p_{AC}} dT + \Delta \tilde{H}_{v_{T_2}}. \tag{5}$$

The amount of heat rejected by the products of decomposition on being cooled, condensed, and reacted in the cell is

$$Q_{out} = \int_{T_1}^{T_2} \left(\tilde{C}_{p_A} + n_C\tilde{C}_{p_C}\right) dT + \Delta \tilde{H}_{v_{T_1}} - T_1 \Delta \tilde{S}_{cell}. \tag{6}$$

From the first law of thermodynamics, for any cyclic process, w = Q. That is, the amount of work available equals the net amount of heat supplied. Therefore,

$$w = Q_{in} - Q_{out} \tag{7}$$

or

$$w = \int_{T_1}^{T_2} \left(n_{AC}\tilde{C}_{p_{AC}} - \tilde{C}_{p_A} - n_C\tilde{C}_{p_C}\right) dT + \Delta \tilde{H}_{v_{T_2}} - \Delta \tilde{H}_{v_{T_1}} + T_1 \Delta \tilde{S}_{cell} \tag{8}$$

From the second law of thermodynamics, there is no entropy change for the system on passing reversibly through a complete cycle. That is,

$$d\underset{\sim}{S} = \frac{\Delta \underset{\sim}{H}_{v_{T_2}}}{T_2} - \frac{\Delta \underset{\sim}{H}_{v_{T_1}}}{T_1} + \oint_{T_1}^{T_2} \left(\frac{n_{AC}\tilde{C}_{p_{AC}} - \tilde{C}_{p_A} - n_C\tilde{C}_{p_C}}{T} \right) dT$$

$$+ \Delta \underset{\sim}{S}_{cell} = 0. \tag{9}$$

Solving Eq. 9 for $\Delta \underset{\sim}{H}_{v_{T_1}}$ and substituting this into Eq. 8 produces

$$w = \Delta \underset{\sim}{H}_{v_{T_2}} \left(\frac{T_2 - T_1}{T_2} \right) + \oint_{T_1}^{T_2} \left(\frac{T - T_1}{T} \right) \left(n_{AC}\tilde{C}_{p_{AC}} - \tilde{C}_{p_A} - n_C\tilde{C}_{p_C} \right) dT. \tag{10}$$

For the special case of $\left(n_{AC}\tilde{C}_{p_{AC}} - \tilde{C}_{p_A} - n_C\tilde{C}_{p_C} \right) = 0$, Eq. 10 reduces to

$$\mathrm{Eff}_C = \frac{w}{\Delta \underset{\sim}{H}_{v_{T_2}}} = \frac{T_2 - T_1}{T_2}, \tag{11}$$

which is the Carnot-cycle efficiency. Hesson and Shimotake[24] have discussed this case in more detail.

We have not yet shown that work w can indeed be obtained from the galvanic cell. We have only shown that work w can be obtained in some form from a system operating on the cycle of Fig. 3. For a simple system in which metal A can be separated completely from metal C by single-stage vaporization, and in which no specific interactions modifying the specific heats take place, we can show that the electrical energy from the galvanic cell, divided by the heat input to the regenerator, is equal to the Carnot-cycle efficiency. This is done as follows: The electrical energy from the cell, when operating reversibly, is

$$\text{Energy out} = N\underset{\sim}{F}\underset{\sim}{E} = -\underset{\sim}{R}T_1 \ln \frac{a_{A \text{ in } C}}{a_{\text{pure } A}}. \tag{12}$$

The activity of pure A is unity, and the activity of A in C at the cell temperature is given by

$$a_{A \text{ in } C} = \frac{f_A}{f_A^\circ} \simeq \frac{p_A}{p_A^\circ}.$$

Since the regenerator and the cell are at equal pressures,

$$p^\circ_{A_{T_1}} = p_{A_{T_2}},$$

and Eq. 12 becomes

$$NF\underset{\sim}{E} = -\underset{\sim}{R}T_1 \ln \frac{p_{T_1}}{p_{T_2}}, \tag{13}$$

where p is the partial pressure of metal A over the cathode alloy. The heat input to the regenerator is given by $\Delta\underset{\sim}{H}_{v_{T_2}}$, provided that

$$n_{AC}\tilde{C}p_{AC} - \tilde{C}p_A - n_C\tilde{C}p_C = 0.$$

We now have

$$\frac{\text{electrical energy out}}{\text{heat energy in}} = \frac{\underset{\sim}{R}T_1 \ln \frac{p_{T_2}}{p_{T_1}}}{\Delta\underset{\sim}{H}_{v_{T_2}}}. \tag{14}$$

The Clapeyron equation gives the following useful relationship between the pressure and $\Delta\underset{\sim}{H}_v$:

$$\Delta\underset{\sim}{H}_v = T\Delta V \frac{dp}{dT}, \tag{15}$$

where $\Delta V = V_{(g)} - V_{(\ell)}$. For systems at high temperature and low pressure, as in regenerators, $V_{(g)} >> V_{(\ell)}$, and $V_{(g)} = \underset{\sim}{R}T/p$; therefore,

$$\Delta\underset{\sim}{H}_v = \frac{\underset{\sim}{R}T^2}{p} \cdot \frac{dp}{dT}, \tag{16}$$

and, where $\Delta\underset{\sim}{H}_v$ is constant,

$$\ln \frac{p_{T_2}}{p_{T_1}} = -\left(\frac{\Delta\underset{\sim}{H}_v}{T_2\underset{\sim}{R}} - \frac{\Delta\underset{\sim}{H}_v}{T_1\underset{\sim}{R}}\right). \tag{17}$$

Substituting Eq. 17 into Eq. 14 yields

$$\frac{\text{electrical energy out}}{\text{heat energy in}} = \frac{T_1\left(\frac{\Delta\underset{\sim}{H}_v}{T_1} - \frac{\Delta\underset{\sim}{H}_v}{T_2}\right)}{\Delta\underset{\sim}{H}_v}. \tag{18}$$

Equation 18 reduces to

$$\frac{\text{electrical energy out}}{\text{heat energy in}} = \frac{T_2 - T_1}{T_2} = \text{Eff}_C. \tag{19}$$

Where compounds such as AC form, then

$$\int_{T_1}^{T_2} \left(n_{AC}\tilde{C}_{p_{AC}} - \tilde{C}_{p_A} - n_C\tilde{C}_{p_C} \right) dT$$

is not zero, $\Delta\tilde{H}_{v_{T_2}}$, is not equal to $\Delta\tilde{H}_{v_{T_1}}$, and the expression for efficiency does not reduce directly to the Carnot-cycle efficiency; however, it can never exceed the Carnot-cycle efficiency.

2. Current Efficiency (Eff_I)

In addition to the Carnot-cycle efficiency, which represents the upper limit when all portions of the system operate reversibly, other efficiencies must be taken into account. The current efficiency (Eff_I) represents the fraction of the reactants consumed by the galvanic process, which results in current I being delivered to the external circuit; that is,

$$Eff_I = \frac{I}{NF\left(\frac{dn}{d\Theta}\right)} \tag{20}$$

where $dn/d\Theta$ is the rate of consumption of anode metal in moles/sec. Eff_I will be less than unity if any side reactions or unintentional consumption of reactants takes place. The unintentional consumption of reactants can be classified as a self-discharge process. The transfer of either reactant to the opposite electrode by means of dissolution in, and diffusion through, the electrolyte is such a process. Another source of decreased current efficiency is the electrochemical consumption of reactants caused by the internal electrical short-circuiting effect of electronic conduction in the electrolyte. This electronic conduction can be caused by anode or cathode metal dissolved in the electrolyte. The larger the concentration of dissolved metal, the higher the electronic conductivity. It is, therefore, desirable to minimize the solubility of anode and cathode metals in the fused-salt electrolytes. This is generally done by proper choice of systems and by minimizing the operating temperature.

3. Voltage Efficiency (Eff_E)

The voltage efficiency (Eff_E) represents the fraction of the cell voltage available to the external circuit for useful work.[25,26] The difference between the emf $\tilde{E}$ for the cell operating reversibly and the operating-cell voltage E represents the sum of all voltage losses due to various irreversibilities such as concentration overvoltage (slow mass transport), activation overvoltage (slow electrode reactions), resistance overvoltage (ohmic losses), and the overvoltage caused by the self-discharge processes mentioned above. The voltage efficiency is, therefore,

$$\mathrm{Eff}_E = \frac{E}{\underset{\sim}{E}} = \frac{\underset{\sim}{E} - \eta}{\underset{\sim}{E}}, \tag{21}$$

where η is the total overvoltage.

4. Gibbs Free-energy Efficiency (Eff_G)

The rate of energy conversion by the cell is, of course, EI, and the Gibbs free-energy efficiency (Eff_G) is correspondingly[25,26]

$$\mathrm{Eff}_G = \mathrm{Eff}_E \cdot \overline{\mathrm{Eff}_I}. \tag{22}$$

The Gibbs free-energy efficiency is a measure of the cell efficiency, in terms of the fraction of the chemical energy converted into useful electrical energy.

5. Overall Efficiency (Eff_S)

The overall efficiency (Eff_S) of the system (cell plus regenerator) is given by

$$\mathrm{Eff}_S = \frac{\int EI d\Theta}{Q_{in}} \tag{23}$$

and is always less than the Carnot-cycle efficiency. In the absence of unintentional heat losses to the surroundings, the system thermal efficiency is

$$\mathrm{Eff}_S = \mathrm{Eff}_C \cdot \mathrm{Eff}_G \cdot \mathrm{Eff}_h, \tag{24}$$

where Eff_h is the heat-exchange efficiency, which is a measure of how well the heat-exchange process is carried out between the cell and the regenerator. Hesson and Shimotake[24] have estimated Eff_S for several thermally regenerative systems, some of which are summarized in Table I. For regenerator temperatures of 1073-1323°K and cell temperatures of 698-859°K, system efficiencies of 11 to 14% were estimated, based on Eff_G values of 0.5 to 0.6.

TABLE I. Efficiencies for Thermally Regenerative Bimetallic Cells[a]

System	Li-Sn	Na-Sn	Na-Pb	Na-Bi
Regeneration temperature, T_2, °K	1323	1073	1100	1310
Condenser temperature, T_1, °K	1005	785	795	859
Regeneration pressure, P, Torr	0.75	5.3	6.38	4.9
Carnot-cycle efficiency, Eff_C, %	24	27	27	38
Gibbs free-energy efficiency, Eff_G, %	60	60	60	60
Heat-exchange efficiency, Eff_h, %	75	75	75	75
Overall efficiency, Eff_S, %	11	12	12	12

[a]Computed for 20 m/o anode metal in cathode metal.

From an efficiency standpoint, it is desirable to have a high regeneration temperature, e.g., 1500°K (which may be feasible with the lithium-tin system), and a low cell temperature (623°K can be achieved with ternary lithium halide electrolytes; see Section V.C). This situation corresponds to a Carnot-cycle efficiency of 0.585. A value of 0.75 is reasonable for the heat-exchange efficiency Eff_h, including the small losses in the regenerator. By minimizing the cell temperature, we can reduce the self-discharge process to a low rate, so that a value of Eff_G of 0.7 can be obtained at reasonable current densities. The overall system efficiency for this case (Li/LiX/Li in Sn; T_2 = 1500°K, T_1 = 623°K) is 0.31. This figure represents a goal that might be achieved, not the current status.

6. Cell and Regenerator Requirements

The selection of appropriate bimetallic systems for thermally regenerative galvanic cells is difficult because of the many requirements to be fulfilled. Some of these requirements for the cell are:

a. The anode metal should have a low electronegativity; i.e., it should give up electrons readily and, therefore, occupy a high position in the electromotive series that obtains in fused-salt media.

b. The cathode metal should have a high electronegativity, occupying a relatively low position in the electromotive series.

c. The anode and cathode metals should form intermetallic compounds with reasonably large negative free energies of formation, so that the cell voltage is high enough to tolerate a reasonable overvoltage without serious efficiency losses.

d. The anode and cathode metals must melt at temperatures below the desired cell-operating temperature (500-850°K).

e. The anode and cathode metals and their intermetallic compounds should have low solubilities in the electrolyte at the cell operating temperature.

f. The electrolyte should have a low melting point, a low vapor pressure, and a high ionic conductance at the cell-operating temperature.

g. The electrolyte should contain a large concentration of the anode metal cation, preferably only the anode metal cation.

h. Anode metal, cathode metal, and electrolyte should not attack cell construction materials.

Requirements for the regenerator are:

a. The anode metal should be much more volatile than the cathode metal so that they be easily separated.

b. The intermetallic compounds should be of only moderate stability so that they can be decomposed at regeneration temperatures (up to about 1500°K).

c. On the temperature-composition phase diagram, the vapor-liquid loop should not intersect the solid-liquid equilibrium line at the pressure of regenerator operation.

d. The regenerator should operate at the maximum reasonable vapor pressure of the anode metal in order to maximize the regeneration rate.

e. The regenerator should not be corroded by the cathode alloy at the regeneration temperature.

Bimetallic cells meriting further consideration are limited by the cell requirements. The anode metals fulfilling cell requirements a and d include the alkali metals Li, Na, K, Rb, and Cs. The cathode metals satisfying cell requirements b and d include such metals as Zn, Cd, Hg, Ga, In, Tl, Sn, Pb, P, Sb, Bi, Se, and Te.* The alkali metals show higher cell potentials as the atomic weight decreases, lithium being most attractive from both a voltage and a weight viewpoint. In addition, a nonmetal of particular interest as a cathode reactant is hydrogen. With respect to cell requirement c, the free energies of formation of many of the intermetallic compounds formed by the anode and cathode metals are not known. A method of selecting systems of interest that does not require this knowledge is therefore desirable. As pointed out by Foster[11] and by Fischer,[27] indications of compound formation and stability can be obtained from the phase diagrams.[28] The higher the melting point of the intermetallic compound, the more stable it is. The intermetallic compounds formed between the alkali metals and the cathode metals mercury, gallium, and indium do not have a large enough (negative) free energy of formation[29] to be of further interest for most applications.

Cell requirement e is best satisfied by the lower-atomic-weight alkali metals, the solubility of the alkali metals in their halide salts increasing with atomic weight.[30-34] This requirement eliminates cesium, rubidium,

*The locations of these elements on the periodic chart are indicated by the white areas in Fig. 4. Generally speaking, the electronegativity of the elements increases toward the upper right-hand portion of the chart, but the electrical conductivity decreases. Therefore a compromise region of interest results, as indicated by the white area on the right-hand side of Fig. 4.

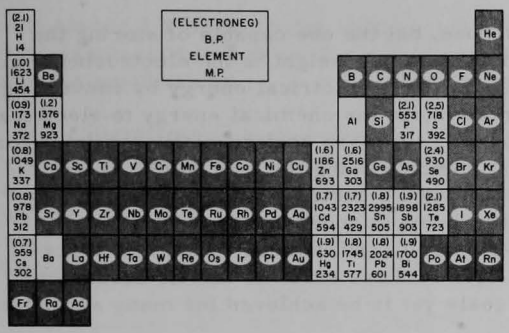

108-9004 Rev. 2

Fig. 4. Periodic Chart Showing Location of Anode and Cathode Materials Suitable for Use in Galvanic Cells

and probably potassium from further consideration. Ternary mixtures of halides satisfy cell requirements f and g; for the sodium system, the NaF-NaCl-NaI eutectic is useful,[23,25] and for the lithium system, some ternary halide mixtures, including the LiF-LiCl-LiI and LiCl-LiI-KI, are particularly attractive.[36] Cell requirement h can be satisfied by stainless steels and other ferrous alloys where metals are to be used.[22,24] Alumina is adequate as an insulator in sodium-anode cells, but some other material, probably a double oxide, will be necessary for lithium-anode cells.

Considerations of regenerator requirements limit the number of bimetallic systems worthy of further study. Both lithium and sodium are volatile enough to be useful in thermally regenerative cells, although lithium is limited to regenerator temperatures above 1250°K, while sodium should be useful at temperatures as low as 1000°K. In the lithium-hydrogen cell, with hydrogen as a cathode reactant, the compound LiH is easily decomposed thermally, and the hydrogen and lithium are separated.[37] The requirement of very low volatility for the cathode metals eliminates Zn, Cd, Hg, Se, and Te from further consideration.[38] In the lithium-anode systems, lead and bismuth were not included as suitable cathode materials because they have vapor pressures too close to that of lithium,[38] making the separation process more difficult. Since sodium has a much higher vapor pressure than lithium, the regeneration process can be carried out with the sodium-lead and sodium-bismuth systems. This leaves the following bimetallic systems for more detailed study:

Sodium Anode	Lithium Anode
Na-Bi	Li-Sn
Na-Pb	Li-H_2
Na-Sn	

The systems suitable for thermal regeneration that have been investigated at Argonne are Na-Bi, Na-Pb, Li-Sn, and Li-H_2. These systems will be discussed in detail in Sections IV and V of this report.

B. Secondary Cells--The Storage of Electricity

In addition to the conversion of thermal energy to electricity, means for the storage of electrical energy are also important. Several

devices are available for this purpose, but the one capable of storing the largest amount of energy-per-unit volume or weight is the electrochemical cell. The so-called secondary cell* stores electrical energy by converting it to chemical energy, and then reconverts the chemical energy to electrical energy on demand. Several secondary cells are commercially available for this application, some of the most common being the lead-acid battery ($Pb/H_2SO_4/PbO_2$) used in automobiles and industrial vehicles, the nickel-cadmium cell ($Cd/KOH/Ni_2O_3$) used in applicances and some portable military devices, and the silver-zinc cell ($Zn/KOH/Ag_2O$) used in spacecraft and aircraft applications. Each of these systems has its advantages and disadvantages. Some of the goals yet to be achieved for many secondary-cell applications are:

a. Fast charge acceptance without deterioration of capacity or current-voltage characteristics. Present cells require several hours for charging.

b. High current-density discharge without damage to cells. Present cells lose capacity when discharged rapidly on a repeated basis.

c. Higher energy-to-weight ratios. Lead-acid and nickel-cadmium batteries average 10-20 W-hr/lb. Ratios above 50 W-hr/lb (or 397 W-sec/g) are desired for many applications.

d. Longer cycle-life. More than 1000-2000 cycles, including fast charge-fast discharge operation, are desired.

e. Longer shelf-life. Storage periods in excess of one year are sometimes required.

To achieve high charge and discharge rates with good charge-discharge efficiencies,

$$\mathrm{Eff}_{C\text{-}D} = \frac{(\int EId\theta)\ \text{charge}}{(\int EId\theta)\ \text{discharge}}, \tag{25}$$

the electrode reactions must be reversible with low overvoltages at high current densities and the internal resistance of the cell must be minimized. Many fused-salt electrolytes have higher conductivities (lower resistances) than either aqueous or nonaqueous (organic) electrolytes, including those normally used in secondary cells. The loss of efficiency due to resistive losses and overvoltage losses can be minimized by using the highest voltage couple available. For example, a loss of 0.2 V is 40% of the cell voltage for a cell having 0.5 V open-circuit voltage, but is only a 10% loss for a

*A secondary cell is defined as an electrochemical cell that can be recharged electrochemically, reversing the electrochemical reaction that takes place on discharge.

cell having 2 V open-circuit voltage. In addition, high-voltage cells have the advantage that fewer cells are required for series connection in higher-voltage applications.

Significantly higher energy-to-weight ratios are impossible for many secondary cells (e.g., lead-acid and nickel-cadmium) since the mass of the anode and cathode materials is the major contribution to the total cell weight. By using high-voltage couples and elements of low equivalent weight, we can obtain a significant increase in the energy-to-weight ratio, as will be illustrated by the lithium-tellurium cell described in Section V.

Longer cell cycle-life is difficult to achieve in ordinary secondary cells because of the difficulty in redepositing the anode material in the desired physical form (no dendrites or uneven deposition) during the charging process. Liquid-metal electrodes do not suffer from this problem. Very long shelf-life is possible with fused-salt bimetallic cells because they are stored with all components in the solid form. The cell is inert until heated to operating temperature.

The selection of bimetallic systems for use in secondary cells imposes somewhat different requirements from those for thermally regenerative systems. Of course, none of the thermal regeneration requirements need be met. This means that much stronger interactions between anode and cathode metals can be allowed, with the formation of more stable intermetallic compounds and the yielding of higher cell voltages. In addition, no relative volatility restrictions are necessary. For secondary cells with high energy-to-weight ratios, the systems worthy of detailed investigation are primarily those with lithium and sodium anodes, because lithium and sodium are higher in the electromotive series than the other alkali metals and have the lowest equivalent weights. Some of the systems suitable for use as secondary cells that have been investigated at Argonne are: Na-Bi, Li-Bi, Li-Sn, Li-Te, Li-Se, Li-Cd, Li-Zn, and Li-Pb. The lithium systems have been favored for secondary cells because of the higher cell voltages, lower operating temperatures (615-725°K for lithium cells versus 810-900°K for sodium cells), and generally lower solubilities of lithium and lithium intermetallic compounds in the electrolyte.

The following sections will discuss in more detail the research and engineering work on galvanic cells with fused-salt electrolytes performed at Argonne.

IV. CELLS WITH SODIUM ANODES

The research and engineering work on galvanic cells with fused-salt electrolytes can be divided into two parts. The first part (Section IV) describes the work applicable to cells having sodium anodes; the second part (Section V) does the same for cells having lithium anodes. The work described in this section emphasizes the thermodynamic properties of binary alloys containing sodium at cell and regenerator temperatures. Also reported are phase relationships for some sodium halide electrolytes, some of the physicochemical properties of sodium-containing alloys and electrolytes, and studies of cells, regenerators, and systems.

A. Thermodynamics of Sodium-containing Systems

To predict the ideal behavior of a galvanic cell, the values of the thermodynamic functions for the cell reaction must be known. For a bimetallic cell with an alkali-metal anode, the chemical potential of the alkali metal in the binary cathode alloy may be used to calculate the open-circuit potential of the cell if the cell is a concentration cell without transference.[39] In addition, the chemical potential of the alkali metal in the cathode alloy is useful in calculating the partial pressure of the alkali metal over the alloy for various proposed regeneration conditions.

Two general techniques have been used to elucidate the thermodynamic properties of binary alloys containing alkali metals. The first is the emf technique, in which the open-circuit potential of a reversible cell is measured as a function of temperature and (cathode) alloy composition. The second is the vapor-pressure technique, in which one measures the pressure and composition of the vapor in equilibrium with a liquid alloy as a function of temperature and alloy composition. In most cases, the emf technique appears to be the better at low temperatures, where the vapor pressure of the alloy is low. At high temperatures, however, operation of a cell can prove difficult for several reasons, and the vapor-pressure method is better.

1. Thermodynamic Measurements by the Emf Method

The reversible open-circuit potential of a cell is directly related to the thermodynamic properties of interest. Therefore, in using the emf technique, one usually chooses to operate cells that by design are not capable of producing significant currents. For example, several workers in the past have operated cells with sodium anodes in which the electrolyte consisted of a glass containing sodium ions.[40,41] Similarly, electrolytes of solid NaCl have been used in this laboratory.[42] Electrolytic conduction in solid, single-crystal NaCl is known to take place exclusively by the migration of the sodium ion at 673°K, the migration of the chloride ion becoming more important at higher temperatures.[43]

Since the alkali metals and their alloys react rapidly with water vapor and oxygen, all the cells were operated in a helium atmosphere, using furnace wells attached to an inert atmosphere working enclosure containing high-purity helium.* The helium was continuously recirculated through a purification system as shown in Fig. 5. Details of this system are given in Appendix A. The most important unit in the system is the activated carbon bed held at the boiling point of liquid nitrogen. As a result of the efficacy of the purification system, the atmosphere of the working enclosure routinely contained as impurities less than 1.5 ppm water vapor and less than 5 ppm each of oxygen and nitrogen.[44,45]

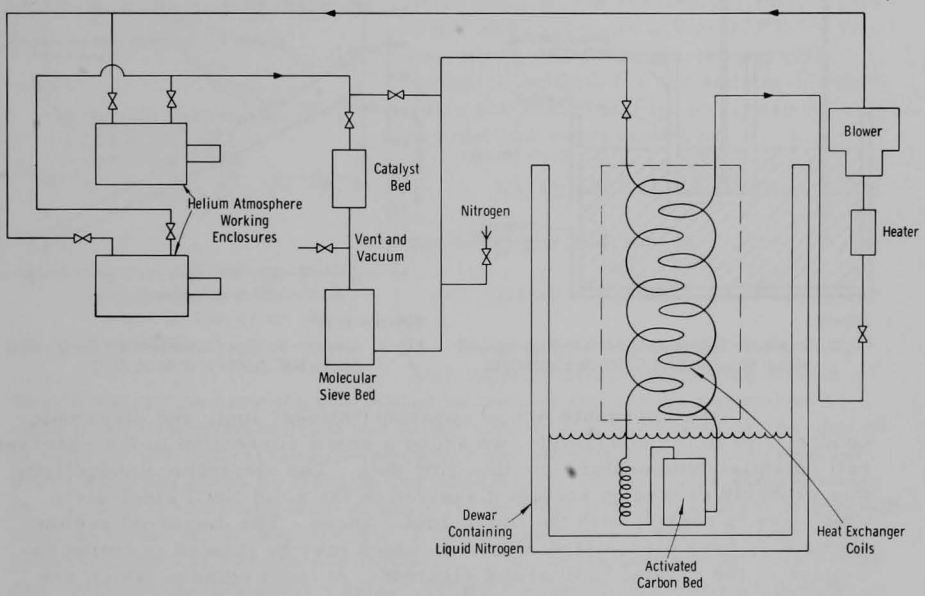

308-229

Fig. 5. Schematic Diagram of the Helium-purification System

The apparatus used in these experiments is shown in Fig. 6. The solid NaCl electrolyte was obtained in the form of cups, machined from single-crystal NaCl, with 3.2-mm-thick walls and bottoms. The sodium anode was inside the cup electrolyte, which was in turn suspended in liquid sodium-bismuth alloy to a depth approximately equal to the height of the sodium anode (2-3 cm). Tantalum rods were used as the electrode contacts. The cell potentials were measured with a potentiometric electrometer having an input impedance of 10^{13} ohms and capable of 0.01% accuracy. Forward and reverse current-voltage curves were measured by passing small currents through the cell. The current-voltage relationships so obtained were

*Unless otherwise specified, all experimental work discussed in this report was performed under a pure helium atmosphere.

linear, consistent with the behavior of reversible electrodes. Typical current-voltage curves for cell temperatures of 810 and 1051°K are shown in Fig. 7. The linearity of these curves suggests that the cell is reversible, but does not prove the existence of equilibrium in the cell. At 523°K, the internal cell resistance was approximately 2.2 x 10^7 ohms, indicating that an electrometer or similar high-input-impedance device for measuring the cell potential was required. At 1051°K, the internal cell resistance dropped to about 31 ohms, as indicated in Fig. 7.

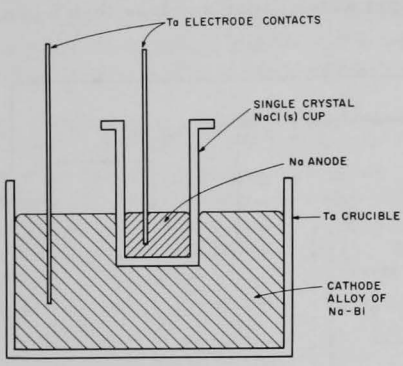

308-523

Fig. 6. Schematic Diagram of a Sodium-Bismuth Cell with a Solid Sodium Chloride Electrolyte

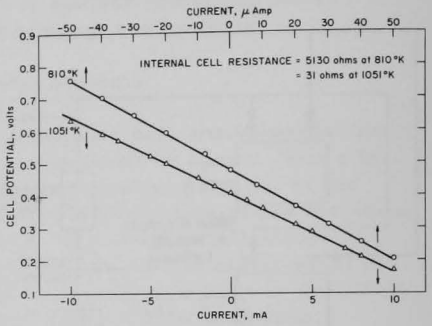

308-504 Rev. 1

Fig. 7. Current-Voltage Characteristics for the Cell Na(ℓ)/NaCl(s)/40 a/o Na in Bi(ℓ)

To compensate for an apparent "mixed" ionic and electronic conductivity in the electrolyte, we added a small correction to the observed cell potential-temperature-composition data. The electronic conductivity was probably caused by sodium dissolved in the solid NaCl electrolyte which was in contact with the liquid-metal anode. The dissolved sodium atoms may have dissociated into ions (which may be located in cation vacancies in the crystal lattice) and electrons, at least some of which are located in F-centers (or anion vacancies). The electronic conductivity could arise from the thermal excitation of electrons from F-centers into conduction bands.

The error caused by mixed conduction in the electrolyte was not known for the sodium-bismuth cell, but an estimate of the value of the correction term was made by comparing the measured voltage of the experimental cell,

$$\mathrm{Na}(\ell)/\mathrm{NaCl}(s)/40\ a/o\ \mathrm{Na\ in\ Pb}(\ell), \tag{26}$$

as a function of temperature, both with emf data from the literature and with emf data calculated from vapor-pressure measurements at 973°K. Values of the emf for this cell were reported by Hauffe and Vierk[40] and by Lantratov,[41] who used solid-glass electrolytes containing sodium oxide.

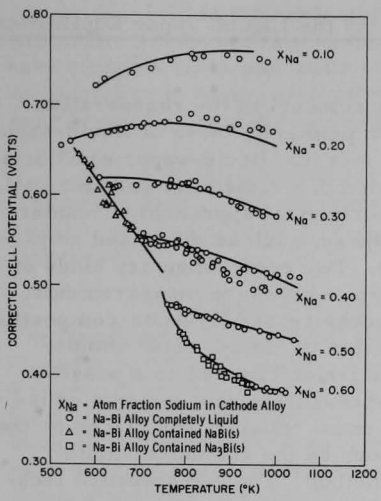

308-270 Rev. 1

Fig. 8. Corrected Potentials for the Cell Na(ℓ)/NaCl(s)/Na in Bismuth, as a Function of Temperature and Composition

Their results agree with those reported by Porter and Feinleib,[46] who used an electrolyte of alumina impregnated with sodium carbonate. The vapor pressure of sodium over a 40 a/o sodium in lead alloy at 973°K was measured by Fischer;[23] from this result, the cell emf was calculated to be about 8 mV higher than that reported by Porter and Feinleib. The correction term for cell potentials using solid NaCl as the electrolyte ranged from 4 mV at 673°K to 36 mV at 973°K.[42] The corrected cell potential-temperature-composition data for the sodium-bismuth cells are shown in Fig. 8. These data are for the cell represented by

$$\text{Na}(\ell)/\text{NaCl}(s)/\text{Na-Bi alloy}, \quad (27)$$

for which the reaction is

$$\text{Na}(\ell) \rightarrow \text{Na (in Na-Bi alloy)}. \quad (28)$$

Figure 8 shows that when cells with cathode alloys containing 30 and 40 a/o sodium in bismuth are cooled below 610 and 690°K, respectively, solid NaBi precipitates from the liquid alloys; this is evident by the change in slope of the emf-versus-temperature curves and is predicted from the phase diagram given by Hansen and Anderko (p. 322).[29] Less clearly seen in Fig. 8 is the precipitation of solid Na_3Bi from a 60 a/o sodium in bismuth alloy at about 945°K, which again is the temperature predicted from the phase diagram of Hansen and Anderko. The curves through the data points are those calculated from a single equation relating the cell potential to temperature and cathode alloy composition. Although a better fit might be obtained by considering the data for each curve separately, the accuracy of the data did not seem to warrant such a treatment.

Experiments are currently being conducted in which a different approach is used to directly measure the thermodynamic open-circuit emf of bimetallic cells containing sodium by rendering electronic conduction in the electrolyte negligible. These cells use a molten electrolyte, a cathode alloy containing sodium, and a small anode of sodium. The sodium is electrochemically deposited on a bare metal wire to form the anode by passing a current pulse of short duration (typical values: 1 Amp for 10 msec) between the bare wire and a counterelectrode. The potential of the anode is then measured immediately on interruption of the current pulse--before any appreciable amount of sodium dissolves in the electrolyte. This technique is feasible because of the extremely rapid establishment of equilibrium at the sodium anode.

2. Thermodynamic Measurements by the Liquid-Vapor Equilibrium Method

Thermodynamic property measurements in the regeneration-temperature region (1000-1400°K) have been primarily those of liquid-vapor equilibria. This situation results from the fact that liquid-vapor equilibria are involved perforce in thermal regeneration of a bimetallic galvanic cell, and emf measurements (the alternative experimental approach) encounter practical difficulties at the higher temperatures, such as increased solubility of the alkali metals in the electrolyte. Two complementary kinds of measurements have been made: (1) total vapor-pressure measurements, as a function of alloy composition and temperature; and (2) vapor-composition and vapor-density measurements, as a function of liquid-phase composition at a selected temperature (a temperature anticipated as a possible one for regeneration). For the total vapor-pressure measurements on the sodium-bismuth and sodium-lead systems, main reliance was placed on the quasi-static method, although part of the work on the sodium-bismuth system was also done by the boiling-point method. The transpiration technique was used to obtain the vapor-composition and vapor-density data. The transpiration technique is in common use; however, the quasi-static method is relatively unknown. The various techniques are discussed in detail in Appendix C and summarily in the following paragraphs.

a. Total Vapor-pressure Measurements. Vapor-pressure measuring techniques generally fall into one of two categories, dynamic and static. The dynamic method is the measurement of the boiling point of the material of interest under a known, constant pressure. The static method involves measuring the pressure exerted by the vapor in a region that has come to equilibrium with the sample and is saturated with vapor. Usually the static method involves a closed system.

A quasi-static method of measuring vapor pressures was introduced by Rodebush and his students about 40 years ago. They used this method to measure alkali-metal vapor pressures and obtained data that are still considered to be of good accuracy. The quasi-static method involves establishing a succession of closed systems and examining them in respect to the dynamic behavior of the contained gas and vapor. Essentially, this dynamic behavior provides a means for judging the end point of a series of reductions of the external pressure aimed at matching the vapor pressure. The boiling-point method can be difficult to apply to liquid-metal systems because of superheating problems. On the other hand, a true static method is subject to error from the degassing of the samples, and metals are notorious degassers. Also, a true static method requires the use of a pressure transducer, and none is available that functions at high temperature and is resistant to attack by the binary liquid-metal systems involved in the program. The quasi-static method avoids these problems.

In the early part of the program, the boiling-point method was used in conjunction with the quasi-static method. This was done partly to have a usable technique while the quasi-static method was being developed, and partly to have an independent measurement with which to compare results from the quasi-static method.

A special form of the boiling-point method using an ebulliometer based on the Cottrell pump was tried. The method worked well for pure sodium, but was erratic when used for sodium-bismuth mixtures. It was abandoned.

b. Vapor Density and Composition by the Transpiration Method. The transpiration experiment basically consists of allowing inert carrier gas, of known volume, to become saturated with vapor while streaming over the sample. A determination of the amount of vapor picked up by the carrier gas, together with the measurement of the volume of carrier gas, provides the basic data of the experiment. From this information and the assumption of ideal gas behavior, the vapor density and the vapor pressure can be calculated. If the vapor contains several components, analysis of the transported vapor for the individual components provides data for calculating the partial pressures of the components. In the calculation of pressures, some knowledge of the molecular constitution of the vapor is necessary; i.e., one needs to know if there are compound species or polyatomic component species in the vapor.

c. Results for the Sodium-Bismuth System from Liquid-Vapor Measurements. Part of the thermodynamic analysis of the liquid-vapor equilibrium data for the sodium-bismuth system hinges on a knowledge of the vapor pressure and the Bi-Bi_2 equilibrium over pure bismuth. The literature on this subject revealed some discordances, which made it desirable to check the total vapor pressure of bismuth and the partial pressures of the Bi and Bi_2 species.[48] This information was needed for the thermodynamic study and was limited to 1173°K, the projected regeneration temperature. The results from the total vapor-pressure studies for pure bismuth are included in Table II, along with the results for the sodium-bismuth system. The A and B entries on this table are the coefficients

TABLE II. Total Vapor Pressure for the Sodium-Bismuth System

Vapor pressures expressed as $\log P\ (\text{Torr}) = -\frac{A}{T} + B$

Liquid Composition, a/o Sodium	A	B	Root-mean-square Error in Log P	Technique Used[b]
100	5342.3 ± 18.3	7.5087 ± 0.0194	0.0070	QS
90	5118.6 ± 24.3	7.2478 ± 0.0247	0.0067	QS
80 upper[a]	4793.0 ± 35.8	6.8599 ± 0.0316	0.0036	BP
80 lower[a]	3832.9 ± 64.8	5.9612 ± 0.0622	0.0024	BP
77.5 upper[a]	4612.4 ± 33.3	6.5931 ± 0.0293	0.0027	BP
77.5 lower[a]	3888.1 ± 58.6	6.0172 ± 0.0564	0.0016	BP
75 upper[a]	7634.1 ± 110.4	8.5961 ± 0.0938	0.0108	BP
75 lower[a]	9582.9 ± 287.3	10.3285 ± 0.2626	0.0087	BP
60	7978.6 ± 132.4	8.1382 ± 0.1114	0.0105	QS
50	8197.2 ± 70.9	8.0041 ± 0.0586	0.0043	QS
40	8852.9 ± 182.2	8.2046 ± 0.1491	0.0080	QS
33.2	8391.5 ± 268.9	7.5935 ± 0.2213	0.0252	QS
0.00[48]	9150.3 ± 440.2	7.6326 ± 0.3592	0.0219	QS and BP

[a]"Upper" and "lower" refer to the parts of the curve above and below the breaks, respectively, in Fig. 9. For the 77.5 a/o sodium case, the points on the linear part of the curve below the break were used to obtain the log P equation given here. The "lower" listings are for three-phase equilibria.

[b]QS means quasi-static method; BP means boiling-point method.

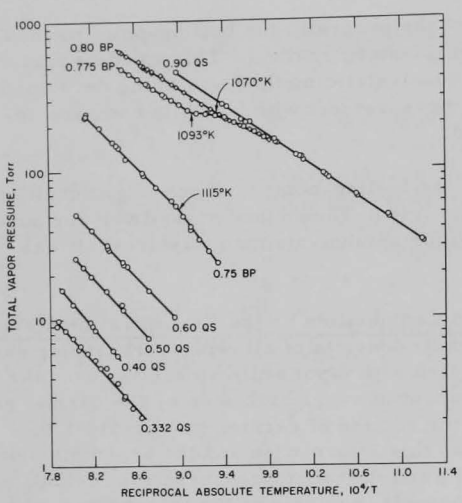

308-28 Rev. 1

Fig. 9. Total Vapor Pressures in the Sodium-Bismuth System. Curves are labelled with atom fraction sodium and with technique used: QS for quasi-static method, and BP for boiling-point method.

that define the lines in the plot of log P (Torr) = $-A/T + B$, shown in Fig. 9. The coefficients were obtained by the least-squares method.

The changes in slope (breaks) occurring in some of the lines in Fig. 9 are significant. The temperature at which a break occurs is the temperature at which contact is made between the points corresponding to (1) the initial system composition on the liquidus of the liquid-vapor loop and (2) the same composition on the liquid-solid solubility curve. The locus of the breaks traces the latter curve. The measurements reported here show that the phase diagram of Hansen and Anderko[29] contains an error. This diagram, based on work done in the early decades of this century, shows the melting point of Na_3Bi to be 1048°K. The break in the 0.75 atom fraction sodium curve in Fig. 9 indicates that the melting point is 1115°K. A thermal analysis on this system showed a break at 1113°K, which is in excellent agreement with the conclusion based on the total vapor-pressure results. Oxide contamination is a likely cause for a false low melting point in the early work. Similar difficulties may have prevented Egan and Bracker from observing the required breaks in the vapor-pressure curves they reported.[49]

Before transpiration data are reported, some discussion is needed of the calculation of partial pressures from the raw data. Essentially, the transpiration technique is a gas density measurement. To calculate pressures from density data, the molecular constitution of the vapor must be known. For the sodium-containing systems under consideration here, it is known that sodium vapor contains the two species, Na and Na_2, in equilibrium with each other. Bismuth vapor also contains two species, Bi and Bi_2. The value of the equilibrium constant, K, is known from the literature for the reaction

$$\text{dimer (g)} \rightleftarrows 2 \text{ monomer (g)}. \qquad (29)$$

If no compounds of the two components exist in the vapor phase, the four partial pressures, p_{Na}, p_{Na_2}, p_{Bi}, and p_{Bi_2}, can be calculated. (For the sodium-lead system, discussed below, only p_{Pb} is involved, in addition to p_{Na} and p_{Na_2}.) The necessary equation is

$$p_m^2 + \frac{Kp_m}{2} - \frac{K\rho \underset{\sim}{R} T}{2M} = 0, \tag{30}$$

where p_m is the partial pressure of the monatomic species in atmospheres, ρ is the gas density in units of grams of the component in question per liter, and M is the atomic weight of the monatomic species. By somewhat more complicated mathematics, which interrelates the transpiration experiment and a total pressure measurement, we can also calculate the partial pressure of a fifth species, a compound of the two components. For this added species, though, evidence is required that it is the only significant extra species present in the vapor. Then, too, the compound species must be present in an appreciable concentration if its partial pressure is to be calculated with reasonable accuracy. An example of the fifth-species problem occurs in Beusman's study[50] of the $KCl-FeCl_2$ system by transpiration and total-pressure methods; $KFeCl_3$ was the fifth vapor species. In the sodium-bismuth and sodium-lead work reported here, compound species were assumed to be absent. Limited justification for this assumption was obtained from mass-spectrometric studies on the sodium-bismuth system; up to 920°K, no compound vapor species could be detected.[51] For the sodium-lead system, the assumption was based on analogy.

By the above method, partial pressures of Na, Na_2, Bi, and Bi_2 were calculated from the transpiration data for the temperature 1173°K. The results are presented in Table III. The table, shows that for all liquid phases containing 60 a/o or more sodium, the vapor is pure sodium for all practical purposes. This fact permits the total vapor-pressure measurements on sodium-rich liquids to be regarded as measuring only sodium vapor pressure. Figure 10, a plot of log pressure versus log composition, and Fig. 11, a pressure-composition diagram, were constructed by taking advantage of this situation. The lack of bismuth in the vapor over sodium-rich liquids also was exploited in the thermodynamic analysis which is discussed below.

TABLE III. Transpiration Results for the Sodium-Bismuth System at 1173°K

a/o Sodium		Partial Pressures, Torr				Total Pressure, Torr
Liquid	Vapor	p_{Na}	p_{Na_2}	p_{Bi}	p_{Bi_2}	
60	99.7	19.4	0.11	0.042	0.0084	19.5
40	94.9	4.72	0.0065	0.12	0.06	4.90
33.2	86.7	2.40	0.0017	0.15	0.11	2.66
20	58.3	0.81	0.00019	0.20	0.19	1.20
10	~16	~0.16	nil	0.25	0.30	0.71

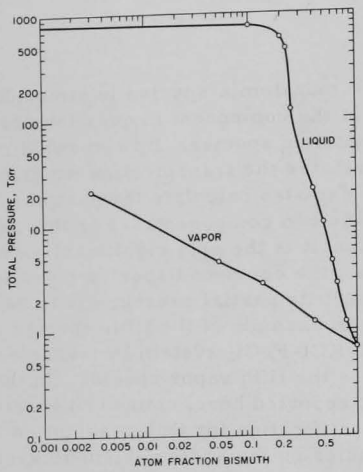

308-526 Rev. 1

Fig. 10. Diagram of Log Pressure vs. Log Composition for the Sodium-Bismuth System at 1173°K

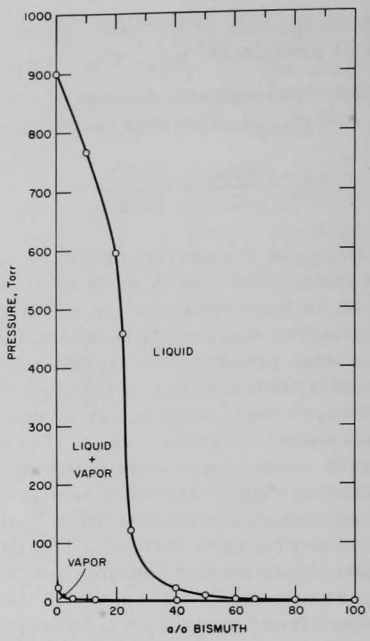

308-30

Fig. 11. Total Pressure as a Function of Composition for the Sodium-Bismuth System at 1173°K

Figure 12 compares the data from the emf measurements with those from vapor-pressure measurements in the composition range where the measurements overlap (10 to 50 a/o sodium). The activities from the vapor-pressure measurements have been converted to emfs in order to plot the two series of data on a common basis. The solid line represents the vapor pressure data across the whole composition range for 1173°K; the various broken lines represent the emf data at 700, 950, and 1050°K. The figure shows that the cell emf is not sensitive to temperature. Emf data were not collected for cells with cathodes richer in sodium than the compositions corresponding to the right-side ends of the broken lines. For sodium-richer cathodes, the cathode system would have been inside a region of the phase diagram in which solid Na_3Bi is present. The broken lines, then, reflect the maximum sodium content of the cathode in cells operating at the respective temperatures of the lines.

d. Results for the Sodium-Lead System from Liquid-Vapor Measurements. Eight liquids covering the composition range from 15.2 to 90 a/o sodium in lead were studied by the quasi-static method. The coefficients in the total vapor-pressure equation,

$$\log P\ (\text{Torr}) = -\frac{A}{T} + B \tag{31}$$

for these eight compositions are presented in Table IV. These coefficients were obtained from a least-squares fit of the log P equation to the data. Root-mean-square errors are given for log P. The equations were solved for T = 1126°K, a projected regeneration temperature; the pressures calculated for this temperature are listed as $P_{1126°K}$. The measurements were not carried to temperatures and pressures low enough to result in overlap of the liquid-vapor loop in the phase diagram with compound-containing regions. For this reason, no changes in slope are expected in the total-pressure curves in the log P versus 1/T plots.

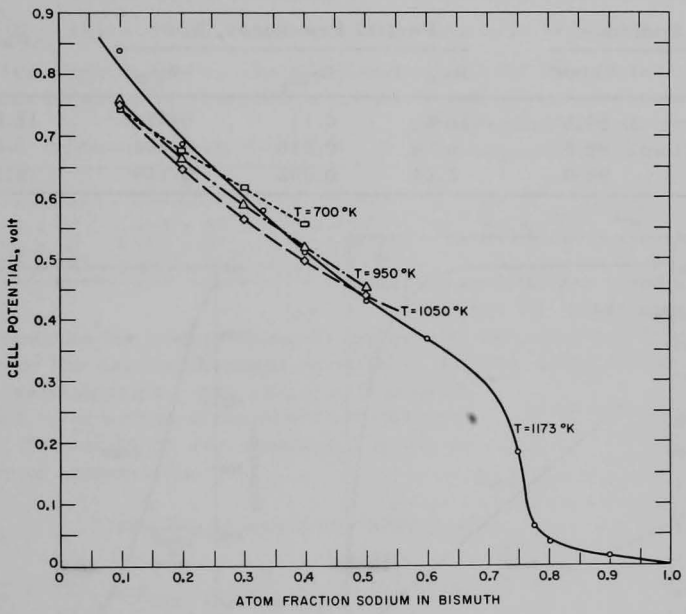

308-628

Fig. 12. Calculated Emfs for the Cell Na(ℓ)/Na⁺ Electrolyte/Na in Bi(ℓ), as a Function of Cathode Alloy Composition for Four Temperatures

TABLE IV. Total Vapor Pressures for the Sodium-Lead System as Measured by Quasi-static Method

$$\log P = -\frac{A}{T} + B$$

Liquid Composition, a/o Sodium	A	B	Root-mean-square Error in Log P	Temperature Range of Measurements, °K	Total Vapor Pressure, Torr, $P_{1126°K}$
15.17	6541.24	6.38436	0.01133	1181-1271	3.76 ± 0.09
30.09	6621.37	7.10098	0.00875	1066-1104	16.6 ± 0.4
39.94	6656.69	7.46188	0.01078	948-1122	35.5 ± 0.9
49.92	6348.62	7.60320	0.00378	962-1140	92.2 ± 0.8
60.28	5981.29	7.50208	0.00424	1015-1146	154.9 ± 1.5
69.97	5744.27	7.50703	0.00582	838-1147	254.4 ± 3.3
79.97	5423.23	7.38649	0.00174	1063-1144	371.6 ± 1.4
89.98	5310.81	7.42567	0.00693	753-1103	511.8 ± 8.0

Table V presents the results from the transpiration experiments. The total pressure calculated from transpiration experiments can be compared with the directly measured total pressure for a liquid phase containing 30 a/o sodium. The transpiration result is 16.6 ± 0.6 Torr, and the pressure calculated from Table IV is 16.6 ± 0.4 Torr; the agreement is excellent. Table V indicates that the vapor is essentially pure sodium over liquid phases that contain more than 30 a/o sodium. This fact is reflected in the diagram of log pressure versus log composition (Fig. 13) and in the diagram of pressure versus composition (Fig. 14) and is used in subsequent calculations of sodium activity from total-pressure measurements.

TABLE V. Transpiration Results for the Sodium-Lead System at 1126°K

a/o Sodium		Partial Pressures, Torr			Total Pressure, Torr
Liquid	Vapor	P_{Na}	P_{Na_2}	P_{Pb}	
30.0	99.6	16.4	0.11	0.0788	16.6 ± 0.6
20.0	98.5	6.76	0.018	0.104	6.88 ± 0.21
10.0	95.0	2.24	0.002	0.119	2.35 ± 0.15

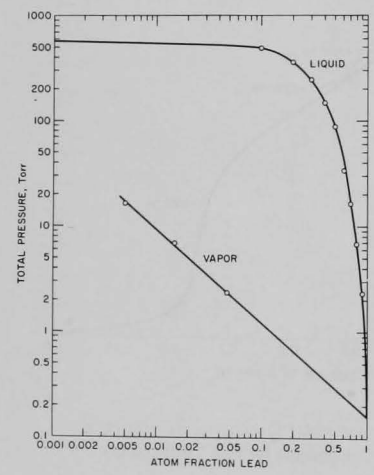

308-527 Rev. 1

Fig. 13. Diagram of Log Pressure vs. Log Composition for the Sodium-Lead System at 1126°K

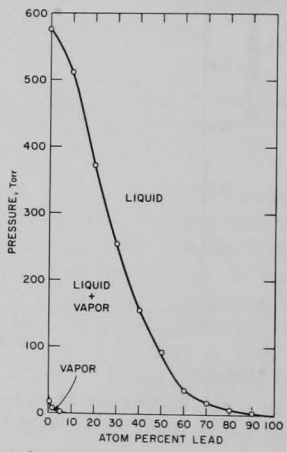

308-500 Rev. 1

Fig. 14. Total Pressure for the Sodium-Lead System at 1126°K, as a Function of Composition

3. Thermodynamic Analysis of the Results for the Sodium-Bismuth System

a. Thermodynamic Properties from the Emf Data. From the corrected cell potential-temperature-composition data shown in Fig. 8, the corresponding excess-chemical potentials of sodium were calculated for liquid sodium-bismuth alloys, using the expression

$$\Delta\mu^E_{Na} = -F\underset{\sim}{E} - \underset{\sim}{R}T \ln X_{Na}, \tag{32}$$

with the standard state of sodium defined as the liquid metal in the cell environment. These data may be considered as describing a surface in $\Delta\mu^E_{Na}$-T-X_{Na} space. With this in mind, the data were treated by a least-squares technique to find an analytical expression for this surface. The best fit was obtained by assuming a quadratic dependence of excess chemical potential on both temperature and composition, namely,

$$\Delta\mu^E_{Na} = \sum_{i=1}^{3}\sum_{j=1}^{3} C_{ij}T^{j-1}X_{Na}^{i-1}. \tag{33}$$

TABLE VI. C_{ij} Coefficients Derived for Eq. 33

	i = 1	i = 2	i = 3
j = 1	-7.4541×10^{3}	-1.4928×10^{4}	6.2273×10^{3}
j = 2	-1.7742×10^{1}	2.5513×10^{1}	3.7930×10^{1}
j = 3	1.1341×10^{-2}	-9.4021×10^{-4}	-4.3586×10^{-2}

The coefficients found are shown in Table VI. Other thermodynamic quantities for sodium-bismuth alloys may be calculated from the equation for the excess chemical potential of sodium, using standard thermodynamic relationships. The calculated activity coefficient, γ, of sodium in liquid sodium-bismuth alloys at 700 and 950°K are shown in Fig. 15 as a function of composition.

Using Eq. 33 and the relationship

$$\underset{\sim}{E} = -\frac{\underset{\sim}{R}T}{F} \ln X_{Na} - \frac{1}{F}\Delta\mu^E_{Na}, \tag{34}$$

we can calculate the emf-T-X_{Na} surface for cells in which the cathode is a liquid alloy. If $\underset{\sim}{E}$ applies to a cell in which the cathode alloy is saturated with a solid intermetallic compound at a particular temperature, then Eq. 34 enables us to calculate the composition of the liquid phase in the cathode. For example, from Fig. 8, a cell operating at 650°K, with a cathode alloy saturated with solid NaBi, will have an open-circuit emf of

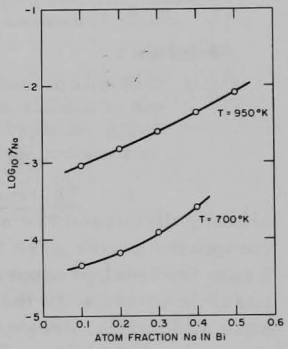

308-525

Fig. 15

Activity Coefficients of Sodium in Sodium-Bismuth Alloys Calculated from Cell-potential Measurements

0.5837 V. From Eq. 34, the composition of the liquid present is 0.36 atom fraction sodium. Figure 16 compares points calculated in this manner with the phase diagram of Kurnakow and Kusnetzow[47] published by Hansen and Anderko.[29] The standard free energies of formation of solid NaBi and Na_3Bi were calculated under the assumption that the pure liquid sodium and bismuth in the cell environment are in their standard states. The compositions given in Fig. 16 and the saturated cell emfs in Fig. 8, along with equations for the excess chemical potentials of sodium and bismuth, were used in these calculations. The results are shown in Fig. 17. Because the results from the emf studies include only bismuth-rich alloys and do not extend over the entire composition range for any temperature, no attempt was made to use the quasi-ideal approach (see pp. 52-57 below) to interpret the results in light of species that might exist in the liquid alloys. Instead, the thermodynamic approach given above was used.

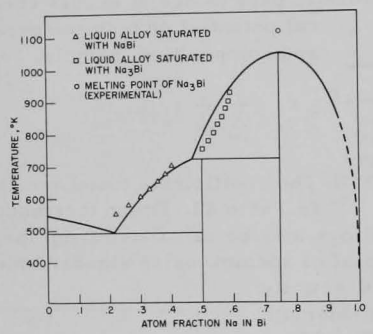

308-269 Rev. 1

Fig. 16. Comparison of Saturation Concentrations Obtained from Emf Data with the Published Phase Diagram[29] for the Sodium-Bismuth System

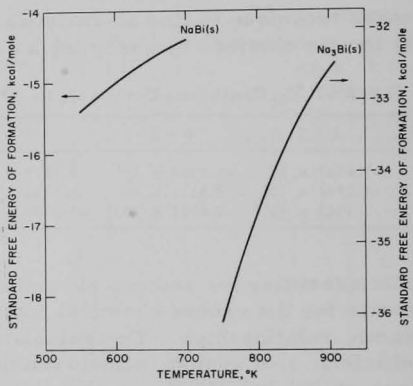

308-507

Fig. 17. Standard Free Energy of Formation of NaBi(s) and $Na_3Bi(s)$ as a Function of Temperature from Cell-potential Measurements

b. Thermodynamic Properties of Pure Bismuth. We have already discussed the need to re-examine the vapor pressure and vapor composition over pure bismuth and the methods used for the examination. From the total pressure and transpiration results for pure bismuth, it was possible to evaluate the reliability of literature values for the total pressure and partial pressures of monatomic and diatomic species, and to make an additional contribution to an understanding of the matter.[48] The average molecular weight of bismuth vapor was found to be 328 ± 19 at 1173°K, where the total pressure was 0.68 ± 0.04 Torr. Literature values ranged from 0.74 to 1.03 Torr. The vapor was calculated to be 57 m/o Bi and 43 m/o Bi_2. By comparing the present results with the data in

Hultgren et al.,[52] a widely used tabulation of thermodynamic properties, we concluded that the total vapor pressure of bismuth derived from Hultgren et al. is higher than the true value by a factor of about 1.5, but that the proportions of Bi and Bi_2 in the vapor are accurate in the temperature range of interest.

Using the values for the free energy function, $(G^\circ - H^\circ_{298})/T$ in Stull and Sinke[53] and taking our calculated values of $p_{Bi} = 0.29$ and $p_{Bi_2} = 0.39$ Torr, we obtained the standard enthalpy of dissociation for the reaction,

$$Bi_2(g) \rightleftarrows 2Bi(g) \qquad \Delta H^\circ_{298} = 47.8 \pm 1.3 \text{ kcal.} \tag{35}$$

Similarly, we obtained the standard enthalpies of vaporization,

$$Bi(s) \rightleftarrows Bi(g) \qquad \Delta H^\circ_{V_{298}} = 50.3 \pm 0.4 \text{ kcal;} \tag{36}$$

$$2Bi(s) \rightleftarrows Bi_2(g) \qquad \Delta H^\circ_{V_{298}} = 52.8 \pm 0.4 \text{ kcal.} \tag{37}$$

c. Bismuth Activities from Sodium-Bismuth Vapor-pressure Data. A graphical Gibbs-Duhem integration was performed, based on sodium activity coefficients, in order to obtain activity coefficients for bismuth across the entire composition range at 1173°K. The prerequisite activities and activity coefficients for sodium were calculated from the total pressure data for the 50 and 75-90 a/o sodium systems and from the transpiration data for the bismuth-richer liquid compositions. For the calculations from total pressure, the vapor was considered to be essentially sodium. The standard state was taken to be pure liquid sodium at 1173°K and 1 atm. The effect of pressure on the chemical potential of the condensed phase is small and was neglected. Calculation of the partial pressure of the monatomic species, p_{Na}, involves the equilibrium constant for the dissociation of the diatomic species already defined above. Sittig[54] lists, for pure sodium, $p^\circ_{Na} = 0.9631$ atm (732 Torr) and $p^\circ_{Na_2} = 0.2016$ atm (153 Torr) as the monatomic and diatomic species partial pressures at 1173°K. The equilibrium constant, K, is 4.601 atm. Then the activity of sodium is $a_{Na} = p_{Na}/p^\circ_{Na}$, and the activity coefficient $\gamma_{Na} = a_{Na}/X_{Na}$, where X_{Na} is the atom fraction of sodium in the melt. Table VII presents the activities and activity coefficients for the sodium-bismuth system.

d. Activity Coefficients from Emf and Vapor-pressure Data. Figure 18 is a plot of activity coefficients as a function of liquid-phase composition for a series of temperatures. These curves are based on both emf and vapor-pressure data. Only the curves from the vapor-pressure data extend across the entire composition range. Only these curves

(for 1173°K) are calculated from the quasi-ideal solution treatment discussed below; actual experimental points are indicated. The emf data were collected at a temperature that was low enough to be below the melting point of Na_3Bi, so that some compositions would fall within the solid Na_3Bi-liquid region of the phase diagram.

TABLE VII. Activities and Activity Coefficients for the Liquid Sodium-Bismuth System at 1173°K

Type of Experiment[a]	a/o Sodium	Sodium Activity, a_{Na}	Sodium Activity Coefficient, γ_{Na}	Bismuth Activity, a_{Bi}	Bismuth Activity Coefficient, γ_{Bi}	Calculated Bismuth Activity Coefficient,[b] γ_{Bi} (G-D)
T	10.0	0.000223	0.00223	0.862	0.956	0.988
T	20.0	0.00111	0.00547	0.683	0.854	0.929
T	33.2	0.00328	0.00976	0.511	0.768	0.737
T	40.0	0.00644	0.0159	0.409	0.683	0.622
P	50.0	0.0141	0.0282			0.366
T	60.0	0.0265	0.0437	0.146	0.366	0.196
P	75.0	0.158	0.211			0.00403
P	77.5	0.548	0.708			9.97×10^{-5}
P	80.0	0.697	0.873			4.23×10^{-5}
P	90.0	0.863	0.959			2.33×10^{-5}

[a]T refers to a transpiration experiment; P refers to a total-pressure measurement.
[b]The values in this column were obtained from a Gibbs-Duhem treatment of the sodium data.

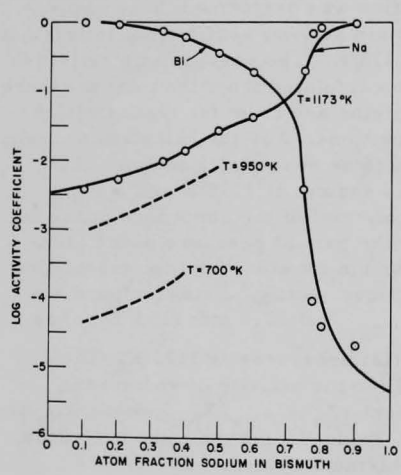

308-627

Fig. 18

Log of Activity Coefficients as a Function of Composition for the Sodium-Bismuth System. The solid lines were calculated from the quasi-ideal solution treatment of the liquid-vapor equilibrium data and are based on the equilibrium constants $K_1(NaBi) = 3 \times 10^2$ and $K_2(Na_3Bi) = 2 \times 10^5$. The data points represent experimentally determined points for sodium and bismuth (the latter derived from the former by a graphical Gibbs-Duhem integration) at 1173°K. The broken lines were obtained from emf measurements at 700 and 950°K.

e. Quasi-ideal Solution Treatment of Vapor-pressure Data. The activity coefficient curve in Fig. 18 obtained from the vapor pressure data was calculated on the basis of a quasi-ideal solution model for the liquid. It is appropriate to discuss the motivation for using this treatment and the assumptions made to derive the expressions involved.

We determined that the partial molar excess entropy of sodium in the 75 a/o sodium liquid has a large negative value, -6.4 eu. This result was obtained from the temperature dependence of the chemical potentials of mixing for sodium $\left(\Delta\mu^{M}_{Na} = RT \ln a_{Na}\right)$, which in turn were derived from the total pressure data. A large negative excess entropy has been taken as indicative of the persistence of short-range order above the melting point of an alloy.[55] The existence of molecules of intermetallic compounds in the molten state is not yet widely established, if, indeed, even established for a few cases. It appears reasonable, nevertheless, to presume that at least some short-range order exists in a molten alloy. We may presume further that the degree of order approximates that of a compound. For supporting evidence, Seymour and Styles[56] found nuclear magnetic resonance data to be interpretable on the basis of the existence of intermetallic compounds in the liquid indium-bismuth system. Furthermore, Vetter and Kubaschewski[57] discussed the consequences of the formation of bonds in the magnesium-antimony and magnesium-bismuth systems, as manifested in the solid compounds Mg_3Sb_2 and Mg_3Bi_2. There appears to be no reason to assume that these bonds should be completely and abruptly disrupted at the melting point. It would be reasonable, on the other hand, to expect more thorough, and probably complete, dissociation at a temperature far above the melting point, with various gradations of dissociation at intermediate temperatures. In the sodium-bismuth system at 1173°K, the temperature is only about 60° above the melting point of Na_3Bi (5% of the absolute temperature of the melting point), so that dissociation should not be too extensive if the compound Na_3Bi is assumed to exist in the melt.

Schmahl and Sieben[58] used a dissociated molecular liquid model to interpret activity data for the magnesium-lead and magnesium-antimony systems. They considered only one compound. Several compounds may be involved in a given case, and Högfeldt[59] extensively examined the thermodynamic consequences of single and multiple compound formation in binary mixtures in terms of a quasi-ideal solution model. Later, he used the method to interpret data on the Tl-Hg, Tl-Pb, and Bi-Cd systems.[60] The present quasi-ideal solution interpretation of the vapor-pressure data for the sodium-bismuth system is based on the assumption of the existence of two compounds in the melt.

The quasi-ideal solution treatment assumes that the species in the solution (including the compound species) behave ideally. For the sodium-bismuth system, the species included in the treatment are Na, Bi, Na_3Bi, and NaBi. The choice of sodium and bismuth as species is obvious. The selection of Na_3Bi as a species is based on the experimental observations in the region of 75 a/o sodium that (1) the excess chemical potentials of the two components change drastically, and (2) the partial molar excess entropy of sodium has a large negative value. Also, at this composition,

the phase diagram shows compound formation in the solid phases. The inclusion of NaBi as a species is justified (1) by the experimental fact that compound formation is shown in the phase diagram at 50 a/o sodium, and (2) by the need to introduce a 1:1 compound to make the quasi-ideal solution treatment consistent with the observed behavior of the activity coefficients, as a function of composition in the limiting cases of pure components.

In the following development, primed quantities refer to species and unprimed ones to components. An expression for the excess chemical potential is derived by the following argument. Since the chemical potential of a substance is the same, whether it is taken as a species or as a component,

$$\mu_A = \mu'_A \tag{38}$$

or, by expanding this,

$$\underset{\sim}{R}T \ln X_A + \Delta\mu_A^E + \mu_A^\circ = \underset{\sim}{R}T \ln X'_A + \Delta\mu'^E_A + \mu'^\circ_A. \tag{39}$$

Since $\mu_A^\circ = \mu'^\circ_A$ and since for a quasi-ideal solution $\Delta\mu'^E_A = 0$ (ideal species behavior is assumed),

$$\Delta\mu_A^E = \underset{\sim}{R}T \ln \frac{X'_A}{X_A} = \underset{\sim}{R}T \ln \gamma_A. \tag{40}$$

For the sodium-bismuth system,

$$X_{Na} + X_{Bi} = 1 \tag{41}$$

and

$$X'_{Na} + X'_{Bi} + X'_{Na_3Bi} + X'_{NaBi} = 1. \tag{42}$$

For the compound-forming reactions,

$$Na + Bi \rightleftarrows NaBi \tag{43}$$

and

$$3Na + Bi \rightleftarrows Na_3Bi, \tag{44}$$

there are the equilibrium constants

$$K_1 = \frac{X'_{NaBi}}{X'_{Na}X'_{Bi}} \tag{45}$$

and

$$K_2 = \frac{X'_{Na_3Bi}}{X'^3_{Na} X'_{Bi}}. \tag{46}$$

The mass-balance requirement leads to

$$X_{Na} = \frac{X'_{Na} + 3X'_{Na_3Bi} + X'_{NaBi}}{1 + 3X'_{Na_3Bi} + X'_{NaBi}}. \tag{47}$$

Combining Eqs. 45-47 and rearranging yields

$$\frac{X'_{Na}}{X_{Na}} = \gamma_{Na} = \frac{1 + K_1\left(2X'_{Na} - X'^2_{Na}\right) + K_2\left(4X'^3_{Na} - 3X'^4_{Na}\right)}{1 + K_1 + K_2\left(3X'^2_{Na} - 2X'^3_{Na}\right)}. \tag{48}$$

Note that this expression contains, beside the K's, only X'_{Na}. Similarly, we can derive

$$\frac{X'_{Bi}}{X_{Bi}} = \gamma_{Bi} = \frac{1 - X'_{Na}}{\left(1 - X_{Na}\right)\left(1 + K_1X'_{Na} + K_2X'^3_{Na}\right)}. \tag{49}$$

The calculation procedure begins with plotting the experimental values for γ_{Na} and γ_{Bi} as a function of X_{Na}. The intersections of the curves with the ordinates in the limits of $X_{Na} = 0$ and $X_{Bi} = 0$ are noted and applied as follows. Equation 48 indicates that in the limit of $X_{Na} \rightarrow 0$, $\gamma_{Na} = (1 + K_1)^{-1}$. Equation 49 shows that in the limit of $X_{Bi} \rightarrow 0$, $\gamma_{Bi} = (1 + K_1 + K_2)^{-1}$. Taken with these two facts, the experimental curves provide a means for obtaining preliminary estimates of K_1 and K_2. The succession of points required to trace out the quasi-ideal γ curves is obtained by using various values of X'_{Na} in the expression for γ_{Na} to calculate corresponding values of γ_{Na}, and then X_{Na}, X_{Bi}, and γ_{Bi} in that order. The closeness of fit between the first computed curves and the experimental points serves as a basis for adjusting the K values in order to compute a new pair of curves. The result shown in Fig. 18 was obtained using $K_1 = 300$ and $K_2 = 2 \times 10^5$.

The success of the quasi-ideal solution treatment in fitting the data is not offered as proof that the assumed compounds exist in the liquid state. The success is suggestive, though, and the question is open to study by independent experimental procedures. Neither is it claimed that the model can account for all deviations. When the tendency toward compound formation is strong, this effect will dominate and the quasi-ideal

solution model may be expected to provide a reasonable representation of the behavior of the system.

4. Thermodynamic Analysis of the Results for the Sodium-Lead System

a. Lead Activities from Sodium-Lead Vapor-pressure Data. To obtain activity coefficients for lead across the entire composition range at 1126°K, we performed a graphical Gibbs-Duhem integration, based on sodium activity coefficients. Sodium activities were calculated from total pressure and transpiration data in the manner already outlined in the discussion of the sodium-bismuth system (Section IV.A.3 above). For the gas-phase equilibrium, $Na_2 \rightleftarrows Na$, at 1126°K, an equilibrium constant, K = 3.26 (in atm), was derived from data by Sittig.[54] Table VIII shows the results from experiment and from the Gibbs-Duhem integration. These results also appear as points in Fig. 19, where the activity coefficients are plotted as a function of composition. The curves in Fig. 19 are the result of the quasi-ideal solution treatment described directly below.

TABLE VIII. Activities and Activity Coefficients for the Sodium-Lead System at 1126°K

a/o Sodium	Sodium Activity, a_{Na}	Sodium-activity Coefficient, γ_{Na}	Sodium Excess Chemical Potential $\left(\frac{\Delta\mu^E_{Na}}{4.57\,T} = \log\gamma_{Na}\right)$	Lead Activity,[a] a_{Pb}	Lead-activity Coefficient,[a] γ_{Pb}	Lead Excess Chemical Potential $\left(\frac{\Delta\mu^E_{Pb}}{4.57\,T} = \log\gamma_{Pb}\right)$
10.0	0.004652	0.04652	-1.332	0.884	0.982	-0.0079
15.17	0.007789	0.05134	-1.289	-	-	-
20.0	0.01404	0.07020	-1.154	0.732	0.915	-0.0385
30.0	0.03406	0.1135	-0.945	0.537	0.767	-0.1150
39.94	0.07269	0.1820	-0.740	0.355	0.592	-0.2275
49.92	0.1848	0.3702	-0.432	0.168	0.337	-0.4730
60.28	0.3037	0.5038	-0.298	0.0900	0.225	-0.6480
69.97	0.4829	0.6902	-0.161	0.0381	0.127	-0.8980
79.97	0.6815	0.8522	-0.069	0.0130	0.0651	-1.1865
89.98	0.9039	1.004	+0.002	0.00270	0.0270	-1.5680

[a]The values in these columns were obtained from a Gibbs-Duhem treatment of the sodium data. The experimental data are: For X_{Na} = 0.1, 0.2, 0.3; a_{Pb} = 0.826, 0.723, 0.548; γ_{Pb} = 0.917, 0.904, 0.784, respectively.

b. Quasi-ideal Solution Treatment of Vapor-pressure Data. The quasi-ideal solution treatment, described above for the sodium-bismuth system, was also applied to the sodium-lead system. Compared to the sodium-bismuth system, a more complex situation exists for the sodium-lead system with respect to compound formation. This is evident from the liquid-solid phase diagram, which shows five compounds in the solid phase: $NaPb_3$, NaPb, Na_9Pb_4, Na_5Pb_2, and $Na_{15}Pb_4$. The last three compounds are

similar in melting point (within a range of 14°) and are grouped closely around the stoichiometry 75 a/o Na-25 a/o Pb; their average composition is, in fact, $Na_{2.9}Pb$. The contribution of these compounds to the thermodynamic behavior of the melt within the context of the quasi-ideal model was averaged and approximated by the hypothetical, representative compound, Na_3Pb. Simplifying the treatment of the contribution of three compounds by introducing a single representative compound may not be a rigorous procedure, but the device is adequate to handle the data within their limits of accuracy and within the limits of the legitimacy of the assumption of species ideality in the quasi-ideal model. Thus, three compound species (Na_3Pb, NaPb, and $NaPb_3$), together with the component species (sodium and lead), served as a basis for the quasi-ideal solution treatment of the sodium-lead system.

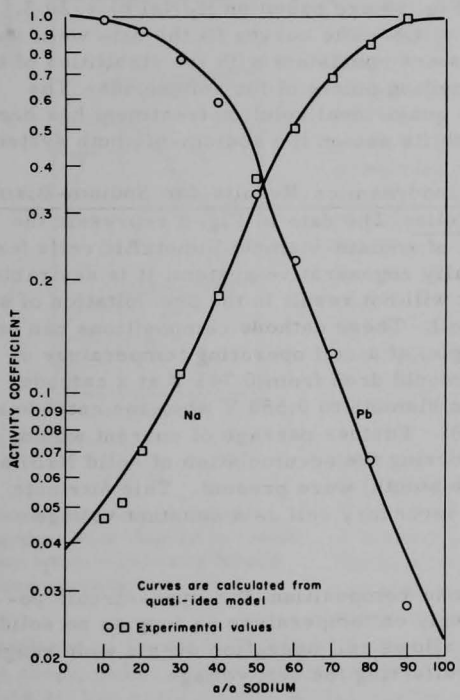

308-317

Fig. 19

Log of Activity Coefficients as a Function of Composition for the Sodium-Lead System at 1126°K. The solid lines were calculated from the quasi-ideal solution treatment of the liquid-vapor equilibrium data and are based on the equilibrium constants $K_1(NaPb) = 20.3$, $K_2(Na_3Pb) = 24.0$, and $K_3(NaPb_3) = 4.8$.

The reactions forming the three compounds and the respective equilibrium constants are

$$Na + Pb \rightleftarrows NaPb, \qquad K_1 = \frac{X'_{NaPb}}{X'_{Na} X'_{Pb}}; \tag{50}$$

$$3Na + Pb \rightleftarrows Na_3Pb, \qquad K_2 = \frac{X'_{Na_3Pb}}{X'^3_{Na}\, X'_{Pb}}; \tag{51}$$

$$Na + 3Pb \rightleftarrows NaPb_3, \qquad K_3 = \frac{X'_{NaPb_3}}{X'_{Na}\, X'^3_{Pb}}. \tag{52}$$

The necessary information for a preliminary evaluation of these K's is contained in a plot of experimental and Gibbs-Duhem values of activity coefficients as a function of X_{Na}. The point of intersection of the curves and the limiting values at both extremes of infinite dilution are the three necessary datum points for the estimation of the K's. The calculation of X'_{Pb} values from the K's and a succession of values of X'_{Na} involves a cubic equation in X'_{Pb}. The curves in Fig. 19 are based on $K_1(NaPb) = 20.3$, $K_2(Na_3Pb) = 24.0$, and $K_3(NaPb_3) = 4.8$. The curves fit the data well, and the relative magnitudes of the K's are consistent with the stabilities of the compounds as suggested by the melting points of the compounds. The significance of the success of the quasi-ideal solution treatment has been discussed above in connection with its use on the sodium-bismuth system.

5. Implications of Thermodynamics Results for Sodium-Bismuth and Sodium-Lead Regenerative Cells. The data in Fig. 8 represent the maximum open-circuit potentials of sodium-bismuth bimetallic cells for the conditions indicated. In a thermally regenerative system, it is desirable to choose cathode compositions that will not result in the precipitation of solid intermetallic compounds in the cell. These cathode compositions can be selected using Fig. 8. For example, at a cell operating temperature of 700°K, the open-circuit potential would drop from 0.745 V at a cathode composition of 0.10 a/o sodium in bismuth to 0.550 V when the cathode alloy becomes saturated with solid NaBi. Further passage of current would probably not change this voltage during the accumulation of solid NaBi as long as any liquid phase (rich in bismuth) were present. This attribute might be particularly useful in a secondary cell as a constant voltage output would result.

At a particular cathode composition, the open-circuit potential does not depend very strongly on temperature as long as no solid phase is present. This condition allows cell operation over a wide range of temperature without seriously affecting the cell voltage.

In the discussion of Fig. 9 in Section IV.A.2.c, the changes in slope in certain curves of log P versus 1/T for the sodium-bismuth system were correlated with the merging of a point on the liquidus of the liquid-vapor loop with a point corresponding to the same composition on the curve that defines solid-liquid coexistence for the congruently melting compound Na_3Bi. The idea may be explained in terms of Fig. 20, and certain implications for a regenerative cell may be deduced.

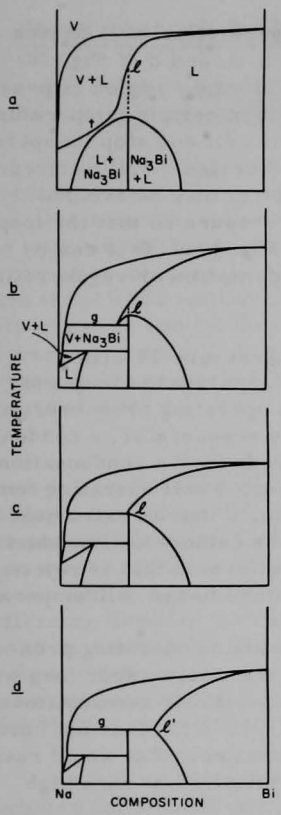

108-9323 Rev. 2

Fig. 20

Sequence of Schematic Temperature-Composition Phase Diagrams for Sodium-Bismuth System at Decreasing Pressures (pressures decreasing from a to d)

In considering Fig. 20, recall that relationships between condensed phases are relatively insensitive to pressure changes. However, phase relationships involving the vapor phase are very sensitive to pressure. These principles are reflected in Fig. 20, which is a sequence of schematic temperature-composition phase diagrams for a series of decreasing pressures. The curves defining the region of coexistence between solid Na_3Bi and liquid ($L + Na_3Bi$ and $Na_3Bi + L$) are not shifted by pressure changes. However, the liquid-vapor loop ($V + L$) moves downward as pressure decreases. For brevity, the $L + Na_3Bi$ region will be termed "the hump" and the liquid-vapor loop, "the loop." For part a of the figure, the pressure is just high enough to separate the loop and the hump; the regions are almost tangent at point t. Imagine a progression of boiling-point measurements on a liquid of 75 a/o sodium. The initial measurement gives point ℓ in part a of the figure. If the pressure is lowered somewhat to that corresponding to part b, the boiling point is at point ℓ in part b. Under these conditions, the pressure is low enough so that the loop and hump have overlapped to form the region $V + Na_3Bi$ (a solid-vapor coexistence region), but the system being measured is still outside this region. Eventually, the pressure can be lowered enough so that the boiling point of the liquid equals the melting point of Na_3Bi. This would correspond to point ℓ in part c. A further reduction in pressure would lower the loop even more, and the additional overlap with the hump would result in a phase diagram like that of part d. Under these conditions, a liquid of 75 a/o sodium can no longer exist. Instead, there is a three-phase system represented by isotherm g, consisting of vapor, liquid ℓ', and solid Na_3Bi. Boiling-point measurements on a system of overall composition 75 a/o sodium at pressures lower than that corresponding to part c are actually measuring the vapor pressure over solid Na_3Bi. The break in the plot of log P versus 1/T for the 75 a/o sodium system in Fig. 9 corresponds to point ℓ in part c of Fig. 20. For other compositions, the break comes at the temperature and pressure at which the given composition point is a single point common to both the hump and the liquidus of the loop.

An important consequence for a regenerative cell arises from the solid-vapor region, $Na_3Bi + V$, in parts b, c, and d of Fig. 20. If the cell is operated at a pressure such that a solid-vapor region is present in the phase diagram, then solid Na_3Bi can deposit in certain temperature regions of the cell. Such deposition could plug the cell and stop its operation. Under some circumstances, it may be possible to design a cell to circumvent this problem. In general, however, the problem may be avoided completely by operating the cell at high enough pressure so that the loop and hump in the phase diagram are separated, as in Fig. 20a. This can be accomplished by choosing a sufficiently high condensation or regeneration temperature.

The breaks in Fig. 9 indicate that a pressure of about 240 Torr is the minimum pressure necessary to separate the loop and hump for the sodium-bismuth system. If, at this operating pressure, pure sodium is collected at the condensation end of the regenerator, a condensation temperature of about 1040°K would be required; such a condensation temperature is considerably higher than the projected cell operating temperature (about 773°K). This condition might require that an extra heat exchanger be incorporated in the design to heat the cathode cell product part way up to the regeneration temperature with the heat that is rejected in cooling sodium from the condensation temperature to the cell temperature.

An additional consequence of the minimum operating pressure of 240 Torr is that the pure-bismuth end of the liquid-vapor loop would be fixed at a minimum of about 1623°K. For likely cathode compositions, the regeneration temperature would be about 1473-1573°K. It is not certain whether practical materials of construction are available that would resist the dynamic corrosion effect of sodium-bismuth mixtures at such high temperatures for long periods of time.

Finally, the pressure-composition diagram for the sodium-bismuth system (Fig. 10) indicates that the vapor from likely cathode compositions contains several atom percent bismuth. This condition will require that refluxing (fractionation) be provided for in the regenerator design. The refluxing requirement will reduce cell efficiency.

In contrast to the sodium-bismuth system, the sodium-lead regenerative-cell system promises to be free of loop-and-hump overlap problems in any reasonable range of operating pressure. The highest melting point of any compound in the sodium-lead system is 673°K. At this temperature, pure sodium has a vapor pressure of 0.35 Torr, and at this pressure, lead has a boiling point close to 1173°K. To increase Carnot efficiency, a regeneration temperature considerably higher than 1173°K would be selected. In the process, a higher operating pressure would be in force, and the loop-and-hump overlap problem would be avoided. The reflux requirement for the regenerator would still be present, however.

B. Physicochemical Properties of Sodium-containing Systems

1. Determination of Density, Viscosity, and Surface Tension of Alloys and Electrolytes

The densities, viscosities, and surface tensions of the fused-salt electrolytes and binary-metal alloys must be known in order to compute or estimate volumes, liquid levels, flow rates, and surface effects for use in the engineering design of bimetallic cells and regenerators. Although information on many physical properties is available in the literature for pure fused salts and liquid metals, little information is available for fused-salt mixtures and for liquid-metal alloys in the temperature range where regenerative cells are expected to operate. We therefore undertook an experimental program with the objective of providing the necessary physicochemical data.

a. Experimental Methods. The method of density determination used was to measure the volume of a liquid sample of known weight using a calibrated crucible.[20,21] A calibrated cylindrical tantalum crucible was used for sodium-bismuth alloys and sodium-lead alloys, while a Type 304 stainless steel crucible was used for fused salts. A micrometer depth-measuring device with a Type 308 stainless steel probe was used to measure the height difference between the bottom of the crucible and the surface of the liquid metal or fused salt. Contact of the measuring probe with the surface of the melt was determined electrically. The thermal expansion of the crucibles was accounted for by using available linear coefficients of thermal expansion.[61] The accuracy of the data is believed to be within 1%.

The viscosity was determined by measuring the time required for a fixed volume of the liquid to flow out through a capillary tube at the bottom of the cup.[20,21] The fixed liquid volume was sensed by immersed electrodes. An analytical expression was developed relating the viscosity to the capillary-cup parameters and time. The cup was calibrated using water and mercury to establish the values of the constants in the analytical expression. The error in the results should be the same as that obtained during calibration, namely, less than 2%.

The surface tension was determined by measuring the force required to detach a calibrated ring from the surface of the liquid.[20,21] The experimental apparatus is shown in Fig. 21. The ring was rounded to resemble the lower half of a torus. The average radius of the ring (r_1) was 1.475 cm, and the ratio of this radius to the small radius (r_2) of the torus surface was about 65. The weight (w) required to detach the ring from the surface was measured by a precision balance. The apparent surface tension is $wg/4\pi r_1$; the actual surface tension is $bwg/4\pi r_1$ dyne/cm, where b is a correction factor determined by Harkins and Jordan[62] as a function of

$r_1^3 \pi/w$ and r_1/r_2. The calibration factor (b) for the present investigation was determined from Harkins and Jordan's data and from experiments with liquids of known surface tension including menthol, isopropyl alcohol, benzene, chloroform, water, and sodium iodide. An error of 2% is believed to be reasonable.

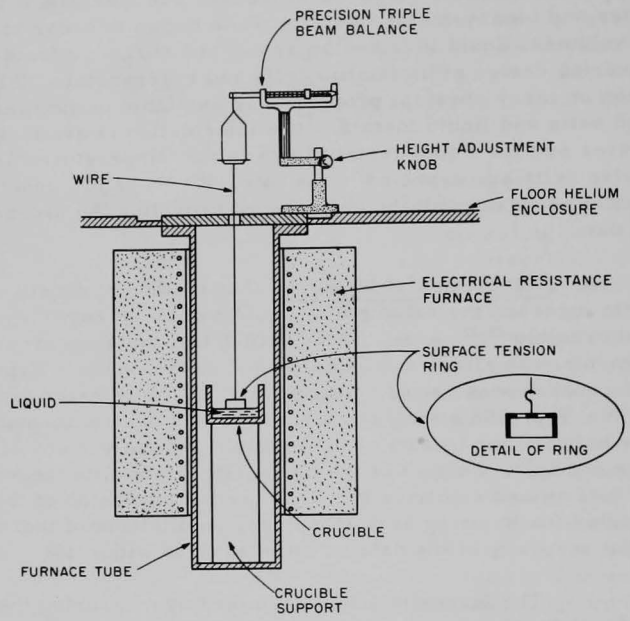

308-510

Fig. 21. Experimental Apparatus for Surface-tension Measurements

b. Results for Sodium-Bismuth Alloys. The densities of sodium-bismuth alloys containing 0, 10.4, 20, 30, 40, and 50 a/o sodium (purity of bismuth was 99.999%) were measured at temperatures from near the melting point of the alloys to 1070°K. The densities varied from about 10.2 to 5.3 g/cm^3, as shown in Fig. 22. The measured densities are considerably greater than densities computed by assuming volume additivity of the pure metals, a result consistent with compound formation in the liquid state. The surface-tension values of sodium-bismuth alloys containing 30, 40, 45, and 50 a/o sodium were measured at about 670-970°K. Over this range of composition and temperature, the surface tension showed little variation (242 to 260 dyne/cm). Figure 23 compares these results with values given in the literature for the pure components.

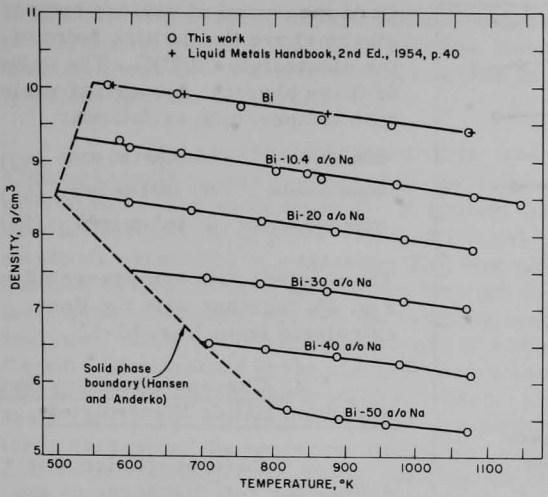

Fig. 22

Densities of Several Sodium-Bismuth Alloys as a Function of Temperature

108-9473 Rev. 2

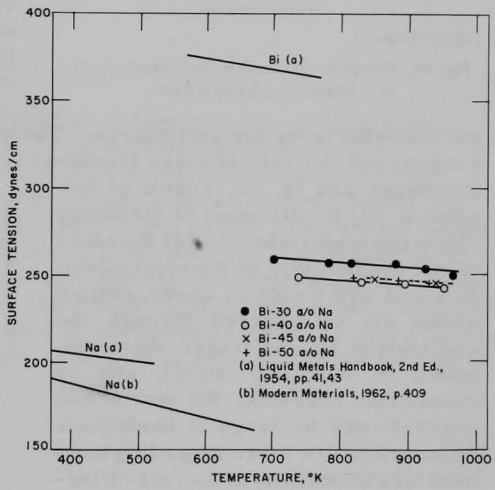

Fig. 23

Surface Tension of Some Sodium-Bismuth Alloys as a Function of Temperature

108-9476 Rev. 2

c. Results for Sodium-Lead Alloys. The densities of sodium-lead alloys containing 0, 10, 20, 30, 41, and 50 a/o sodium (the lead was reagent grade) were measured at temperatures ranging from near the alloy melting point to 970 or 1070°K. The densities were considerably greater than those computed by assuming volume additivity of the pure metals and varied from about 10.7 to 5.6 g/cm^3, as shown in Fig. 24.

d. Results for NaF-NaCl-NaI Electrolyte. The density, viscosity, and surface tension of an electrolyte consisting of the eutectic 15.2 m/o NaF-31.6 m/o NaCl-53.2 m/o NaI (each salt was reagent grade)

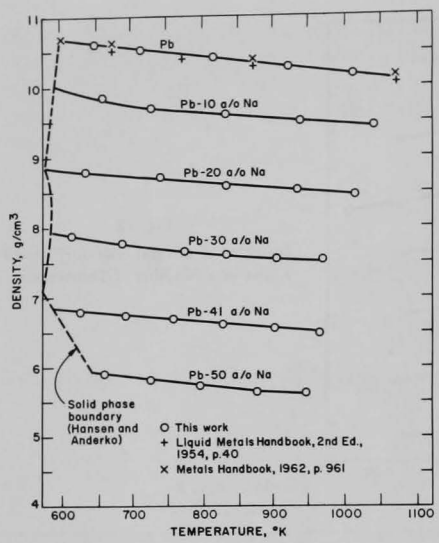

108-9472 Rev. 2

Fig. 24. Densities of Several Sodium-Lead Alloys as a Function of Temperature

were measured at various temperatures above the melting point of the electrolyte (808°K). The values of these physical properties varied with temperature as follows:

density (g/cm^3) = 3.29 - 0.0009 T (810-1070°K); (53)

viscosity (centipoise) = 4.22 - 0.003 T (830-1070°K); (54)

surface tension (dyne/cm) = 152 - 0.06 T (820-1020°K). (55)

The original data are presented in Fig. 25, together with the lines calculated from Eqs. 53-55.

2. Current-efficiency Studies in Sodium Halide Electrolytes

Current efficiency is defined for cell discharge as the ratio of the current flowing in the external circuit to the rate of mass transport from the anode to the cathode (expressed as an equivalent current); the inverse ratio is the current efficiency for cell charge. The difference between the discharge current and the rate of mass transport is referred to as the rate of self-discharge and is the result of two effects: (1) the diffusion of dissolved electrode materials, and (2) the electronic conductivity of the electrolyte. In a cell with a sodium anode, sodium atoms are transferred through the electrolyte by molecular diffusion, which is normally small, and by convection currents; the convection current may be large if inadequate precautions are taken regarding temperature uniformity in the cell. Electronic conductivity in a cell with a sodium anode has its origin in the dissociation of sodium atoms to form electrons and ions. The mobility of the electrons in the molten solution, rather than the mobility of the sodium atoms, may contribute most of the self-discharge. In this case, a minimum current efficiency should be observed in a cell containing an electrolyte saturated with sodium. Since

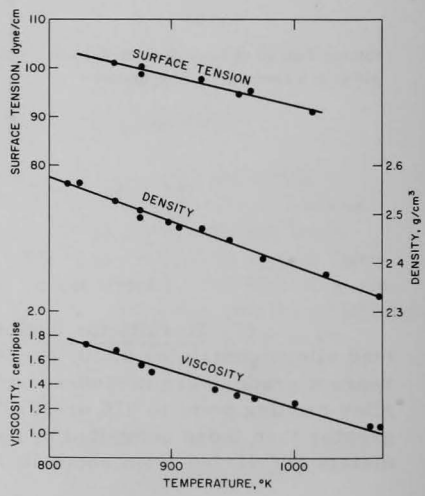

308-513 Rev. 1

Fig. 25. Density, Viscosity, and Surface Tension for the 15.2 m/o NaF-31.6 m/o NaCl-53.2 m/o NaI System

saturation with respect to pure sodium would be difficult, if not impossible, to obtain with an alloy electrode present, the minimum current efficiency must be observed in a cell in which sodium is electrochemically transferred from one location to another.

The current efficiency under the unfavorable conditions of sodium saturation was measured in two cells in which the electrolyte was presaturated with sodium metal. A sodium anode was allowed to equilibrate with the electrolyte of molten NaF-NaCl-NaI for several hours, after which a cathode consisting of a tantalum flag was placed in the cell. Eighteen hundred coulombs were discharged through the cell, and then the cathode, the deposited sodium, and the surrounding electrolyte were removed for analysis. After correcting the amount of sodium found in the cathode by the amount dissolved in the electrolyte, we calculated an integrated current efficiency. At 841°K, the integrated current efficiency was 90%, and at 886°K, 82%. The current efficiency is probably lower at higher temperatures because of the increased solubility of sodium (and the increased electronic conductivity). These then are the minimum current efficiencies to be expected in sodium bimetallic cells in the absence of convection currents.

3. Sodium-transfer Studies

a. Sodium-transfer Studies at Open-circuit and Constant-current Density. During the study of the sodium-bismuth cell (see Section IV.A.1), it became apparent that self-discharge caused by the spontaneous transfer of sodium from the anode to the cathode was taking place. The total sodium transfer consists of two parts: the transfer leading to the flow of electrons in the external circuit, and that corresponding to the self-discharge process. The latter consists of ordinary mass transfer by diffusion and convection, due to the solubility of sodium in the electrolyte, plus electrochemical transfer caused by the short-circuiting effect of electronic conduction in the electrolyte. The rate of sodium transfer due to self-discharge is given by

$$j_{Na} = \frac{w}{A} = \frac{m}{A\theta} - \frac{MI}{nFA}, \tag{56}$$

where j_{Na} is the mass flux of sodium (g/(cm^2-sec)), w is the rate of sodium transfer (g/sec), m is the total sodium transferred from the anode to the cathode during the experiment, and A is the area of the electrodes.

(1) Experimental Procedure. Sodium-bismuth cells were operated under both open-circuit and constant current conditions at differing temperatures and various interelectrode distances. Table IX summarizes the characteristics of these cells and the operating conditions for each.

TABLE IX. Characteristics of Sodium-Bismuth Cells Used in Study of Self-discharge Sodium Transfer

Type of Cell	Current Density, mA/cm²	Electrode Area, cm²	Electrolyte Depth, cm	Cell Temperature, °K	Electrolyte Composition	Cathode Composition, a/o Na in Bi
1	0	3.9	5.0	833-956	.37 m/o NaCl-NaI 5 m/o NaF-35.2 m/o NaCl-59.8 m/o NaI	0-40
	0	39.6	1.5	820-923	NaF-NaCl-NaI eutectic[a]	0-40
2	0	3.58	4.31	817	NaF-NaCl-NaI eutectic[a]	30-38
3	50 to 300	3.9	5.0	863	NaF-NaCl-NaI eutectic[a]	0-40
	-100 to +770	3.9	0.7	863	NaF-NaCl-NaI eutectic[a]	0-40
4	250	3.58	0.5	842	NaF-NaCl-NaI eutectic[a]	5-27
	250	3.58	1.6	842	NaF-NaCl-NaI eutectic[a]	5-27

[a]Eutectic composition: 15.2 m/o NaF-31.6 m/o NaCl-53.2 m/o NaI.

Data for cells of Types 1 and 3 were obtained using the experimental apparatus shown in Fig. 26.[19,63] A stainless steel cathode cup containing bismuth was immersed in the electrolyte, which itself was contained in a stainless steel crucible. The sodium anode was held in a stainless steel-fiber disc (the disc spreads the sodium uniformly over the electrolyte surface), which was mounted in a stainless steel cup with a hole in the bottom; the hole defined the active area of the anode.

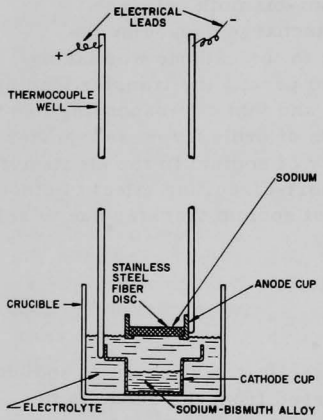

308-618

Fig. 26. Schematic Diagram of Types 1 and 3 Sodium-Bismuth Cells Used in the Study of Self-discharge Sodium Transfer

The experimental apparatus for Type 2 cells, shown in Fig. 27, differed somewhat from that for Type 1 cells. It was composed of a crucible in which the NaF-NaCl-NaI electrolyte separated the sodium-bismuth alloy cathode layer from the sodium anode. The sodium was held by a stainless steel-fiber disc, which had a diameter slightly less than that of the crucible. Neither the cathode nor the anode was mounted as in Type 1 cells. The entire assembly was encased by a copper block (not shown) to minimize temperature gradients; a gradient of 0.6°K from top to bottom was obtained with this assembly.

In a typical experiment, a weighed amount of sodium was placed in the anode cup. This mass of sodium was the total amount of sodium transferred in the experiment. When the cell was operated at open circuit (Types 1 and 2), the procedure was to monitor the cell voltage until a sharp drop indicated that the anode was depleted. This marked the termination point of the experiment and the time of the run, θ, was noted. When constant-current conditions were required, as in Type 3 cells, a dc constant-current source was used to operate the cell. Again, a sharp drop of the cell voltage signaled the end of the experiment.

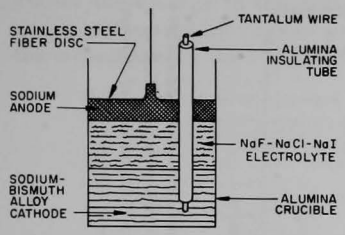

308-610

Fig. 27. Schematic Diagram of Type 2 Sodium-Bismuth Cell Used in the Study of Self-discharge Sodium Transfer

A modification of the Type 2 cell assembly was used in experiments with Type 4 cells. Figure 28 shows that in this apparatus the effective areas of the electrodes and electrolyte were defined by an alumina tube containing both the cathode alloy and electrolyte of molten NaF-NaCl-NaI. The anode, consisting of sodium held in a stainless steel-fiber disc, was contained by the alumina tube. The temperature gradient was about 7°K over the total height of the cell. In experiments with the Type 4 cell, the anode containing a known amount of sodium was placed in position for a given length of time (the prerun equilibration time) before the constant current was applied. The cell voltage was monitored using leads separate from those carrying the current. The initial overvoltage was subsequently used to calculate the conductivity of the electrolyte. As for previous cells, the complete consumption of the anode was indicated by an abrupt drop in voltage, which signified the completion of the experiment. The integrated current efficiency was calculated using the duration and value of the constant current. This efficiency is somewhat low because of the discounting of any self-discharge sodium transfer that took place during the prerun equilibration time when the cell was at open circuit. Similarly, the rate of sodium transfer was somewhat high.

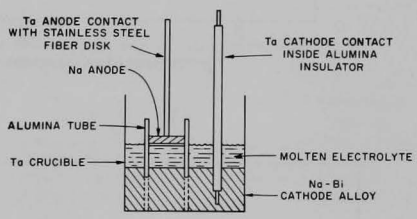

308-519

Fig. 28. Schematic Diagram of Type 4 Sodium-Bismuth Cell Used in the Study of Self-discharge Sodium Transfer

(2) Results. The open-circuit self-discharge sodium-transfer rate as a function of temperature for Type 1 cells is given in Figs. 29 and 30. Values of the cell electrical conductance are also seen in these two figures. For cells of Type 2, a self-discharge sodium-transfer

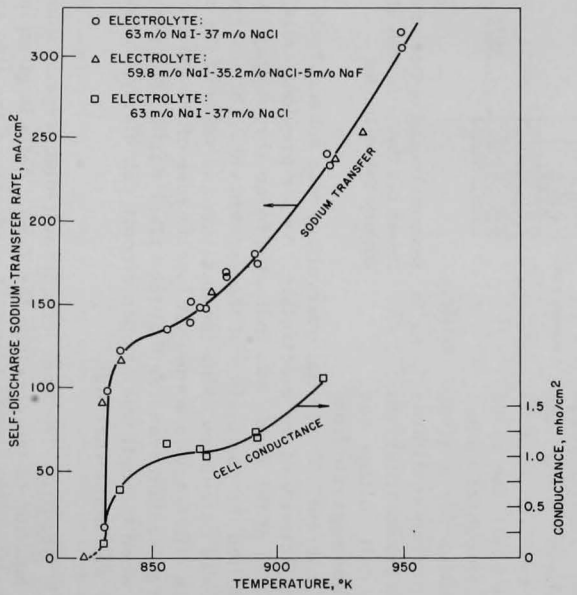

108-8559 Rev. 2

Fig. 29. Self-discharge Sodium-transfer Rate and Conductance at Open Circuit for a Type 1 Sodium-Bismuth Cell as a Function of Temperature for Electrode Area of 3.9 cm^2 and Interelectrode Distance of 5 cm

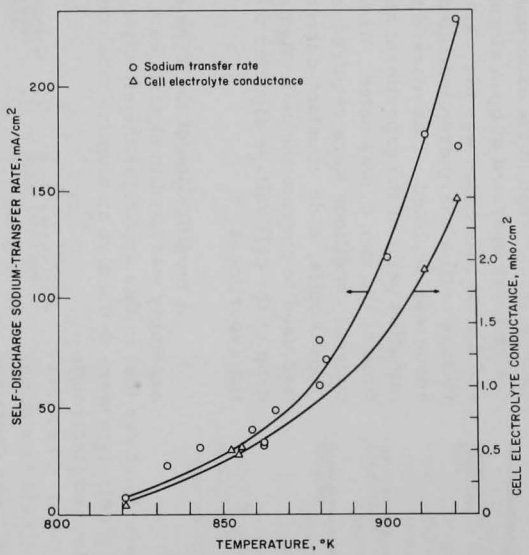

108-9468 Rev. 2

Fig. 30. Self-discharge Sodium-transfer Rate and Conductance at Open Circuit for a Type 1 Sodium-Bismuth Cell as a Function of Temperature for Electrode Area of 39.6 cm^2 and Interelectrode Distance of 1.5 cm

rate of less than 0.0131 g/(cm^2-hr) was obtained at open circuit. This corresponds to an equivalent current density of 15.3 mA/cm^2. Figure 31 shows the change in the self-discharge sodium-transfer rate as the cell current density increases for Type 3 cells. Table X shows the results of the experiments on Type 4 cells.

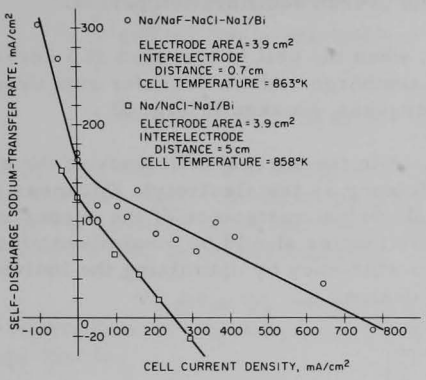

Fig. 31

Self-discharge Sodium-transfer Rate of Type 3 Sodium-Bismuth Cells as a Function of Current Density

308-631 Rev. 1

TABLE X. Self-discharge Sodium-transfer Rate in Type 4 Sodium-Bismuth Cells Operating at 250 mA/cm^2 and 842°K

Experiment Series	Electrolyte Depth, cm	Coulombic Efficiency, %	Sodium-transfer Rate		Electrolyte Specific Conductivity, mhos/cm
			g/(cm^2-hr)	mA/cm^2	
1	0.5	778 ± 1.7	0.061 ± 0.006	71 ± 7	1.66 ± 0.07
2	1.6	83.2 ± 2.7	0.043 ± 0.008	50 ± 9	2.0 ± 0.4

The following general conclusions on the behavior of the self-discharge sodium-transfer rate can be drawn from these experiments:

(a) As the cell temperature is increased, the sodium-transfer rate increases, which is consistent with increased sodium solubility, conductivity, and diffusion coefficient at higher temperatures.

(b) When the current drawn from the cell is increased, the sodium-transfer rate decreases, which is in accord with the theory of sodium transfer discussed in Section b below.

(c) The change from a NaCl-NaI electrolyte to a NaF-NaCl-NaI electrolyte does not appreciably affect the sodium-transfer rate.

(d) Interelectrode distance appears to have little effect on the sodium-transfer rate at open circuit.

(e) Current efficiency is not dependent on cathode compositions between 5 and 27 a/o sodium in bismuth.

(f) Shorter equilibration times yielded higher coulombic efficiencies, which may be explained on the basis that convectional mass transfer occurred during the prerun equilibration period.

(g) Finally, when the cell is operated at a current density of 250 mA/cm^2, the self-discharge sodium-transfer rate drops as the interelectrode distance increases, as seen in Fig. 32.

The last point indicates an increase in the current efficiency of the cell and a decrease in the voltage efficiency as the electrolyte thickness increases, because of the greater electrical resistance of the deeper electrolyte. The product of these two efficiencies should be maximized since it is desirable to maximize the overall efficiency by optimizing the individual efficiencies in any practical cell design.

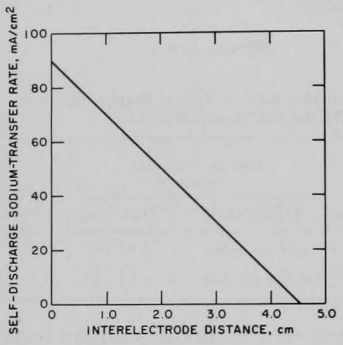

308-630 Rev. 1

Fig. 32

Self-discharge Sodium-transfer Rate in Types 3 and 4 Sodium-Bismuth Cells as a Function of Interelectrode Distance

b. Quasi-thermodynamic Analysis of Self-discharge Sodium Transfer. The results of the self-discharge sodium-transfer experiments presented above prompted a theoretical study in which an equation was developed for the sodium transfer in a bimetallic cell containing an electrolyte with dissolved anode metal (sodium).[21] The detailed development of this equation is given in Appendix B. Briefly, the differential equation to be solved is

$$J_{Na} = -\left[\frac{F\mathcal{D}_{Na-m}\rho X_{Na}}{M} + \frac{\kappa_e \kappa_i \underset{\sim}{R}\, T}{F(\kappa_i + \kappa_e)}\right]\frac{d \ln X_{Na}}{dx} - \frac{\kappa_e i}{\kappa_i + \kappa_e}, \qquad (57)$$

where the symbols are defined for this particular case as

J_{Na} = equivalent flux of sodium atoms being transferred by the self-discharge transfer mechanism in Amps/cm^2;

$\mathcal{D}_{Na-m}$ = effective diffusion coefficient of the sodium atoms dissolved in the electrolyte, cm^2/sec;

ρ = density of the electrolyte, g/cm^3;

M = molecular weight of the electrolyte, g/mole;

X_{Na} = mole fraction of sodium metal in the electrolyte;

κ_e = electronic conductivity of the electrolyte, mhos/cm;

κ_i = sodium ion conductivity of the electrolyte, mhos/cm;

and

x = distance from the anode, cm.

The first term inside the brackets in Eq. 57 represents the portion of the sodium transfer due to the diffusion of neutral sodium atoms. The other terms in the equation represent the portion of the transfer due to the electronic conductivity of the electrolyte.

To solve Eq. 57, we assumed that the electronic conductivity of the electrolyte is directly proportional to the concentration of dissolved sodium; that is,

$$\kappa_e = K_e X_{Na}. \tag{58}$$

The boundary conditions used are $X_{Na} = X_{an}$ at $x = 0$, i.e., in the electrolyte immediately contiguous with the anode (anolyte); and $X_{Na} = X_{ca}$ at $x = L$, i.e., in the electrolyte immediately contiguous with the cathode (catholyte), the electrolyte thickness being L cm. The integrated equation is

$$J_{Na} + i = \left(\frac{\kappa_i \underset{\sim}{R} T}{FL} + \frac{F\mathcal{D}_{Na-m}\rho\kappa_i i}{LMK_e(i + J_{Na})}\right) \ln \frac{J_{Na}\kappa_i + (J_{Na} + i)\, K_e X_{an}}{J_{Na}\kappa_i + (J_{Na} + i)\, K_e X_{ca}}$$

$$+ \frac{F\mathcal{D}_{Na-m}\rho(X_{an} - X_{ca})}{LM}. \tag{59}$$

Two special cases of Eq. 59 are of interest. First, when the cell is at open circuit ($i = 0$), the self-discharge transfer rate is

$$i_{Na,oc} = \frac{\kappa_i \underset{\sim}{R} T}{FL} \ln \frac{\kappa_i + K_e X_{an}}{\kappa_i + K_e X_{ca}} + \frac{F\mathcal{D}_{Na-m}\rho}{LM}(X_{an} - X_{ca}). \tag{60}$$

Second, when the sodium-transfer rate is reduced to zero ($J_{Na} = 0$), the current density is

$$i\Big|_{J_{Na}=0} = \left(\frac{\kappa_i \underset{\sim}{R} T}{FL} + \frac{F\mathcal{D}_{Na-m}\rho\kappa_i}{LMK_e}\right) \ln \frac{X_{an}}{X_{ca}} + \frac{F\mathcal{D}_{Na-m}\rho}{LM}(X_{an} - X_{ca}). \tag{61}$$

The cell voltage, E, is always less than the theoretical open-circuit emf, $\underset{\sim}{E}$, and these are related by the expression (see Appendix B, Eq. B.33)

$$E = \underset{\sim}{E} - \frac{F\mathcal{D}_{Na-m}\rho}{MK_e} \cdot \frac{\kappa_{e,ca} - \kappa_{e,an}}{\kappa_i} - \frac{(J_{Na} + i)\,L}{\kappa_i}, \tag{62}$$

where

$\kappa_{e,ca}$ = electronic conductivity of the catholyte, mhos/cm;

$\kappa_{e,an}$ = electronic conductivity of the anolyte, mhos/cm.

At open circuit, i = 0; substituting Eq. 60 in Eq. 62 yields the open-circuit voltage,

$$E_{oc} = \underset{\sim}{E} - \frac{RT}{F} \ln \frac{\kappa_i + \kappa_{e,an}}{\kappa_i + \kappa_{e,ca}}, \tag{63}$$

which shows that the open-circuit voltage of the cell is less than the theoretical open-circuit emf.

If, at some current density, $i|_{J_{Na}=0}$, the sodium-transfer rate is zero, then the cell voltage will be $E|_{J_{Na}=0}$, where

$$E|_{J_{Na}=0} = -\frac{F\mathcal{D}_{Na-m}\rho}{MK_e} \ln \frac{X_{an}}{X_{ca}}. \tag{64}$$

Equation 64 indicates that a negative cell voltage is necessary to reduce the self-discharge sodium transfer to zero.

Equation 59 was solved, assuming the following values for the variables:

$$L = 1 \text{ cm},$$
$$\mathcal{D}_{Na-m} = 1 \times 10^{-4} \text{ cm}^2/\text{sec},$$
$$\kappa_i = 1 \text{ mho/cm},$$
$$K_e = 100 \text{ mhos/cm},$$
$$M = 105 \text{ g/mole},$$
$$X_{an} = 0.004,$$
$$X_{an}/X_{ca} = 10^4,\ 10^2, \text{ and } 10,$$
$$T = 858°\text{K},$$

and

$$\rho = 2.5 \text{ g/cm}^3.$$

The two terms in Eq. 59 involving $FD_{Na\text{-}m}\rho/LM$ are small. The fact that the expression $(FD_{Na\text{-}m}\rho/LM)(X_{an} - X_{ca})$ is relatively small indicates that the self-discharge sodium transfer is largely caused by electronic conduction in the electrolyte rather than by direct diffusion of sodium atoms.

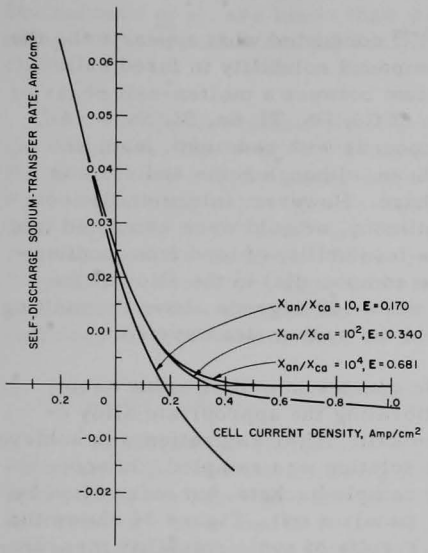

108-9471 Rev. 4

Fig. 33. Solution of Eq. 59 for $K_eX_A/\kappa_i = 0.4$, $K_e/\kappa_i = 100$, $K_eX_A = 0.4$, $\kappa_i = 1$

The solution of Eq. 59 can be expressed as a plot of J_{Na} as a function of i for the various values of X_{an}/X_{ca}. The results are shown in Fig. 33.

The solutions shown for the theoretical equation for self-discharge sodium transfer qualitatively explain one unexpected phenomenon noted in the experimental work: The sodium transfer rate decreases with increasing current density. We might have expected that the self-discharge sodium transfer would be independent of cell current.

The results of this analysis have yet to be verified quantitatively by experiment.

4. Solubility of Intermetallic Compounds in Fused Salts

Metals and intermetallic compounds show solubilities in fused salts ranging from traces to total miscibility. Metals and intermetallic compounds dissolved in the electrolyte can cause difficulties in the operation of bimetallic cells, since the anode may change composition due to the extraction of cathode metal or intermetallic compounds (or related species) from the electrolyte solution. Not only may the activity of the anode metal be lowered, thus reducing the cell potential, but it may also be difficult to remove the cathode metal that may so appear in the anode. As protection against this potential problem, an electrolyte with reduced ability to dissolve the cathode metal and intermetallic species from the cathode should be used. A fortunate condition concerning the solubility of intermetallic species in the anode is that ideal solutions apparently are formed when the concentration of the cathode metal in the anode is small. This results in a minimal reduction of the cell voltage. A more formidable problem may be the effect of the buildup of cathode metal in the anode. If this occurs, it should be met with special regeneration techniques, such as continuously removing a fraction of the anode material and combining it with the cathode alloy

sent to the regenerator. Knowledge of the solubilities in fused salts of intermetallic species from possible cathode alloys will help anticipate such situations.

Heymann and co-workers[65-69] conducted what appear to be the first investigations of intermetallic compound solubility in fused salts. These were distribution studies of sodium between a molten-salt phase of NaBr or NaI and a molten-metal phase of Cd, Pb, Tl, Sn, Bi, Sb, or Au. They found that at 1043°K, sodium compounds with cadmium, lead, and thallium were not soluble in the salt phase, although some sodium was apparently extracted from the metal phase. However, intermetallic compounds of sodium with tin, bismuth, antimony, or gold were extracted into the salt phase. Heymann attributed the insolubility of lead from sodium-lead mixtures to the dissociation of the compound(s) in the alloy at the experimental temperature, which was some 400 degrees above the melting point of the highest melting compound in the sodium-lead system.

Solubilities of intermetallic species in molten salts were measured in the present work by equilibrating the appropriate alloy or intermetallic compound with the molten salt. After saturation was achieved (usually about 2 hr was sufficient), the solution was sampled. In some cases, this was accomplished by using sample buckets, but more often by filtering part of the solution through a tantalum frit. Figure 34 shows the results of some solubility measurements. The point for $Na_{0.6}Bi_{0.4}(\ell)$ in equilibrium with NaBr is Heymann's. This point is expected to be below the upper curve, which represents the solubility of $Na_3Bi(s)$ in molten NaF-NaCl-NaI, because the liquid alloy of Heymann's work was not saturated with Na_3Bi. The heat of fusion of Na_3Bi calculated from the upper line is 10.7 kcal/mole. The solubility of the unsaturated alloy ($Na_{0.55}Bi_{0.45}(\ell)$) in the NaF-NaCl-NaI eutectic was appreciably lower than that of the solid compound Na_3Bi. In addition, the Na:Bi ratios in the molten salt were appreciably higher than in the liquid alloy. The possibility of multiple species is indicated by these higher, variable values of the Na:Bi ratio in the salt phase. The lack of intersection of the two sodium-bismuth curves at a temperature near 800°K may indicate a phase-diagram error since the phase diagram listed by Hansen and Anderko[29] shows that $Na_3Bi(s)$ should precipitate on cooling the unsaturated alloy to approximately 798°K.

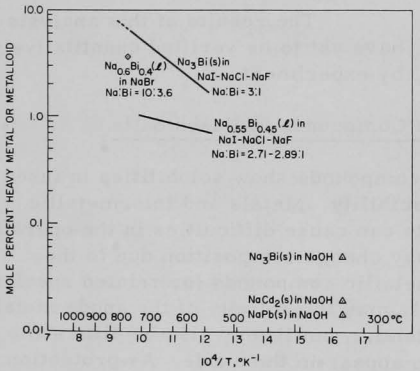

308-605 Rev. 1

Fig. 34 Solubility of Sodium-containing Intermetallic Species in Molten Salts

The solubilities of solid Na_3Bi, $NaCd_2$, and NaPb in molten NaOH were measured at 613°K by Delimarskii et al.[70] and are shown in Fig. 34 for comparison. The solubilities of Na_3Bi and NaPb in molten NaOH reported by Delimarskii et al. are lower than those calculated from the present results using a heat of fusion of 16.6 kcal/mole for Na_3Bi and 3.9 kcal/mole for NaPb.

The freezing-point depression of Na_3Bi in LiCl and NaI has also been studied. The results indicated that, in dilute molten-salt solutions of Na_3Bi all three sodium atoms are ionized (or at least replaceable) and that the bismuth exists in a species that is monatomic in bismuth. Electrochemical studies of Na_3Bi dissolved in molten salts made by Delimarskii and Pavlenko and co-workers[71-75] are in agreement with the freezing-point depression results and apparently indicate the presence of Bi^{-3} ions in solution. Further discussion of intermetallic compounds in molten-salt solutions is presented in Section V.B.3.

C. Phase Relationships for Sodium Halide Electrolytes

A successful design of a regenerative cell will require a fused-salt electrolyte that has the following properties: 1) thermodynamic stability with respect to reaction with the anode metal; 2) high electrolytic conductivity to minimize ohmic losses in the cell; 3) low solubility for the anode metal and cell products so that self-discharge transfer of the anode metal and/or cell products is minimized; and 4) low melting point to minimize corrosion of the cell components and to maximize the Carnot-cycle efficiency by allowing the cell to operate at a low temperature.

To avoid possibility of exchange between electrolyte cations and the anode metal at the relatively high temperatures normally used for sodium cells, only sodium salts were considered.

Weaver et al.[76] report that anions found compatible with a sodium system include the halides (F^-, Cl^-, Br^-, I^-), CN^-, $CO_3^=$, and OH^-. The hydroxide ion is attractive because its salts have very low melting points. However, hydroxides would require some finite hydrogen-gas pressure to stabilize the salt system, and the presence of hydrogen would cause hydride formation from the anode metal, an undesirable result. Further degeneration to the oxide may occur (see Eq. 65), and thereby result in desirable changes in the electrolyte characteristics. By an analogous reaction (see Eq. 66), sodium carbonate can readily undergo degradation to free carbon and sodium oxide.

$$NaOH + 2Na \rightarrow Na_2O + NaH \qquad \Delta \tilde{G}^\circ_{750} = -15 \text{ kcal/mole}; \tag{65}$$

$$Na_2CO_3 + 4Na \rightarrow C + 3Na_2O \qquad \Delta \tilde{G}^\circ_{750} = -10 \text{ kcal/mole}. \tag{66}$$

Though the cyanide salt is low melting, the paucity of data on this particular compound, combined with its potential hazard, precluded its use. The electrolyte search was thus restricted to binary and ternary mixtures of sodium halides.

Because phase diagrams of some of the sodium halide systems were not available in the literature, an experimental program was undertaken to provide data necessary for the selection of a suitable electrolyte.

1. Experimental Method

The phase-diagram investigations were carried out using the thermal-analysis method. The thermal-analysis apparatus was patterned after that described by Smith,[77] and the essential parts of this apparatus are shown in Fig. 35. The furnace tube was connected directly to the floor of a high-purity inert-atmosphere box[44] so that reactive salts and metals could be weighed and introduced into the sample holder without risk of contamination with moisture, oxygen, or nitrogen. The sample was placed in a Type 347 stainless steel crucible (2.54-cm OD x 3.81 cm high with a 0.0381-cm-thick wall and bottom), which in turn was placed in a firebrick container of low thermal conductivity. The firebrick was enclosed in Type 347 stainless steel. The tip of the central thermowell had three 0.0254-cm-thick circular heat-conducting fins, which extended to the wall of the sample crucible.

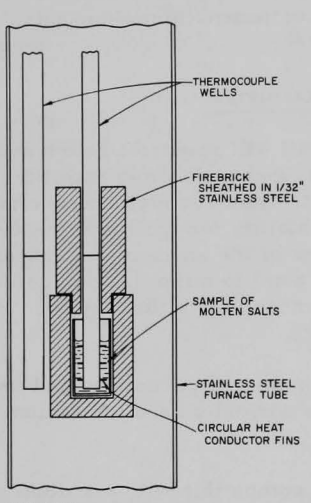

108-6805

Fig. 35. Thermal-analysis Sample Assembly

In all experiments, the temperature of the furnace was maintained at a constant differential above or below the sample temperature to control the heating or cooling rate. This was achieved by using a separate differential thermocouple with its junctions inside and outside the sample container to measure and control the temperature difference. The output of this differential thermocouple was sensed by a differential dc amplifier which controlled the heating and cooling rate of the sample by activating a proportioning controller, which in turn operated a magnetic amplifier. The power to the furnace surrounding the sample was supplied through a saturable core reactor controlled by the magnetic amplifier. The versatility in adjustment of the differential amplifier allowed heating and cooling rates to be set at any value in the range from 0.2 to 10°K/min.

A recording potentiometer with adjustable span and adjustable suppression was used to record the temperature of the melt. Temperatures were measured with calibrated platinum-platinum 10% rhodium thermocouples,

which were calibrated against the melting points of N.B.S. pure zinc (m.p. 692.7°K) and N.B.S. pure aluminum (m.p. 933.2°K). The accuracy of the temperature measurements was estimated to be ±0.3°K

Reagent-grade sodium fluoride, sodium chloride, and sodium iodide were used throughout this investigation. The salts were relatively dry crystals, which were further dried by evacuating and heating to 423°K. Because the inert-solids (e.g., carbon) content of sodium iodide was somewhat higher than desired, this salt was filtered through an extra-fine quartz frit before use. The melting points of the pure salts were 1263, 1074, and 932.5°K, respectively.

In all experiments, pure crystalline materials were weighed into a Type 347 stainless steel crucible, and the entire assembly (Fig. 35) was introduced into the furnace well, which was connected to the floor of the high-purity inert-atmosphere box. The sample was melted and held in the liquid state for 1 hr. The temperature was then decreased, and the first break in the cooling curve was observed. This melting and cooling operation was repeated until the location of the first break was constant, after which complete cooling and heating curves were determined. This procedure was followed to ensure complete mixing of the components in the system. The heating and cooling rates generally were maintained between 1 and 2°K/min, which were low enough to clearly characterize the thermal breaks and yet were not so high as to cause problems with supercooling.

The sample composition was calculated from the weights of the pure materials; however, periodic checks were made by chemical analysis for the constituents of the salt system.

2. Thermal-analysis Results

Crystallization temperature data were obtained for the NaF-NaCl, NaCl-NaI and NaI-NaF binary mixtures as a function of composition. These data are listed in Table XI, and the phase diagrams appear in Fig. 36. Each of these systems is a simple eutectic system with no evidence for solid solution at the eutectic temperature.

TABLE XI. Crystallization Temperatures for Sodium Systems

System NaF-NaCl			System NaCl-NaI			System NaI-NaF		
m/o NaCl	Liquidus Temp, °K	Eutectic Temp, °K	m/o NaI	Liquidus Temp, °K	Eutectic Temp, °K	m/o NaF	Liquidus Temp, °K	Eutectic Temp, °K
0.0	1263	-	0.0	1074	-	0.0	932.5	-
35.0	1131	952.2	15.0	1028	845.6	5.0	916.6	869.8
45.0	1077	954.7	30.0	979.8	845.4	15.0	862.7	870.5
60.0	993.2	953.7	40.0	944.3	845.4	18.0	870.3	869.9
65.0	956.4	953.8	50.0	907.2	846.6	25.0	934.3	870.2
65.8	966.6	953.9	52.5	888.3	846.1	35.0	1016	870.6
67.0	953.6	954.6	55.0	875.4	846.3	45.0	1081	870.6
68.2	958.9	954.3	57.5	865.3	846.2	55.0	1129	870.6
75.0	985.5	953.4	60.0	849.4	847.2	100.0	1263	-
85.0	1024	952.3	63.1	849.8	846.6			
100.0	1074	-	65.0	854.3	846.1			
			69.9	867.9	845.3			
			80.0	892.2	845.8			
			90.0	911.5	845.5			
			100.0	932.5	-			

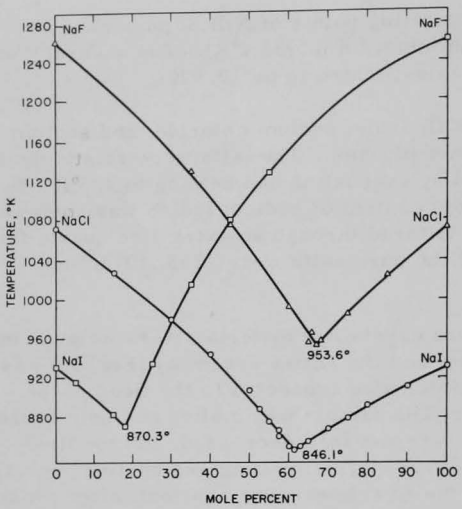

108-9691 Rev. 1

Fig. 36. Crystallization Temperatures for the Binary Systems NaF-NaCl, NaCl-NaI, NaI-NaF

In the NaF-NaCl binary system, a eutectic composition of 33.0 m/o NaF was observed with a eutectic temperature of 953.6°K. Results of other studies of this system varied over an eight-degree range for the eutectic temperature and a 1.6 m/o range in eutectic composition. Plato[78] reported a eutectic temperature of 953.0°K at 34.6 m/o NaF; Rassonskaya and Bergman[79] obtained 947.2°K as the eutectic temperature at 33.0 m/o NaF; Kuvakin and Kusakin[80] reported a eutectic temperature of 955.2°K at a eutectic composition of 33.2 m/o NaF.

For the NaCl-NaI binary system, a eutectic composition of 38.5 m/o NaCl melting at 846.1°K was observed. Amadori[81] reported the eutectic temperature as 851.2°K at 37.0 m/o NaCl, whereas Ilyasov and Bostandzhiyan[82] observed a eutectic melting point of 858.2°K with a composition of 37.5 m/o NaCl.

The NaF-NaI binary system was observed to have a eutectic composition of 18.0 m/o NaF melting at 870.3°K. Ruff and Plato[83] reported a eutectic temperature of 893.2°K at a composition of 20 m/o NaF, whereas Dombrovskaya[84] reported the eutectic to melt at 876.2°K with a composition of 18 m/o NaF.

The present investigation was concerned mainly with the liquidus surface and not with the complete characterization of the ternary NaF-NaCl-NaI system. Liquidus temperature data for various NaCl:NaI mole ratios radiating from the NaF corner of the ternary diagram are given as Series I to V in Table XII. An additional cross section, the 8.5:1.5 mole ratio of NaI:NaF radiating from the NaCl corner, was studied to describe completely the area of the minimum temperature in the system. The data for this cross section appear in Table XII as Series VI. A contour diagram of the liquidus isotherms for the ternary system, given in Fig. 37 was constructed from the pseudobinary systems. The solid-line isotherms in Fig. 37 are interpolations of experimental data; the broken-line isotherms are extrapolations from the experimental data. Figure 37 indicates that the system is of a simple eutectic type with three fields of crystallization: one of pure NaF, one of pure NaCl, and one of pure NaI. The ternary eutectic composition is 15.2 m/o NaF, 31.6 m/o NaCl, 53.2 m/o NaI with a melting point of 802.6°K.

TABLE XII. Crystallization Temperatures for NaF-NaCl-NaI Ternary

Series I			Series II			Series III		
Mole Ratio NaCl:NaI 1:4			Mole Ratio NaCl:NaI 2:3			Mole Ratio NaCl:NaI 3:2		
m/o NaF	Liquidus Temp, °K	Eutectic Temp, °K	m/o NaF	Liquidus Temp, °K	Eutectic Temp, °K	m/o NaF	Liquidus Temp, °K	Eutectic Temp, °K
0.0	880.5	-	0.0	852.7	-	0.0	941.9	-
5.0	876.2	802.8	5.0	842.5	802.4	5.0	925.8	802.6
10.0	859.1	802.6	10.2	829.4	802.6	10.0	910.3	801.8
15.0	844.3	802.9	15.0	812.7	802.6	15.0	897.0	802.7
20.0	871.0	802.6	20.0	840.7	802.7	20.0	881.6	802.5
25.0	928.7	803.4	25.0	907.4	802.8	25.0	906.2	802.9
30.0	981.1	803.0	25.0	915.4	802.6	30.1	942.8	803.0
35.0	1009	802.6	30.0	961.2	802.8	34.9	983.5	802.8
40.0	1041	800.4	35.0	998.9	802.6	40.0	1025	802.7
45.0	1077	802.9	40.0	1035	802.4	45.0	1052	802.4
50.0	1109	802.6	45.0	1067	801.9	50.0	1079	803.0
55.0	1122	802.9	50.0	1095	802.0	55.0	1109	802.7
100.0	1263	-	55.0	1117	802.9	60.0	1128	803.0
			100.0	1263	-	100.0	1263	-

Series IV			Series V			Series VI		
Mole Ratio NaCl:NaI 7:3			Mole Ratio NaCl:NaI 4:1			Mole Ratio NaI:NaF 8.5:1.5		
m/o NaF	Liquidus Temp, °K	Eutectic Temp, °K	m/o NaF	Liquidus Temp, °K	Eutectic Temp, °K	m/o NaCl	Liquidus Temp, °K	Eutectic Temp, °K
0.0	1039	-	0.0	1012	-	0.0	882.7	-
5.0	966.5	802.4	5.0	994.7	802.7	15.1	859.9	801.8
10.0	961.7	802.6	10.0	980.0	802.5	25.0	840.8	802.8
14.9	934.8	801.8	15.0	963.4	803.0	35.0	836.0	802.6
20.0	918.4	803.0	19.9	946.6	802.8	45.0	877.2	802.4
24.9	899.9	802.6	25.0	929.9	802.7	55.0	920.1	802.8
30.0	936.9	802.6	30.0	938.6	803.4	65.0	956.4	802.6
35.0	984.2	802.5	35.0	970.2	802.2	75.0	993.3	801.9
40.0	1012	802.1	40.0	997.7	802.6	100.0	1074	-
45.0	1045	802.5	45.0	1036	802.4			
50.0	1077	802.4	50.0	1076	802.6			
55.0	1101	802.6	55.0	1093	802.6			
60.0	1126	802.2	60.0	1117	802.8			
100.0	1263	-	100.0	1263	-			

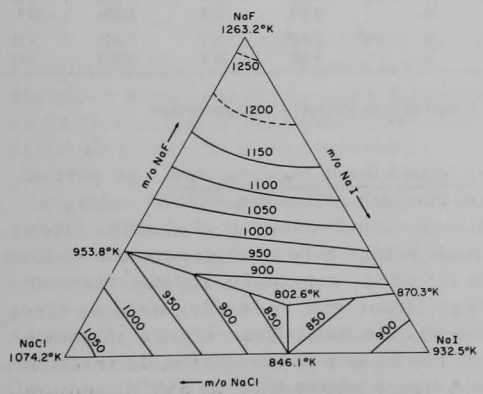

308-636 Rev. 1

Fig. 37. Crystallization Temperatures for the Ternary System NaF-NaCl-NaI

It is of interest to speculate on the conductivity of this sodium halide mixture when used as the electrolyte in a galvanic cell. For calculational purposes, 823°K was chosen as a typical cell operating temperature. With no experimental data available for the ternary mixture, the conductivity equations for each pure salt were extrapolated to the cell temperature. These data were then weighted according to the mole fraction of each component in the ternary mixture and then summed to give a calculated specific conductivity of 2.2 mhos/cm (0.44 ohm-cm) at 823°K.

D. Studies of Cells, Regenerators, and Systems

1. Sodium-Bismuth Experimental Cells

As a part of the engineering effort directed toward developing practical bimetallic cell systems, experimental cells of two types were operated. These are designated as "open cells" and "closed cells." An open cell refers to a cell assembly consisting of an anode cup and a cathode cup immersed in an electrolyte bath. This type cell must be operated in a high-purity inert-atmosphere box since there is no housing to protect it from air and water vapor in the atmosphere. An open-cell method provides a quick means to screen various cell systems and allows visual observations to be made during cell operation. A closed cell refers to a cell assembly with an air-tight housing, which permits it to be operated in an ordinary air environment.

Table XIII summarizes some of the pertinent data concerning bimetallic cells with sodium anodes. A more detailed description of the experiments with sodium-bismuth cells is presented directly below. Sodium-lead cells were run in conjunction with regenerators, as complete systems. The studies of complete systems are discussed in Section IV.D.3.

TABLE XIII. Calculated Characteristics of Bimetallic Cells with Sodium Anodes

Anode Metal					Cathode Alloy				Cathode Metal Requirement, g per g Anode Metal	Specific Energy	
Metal	Atomic Weight	Melting Point, °K	Amp-hr/g	Amp-hr/cm^3	Cathode Metal	a/o Sodium	Cell Temp, °K	Cell Potential, V		W-hr per g Active Material	W-hr per lb Active Material
Na	22.99	370.9	1.16	0.948[a] (at 820°K)	Bi	20	820	0.650	36.4	0.0202	9.15
						30		0.585	21.2	0.0305	1.38
					Sn	20	820	0.382	20.4	0.0207	9.36
						30		0.319	12.0	0.0284	12.9
					Pb	20	698[b]	0.400[c]	36.0	0.0125	5.66
						30		0.330	21.8	0.0168	7.61

[a]Density data taken from Liquid Metal Handbook.[86]
[b]This temperature was chosen for purposes of calculation only. It would not be the actual cell-operating temperature.
[c]Calculated from data compiled by Hultgren et al.[52]

a. Cells and Batteries with Liquid Electrolytes. As part of the preliminary work on the sodium-bismuth cell, open-circuit voltages were measured using anode and cathode cups consisting of alumina tubes with closed ends provided with a small bridge hole to minimize the sodium transfer.[18,63] Sodium was placed in the anode cup, and a sodium-bismuth mixture was placed in the cathode cup. Tantalum rods were used as electrical contacts. The electrolyte was 38 m/o NaCl-NaI. Figure 38 shows the open-circuit voltages obtained at 859°K as a function of mole fraction sodium in the bismuth cathode. This figure shows that, at 859°K, sodium is soluble up to about 55 a/o in the bismuth cathode, which indicates that the cell could be operated at cathode compositions up to 55 a/o sodium

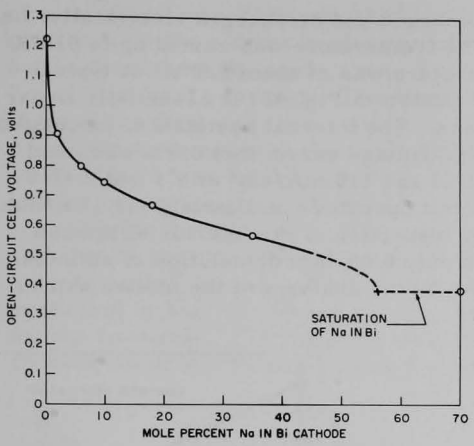

108-7994

Fig. 38. Open-circuit Potential of a Sodium-Bismuth Cell at 859°K as a Function of Cathode Composition; 38 m/o NaCl-NaI Electrolyte

without solid sodium-bismuth compound formation. It is also apparent that the cell voltage does not change greatly if the composition of sodium in the bismuth cathode is between about 20 and 40 a/o sodium.

A series of open-cell experiments was performed using the sodium-bismuth cell shown in Fig. 26. The anode consisted of a stainless steel cup (2.22-cm diameter) with a hole in the bottom over which a stainless steel-fiber disc was placed for distributing the sodium. The cathode cup (2.22-cm diameter), also made of stainless steel, was supported by a hollow rod which served as the thermocouple well. The electrolyte, 37.5 m/o NaCl-62.5 m/o NaI, was contained in either stainless steel or tantalum crucibles. During cell operation, the bismuth was placed in the cathode cup and the cup immersed in the electrolyte. (In some experiments, the bismuth was placed directly in with the electrolyte.) The anode cup was immersed until the two electrodes were separated by 5 cm of electrolyte (the interelectrode distance). Cell operating temperature ranged from 833 to 956°K. Cell resistances varying from about 3 to 0.15 ohms and current densities up to 145 mA/cm^2 at 0.28 V were measured with these cells.

Experiments were performed with similar cells using 86 m/o NaOH-14 m/o NaI electrolyte. However, the hydroxide corroded the stainless steel crucible and, as discussed in Section IV.C, using hydroxide as an electrolyte brings about undesirable side reactions. Thus, we abandoned this line of experimentation.

Two experimental sodium-bismuth closed cells have been constructed and operated. The first cell[26,63] shown in Fig. 39 was made of stainless steel, had 7.5-cm-diam electrodes and used a combination of silicone rubber and frozen electrolyte as both an electrical insulator and pressure seal. The cell was loaded with 15.2 m/o NaF-31.6 m/o NaCl-53.2 m/o NaI electrolyte (the eutectic composition), which constituted a molten layer of approximately 2.5-cm thickness, and 400 g of bismuth. Using stainless steel-sheathed heating elements, the cell was heated to an operating temperature of about 825°K, and 15.5 g of sodium was added to the anode chamber. With this amount of sodium, the bulk sodium concentration of the cathode alloy at the completely discharged state should have been

26 a/o. The cell was periodically charged and discharged electrically; i.e., it operated as a secondary cell. The temperature was varied up to 920°K, but for most of the time, the temperature was at about 820°K. A typical current-voltage curve for this cell (shown in Fig. 40) is essentially linear except at the higher current densities. The internal resistance, calculated from the slope of the current density-voltage curve, was 0.050 ohm, and cell-discharge current densities of 90 and 110 mA/cm^2 at 0.5 and 0.45 V, respectively, were obtained. This cell operated continuously for 17 months without failure. Upon disassembly, inspection of the interior of the cell revealed very little corrosion, with only 0.05-mm dissolution of stainless steel in the electrode chambers. An X-ray analysis of the molten salt indicated no decomposition.

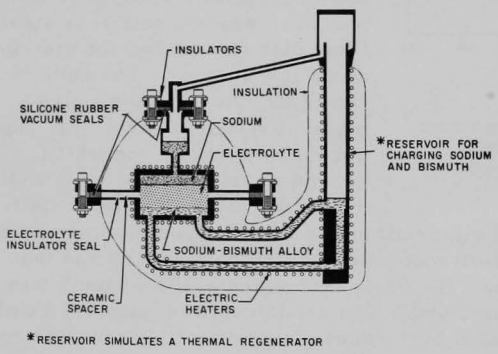

108-8378 Rev. 2

Fig. 39. Experimental Sodium-Bismuth Cell

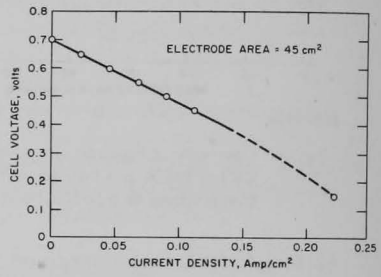

308-517 Rev. 1

Fig. 40. Voltage-Current Density Curve for a Sodium-Bismuth Cell at 823°K as a Function of Current Density; 20 a/o Sodium in Bismuth Cathode; Interelectrode Distance = 2.5 cm; Electrolyte Composition = 15.2 m/o NaF-31.6 m/o NaCl-53.2 m/o NaI

The second closed cell,[7] which had been designed to give improved performance over that of the first cell, is shown in Fig. 41. This cell contained an improved sodium retainer-current collector, in the form

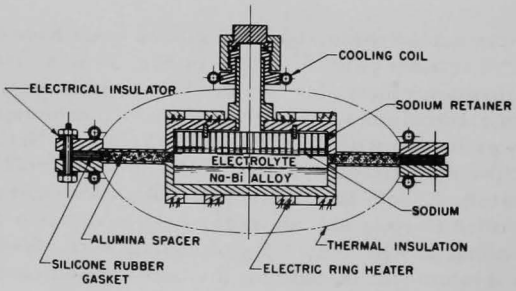

Fig. 41
Improved Sodium-Bismuth Cell with Liquid Electrolyte

308-246-A

of a stainless steel (1.5-mm-thick) spiral, mounted in the anode compartment to hold the sodium in place and to maintain a uniform current distribution throughout the anode area. The eight-turn spiral had a diameter of 7.5 cm and was 1 cm high. The dimensions of this cell were the same as those of the first cell, two cylindrical 7.5-cm-diam electrode compartments providing a geometrical electrode area of 45 cm^2. The lower (cathode) compartment was loaded with 30 a/o Na-Bi alloy, above which a sufficient amount of electrolyte (NaF-NaCl-NaI eutectic) was added to make an electrolyte layer 0.4 cm thick. (The loading process was performed in the high-purity helium-atmosphere enclosure.) Two 300-W electric ring heaters heated the cell. Typical cell current density-voltage curves are presented in Fig. 42. These curves are essentially linear, as were those for the first cell. The linearity indicates that no significant activation or concentration overvoltages existed at the electrodes.

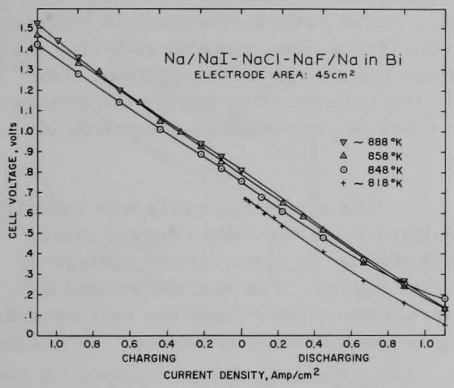

308-246-B Rev. 2

Fig. 42. Voltage of the Sodium-Bismuth Cell as a Function of Current Density. Interelectrode distance = 0.4 cm.

The terminal voltage of the cell may be expressed as

$$E = E_{oc} - IR. \tag{67}$$

Calculation of the total internal resistance from this equation and the data of Fig. 42 gave a value of approximately 0.0136 ohm. This compares with the 0.004-ohm electrolyte resistance calculated from an estimated specific resistance of 0.44 ohm-cm.

In further experiments, the cell was charged and discharged at currents up to 50 Amp (1.1 Amp/cm^2) at temperatures ranging from the melting point of the electrolyte (808°K) to 885°K. The charge cycle was initiated from the completely discharged state and conducted at a constant current. During the charging process, the emf of the cell rises in accordance with the following relations:

At the sodium-bismuth electrode

$$Na^{\circ} \rightarrow Na^{+} + e^{-}; \tag{68}$$

$$\underset{\sim}{E} = -\frac{\underset{\sim}{R}T}{N\underset{\sim}{F}} \ln a_{Na(Bi)}. \tag{69}$$

However, self-discharge takes place at the same time, resulting in the transfer of some sodium from anode to cathode. Since the direction of the ionic transfer of sodium on charging and the direction of the self-discharge transfer of sodium are opposite, there is a charging current for every final charged voltage (at steady-state) below which the rate of the self-discharge transfer equals that of charge. As a result, no additional charge can be accumulated. At the cell temperature of 853°K, the minimum charge rate was 5 Amp for 0.85 V. As the cell approaches the fully charged state, the terminal voltage rises rapidly. Since the decomposition voltage of the electrolyte is approximately 2.2 V at the normal cell temperature, the charging process must be terminated before the resistance-free cell voltage exceeds this value. At the termination point, the cell open-circuit voltage usually exceeds 1.2 V, which indicates that the interfacial sodium concentration in the cathode alloy is small. However, after a high current charge (50 Amp), the bulk concentration of sodium in the cathode was still considerably higher than the concentration at the cathode/electrolyte interface. Allowing the cell to stand at open circuit for a short time or reducing the charge rate made it possible to continue the charge to completion. The interfacial concentration of sodium in the cathode alloy during the charge and discharge cycles at different currents is presented as a function of time in Fig. 43.

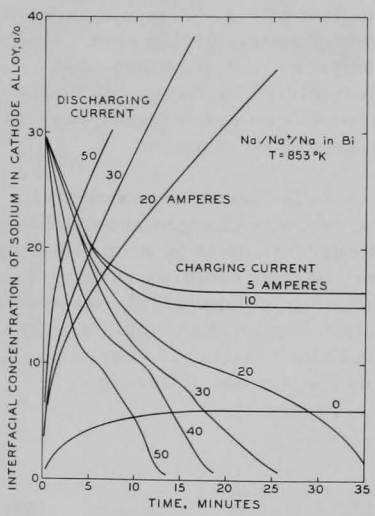

308-246-C Rev. 2

Fig. 43. Interfacial Sodium Concentration during Charge and Discharge of a Sodium-Bismuth Cell. Electrode area = 45 cm^2; interelectrode distance = 0.4 cm.

The discharge cycle was usually initiated from the fully charged state, indicated by an open-circuit voltage of 1 V or higher. The emf decreased as current was drawn from the cell according to the following relations:

At the anode

$$Na^{\circ} \rightarrow Na^{+} + e^{-}; \tag{70}$$

$$\underset{\sim}{E} = -\frac{\underset{\sim}{R}T}{NF} \ln a_{Na(Bi)}. \tag{71}$$

Comparison of Figs. 43 and 44 shows the correspondence of concentration and voltage changes in accordance with Eq. 71. Because of the self-discharge process, some charge was always lost. Consequently the combined charge-discharge current efficiency, defined as

$$Eff_{C-D} = \frac{\int i_D dt}{\int i_C dt}, \tag{72}$$

is less than unity. In the present cell, the combined charge-discharge efficiency was approximately 80% for a current density of 665 mA/cm^2 at 838°K.

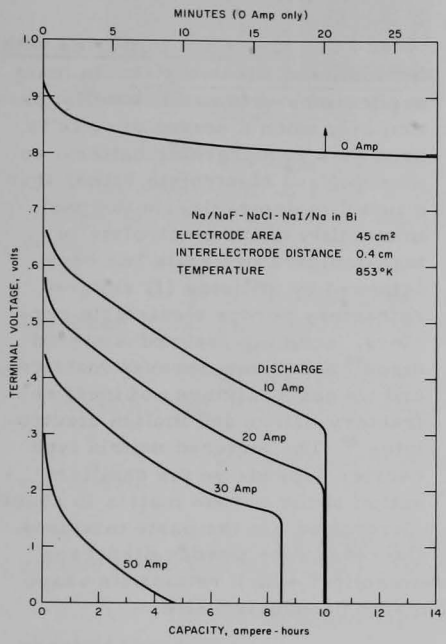

308-957

Fig. 44. Terminal Voltage during Constant-current Discharge of a Sodium-Bismuth Cell. Electrode area = 45 cm^2; interelectrode distance = 0.4 cm.

Figure 44 shows the terminal voltage as a function of cell capacity during discharge at various constant currents at 853°K. The cell contained sodium equivalent to approximately 15 Amp-hr. In the heavy-discharge region, i.e., above 40 Amp, the interfacial concentration of sodium in the cathode alloy reaches the solid alloy formation concentration while the bulk sodium concentration is still considerably lower (see Fig. 43). Apparently, then, a method of renewing the cathode interface, such as convectional stirring of the bulk cathode alloy, should improve the charge-discharge performance at high current densities. The ability of the cell to retain charge is indicated by the curve labeled as "0 Amp" in Fig. 44. The loss of charge occurs by the self-discharge transfer of sodium (see discussion in Section IV.B.3).

The charge-discharge operations were repeated over 50 times at various temperatures, and the cell showed no sign of deterioration.

The combination of sodium-bismuth cells to form batteries has been considered, and several conceptual designs of batteries have been devised. To achieve a compact battery for use with liquid electrolytes and a regenerator, the design shown in Fig. 45 has been proposed.[87] In this system, the anode metal (sodium) from the regenerator enters the vertically stacked three-cell battery at the top and distributes itself among the cells by flowing through the downcomers. The sodium reacts electrochemically with the cathode metal (bismuth) in each cell, and, as the cathode liquid levels rise, the cell product in the cathode alloy flows down to lower stages successively through the bismuth downcomers. The cathode alloy leaving the bottom cell is fed to the regenerator. Since the densities of liquid sodium, NaF-NaCl-NaI eutectic electrolyte, and 30 a/o sodium-bismuth alloy are (approximately) 1.0, 2.5, and 7.3 g/cm^3, respectively, at

the cell temperature of 820°K, each liquid layer is clearly separated from the other. However, hydrodynamic stability of the liquid stream must be carefully established.

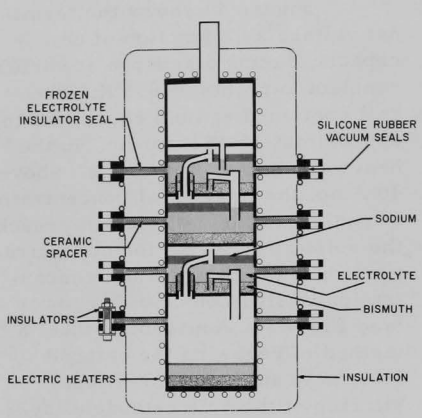

108-8379 Rev. 1

Fig. 45. Three-cell Bimetallic Battery Designed to Utilize Liquid Electrodes and a Liquid Electrolyte

b. Cells and Batteries with Immobilized Electrolytes. In many applications of bimetallic cells, particularly when a series of cells is used as a rechargeable battery, an immobilized electrolyte rather than a liquid is desirable. In the past, immobility of the electrolyte in high-temperature cells has been achieved by utilizing (1) sintered refractory porous electrolyte carriers, including pressed-sintered discs[88] and flame-sprayed matrices, and (2) paste mixtures of inert refractory fillers and molten electrolytes.[89] The sintered matrix type carrier depends on the capillary action of the porous matrix to absorb electrolyte. In the paste mixtures, the refractory powder disperses in the molten electrolyte forming a "semisolid," which retains its shape by means of surface-tension forces and high pseudoviscosity.

In making a paste electrolyte, submicron size refractory powder is essential;[89] for $MgO-LiNaCO_3$ paste, MgO powder having a mean particle size as small as 0.05 μ has been used.[90,91] Yoshizawa et al.[92] found that the mobility of KCl-LiCl electrolyte ceased with the addition of 40 w/o α-Al_2O_3 at 773°K while the electrolytic conductivity was reduced to 75% of the value for pure electrolyte. Our preliminary findings with alumina powder (nominal mean particle size = 3.0 μ) mixed with various amounts of NaF-NaCl-NaI eutectic at 873°K indicate that plastic deformation of the electrolyte becomes acceptably small with about 40 w/o Al_2O_3 in the mixture.

Paste electrolytes containing lithium halides and an inert filler have also been studied. The results are described in Section V.E.2.b.

When an immobilized electrolyte is used in a battery, the design can be simplified considerably over that described above for liquid electrolytes. A bipolar-type battery design currently under study is shown in Fig. 46. This design uses a "hot-seal," instead of the previously used frozen-electrolyte seal. A battery of two cells based on this design has been built and is being tested.

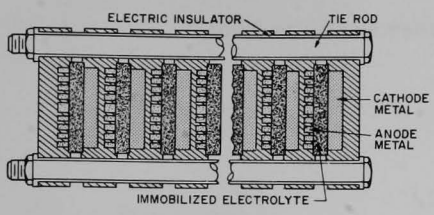

Fig. 46
Bimetallic Battery Designed to Utilize an Immobilized Electrolyte

The experience gained to date concerning the bimetallic cells has shown that, to achieve maximum current density at a given cell voltage, the following factors must be carefully considered for the cell design:

(1) Effective use of anode area to distribute and retain the alkali metal and to provide low resistance in collecting current.

(2) Effective means of surface renewal for cathode alloy to promote rapid alkali-metal dispersion in the cathode alloy.

(3) Thin electrolyte and low specific resistance of the electrolyte.

(4) Minimum self-discharge by reducing thermal convection in the electrolyte as in the use of pastes.

(5) Minimum reactions other than the desired electrochemical reactions.

Further engineering studies of the bimetallic cells are planned along these lines.

2. Regenerator and Condenser Studies

a. Design Considerations. The successful application of regeneration techniques depends upon an understanding of the equilibria that exist between vapor and liquid. This point has been discussed previously (see Section IV.A.5). This discussion assumes that a suitable combination of pressure and temperature has been selected for the regenerative bimetallic cell system. Only the points that are pertinent to regenerator and condenser design--namely, heat and mass balance, cathode-metal circulation, heat transfer, and mass transfer--will be discussed. The considerations of this section apply to bimetallic cells with sodium anodes.

(1) Heat and Mass Balance. The following heat and mass balances apply to the system of regenerator and condenser:

Overall mass balance,

$$w_A + w_{C_2} = w_{C_1}; \tag{73}$$

Component mass balance,

$$w_A X_A + w_{C_2} X_{C_2} = w_{C_1} X_{C_1}; \tag{74}$$

Regenerator heat balance,

$$q_{input} + w_{C_1} \tilde{\underset{\sim}{H}}_{C_1} = w_A (\tilde{\underset{\sim}{H}}_A + \Delta \tilde{\underset{\sim}{H}}_v) + w_{C_2} \tilde{\underset{\sim}{H}}_{C_2}; \tag{75}$$

Condenser heat balance,

$$q_{con} + w_A \tilde{\underset{\sim}{H}}_A = w_A (\tilde{\underset{\sim}{H}}_A + \Delta \tilde{\underset{\sim}{H}}_v). \tag{76}$$

Figure 47 is a schematic representation of the mass and heat balances. We may write $\tilde{\underset{\sim}{H}}_i = \tilde{\underset{\sim}{H}}_i^\circ + (\overline{\tilde{C}_{p_i}})(T_i - T^\circ)$, where $\tilde{\underset{\sim}{H}}_i^\circ$ is the standard enthalpy of formation of the ith species from its constituent elements at a reference temperature, T°. Then Eq. 75 becomes

$$q_{input} = w_{C_2}\left[\tilde{\underset{\sim}{H}}_{C_2}^\circ + \tilde{C}_{p_{C_2}}\left(T_{C_2} - T^\circ\right)\right] - w_{C_1}\left[\tilde{\underset{\sim}{H}}_{C_1}^\circ + \tilde{C}_{p_{C_1}}\left(T_{C_1} - T^\circ\right)\right]$$
$$+ w_A(\Delta \tilde{\underset{\sim}{H}}_v) + w_A\left[\tilde{\underset{\sim}{H}}_A^\circ + \tilde{C}_{p_A}(T_A - T^\circ)\right]. \tag{77}$$

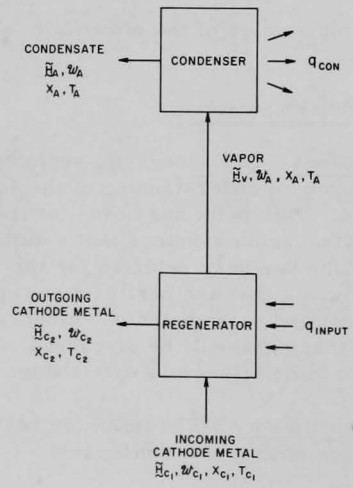

Fig. 47

Heat and Mass Balance around a Regenerator and a Condenser

308-522 Rev. 1

Combination and rearrangement of Eqs. 74 and 75 yield

$$w_{C_1} = w_A\left(1 + \frac{X_A - X_{C_1}}{X_{C_1} - X_{C_2}}\right) = w_A \frac{X_A - X_{C_2}}{X_{C_1} - X_{C_2}}; \tag{78}$$

$$w_{C_2} = w_A \frac{X_A - X_{C_1}}{X_{C_1} - X_{C_2}}. \tag{79}$$

Equations 78 and 79 allow us to calculate the cathode-alloy molar flow rate corresponding to a unit molar flow rate of the anode metal condensate. Since, in general, the condensate is pure metal, $X_A = 1$. Thus Eqs. 78 and 79 become

$$\frac{w_{C_1}}{w_A} = \frac{1 - X_{C_2}}{X_{C_1} - X_{C_2}}; \tag{80}$$

$$\frac{w_{C_2}}{w_A} = \frac{1 - X_{C_1}}{X_{C_1} - X_{C_2}}. \tag{81}$$

The heat input per unit anode metal flow rate is obtained by introducing Eqs. 78 and 79 into Eq. 77 to give

$$\frac{q_{input}}{w_A} = \frac{X_A - X_{C_1}}{X_{C_1} - X_{C_2}}\left[\left(\tilde{H}^\circ_{C_2} - \tilde{H}^\circ_{C_1}\right) + \left(\tilde{C}_{p_{C_2}} T_{C_2} - \tilde{C}_{p_{C_1}} T_{C_1}\right)\right]$$
$$- \left[\tilde{H}^\circ_{C_1} + \tilde{C}_{p_{C_1}}\left(T_{C_1} - T^\circ\right)\right] + \Delta\tilde{H}_v + \tilde{C}_{p_A}\left(T_A - T^\circ\right). \tag{82}$$

If $X_A = 1$, $\tilde{C}_{p_{C_1}} = \tilde{C}_{p_{C_2}}$, and $\tilde{H}^\circ_{C_1}$ is negligibly small compared to $\Delta\tilde{H}_v$. Then Eq. 82 reduces to

$$\frac{q_{input}}{w_A} = \frac{1 - X_{C_1}}{X_{C_1} - X_{C_2}} \tilde{C}_{p_{C_2}}\left(T_{C_2} - T_{C_1}\right) + \Delta\tilde{H}_v + \tilde{C}_{p_A} T_A - \tilde{C}_{p_{C_1}} T_{C_1}. \tag{83}$$

(2) Cathode-metal Circulation. In the present design, the cathode alloy is circulated by natural convection, which depends on (1) thermal convection, (2) the density change due to acquisition of the anode metal at the cell cathode, and (3) the density change due to depletion of the anode metal in the regenerator. Figure 48 is a schematic diagram of the heat flow and cathode alloy flow; Fig. 49 shows the effects of these density changes. Thermal convection takes place due to the density difference of the liquid

metal caused by the temperature difference between the cell and regenerator (shown as T_{cell} and $T_{regenerator}$ in Fig. 49). The density change corresponding to acquisition of the anode metal at the cell cathode is indicated as the density change accompanying the concentration change from C_1 to C_2 at approximately T_{cell}. The density change resulting from depletion of the anode metal at the regenerator is presented as the density change due to the concentration change from C_2 to C_1 at approximately $T_{regenerator}$.

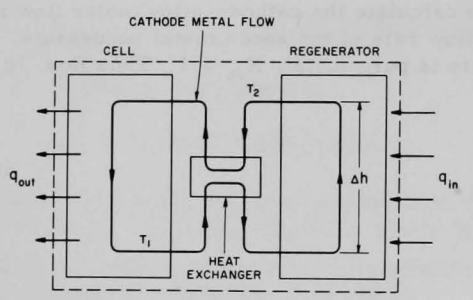

308-520

Fig. 48. Cathode-metal Flow Diagram for a Thermally Regenerative Galvanic Cell

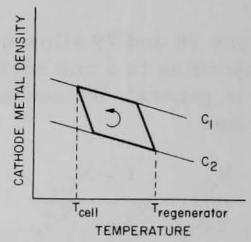

308-608 Rev. 1

Fig. 49. Schematic Representation of Density-Temperature-Composition Relationships for Natural Convection Circulation of Cathode Alloys. $C_1 < C_2$; C is the anode-metal concentration in the cathode alloy.

By taking an energy balance around the cathode alloy circulation loop, as shown in Fig. 49, we obtain

$$\frac{g}{g_c} \oint dz + \frac{1}{g_c} \oint v\, dv + \oint V\, dp = -W - l\overline{w}. \tag{84}$$

Since no work was done by the liquid metal (W = 0), and no pressure or velocity changes occurred (dp = 0 and dv = 0), we have

$$\frac{g}{g_c} \oint dz = -l\overline{w}, \tag{85}$$

or

$$\frac{g}{g_c} \oint dz = \oint f \frac{v^2}{2Dg_c}\, dx. \tag{86}$$

For laminar-flow regime, using the relation $f = 64/\mathrm{Re} = 64\,\nu/vD$, Eq. 86 becomes

$$\frac{g}{g_c}\oint dz = \frac{128\,w}{\pi g_c}\oint \frac{\nu}{D^4\rho}\,dx. \tag{87}$$

Equation 87 may be solved graphically. For noncircular cross sections, four times the hydraulic diameter may be used in place of D. Introducing the Reynolds number in Eq. 86 yields the general expression

$$\frac{g}{g_c}\oint dz = \oint f\frac{\mathrm{Re}^2\nu^2}{2D^3 g_c}\,dx. \tag{88}$$

By using average values of f, Re, and ν over the entire pass of the liquid metal, we obtain

$$\log \overline{f} = \log\frac{\dfrac{g}{g_c}\displaystyle\oint dz}{\dfrac{\overline{\nu}^2}{2D^3 g_c}\,\Delta x} - 2\log\overline{\mathrm{Re}}. \tag{89}$$

Since the relation between Re and f has been experimentally determined and is available in graphical form, Eq. 89 may be solved graphically. The procedure is shown in Fig. 50. The solution yields the flow rate expected from a given set of experimental conditions.

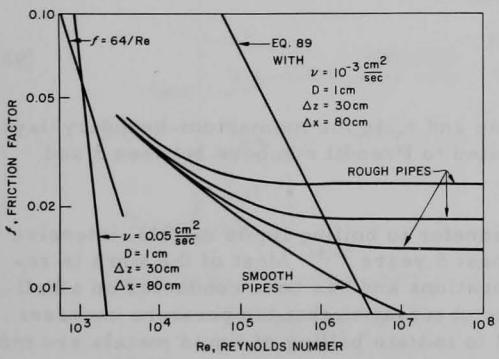

308-607 Rev. 1

Fig. 50. Schematic Representation of Procedure for Graphical Solution of Eq. 89

(3) Heat Transfer. The important heat-transfer processes involved in an analysis of the regenerator are: (1) heat transfer by natural convection, (2) heat transfer to boiling liquid metal, and (3) heat transfer in condensing metal vapors. The fundamental nature of these processes is so complex that we must use heat-transfer coefficients that are experimentally determined. As will be discussed in Section IV.E., liquid metal systems present unique problems

because of their low Prandtl numbers, which are a measure of the relative magnitude of heat transfer by convective transport and by molecular conduction. The rate of heat transfer is

$$q = hA\Delta T. \tag{90}$$

For the heat transfer in natural convection with $Pr \ll 1$, the experimental data have been correlated by

$$Nu = \Phi(Ra \cdot Pr). \tag{91}$$

In the range of $Ra \cdot Pr$ from 10 to 10^4, Hyman et al.[93] proposed, for liquid metals flowing transversely around a cylinder, that

$$Nu = 0.53(Ra \cdot Pr)^{1/4}.$$

Dropkin and Somerscales[94] investigated the flow of liquids between two parallel plates inclined at various angles with respect to the horizontal. The study was restricted to liquids having Prandtl numbers between 2×10^{-2} and 1.2×10^4 and Rayleigh numbers between 5×10^4 and 7.2×10^8. The equation

$$Nu = BRa^{1/3}Pr^{0.074} \tag{92}$$

applies to this case, where the coefficient B varies from 0.069 for the horizontal case when the lower plate is heated to 0.049 for the vertical. This may be compared over the corresponding experimental Rayleigh number range ($4 \times 10^4 \leq Ra \leq 10^8$) with the proposed correlation for the vertical plates by Emery and Chu,[95]

$$Nu = 0.28(Ra)^{1/4}\left(\frac{z}{\delta_v}\right)^{-1/4}, \tag{93}$$

where z is the height of the plate and δ_v is the momentum-boundary-layer thickness. This equation is limited to Prandtl numbers between 3 and 3×10^4.

For heat transfer to boiling liquid metals, intensive work has been done during the past 5 years.[96,97] Most of the work is related to space power-plant applications and has been conducted on alkali metals. The findings include the observation that temperature excesses above the boiling point required to initiate boiling of liquid metals are much larger than for other fluids. Another complication derives from the fact that in most applications of liquid metal boiling, pressures are low compared to the thermodynamic critical pressure. Since the specific volume of the vapor phase is large at these low pressures, the first formation of

vapor during the initiation of boiling creates large volume changes, and stable operation becomes difficult. Our experience with a sodium-lead regenerator indicates that mechanically entrained and/or dissolved gas in the liquid metal may also contribute to boiling instabilities.

At present, no standard correlations are available for either the boiling of liquid metals or the condensation of metallic vapors.

(4) Mass Transfer. In a regenerator, the lower-boiling component from a dissociated intermetallic compound diffuses through the liquid metal to the evaporating surface, where it is distilled off while the higher-boiling component returns to the cell. Therefore, two mass-transfer processes are involved in the regenerator: (1) diffusion of alkali metal in the liquid, accompanied by dissociation, and (2) evaporation of the alkali metal at the evaporating surface.

In the first case, a question arises as to whether the dissociation starts at the vapor-liquid interface or in the bulk liquid. Still another question follows concerning the dissociation rate: Is it high, intermediate, or low? At present, there are no definite answers. Thus a model for analysis must be constructed using reasonable assumptions. We assume that dissociation starts in the bulk liquid and dissociation is very rapid.

Then assuming that there is a fictitious film in the liquid phase at the interface such as shown in Fig. 51, we consider the steady-state process of diffusion accompanied by dissociation. Hatta[98] first suggested this type of analysis.

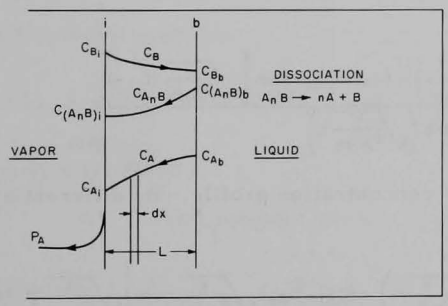

Fig. 51
Concentration Distribution in the Liquid-film Model for a Regenerator

308-505 Rev. 1

The rate of dissociation may be expressed by

$$-\frac{dC_A}{d\theta} = k(C_A - C_{Ae}), \tag{94}$$

where C_{Ae} is the concentration of the alkali metal A in equilibrium with the heavy metal B. A component mass balance yields

$$\frac{dJ_A}{dx} = -\mathcal{D}_{A\text{-}m}\frac{d^2C_A}{dx^2}. \tag{95}$$

The loss of mass of the component A, in a unit volume, a unit cross section, and a unit time, equals

$$\frac{\Delta J_A}{dx} = \frac{dC_A}{d\theta}. \tag{96}$$

Therefore,

$$\frac{dC_A}{d\theta} = -\mathcal{D}_{A\text{-}m}\frac{d^2C_A}{dx^2}. \tag{97}$$

From Eqs. 94 and 97,

$$\frac{d^2C_A}{dx^2} = \frac{k}{\mathcal{D}_{A\text{-}m}}(C_A - C_{Ae}). \tag{98}$$

For the boundary conditions

$$x = 0, \quad C_A = C_{Ai}, \tag{99}$$

and for

$$x = L, \quad C_A = C_{Ab}, \tag{100}$$

integration of Eq. 98 yields

$$C_A - C_{Ae} = \frac{(C_{Ab} - C_{Ae})\sinh\left(\sqrt{\frac{k}{\mathcal{D}_{A\text{-}m}}}\,x\right) + (C_{Ai} - C_{Ae})\sinh\left[\sqrt{\frac{k}{\mathcal{D}_{A\text{-}m}}}\,(L - x)\right]}{\sinh\left(\sqrt{\frac{k}{\mathcal{D}_{A\text{-}m}}}\,L\right)}. \tag{101}$$

This equation establishes the concentration profile. By differentiating Eq. 101, we obtain

$$\frac{dC_A}{dx} = \frac{(C_{Ab} - C_{Ae})\sqrt{\frac{k}{\mathcal{D}_{A\text{-}m}}}\cosh\left(\sqrt{\frac{k}{\mathcal{D}_{A\text{-}m}}}\,x\right) - (C_{Ai} - C_{Ae})\sqrt{\frac{k}{\mathcal{D}_{A\text{-}m}}}\cosh\left[\sqrt{\frac{k}{\mathcal{D}_{A\text{-}m}}}\,(L - x)\right]}{\sinh\left(\sqrt{\frac{k}{\mathcal{D}_{A\text{-}m}}}\,L\right)} \tag{102}$$

Since $J_A = -\mathcal{D}_{A\text{-}m}\, dC_A/dx$, we have

$$-J_A = \sqrt{k\mathcal{D}_{A\text{-}m}}\,\frac{(C_{Ab} - C_{Ae})\cosh\left(\sqrt{\frac{k}{\mathcal{D}_{A\text{-}m}}}\,x\right) - (C_{Ai} - C_{Ae})\cosh\left[\sqrt{\frac{k}{\mathcal{D}_{A\text{-}m}}}\,(L - x)\right]}{\sinh\left(\sqrt{\frac{k}{\mathcal{D}_{A\text{-}m}}}\,L\right)}. \quad (103)$$

At the interface,

$$J_A\Big|_{\substack{x=0\\ \text{diss.}}} = \sqrt{k\mathcal{D}_{A\text{-}m}}\,\frac{(C_{Ai} - C_{Ae})\cosh\left(\sqrt{\frac{k}{\mathcal{D}_{A\text{-}m}}}\,L\right) - (C_{Ab} - C_{Ae})}{\sinh\left(\sqrt{\frac{k}{\mathcal{D}_{A\text{-}m}}}\,L\right)}. \quad (104)$$

Equation 104 gives the rate of transfer of A to the surface of the cathode alloy during regeneration. It may be used to calculate the limiting regeneration rate for a known set of operating conditions if dissociation is the controlling process. The value of $\mathcal{D}_{A\text{-}m}$ is usually not known, but may be estimated.

For the evaporation of an alkali metal, an analysis may be made assuming (1) a semi-infinite liquid layer in the evaporating surface and (2) a rate of evaporation directly proportional to the difference between the alkali-metal concentration, C_{Ai}, in the surface and the concentration, C_{A0}, which corresponds to the vapor pressure of the alkali metal in the vapor space. Then we have

$$\frac{dC_A}{d\theta} = \mathcal{D}_{A\text{-}m}\frac{d^2C_A}{dx^2} \quad (105)$$

with the boundary condition

$$-\mathcal{D}_{A\text{-}m}\frac{dC_A}{dx} = k_c(C_{A0} - C_{Ai}) \text{ at } x = 0, \quad (106)$$

where k_c is a constant.

The solution for Eq. 106 is[99]

$$\frac{C_A - C_{Ab}}{C_{A0} - C_{Ab}} = \operatorname{erfc}\frac{x}{2\sqrt{\mathcal{D}_{A\text{-}m}\theta}} - \exp\left[\frac{k_c}{\mathcal{D}_{A\text{-}m}}x + \left(\frac{k_c}{\mathcal{D}_{A\text{-}m}}\right)^2\mathcal{D}_{A\text{-}m}\theta\right]\operatorname{erfc}\left(\frac{x}{2\sqrt{\mathcal{D}_{A\text{-}m}\theta}} + \frac{k_c}{\mathcal{D}_{A\text{-}m}}\sqrt{\mathcal{D}_{A\text{-}m}\theta}\right). \quad (107)$$

Since the rate of vaporization of A is

$$J_A\Big|_{x=0} = -\left(\mathcal{D}_{A-m}\frac{\partial C_A}{\partial x}\right)_{x=0}, \tag{108}$$

differentiation of Eq. 107 and evaluation at x = 0 yields

$$J_A\Big|_{x=0} = k_c(C_{Ab} - C_{A0})\exp\left[\left(\frac{k_c}{\mathcal{D}_{A-m}}\right)^2 \mathcal{D}_{A-m}\theta\right]\operatorname{erfc}\left(\frac{k_c}{\mathcal{D}_{A-m}}\sqrt{\mathcal{D}_{A-m}\theta}\right). \tag{109}$$

Equation 109 gives the mass transfer rate of the alkali metal crossing the interface and vaporizing at the surface of the cathode alloy during regeneration. It also provides the limiting rate if vaporization is the controlling process.

A study has been planned to collect fundamental data on the mass and heat transfer in the regenerator.

b. Experimental Studies of Sodium-Lead Regenerators. To show the feasibility of operating a thermally regenerative sodium-lead cell, we constructed and tested a laboratory-scale regenerator. The apparatus, shown in Fig. 52, was fabricated of stainless steel and consisted of a vertical cylindrical reservoir for containing the cathode metal, 30 a/o Na-70 a/o Pb, and a vertical cylindrical still and column with a sodium condenser at its upper end. The reservoir was connected to the still by two horizontal tubes through which the bimetallic alloy was thermally circulated. The sodium vapor was distilled from the sodium-lead alloy, condensed at the upper end of the still, and returned to the reservoir, where it mixed with the sodium-lead alloy for continuous circulatory operation. During operation, a sampling cup could be positioned under the sodium-return tube to catch the distilled sodium for a predetermined period of time (usually 15 to 20 min). This allowed measurement of the distillation rate and provided a sample (up to 5 g) of the distilled sodium for analysis. An amount

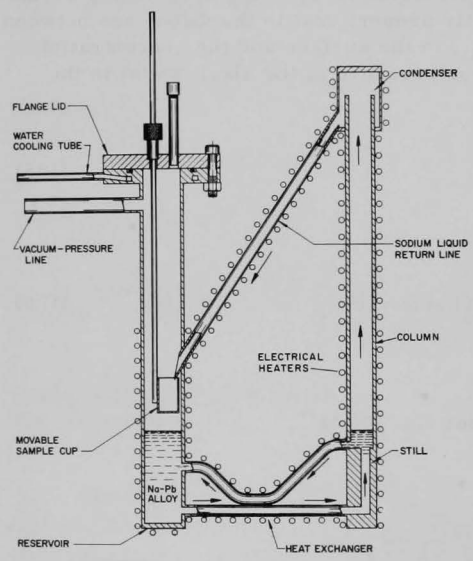

108-8605 Rev. 2

Fig. 52. Thermal Regenerator No. 1 for the Sodium-Lead System

of sodium equal to the sample removed was added to the reservoir to maintain the alloy composition.

A series of 33 test runs was performed under various operating conditions for a total regenerator operating time of 112 hr. Still temperatures ranging from 1020 to 1100°K and distillation pressures from 3 to 8 Torr were used. A total maximum distillation rate of about 14 g · Na/hr corresponding to a specific distillation rate of about 1.3 x 10^{-3} g · Na/sec-cm^2 was obtained. This rate corresponds to a current density of 4.7 Amp/cm^2 at the liquid surface in the still.

During operation of the sodium-lead thermal regenerator, circulation of the sodium-lead alloy was erratic. To determine the cause of this, we conducted some exploratory experiments using the regenerator apparatus (the same as shown in Fig. 52) which had been cleaned and loaded with 649.8 g of 30 a/o sodium-lead alloy. Under 1020 mm Hg argon cover gas that suppressed the distillation of sodium in the still, the liquid metal circulated continuously for over 20 hr. When the system was evacuated to 5 mm Hg pressure, the circulation stopped after 175 min. The apparatus was then filled with argon and after approximately 2 hr, circulation resumed. When the unit was again evacuated to 5 mm Hg pressure, the circulation stopped after 190 min. To determine if the liquid level affected circulation, 58.2 g of alloy were removed from the reservoir. Under argon cover gas, circulation continued for over 15 hr without stoppage. However, when the system was evacuated, circulation stopped after 205 min. During these tests the temperatures of the liquid metal at the inlet and outlet of the regenerator were about 963 and 1073°K, respectively; the maximum flow rate of the liquid metal was 37.7 kg/hr.

Since the above experiments had indicated that system pressure was important in the liquid-metal circulation, radiographic photographs were taken, using a portable ^{192}Ir source as the pressure was varied during experiments. The photographs showed that, upon evacuation, the liquid level in the regenerator section dropped by 3.5-13 mm. If sodium condensate was accumulating in the return line, this could cause the depression of the liquid-metal level in the still. To substantiate this contention, the sodium-lead alloy was replaced with pure lead (which does not distill, hence no condensate flow). With this change, the liquid metal continued to circulate for 8 hr under vacuum.

The radiographic photographs taken under the vacuum conditions showed several small areas of lower optical density, approximately 1 to 2 mm in size, in the feed line to the still. These areas were believed to be gas bubbles in the liquid metal. Similar gas bubbles were also found in the case of pure lead where the circulation stoppage was not observed. Later experiments showed, however, that for the sodium-containing alloy,

evacuation of the liquid metal to remove the mechanically entrained gas is essential to achieve stable circulation.

Based on the above findings, an experimental unit as shown in Fig. 53 was built. The following changes were incorporated into the apparatus: (1) the sodium-return line was enlarged from 0.63 to 1.6 cm ID; (2) the circulation lines were enlarged from 0.63 to 1 cm ID and inclined upward toward the still; and (3) a higher hydrostatic head, from 5.6 to 20.6 cm, was provided. This unit was charged with 30 a/o Na-Pb alloy and placed in operation with the still at 1073°K and the reservoir at 823°K under a condenser pressure of approximately 5 mm Hg. During the first few days, there was some erratic circulation, but continued degassing improved the stability of circulation. After three days of operation, circulation rates and condenser pressure patterns were stable. The unit operated continuously for 935 hr, except for occasional periods of shutdown to examine the system behavior on startup. No difficulties were encountered during the repeated start-up operations. After the experiment, the inside of the unit was examined by means of a borescope. Little corrosion was found in either the still or the reservoir sections. This redesigned regenerator is considered adequate for thermally regenerative cells with sodium anodes.

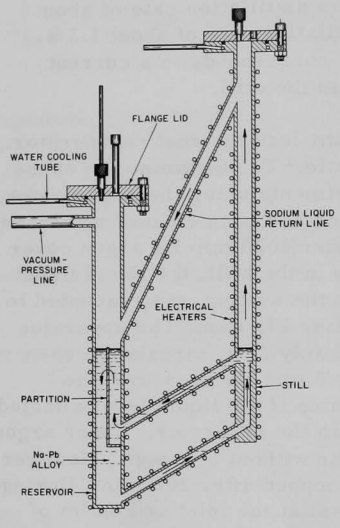

308-958

Fig. 53. Thermal Regenerator No. 2 for the Sodium-Lead System

3. Systems Based on Cells with Sodium Anodes

a. Schematic Representations. A thermally regenerative bimetallic cell system consists of four components: cell, regenerator, heat exchanger, and vapor condenser. A schematic arrangement of these components is shown in Fig. 54. In this system, the cathode product, which

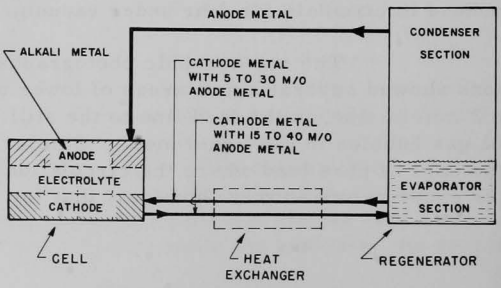

Fig. 54

Flow Diagram of Thermally Regenerative Bimetallic Cell System

108-8717 Rev. 2

is a liquid alloy of the anode and cathode metals, is transferred to the regenerator, where the anode metal is separated by distillation. The alloy, depleted in anode metal, is returned to the cell cathode, after passing through a heat exchanger in which the heat is transferred to the alloy stream coming from the cell cathode to the regenerator. The anode metal vapor is condensed and returned to the cell anode. The circulation of the liquid metal depends on thermal convection. To distill the anode metal rapidly, we must operate the regenerator at 1070°K or higher and the cell at about 820°K. The exact operating temperatures would, of course, depend on the properties of the fused-salt electrolytes and electrode metals involved. The thermodynamics of thermally regenerative galvanic cells were discussed in Sections IV.A.3 and 4.

Several auxiliary components in addition to the four components of Fig. 54 are needed for operation of a laboratory-model regenerative-cell system. These include: vacuum pump, inert gas supply, liquid-metal filtering unit, and emergency cooling unit. Since an alkali metal is regenerated from the heavy metal cathode alloy under vacuum, the vacuum pump is needed for startup. The inert gas supply is necessary to fill the vapor space of the system while the unit is shut down. The liquid-metal filtering unit may be a cold trap, which isolates any mass-transfer corrosion products which may eventually accumulate in the liquid-metal loop. Minute amounts of radioactive impurities may accumulate if the system operates using a nuclear reactor or a radioisotope as a heat source; isolation of some of these might be desirable. The emergency cooling unit is an air-cooling fan used to bring the system to the cathode alloy solidification temperature as quickly as possible in case of an emergency, such as a leak.

Process design calculations for this system involve complex and interrelated heat, mass, and momentum-transfer problems, all closely associated with chemical and electrochemical kinetics.

b. Requirements for Ideal Systems. The requirements for an ideal thermally regenerative galvanic cell system are as follows:

1. Losses due to irreversibility must be minimized. These losses include I^2R losses, self-discharge of the cell, heat losses from the system to surroundings, and pressure drops associated with vapor and liquid flows in the system.

2. The rate processes in the cell and regenerator should be at their optimum rates and must be balanced. The distillation rate of the anode metal in the regenerator must correspond to the anode-metal consumption rate in the cell including both power-producing and self-discharge processes. In this regard, both electrode areas and the regenerator area must be fully and effectively utilized.

3. A high reliability for the system must be sustained a reasonable length of time. Reliability depends upon corrosion resistance of construction materials, chemical stability of the electrolyte, and adequate design of the system. In many applications, the system must withstand mechanical vibration and rotation.

In the present state of the art, reasonable goals for the thermally regenerative bimetallic cells with sodium anodes are as follows:

Cell current density	500 mA/cm^2
Single-cell voltage	0.4 V
Current efficiency	90%
Voltage efficiency	50%
Overall thermal efficiency	15%
Dependable operating life	2 yr
Operating atmosphere	air
Specific power	10 W/lb

c. Heat-, Mass-, and Momentum-transfer Problems Associated with the System. Thermally regenerative bimetallic cells present heat-, mass-, and momentum-transfer problems with unique characteristics because these cells contain circulating liquid metals. The most distinctive feature of liquid metals is their high thermal conductivity; therefore, the mechanism of heat transfer is primarily that of conduction. As a result of the high thermal conductivity of liquid metals, typical values of the Prandtl number (which was defined earlier as a measure of the relative magnitude of heat transfer by convective transport and by molecular conduction) for liquid metals range between 5×10^{-3} and 10^{-2}. In contrast, the hydrodynamic properties of liquid metals do not differ appreciably from those of common liquids, provided that the walls are wetted sufficiently by the flowing liquid metal.

Since the flow rates of concern here lie mainly in the laminar regime, the uniqueness of the heat-, mass-, and momentum-transfer problems arising in the system may be best illustrated by discussing laminar boundary layers that form along the system walls. For fluids with $Pr = 1$ (e.g., gases), the thermal and momentum boundary-layer thicknesses are essentially the same. Since the Schmidt number, Sc, of many gases is nearly unity, the diffusion boundary-layer thickness is also of the same order. For fluids with $Pr > 1$ (e.g., common liquids), the thermal boundary layer becomes thinner than that of the momentum boundary layer, indicating that heat transfer by convection predominates over conduction. The Schmidt number for common liquids such as water is nearly 10^3, and the diffusion boundary layer is therefore approximately one-tenth of the thickness of the momentum boundary layer thickness. This indicates that the mode of mass transfer is largely convection. For liquid metals, because of the extremely low values of Pr ($\ll 1$) and high

values of Sc (10 to 10^2), the thermal boundary layer becomes very thick while the diffusion boundary layer remains thin. This means that the transport of matter in a liquid-metal system is primarily by convection while the transport of thermal energy is largely by conduction. Boundary layers for gases, common liquids, and liquid metals are schematically compared in Fig. 55.

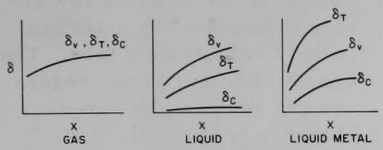

308-516

Fig. 55. Heat, Mass, and Momentum Boundary-layer Thicknesses in Gases, Liquids, and Liquid Metals (Schematic Comparison)

The shapes and thicknesses of thermal, diffusional, and momentum boundary layers for liquid-metal systems under natural convection conditions are not well known. This is perhaps due to a lack of interest in the theory of natural-convection phenomena in liquid metals. The available experimental data on natural convection have been compiled in the form Nu = f(Ra · Pr), where Ra is the Rayleigh number. Some of the appropriate equations have been given above in Section IV.D.3. These correlations are usually based on the assumption that the fluid density is the only temperature-dependent property and then only in the term accounting for body forces. However, particularly at low flow rates, other temperature-dependent properties may influence the boundary layers.

Boiling instability of liquid metals has been widely observed. Some authors[101] attribute the instability to unstable nucleation. In our experience with a sodium-lead regenerator, where sodium vapor was continuously distilled from a 30 a/o Na-Pb alloy being circulated by thermal convection, unstable boiling was observed when a noncondensable gas was present in the liquid metal. There has been great interest in the field of liquid-metal-boiling heat transfer recently and several reviews on this topic have appeared.[102-104] (For additional discussion of boiling heat transfer in liquid metal systems, see Section IV.D.2.)

d. System Designs. There are two general design concepts of thermally regenerative cell systems: linear combination and composite. Figure 56 is a typical arrangement of a linear-combination system. A unit built on this design is discussed in Section e below. The advantage of this design is that every component in the system is separately accessible and, therefore, convenient for laboratory use.

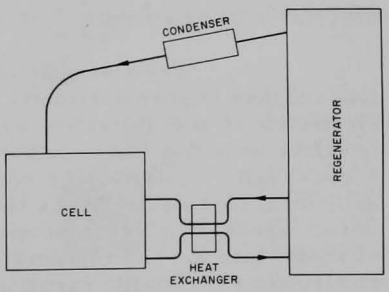

308-518

Fig. 56. Thermally Regenerative System Based on a Linear-combination Design

In the composite design, all components are contained in one

vessel as a unit, thus achieving a high degree of compactness. A typical design is shown in Fig. 57. A vertical cylindrical shell with a conical bottom is divided into two annular chambers by a vertical cylindrical ceramic tube. The center chamber is the regenerating section; the outer chamber is the cell. Two metal partitions on each side of the ceramic tube provide for liquid-metal circulation to cause a countercurrent heat exchange between the incoming and outgoing liquid metals of the cell section. A helical fin and a corrugated surface are provided in this heat exchange section for better heat transfer. The upflowing section of the regenerator also has a helical ribbon to effect good heat transfer. Since this design has a relatively large vapor space cross section and a short distance between the regenerator evaporating surface and the cell section, it requires a very small pressure drop of vapor flow. (This is an important consideration for low pressure systems such as lithium-tin and will be discussed further in Section III.E.2.) Another distinctive advantage of this design is that when radioisotopes are used as the heat source, the surrounding heavy liquid metal layers provide excellent gamma-shielding from the radioactive isotopes.

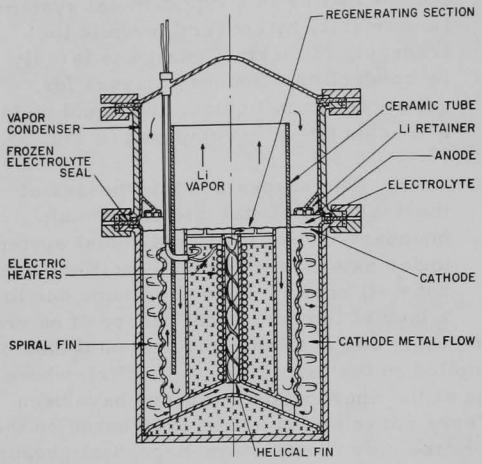

308-612

Fig. 57. Thermally Regenerative System Based on a Composite Design

At present, preliminary studies relating to mass-, heat-, and momentum-transfer data essential for the design of this system are being undertaken using a small mock-up unit.

The aforementioned system designs use free liquid electrolyte and thus require horizontal liquid-liquid interfaces. If an immobilized electrolyte is used instead of a liquid electrolyte, the electrode/electrolyte interface no longer has to be horizontal and systems can be built using vertical cells. A design of a regenerative bimetallic cell system using an immobilized electrolyte is shown in Fig. 58. This figure shows a set of two regenerative cell systems standing side by side. Each cell consists of anode, cathode, and regenerator sections, separated by immobilized electrolyte and metallic partitions. The cathode metal circulates between the cathode and the regenerator section by thermal convection. The regenerated alkali-metal vapor condenses at the condensing surface and flows down to the anode. The advantages of this design over the designs that use

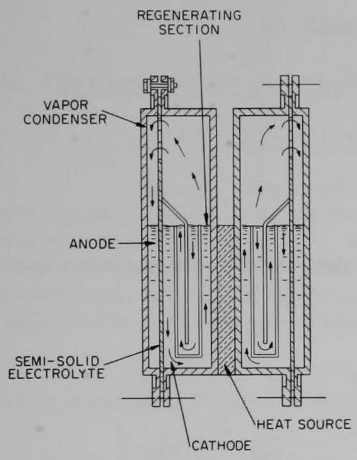

308-602 Rev. 1

Fig. 58. Composite Thermally Regenerative System Designed for Use with Immobilized Electrolyte

liquid electrolytes are compactness, a smaller degree of sensitivity to liquid level, and the absence of ceramic or frozen electrolyte insulators. This design is particularly attractive when many units are assembled side by side to form a battery.

Another design using an immobilized electrolyte is shown in Fig. 59. The relative positions of the anode, cathode and regenerator in this design are similar to those in Fig. 58. However, this design eliminates some of the metal partitions between the cathode and regenerator, which achieves an upward flow of liquid metal in the cathode section, thus simplifying cell construction. The design concepts discussed in this section are being studied. A thermally regenerative system based on the optimum design will be constructed.

e. An Experimental Thermally Regenerative Bimetallic Cell System. An experimental sodium-lead bimetallic cell system has been built and operated. The cell proper was similar to that of the sodium-bismuth cell discussed in Section IV.D.1.a, and the regenerator was similar to the one discussed in Section IV.D.2. Figure 60 shows the complete apparatus. The cell had 7.5-cm-diam anode and cathode sections, and the regenerator had a 2.5-cm-diam evaporation surface. This cell system was loaded with 240.1 g of NaF-NaCl-NaI eutectic electrolyte and 532.7 g of 30 a/o Na-70 a/o Pb alloy before being placed in operation. The cathode metal (Na-Pb alloy) was circulated through the regenerator thermally.

Eleven runs were made in which the regenerator distilled the sodium

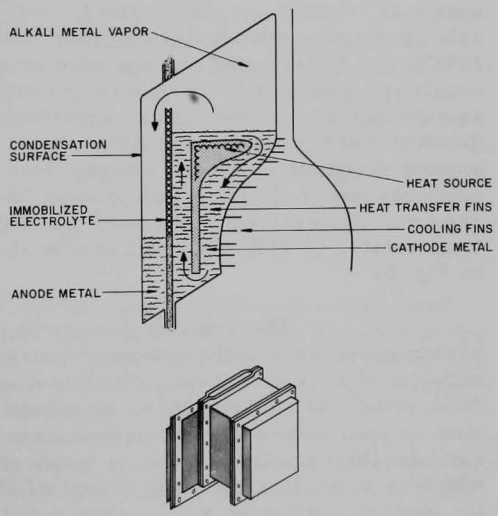

308-614 Rev. 1

Fig. 59. Composite Thermally Regenerative System Designed for Use with Immobilized Electrolyte

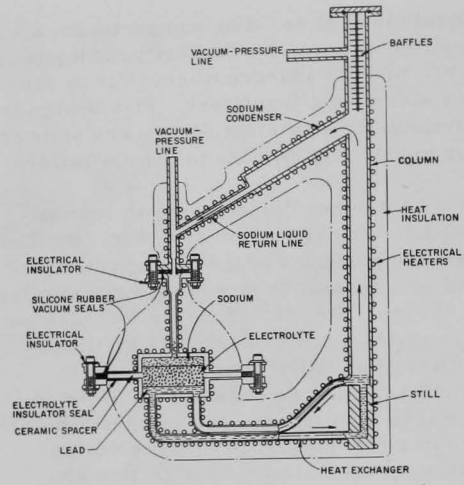

108-9488

Fig. 60
Sodium-Lead Thermally Regenerative System

consumed in the cell. The runs varied in length from 2 to 7 hr for a total operating time of 45 hr during which time the cell was operated at 816-873°K and at 5.7-9 Torr. At 1148°K and 8 Torr, the regenerator furnished sufficient sodium to operate the cell continuously at 7.5 Amp; at 1123°K and 7 Torr, the cell operated continuously at 5 Amp; and at 1098°K and 6 Torr, the cell operated continuously at 2.5 Amp. Cell open-circuit voltages as high as 0.41 V at 848°K were recorded, indicating that the regenerator had reduced the amount of sodium in the cell cathode from the original value of 30 a/o sodium to about 18 a/o sodium. Typical cell performance at 848°K (regenerator at 1148°K and 8 Torr) is shown in Fig. 61.

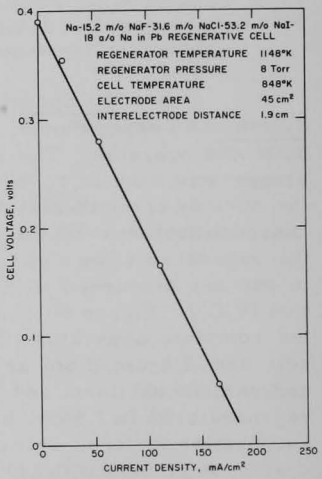

308-506 Rev. 2

Fig. 61. Voltage of a Sodium-Lead Thermally Regenerative Cell at 848°K as a Function of Current Density

The limiting factors in this system appear to be (1) the sodium-evaporating capacity of the regenerator, which is dependent upon the temperature, evaporating-surface area, and sodium concentration in the cathode alloy; and (2) the effective anode area, which is dependent upon the design of the anode to retain and distribute the sodium uniformly and to collect the current.

V. CELLS WITH LITHIUM ANODES*

A. Thermodynamics of Lithium-containing Systems

1. Emf Studies of Lithium Hydride-containing Systems

The only thermodynamic data for lithium hydride available in the literature are those for the enthalpy of formation derived from calorimetric measurements.[105,106] In view of this lack of systematic thermodynamic data, studies were undertaken to establish, by means of emf measurements, values for the standard thermodynamic functions (ΔG_f°, ΔH_f°, ΔS_f°) for the formation of lithium hydride.

Figure 62 shows essential parts of the emf cell. Measurements were made with the cell contained in a furnace well attached to the floor of a high-purity inert-atmosphere box. When in use, the furnace well was isolated from the box atmosphere by a cover on which were mounted insulated holders for the electrodes. The lithium anode, prepared just before each experiment, consisted of about 0.25 g of liquid lithium retained on a sintered stainless steel fiber sponge and held in a small stainless steel crucible. The interfacial tension of the lithium on the sponge was high enough to retain the liquid metal when the sponge was immersed below the surface of the electrolyte. The cathode construction provided for the passage of purified hydrogen over the active Armco iron surface of a bubbler cap held below the surface of the electrolyte. The hydrogen pressure was maintained at 1 atm during each experiment.

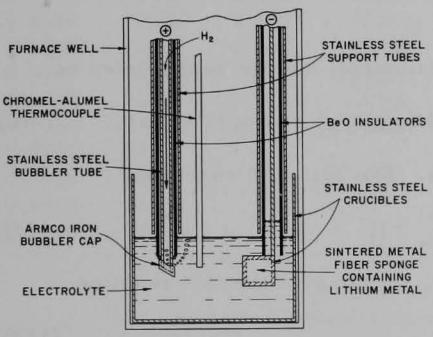

108-8353

Fig. 62. Lithium Hydride Cell Assembly

Lithium chloride, lithium bromide, and lithium iodide, each saturated with lithium hydride, were used as electrolytes. Reagent-grade lithium chloride, lithium bromide, and lithium iodide were purified by standard techniques.[107,108] Lithium hydride was prepared using a technique described by Messer.[109] The compositions of the electrolytes[110,111] were calculated from the weights of the pure components and were chosen so that for each cell, at the temperature of interest, solid lithium hydride was always present. Before each run, the electrolyte was melted and mixed with the lithium hydride to obtain the saturated molten salt. Hydrogen gas at 1 atm was present over the electrolyte to keep lithium hydride from dissociating.

*Unless otherwise indicated, all experiments were performed under helium atmosphere.

In all cell experiments, pure solid was chosen as the standard state for lithium hydride. For hydrogen, the usual standard state of the pure, ideal gas at 1 atm was chosen. The deviations of the gas from ideality under the experimental conditions are negligible in comparison with the accuracy of the emf measurements.

Pure liquid lithium at 1 atm was chosen as the standard state of lithium. The reference state was lithium in equilibrium with the saturated molten salt and solid lithium hydride. The solubility of lithium halides in lithium up to 1300°K is quite small; however, the solubility of lithium hydride in lithium may be significant. Tests indicated that (within the limits of experimental accuracy) even if lithium hydride does dissolve in the lithium anode, its solubility does not noticeably alter the activity of the lithium anode. Under these conditions, there is no significant difference between the reference state and the standard state of pure liquid lithium at 1 atm.

The lithium hydride formation cell may be represented as

$$\mathrm{Li}(\ell)/\mathrm{LiX}(\ell) \text{ saturated with } \mathrm{LiH}(s)/\mathrm{H_2}(g)\ 1 \text{ atm, (Fe)} \tag{110}$$

where LiX represents a lithium halide. The half-cell reactions

$$\mathrm{Li}(\ell) \rightarrow \mathrm{Li}^+ + e^- \text{ and } \tfrac{1}{2}\mathrm{H_2}(g) + e^- \rightarrow \mathrm{H}^- \tag{111}$$

at the anode and cathode, respectively, sum to give the cell reaction

$$\mathrm{Li}(\ell) + \tfrac{1}{2}\mathrm{H_2}(g) \rightarrow \mathrm{LiH}(s). \tag{112}$$

For a cell with all three substances in their standard states (namely, pure liquid lithium, pure solid lithium hydride, and pure hydrogen gas at 1 atm), the Nernst equation,

$$\underset{\sim}{E} = \underset{\sim}{E}^\circ - \frac{\underset{\sim}{R}T}{N\underset{\sim}{F}} \ln\left(a_{\mathrm{LiH}}/a_{\mathrm{Li}}a_{\mathrm{H_2}}^{1/2}\right) \tag{113}$$

reduces to

$$\underset{\sim}{E} = \underset{\sim}{E}^\circ. \tag{113a}$$

Table XIV summarizes the data for cells of differing lithium halide-lithium hydride composition, and Fig. 63 is a composite curve of emf versus temperature for these cells. Since a comparison of the individual cell data with the composite set showed no apparent inconsistencies, the data were treated as a whole. The uncertainty in the data obtained with the chloride cells is somewhat greater than that obtained with the bromide

TABLE XIV. Emf-Temperature Data for Lithium Hydride Cells Using Indicated Electrolytes

59.8 m/o LiI-40.2 m/o LiH		59.8 m/o LiBr-40.2 m/o LiH		55.1 m/o LiCl-44.9 m/o LiH		40.0 m/o LiCl-60.0 m/o LiH	
Emf, V	Temp, °K	Emf, V	Temp, °K	Emf, V	Temp, °K	Emf, V	Temp, °K
0.3934	673.2	0.3440	733.7	0.3076	777.2	0.2845	803.2
0.3915	674.2	0.3412	738.7	0.3033	782.2	0.2822	810.2
0.3864	683.2	0.3368	744.2	0.2993	788.2	0.2764	813.2
0.3822	687.2	0.3324	749.7	0.2951	792.2	0.2747	819.7
0.3797	693.2	0.3275	754.2	0.2908	798.2	0.2690	823.2
0.3739	698.2	0.3253	758.2	0.2870	803.2	0.2690	828.2
0.3698	704.2	0.3247	762.2	0.2828	808.7	0.2605	838.2
0.3628	708.2	0.3197	764.2	0.2828	813.2	0.2629	843.2
0.3598	716.2	0.3183	767.7			0.2520	844.2
0.3522	722.2	0.3183	769.7			0.2517	847.7
0.3520	723.7	0.3178	773.2			0.2510	852.2
0.3440	734.2	0.3120	778.2				
0.3387	742.7						
0.3325	747.2						
0.3318	756.2						
0.3228	766.2						

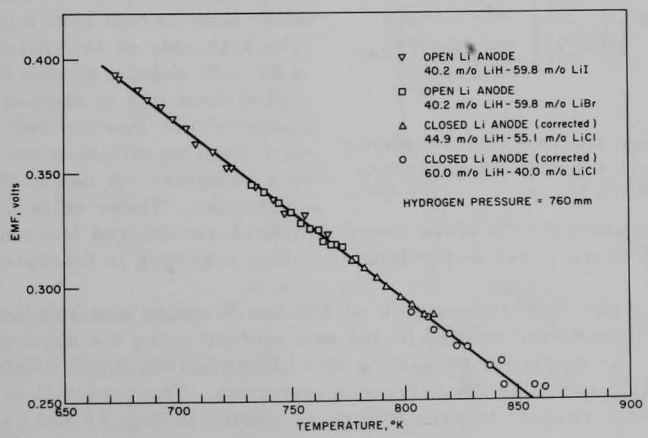

108-8905

Fig. 63. Emf of Lithium Hydride Saturated Cell as a Function of Temperature

and iodide cells. This is primarily due to the higher cell-operating temperatures for the chloride cells, for which the data required small corrections. The corrections varied from 3 mV at 795°K to 20 mV at 852°K. The emf data obtained for the cells with bromide and iodide electrolytes were combined and fitted to an equation that was linear with respect to temperature. The data for the chloride cells were fitted to a second linear equation. For the temperature range considered, a linear function seemed to fit all the data best. The intercept and slope of the final linear equation were obtained by using an average of the values in Eqs. 113 and 113a, weighted according to the number of experimental points in each set of data. The resultant equation

$$\underset{\sim}{E}^\circ = 0.9081 - 7.699 \times 10^{-4}\ T \tag{114}$$

was obtained for the temperature range 673 to 853°K with a standard deviation of ±2 mV.

2. Emf Studies of Lithium-containing Bimetallic Systems

Because of the negligible rate of self-discharge, the measurement of the emf of bimetallic cells with lithium anodes is much simpler than for the corresponding cells with sodium anodes.

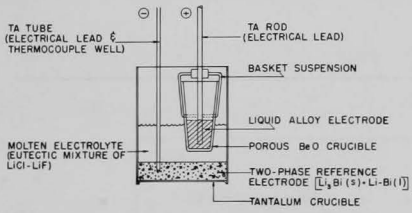

108-9007

Fig. 64. Schematic Diagram of a Lithium-containing Bimetallic Cell with a Reference Electrode of $Li_3Bi(s)$ in Bi

In studying the lithium-anode cells, we could use liquid electrolytes and porous barriers in a cell apparatus such as that shown in Fig. 64. (The high rate of self-discharge for cells with sodium anodes had precluded their use in studies on sodium-anode cells.) Porous BeO crucibles were used as diffusion barriers and as a container for one of the alloy electrodes. These cells were operated only above 775°K since lower temperatures caused freezing of the electrolyte in the pores of the BeO crucible, resulting in fracture.

The thermodynamics of lithium-bismuth and lithium-tin alloys[114,115] have been studied by the emf method using the apparatus just described. An electrode consisting of a bismuth-rich liquid alloy saturated with $Li_3Bi(s)$ served as the reference electrode. The potential of this electrode with respect to pure lithium is plotted in Fig. 65 and can be expressed as

$$\underset{\sim}{E} = 0.5303 + 7.3272 \times 10^{-4}\ T - 6.4317 \times 10^{-7}\ T^2, \tag{115}$$

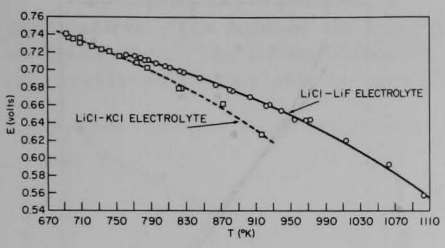

108-6806 Rev.

Fig. 65. Emf for the Cells Li(ℓ)/LiCl-LiF or LiCl-KCl/Bi(ℓ) Saturated with Li_3Bi, as a Function of Temperature

where T is in the range 760-1100°K. The use of this reference electrode resulted in two benefits. First, the reference electrode alloy is invariant in composition, with respect to the addition of lithium. (This addition may occur through the solubility of lithium in the electrolyte.) Second, the activity of lithium in the reference electrode is greatly reduced below that of the pure metal, which means a lower concentration of lithium is in the electrolyte. As a result, we were able to observe stable cell potentials using the reference electrode versus dilute alloys of lithium. The observed cell voltages could be converted to those for the cell containing a pure lithium anode by using Eq. 115. Figures 66 and 67 show the voltage-temperature-composition characteristics of lithium-bismuth and lithium-tin cells. These data represent the reversible open-circuit potentials for lithium-bismuth and lithium-tin cells, as a function of composition and temperatures. Figures 68 and 69 show the open-circuit potentials of lithium-bismuth and lithium-tin cells,

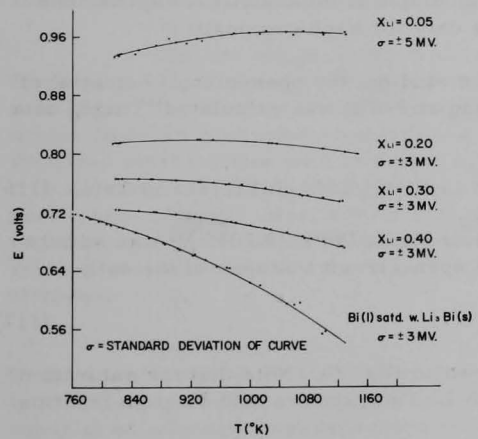

108-6280 Rev.

Fig. 66. Emf-Temperature-Composition Characteristics of the Cell Li(ℓ)/LiCl-LiF(ℓ)/Li in Bi(ℓ) (X_{Li} = atom fraction lithium)

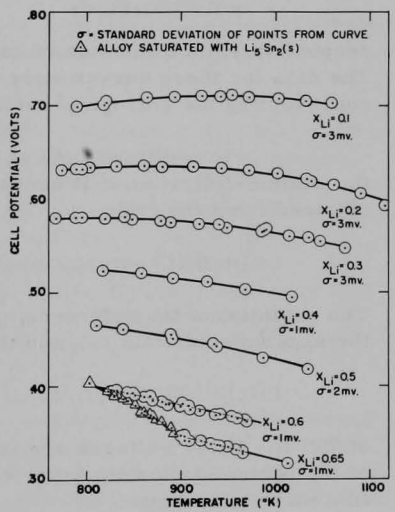

108-9249

Fig. 67. Emf-Temperature-Composition Characteristics of the Cell Li(ℓ)/LiCl-LiF(ℓ)/Li in Sn(ℓ) (X_{Li} = atom fraction lithium)

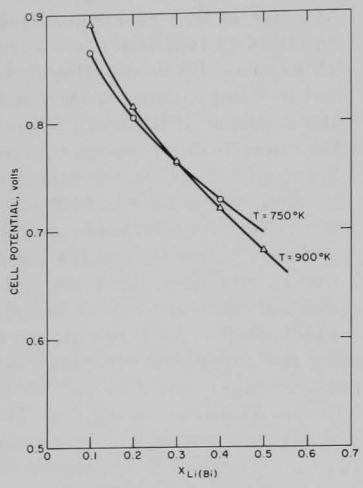

308-521

Fig. 68. Emf of a Lithium-Bismuth Cell as a Function of Cathode Composition at T = 750 and 900°K

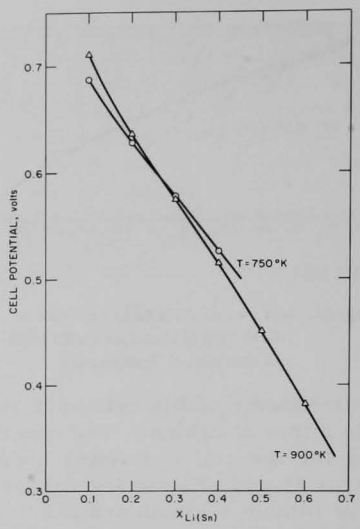

308-515

Fig. 69. Emf of a Lithium-Tin Cell as a Function of Cathode Composition at T = 750 and 900°K

respectively, as a function of cathode alloy composition at 750 and 900°K. The data for these curves were calculated from analytical expressions representing the emf-temperature data for each composition.

In addition to the above studies, the open-circuit potential of the lithium-tellurium cell operating at 798°K was calculated[116] using data obtained from the cell:

$$\text{Li (in Bi}(\ell)\text{ saturated with Li}_3\text{Bi(s))/LiCl-LiF}(\ell)\text{/Li in Te}(\ell). \quad (116)$$

The potential of the reference electrode at 798°K (0.7055 V) was added to the experimental data to yield the open-circuit voltages of the cell,

$$\text{Li}(\ell)\text{/LiCl-LiF}(\ell)\text{/Li in Te}(\ell) \quad (117)$$

at 798°K. These voltages are shown in Fig. 70. Note that the saturation of the lithium-tellurium alloy with $Li_2Te(s)$ occurs at 0.39 atom fraction lithium in tellurium.

The voltages of the lithium-bismuth, lithium-tin, and lithium-tellurium cells make them attractive candidates for cell development. However, the fact that the vapor pressures of bismuth and tellurium over their lithium alloys are high makes thermal regeneration of these cells

unattractive. The lithium-tin alloy probably can be thermally regenerated by distillation. The lithium-bismuth and lithium-tellurium systems will be considered further only for use in secondary cells.

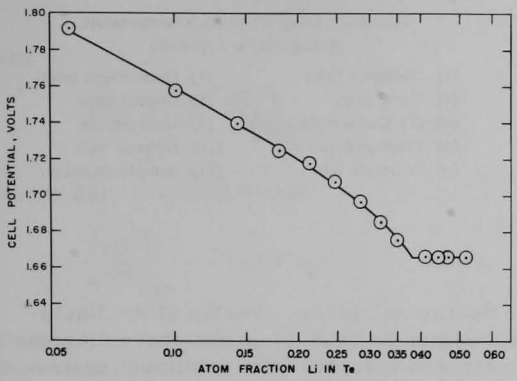

Fig. 70

Emf of the Cell Li(ℓ)/LiCl-LiF(ℓ)/ Li in Te(ℓ), as a Function of Cathode Composition at T = 798°K

108-9022 Rev 1

3. Liquid-Vapor Equilibrium Measurements on the Lithium-Tin System

Liquid-vapor equilibrium measurements on the lithium-tin system are just beginning. There are three separate experimental phases to this program: low-temperature transpiration studies, high-temperature transpiration studies, and total-vapor-pressure studies.

The low-temperature transpiration apparatus is a carryover from work on sodium-containing systems and is described in Appendix C (see Fig. C.3). It is serviceable up to about 1250°K, a limitation that arises from its Nichrome-wound furnace and from oxidation by air of the stainless steel furnace well at higher temperatures. Interior fittings in this apparatus are being reconstructed of tantalum to withstand the corrosive action of tin. Also, the carrier-gas purity has been improved by introducing a purification train consisting of a molecular sieve trap to remove residual moisture and a hot calcium bed to remove oxygen and nitrogen.

High-temperature (>1250°K) transpiration studies are needed to obtain information on the system for temperatures up to 1473°K. This is a likely regeneration temperature if the regenerator is to provide vapor at an adequate pressure for a reasonable rate of cell operation. The apparatus for the high-temperature experiments is of a new design and is not yet complete. It is basically a refinement of the low-temperature apparatus. The sample container, heat baffling, and quenching arrangement have been improved, and provision has been made to protect the main well from air oxidation at the higher temperatures. Figure 71 is a schematic diagram of the assembly.

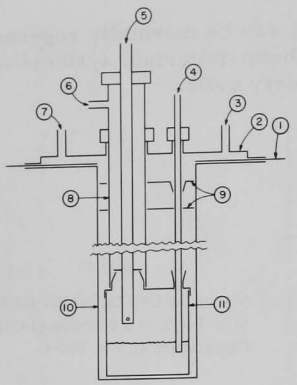

Fig. 71

Schematic Diagram of High-temperature Transpiration Apparatus

(1) Glovebox floor
(2) Cover plate
(3), (7) Carrier-gas inlets
(4) Thermocouple well
(5) Collector tube
(6) Quench-gas inlet
(8) Quench tube
(9) Heat shields
(10) Furnace well
(11) Sample container

308-524

As will be seen in Section 4.b below, overlap of the liquid-vapor loop with the liquid-solid region in the lithium-tin phase diagram is likely to occur. The information to determine the minimum system pressure necessary to avoid this problem is best obtained by means of total-vapor-pressure measurements as was done for the sodium-bismuth system. In contrast to the sodium-bismuth system, however, the expected pressures for the lithium-tin system will be much lower in the temperature and composition region where overlap is likely to occur (about 10^{-5} to 10^{-2} Torr). The pressures will be below the operating range of the quasi-static method. To handle this problem, a new technique will have to be developed.

4. Thermodynamic Analysis of Results for Lithium-containing Systems

a. Thermodynamic Analysis of LiH-containing Systems. In the search for suitable thermally regenerative cell systems, it is desirable to find one in which the free energy of change for the cell reaction at the cell temperature is large and negative but rapidly approaches zero with increasing temperature. If $\Delta\tilde{S}°$ is large and negative, the latter condition is met. As a guide in this search, we can examine the $\Delta\tilde{G}°/\Delta\tilde{H}°$ values for the cell reaction at 300°K;[120] for a cell system to be acceptable, the ratio should be less than 0.9. The lithium-hydrogen cell satisfies both these requirements; at 300°K, $\Delta\tilde{G}° = -16.2$ kcal/mole, $\Delta\tilde{H}° = -21.8$ kcal/mole, and $\Delta\tilde{G}°/\Delta\tilde{H}° = 0.74$. Further, this system could be easily regenerated since pure lithium hydride readily dissociates at 1173°K giving 1 atm of hydrogen pressure. At normal cell operating temperatures (620°K), the lithium hydride cell voltage may vary between 0.6 and 0.43 V, depending on the concentration of lithium hydride in the electrolyte.

With the data from Fig. 63, $\Delta\tilde{G}_f°$, $\Delta\tilde{H}_f°$, and $\Delta\tilde{S}_f°$ were calculated for lithium hydride at 800°K using the following equations:

$$\Delta \tilde{G}^{\circ}_{800} = -NF\underset{\sim}{E}^{\circ}_{800}, \tag{118}$$

$$\Delta \tilde{H}^{\circ}_{800} = NF\left[\left(\frac{\partial \underset{\sim}{E}^{\circ}}{\partial T}\right)_P T - \underset{\sim}{E}^{\circ}\right], \tag{119}$$

and

$$\Delta \tilde{S}^{\circ}_{800} = NF\left(\frac{\partial \underset{\sim}{E}^{\circ}}{\partial T}\right)_P, \tag{120}$$

where $\underset{\sim}{E}^{\circ}_{800} = 0.2922$ V and

$$\left(\frac{\partial \underset{\sim}{E}^{\circ}}{\partial T}\right)_P = -7.699 \times 10^{-4}\ T.$$

Further, by integration of the best available heat-capacity data[117,118] over the range 298-800°K, $\Delta \tilde{G}^{\circ}_f$, $\Delta \tilde{H}^{\circ}_f$, and $\Delta \tilde{S}^{\circ}_f$ were calculated at 298°K using the relationships

$$\Delta \tilde{H} = \Delta H_0 + \int \Delta \tilde{C}_p\, dT, \tag{121}$$

and

$$\left(\frac{\partial \Delta \tilde{G}/T}{\partial T}\right) = -\frac{\Delta \tilde{H}}{T^2}. \tag{122}$$

Table XV gives these results and includes values from the literature for comparison. The literature value of the standard entropy of formation of lithium hydride is based on the absolute entropy calculated from the heat-capacity data from 74 to 93°K and a single point at 293°K.[119]

TABLE XV. Calculated Values[a] and Literature Values for the Enthalpy, Free Energy, and Entropy of Lithium Hydride

	This Work, 800°K	This Work, 298°K	Literature, 298°K	References for Literature Values
$\Delta \tilde{H}^{\circ}_f$ (cal mole^{-1})	-20,940	-21,700 ± 290	-21,340	106
			-21,670	105
$\Delta \tilde{G}^{\circ}_f$ (cal mole^{-1})	-6,740	-16,160 ± 50	-16,450	106, 119
			-16,800	105, 119
$\Delta \tilde{S}^{\circ}_f$ (cal deg^{-1} mole^{-1})	-17.7	-18.9 ± 0.4	-16.3	119

[a] $\Delta \tilde{H}^{\circ}_f = NF\left[T\left(\frac{\partial \underset{\sim}{E}^{\circ}}{\partial T}\right)_P - \underset{\sim}{E}^{\circ}\right]$, $\Delta \tilde{G}^{\circ}_f = -NF\underset{\sim}{E}^{\circ}$, $\Delta \tilde{S}^{\circ}_f = NF\left(\frac{\partial \underset{\sim}{E}^{\circ}}{\partial T}\right)_P$,

where $\underset{\sim}{E}^{\circ}_{800°K} = 0.2922$ V, $\left(\frac{\partial \underset{\sim}{E}^{\circ}}{\partial T}\right)_P = -7.699 \times 10^{-4}$ T V/deg.

b. Thermodynamic Analysis of Lithium-containing Bimetallic Systems. As mentioned in the discussion of the studies of the sodium-bismuth system (Section IV.A.3), the cell potential-composition-temperature data may be thought of as representing the $\Delta\mu^E$ surface in $\Delta\mu^E$-T-X space. In the lithium-bismuth system, the equation for this surface was found to be

$$\Delta\mu^E_{Li} = \sum_{i=1}^{3}\sum_{j=1}^{2} C_{ij}T^{i-1}X_{Li}^{j-1} \quad , \tag{123}$$

where the values of the coefficients, C_{ij}, are given in Table XVI. For the lithium-tin system, the equation was

$$\Delta\mu^E_{Li} \sum_{i=1}^{3}\sum_{j=1}^{3} C_{ij}T^{i-1}X_{Li}^{j-1}, \tag{124}$$

with the coefficients, C_{ij}, as in Table XVII.

TABLE XVI. Coefficents, C_{ij}, Used in Calculating $\Delta\mu^E_{Li}$ in Lithium-Bismuth Alloys from

$$\Delta\mu^E_{Li} = \sum_{i=1}^{3}\sum_{j=1}^{2} C_{ij}T^{i-1}X_{Li}^{j-1}$$

	i = 1	i = 2	i = 3
j = 1	-9397	-18.16	+0.0109
j = 2	-7103	+19.44	-0.0068

TABLE XVII. Coefficients, C_{ij}, Used in Calculating $\Delta\mu^E_{Li}$ in Lithium-Tin Alloys from

$$\Delta\mu^E_{Li} = \sum_{i=1}^{3}\sum_{j=1}^{3} C_{ij}T^{i-1}X_{Li}^{j-1}$$

	j = 1	j = 2	j = 3
i = 1	2019	-38187	33403
i = 2	-35.50	84.92	-53.65
i = 3	0.0214	-0.0448	0.0304

These equations are valid only for the composition-temperature regions studied, namely, for lithium-bismuth: that portion of the phase diagram in which bismuth-rich, unsaturated alloys exist and for temperatures of 775-1100°K; for lithium-tin: that portion of the phase diagram in which tin-rich, unsaturated alloys exist and for temperatures of 800-1050°K.

For the lithium-tellurium system at 798°K, the $\Delta\mu^E_{Li}$ obeyed the equation

$$\Delta\mu^E_{Li} = -36568 - 5736X_{Li} + 11676X^2_{Li} \text{ (cal/mole)} \tag{125}$$

with a standard deviation of 29 cal/mole.

The $\Delta\mu^E_{Li}$ equations were used, along with the Gibbs-Duhem relationship, to calculate the standard free energies of formation of the solid compounds Li_3Bi, Li_5Sn_2, and Li_2Te. These are presented in Table XVIII for various temperatures.

TABLE XVIII. Comparison of Standard Free Energies of Formation for Solid Intermetallic Compounds of Lithium

Temp, °K	Standard Free Energy of Formation, kcal/mole		
	$Li_3Bi(s)$	Li_5Sn_2	Li_2Te
798	-	-	-77.9
800	-50.5	-61.4	
850	-49.7	-59.8	
900	-48.8	-57.9	
950	-47.8	-55.3	
1000	-46.6	-52.4	
1050	-45.3		
1100	-44.0		

The general problem of liquid-vapor loop overlap with solid-liquid regions of the phase diagram has been discussed above (Section IV.A.5). For the sodium-bismuth regenerative cell, overlap posed a recognizable threat, but the problem was avoided by maintaining a minimum system pressure of 240 Torr. For the lithium-bismuth system, no liquid-vapor equilibria were studied, but the overlap problem would be a threat here also. The compound Li_3Bi has a high melting point (1418°K). Therefore for a reasonable regeneration temperature (about 1475-1500°K), and considering that the vapor pressure of pure bismuth at this temperature is about 22 Torr, the condensation temperature (temperature at which the pure lithium vapor pressure is also about 22 Torr) would be about 1225°K. It is difficult to conceive of a liquid-vapor loop of the simple ascendent type, with its ends fixed at 1225 and 1500°K, which will pass a liquid-solid hump that thrusts up to 1418°K, close to the low-temperature end of the loop. A particular kind of loop that could bypass the hump is that describing a maximum-boiling-point azeotrope. Such an azeotrope can be expected in a system having strong negative deviations from ideality, which the lithium-bismuth system has. If an azeotrope occurs in the system, then regeneration of a lithium-bismuth cell would produce liquid of the azeotropic composition and either the anode or the cathode would eventually reach this composition. The outcome is not likely to be acceptable. Thus the lithium-bismuth cell seems likely to be caught between the conflicting requirements imposed by the overlap problem and azeotropy. Details of the analysis of overlap and of the effect of pressure in handling azeotropy problems have been published.[27]

The phase diagram for the lithium-tin system shows a region of liquid-solid coexistence which includes the compound Li_7Sn_2 with a melting point of 1056°K. If a reasonable regeneration temperature is chosen (about 1475-1500°K), and the vapor pressure of the cathode composition at this temperature is assumed to be about 10^{-2} Torr, then the pure-lithium end of the vapor-liquid loop would be at about 800-825°K. Under these conditions, overlap might occur. To avoid overlap, a condensation temperature of 1000°K may be necessary, at which temperature pure lithium has a vapor pressure of 0.78 Torr. It is not known yet if there is a practical combination of cathode composition and regeneration temperature to give such a pressure. If the liquid-vapor loop shows that the vapor is extremely dilute in respect to tin over the cathode composition at the regeneration temperature, we should be able to condense the vapors directly and avoid the overlap problem. These questions will be answered by the liquid-vapor equilibrium studies, the plans for which were outlined in Section A.3 above.

B. Physicochemical Properties of Lithium-containing Systems

The search for suitable electrolytes for use with regenerative galvanic cells has been augmented by fundamental studies on the transport properties of molten salts. Such data as conductivity and density and solubilities of intermetallic compounds are needed in designing a practical cell, since in many cases deviations of these properties from computed values based on ideal behavior are considerable.

1. Conductivity of Lithium Hydride-Lithium Halide Mixtures

The search for an electrolyte suitable for use in a lithium hydride emf cell led to investigation of the temperature-composition characteristics of the lithium hydride-lithium halide (Cl^-, Br^-, I^-) binary fused-salt systems (see Section V.C). A thermodynamic analysis of the solid-liquid equilibrium temperature data indicated that all systems showed positive deviations from ideality. These positive deviations were interpreted to indicate the possible existence of an ionic aggregate such as $LiCl_2^-$ in the system. If such associated species do exist in solution, normal ionic character of the solution would change significantly. Studies of the electrolytic conductivity of these systems should aid considerably in explaining the nature of these fused-salt systems.

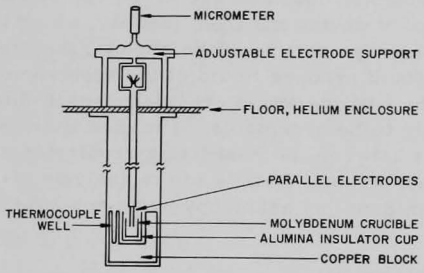

308-616

Fig. 72. All-metal Parallel-electrode Assembly for Measuring the Electrolytic Conductivity of Molten Salts

We have assembled an all-metal conductivity cell (shown in Fig. 72), which employs two rigidly-mounted parallel molybdenum electrodes immersed in the melt held in a molybdenum crucible. The lack of suitable insulators stable to lithium hydride required the exclusive use of metals. The depth of immersion of the parallel electrodes is accurately set by means of a micrometer screw directly attached to the electrodes. The resistance of a homogeneous solution measured with a low-impedance ac bridge is a linear function of the depth of immersion of the electrodes. The change in ac conductance, $1/R$, per unit depth of immersion of the electrodes, S, is a constant over a range of frequencies and electrode depths:

$$\frac{\frac{1}{R_2} - \frac{1}{R_1}}{d_2 - d_1} = S \text{ mho/cm}, \qquad (126)$$

where R_1 and R_2 are resistances at depths d_1 and d_2. R_1 and R_2 are obtained after subtracting, from the total measured resistance, the resistance of the electrodes above the melt plus one-half the resistance of the electrodes immersed in the melt.

Since fused salts have low resistivities, a sensitive bridge is needed for accurate electrolyte resistance measurements. Such a transformer bridge has been built by J. P. Bobis of the Electronics Division, ANL. Figure 73 is a schematic diagram of this bridge, designed to measure resistances of 0.01 to 10 ohms with an accuracy of 3%.

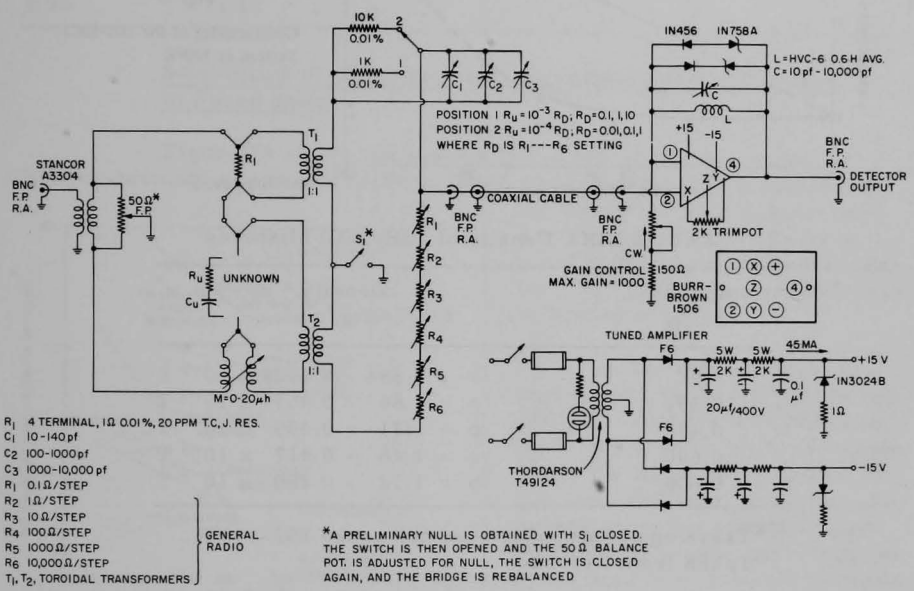

Fig. 73. Circuit Diagram for the Low-impedance AC Bridge

Conductivity has been measured on four compositions of the lithium hydride-lithium chloride binary mixture. These data are given in Fig. 74, where the conductivity of the mixture is plotted as a function of composition. When contrasted with the calculated ideal conductivity (additive), the data indicate that large positive deviations are present in this mixture. Further experiments are planned for the LiH-LiCl system and the other lithium hydride-lithium halide systems.

2. Densities of Lithium Hydride-Lithium Halide Mixtures

Liquid densities have been determined on lithium hydride-lithium chloride binary mixtures by measuring the volume of a known

weight of the mixture in a calibrated crucible. After each successive addition of lithium hydride to the crucible, the depth of the liquid was measured at various temperatures. Liquid density as a function of temperature was measured for four compositions. These data are presented in Table XIX.

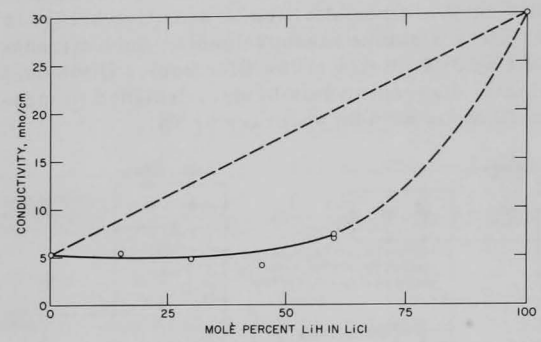

Fig. 74

Conductivity of the LiH-LiCl System at 700°K

308-509 Rev. 2

TABLE XIX. Density of LiH-LiCl Mixtures

Composition, X_{LiH}	Density,[a] ρ, g/cm^3
0.0[b]	$\rho = 1.884 - 0.4328 \times 10^{-3}\ T$
0.201	$\rho = 1.80 - 0.457 \times 10^{-3}\ T$
0.400	$\rho = 1.71 - 0.499 \times 10^{-3}\ T$
0.600	$\rho = 1.46 - 0.417 \times 10^{-3}\ T$
0.800	$\rho = 1.12 - 0.280 \times 10^{-3}\ T$

[a]These equations apply over the range 893-993°K.
[b]Taken from Ref. 121.

The ideal molar volume, $\tilde{V}$, has been calculated at each composition for this binary mixture using the relation

$$\tilde{V}_{ideal} = X_1\tilde{V}_1 + X_2\tilde{V}_2, \tag{127}$$

where $\tilde{V}_i$ is calculated from M_i/ρ_i. The change in volume $\Delta\tilde{V}$ is obtained from

$$\Delta\tilde{V} = \tilde{V} - \tilde{V}_{ideal} = \tilde{V} - \Sigma X_i\tilde{V}_i. \tag{128}$$

These data (given in Table XX) indicate positive deviations from ideality in this mixture.

TABLE XX. Molar Volumes of LiH-LiCl Mixtures at 973°K

X_{LiH}	Molar Volume, cm^3/mole (calc)	Molar Volume, cm^3/mole (expt'l)	$\Delta\tilde{V}$, cm^3/mole	$\frac{\Delta\tilde{V}}{\Sigma\tilde{V}_i}$
0.0	28.98	-	-	-
0.201	25.83	26.0_5	0.22	0.0085
0.400	22.68	23.4_6	0.78	0.0343
0.600	19.54	20.5_1	0.97	0.0496
0.800	16.39	17.5_8	1.19	0.0727
1.00	13.24	-	-	-

3. Solubilities of Lithium-containing Intermetallic Compounds in Fused Salts

Figure 75 shows the results of solubility determinations of lithium-bismuth alloys and Li_2Te in fused alkali halides, along with those for several other intermetallic compounds. These data were taken in the same manner as discussed for sodium-intermetallics in Section IV.B.3.

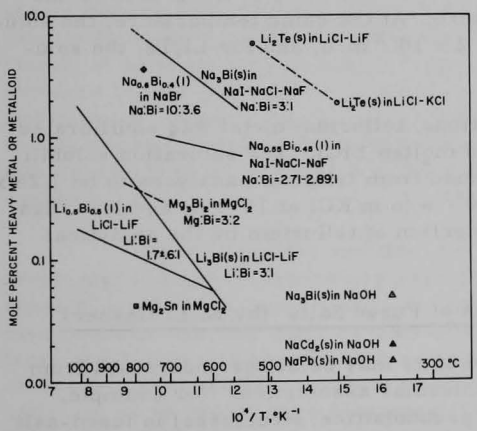

108-9005 Rev. 3

Fig. 75. Solubilities of Some Intermetallic Compounds in Fused Salts, as a Function of Temperature

In the lithium-bismuth studies, the Li:Bi ratio in molten LiF-LiCl eutectic was shown to be 3.0 when solid Li_3Bi was present in the liquid-metal phase.[122] The heat of fusion for Li_3Bi calculated from the solubility data is 18.8 kcal/mole. The solubility of bismuth from a 50 a/o lithium-bismuth alloy was equal to that from Li_3Bi(s) at low temperatures, where the 50 a/o alloy becomes saturated with solid Li_3Bi (883°K). At higher temperatures, the Li:Bi ratio for the 50 a/o alloy decreases sharply, as shown in Fig. 75; experimental difficulties in the determination of the lithium content of the solution precluded fixing a more precise value for the ratio.

The solubility of Mg_3Bi_2 in $MgCl_2$ is shown for a limited temperature range.[123] The Mg:Bi solubility ratio in the salt phase is 3:2.

Figure 75 indicates other isolated points for Mg_2Sn (Ref. 123) and Li_2Te and shows (for comparison) the solubilities of various intermetallic compounds in molten NaOH reported by Delimarskii et al.[70]

These solubilities of Na_3Bi and NaPb in molten NaOH are low compared with values calculated using a value for the heat of fusion of 16.6 kcal/mole for Na_3Bi.

The solubility trend observed suggests that, as the transition metal series on the periodic chart is approached, the trend is to lower solubilities of intermetallic compounds in fused salts. Indeed, this might be predicted on the basis that, as the transition metal series is approached, the bond formed is less ionic in character. The latter is indicated by the lower melting points of the most stable intermetallic compounds (compared with the melting points of the elements).

To test this hypothesis, we determined the solubility of LiHg (m.p. 868°K) in molten LiCl-LiF at 791°K. The compound LiHg was prepared from the elements and activated by neutron bombardment for use in this study. By gamma-counting the radioactive ^{203}Hg in a sample of 69.5 m/o LiF-LiCl (eutectic), which had been equilibrated at temperature with the activated LiHg, we estimated the solubility of LiHg in LiCl-LiF eutectic at 791°K to be 8.6×10^{-5} m/o. At the same temperature, the solubility of $Li_3Bi(s)$ is approximately 2×10^{-2} m/o, and for Li_2Te, the solubility is nearly 3 m/o.

In additional investigations, tellurium metal was equilibrated with molten CsCl, molten KCl, and molten LiCl. The saturation solubilities in these alkali halides were found from tellurium analyses to be 1.28×10^{-2} w/o in CsCl at 944°K; 3.5×10^{-2} w/o in KCl at 1075°K; and less than 5×10^{-4} w/o (the lower limit of detection of tellurium by the analytical method used) in LiCl at 900°K.

4. Raman Spectral Studies of Fused Salts (by E. L. Gasner)

The behavior of molten salts may be better understood from the identification of species and molecular associations (for example, complex ions, neutral molecules, pseudolattice structures) in fused-salt systems. The occurrence of molecular association usually results in apparently nonideal behavior of properties such as solubilities, freezing points, and vapor pressures. Nonideal behavior of these properties precludes the use of ideal-solution rules for predicting the behavior of systems of varying compositions. Much expensive and time-consuming experimental work is then required in order to have confidence that the physical behavior of a system is understood. Spectral studies of fused salts aid in the understanding of the nonideal behavior of fused-salt systems.

The discovery of vibrational Raman spectra in ionized alkali halide and alkali hydride systems can provide unambiguous proof of the existence of complex species. A study of the intensity of the Raman spectra can give exact quantitative information as to the nature, concentration, and

temperature dependence of such species. This type of information can be of great value in predicting and explaining the behavior of systems of interest. Apparently nonideal behavior may be nearly ideal when interpreted in terms of the complex species present as, for instance, in the quasi-ideal treatment discussed in Section IV.A.2.

The results of cryoscopic and electrical conductivity investigations of molten LiH-LiCl solutions indicate large deviations from ideal-solution behavior (see Sections V.B.1 and V.C). The behavior of this system is consistent with the behavior expected if most of the chlorine were present in complex ions such as $LiCl_2^-$. However, alternative explanations of the observed nonideal behavior are also possible. The discovery of the appropriate Raman spectrum could resolve this uncertainty.

Investigation of solutions of intermetallic compounds in molten salt solvents is also important since knowledge of the solubilities of electrode materials in the electrolyte is necessary for the proper design and construction of bimetallic cells. Solubility studies (see Section V.B.3) have shown that the total bismuth concentration in LiF-LiCl eutectic at equilibrium with Li_3Bi is more than an order of magnitude higher than the concentration of pure bismuth in LiF-LiCl eutectic. This is almost conclusive evidence for the existence of a complex ion or molecule involving lithium and bismuth. Raman spectral investigations might establish the formula of this species and provide enough information concerning its chemical reactivity to allow the prediction of its importance in hitherto unstudied systems.

Raman spectra and infrared spectra are complementary to each other, and in an ideal laboratory provision would be made for obtaining both types of spectra. Economic considerations often require that a choice be made between the two types of instrumentation. Although each has advantages and disadvantages, the Raman equipment appears to be the better choice for many molten-salt investigations. Species of interest, such as $LiCl_2^-$ or Li_3Bi, would have fundamental vibrations in the range of 100-700 cm^{-1}. This is a normal working area for Raman investigations.

Unfortunately, commercially obtainable Raman spectrophotometers are not readily adaptable for use with corrosive molten-salt samples at high temperatures. For this reason, we have designed and constructed a versatile Raman spectrophotometer, making use of commercially available components for most parts of the apparatus. Figure 76 is a schematic diagram of the more important parts of the apparatus. Appendix D describes its operation in detail.

Before its use in the study of fused-salt solutions, the spectrophotometer as a whole was tested by obtaining the spectrum of liquid carbon tetrachloride. Figure 77 shows the high signal-to-noise ratio and the resolution of the isotopic fine structure obtained for the anti-Stokes 459-cm^{-1} band of liquid carbon tetrachloride. A Model 211-0537 Perkin-Elmer

multireflection sample cell was used in this experiment. The intensity obtainable with this cell is 25 times as great as that obtained with a single pass of the laser beam through the sample. In work performed in collaboration with Dr. Howard Claassen and Dr. Boris F. Frlec of the ANL Chemistry Division, spectra of liquid and gaseous XeF_6 and NpF_6 were obtained using only a single pass of the laser beam. Details of the results obtained with the hexafluorides are reported elsewhere.[124]

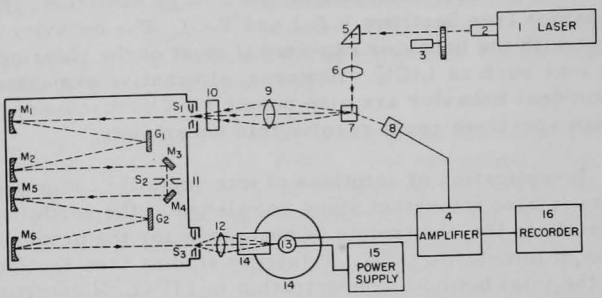

308-637

Fig. 76. Schematic Diagram of Laser-excited Raman Spectrophotometer

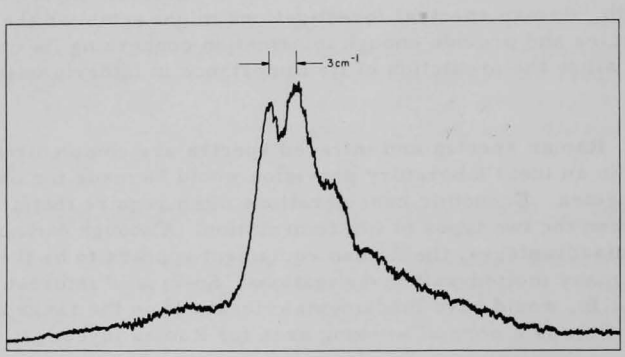

308-620

Fig. 77. The Anti-Stokes 459-cm^{-1} Raman Band of Carbon Tetrachloride at 295°K. Slit width ≈ 1.25 cm^{-1}; time constant = RC = 5 sec.

The system chosen for the first fused-salt investigation was LiH-LiCl. The physical and chemical nature of the LiH-LiCl system presented several experimental difficulties: (1) Molten LiH-LiCl mixtures react with all known window materials; (2) a hydrogen atmosphere is required to reduce the dissociation of the LiH; (3) the sample must be maintained at 750-1050°K; and (4) ionic bonding of any polyatomic species present would probably result in low specific Raman intensities. The apparatus as a whole, while capable of handling molten LiH-LiCl, should

have a sensitivity comparable to, or higher than, the sensitivity attainable with conventional samples. Most of the experimental difficulties described above appear to have been overcome.

A sample cell (the 45° mirror cell), capable of handling molten LiH-LiCl, has been designed, constructed, and tested. Figure 78 illustrates the design and operation of this cell. A metal sample cell is used to contain the melt. A slot, 2.5 cm long by 3 mm wide, in the lid of the sample cell permits the entrance of the laser light and the exit of the Raman light. A stainless steel 45° mirror (4 in Fig. 78), immersed in the melt, causes the laser beam to pass horizontally down the length of the melt. A large 45° mirror outside the furnace allows the Raman light originating from the horizontal "rod" of illuminated sample to be focused on the vertical entrance slit of the spectrometer.

The sample cell (1) is surrounded by a nickel block (6). A small wedge-shaped hole in the nickel block provides for the necessary passage of light (8). The nickel block is enclosed in a quartz tube (7) to provide a controlled atmosphere around the sample. Passage of a stream of purified hydrogen, in the direction indicated by the arrows, prevents corrosive vapors of the sample from reaching the quartz jacket. A metal shutter (9) may be placed over the sample by means of a control rod (10) to prevent spattering of sample onto the quartz envelope during the melting of the sample. An extension on the shutter provides space for an optional secondary window. The entire sample region is surrounded by a tube furnace, which can be operated at temperatures up to 1300°K.

The effectiveness of the 45° mirror cell has been tested at 523°K with a molten $NaNO_3$-KNO_3 eutectic mixture. Figure 79 is an example of the spectrum attainable with the molten nitrate sample. This spectrum was obtained using a high scanning speed (125 cm^{-1}/min) and a short time constant (t.c. = RC = 1 sec). In spite of the use of such a short time constant, the line at $\sim$1650 cm^{-1} is clearly visible above the background noise. Molten nitrates were investigated previously by Janz and James[125] using the conventional mercury-arc excitation with the mercury arcs surrounding a transparent quartz sample cell. This favorable sample geometry would be expected to give an intense Raman signal. Janz and James, however, although able to detect the 1650-cm^{-1} line photographically, were unable to observe this line when using photoelectric detection. We may therefore conclude that the special Raman apparatus developed in this laboratory will allow molten LiH-LiCl to be investigated with at least the same sensitivity as can be achieved elsewhere with conventional samples.

Raman spectral investigations of molten LiH-LiCl mixtures are under way. Samples have been maintained at 773°K for many hours with no appreciable discoloration of the quartz sample envelope or of the 45° mirror immersed in the melt. At higher temperatures, however, maintaining a clear melt and clear windows is considerably more difficult. This problem is currently being studied.

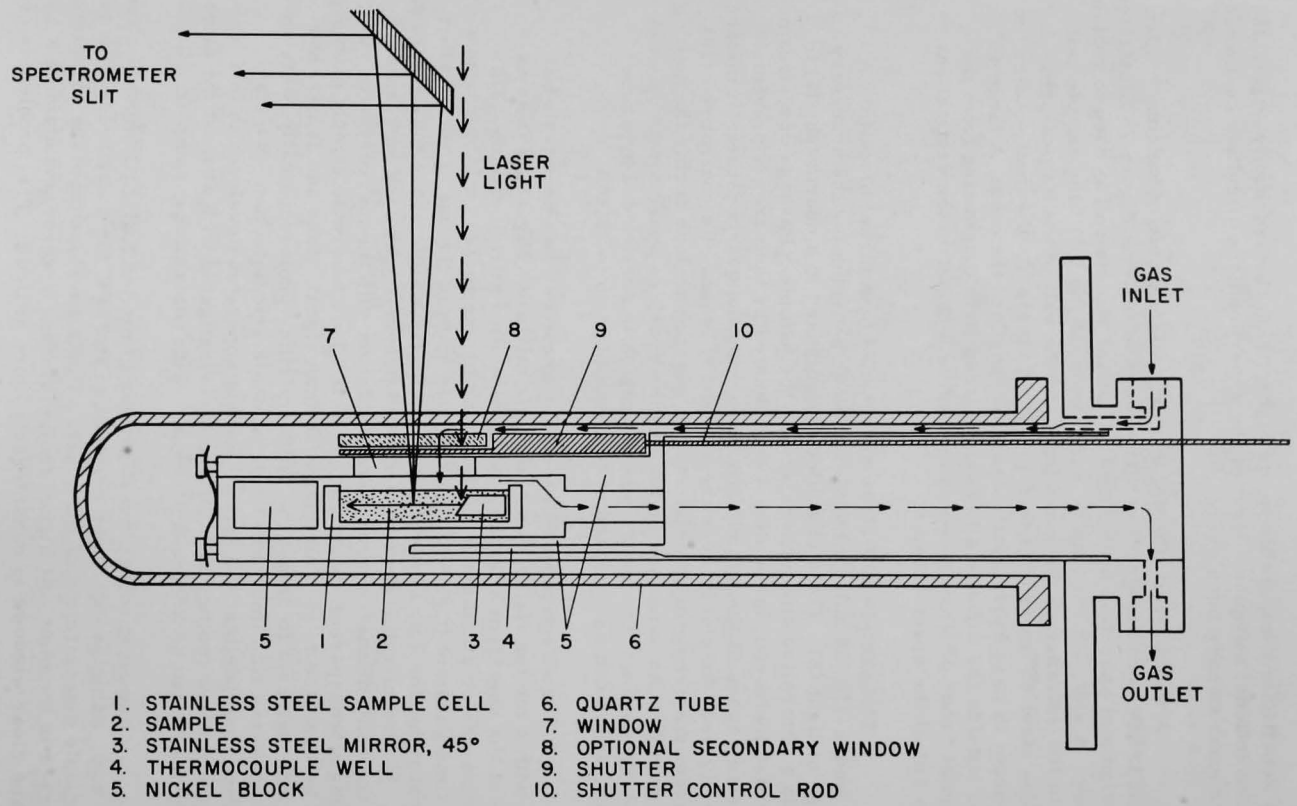

308-421 Rev. 1

Fig. 78. Fused-salt Sample Cell and Its Peripheral Apparatus

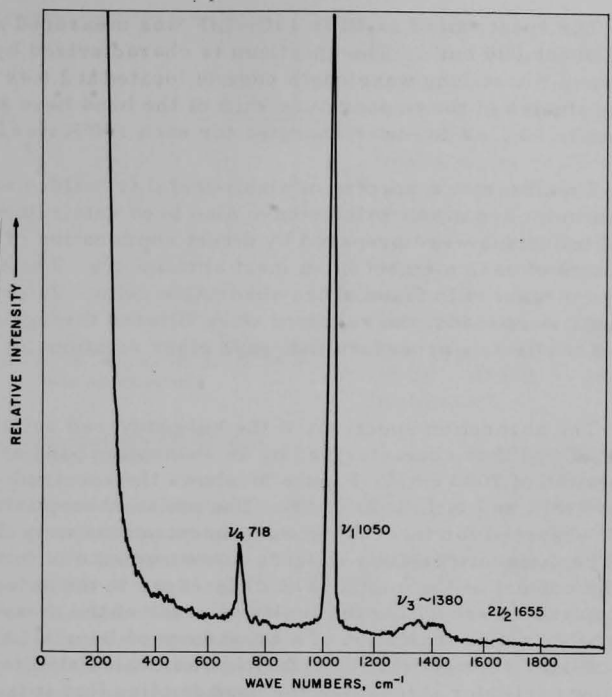

308-417

Fig. 79. Raman Spectrum of the $NaNO_3$-KNO_3 Eutectic Mixture at 523°K

5. Visible Absorption Spectra

The solubilities of intermetallic species in the electrolyte of a bimetallic cell may have several implications for cell operation. First, the intermetallic species may cause (additional) electronic conduction, which would reduce the current efficiency of the cell. Secondly, the intermetallic species may be extracted from solution by the anode, causing a buildup of cathode metal in the anode. To better understand the nature of the dissolved species, we have studied optical absorption spectra of these species.

The absorption spectrum of the deep-red solution of Li_3Bi in molten LiCl-LiF eutectic was determined as follows:[122] The mixture was contained in the rectangular well of a 1.27 x 3.81-cm sapphire absorption cell. The sapphire cell was placed in a quartz outer envelope having a rectangular bottom and a round upper portion provided with a vacuum stopcock. The cell was loaded in a high-purity helium atmosphere. The quartz and sapphire assembly was evacuated and placed in the heated sample chamber of a Cary 14H spectrophotometer.

The spectrum of Li_3Bi in LiCl-LiF was measured at 798°K in the range 5000-30,000 cm^{-1}. The spectrum is characterized by an intense absorption band whose long wavelength edge is located at 2.0 eV (16,300 cm^{-1}). Preliminary studies of the temperature shift of the band have shown that the band edge shifts ~0.1 eV to lower energies for each 100°K rise in temperature.

The absorption spectra of alkali-metal tellurides and of elemental tellurium in molten alkali halides have also been determined.[126] The alkali metal tellurides were prepared by direct combination of stoichiometric amounts of each element in an inert atmosphere. The absorption spectra were measured in fused silica absorption cells. Before spectral measurements were made, the solutions were filtered through fine-porosity fritted discs of silica, a procedure that gave clear solutions in the absorption cells.

The absorption spectrum of the burgundy-red solution of Li_2Te in LiCl-LiF at 798°K is characterized by an absorption band at 21,250 cm^{-1} with a half-width of 7000 cm^{-1}. Figure 80 shows the spectrum of Li_2Te in LiCl-LiF at 798°K and in LiCl at 923°K. The molar absorptivities at 21,250 cm^{-1} observed for three different concentrations were 25.1, 24.0, and 33.4. The major uncertainty in these measurements is in the analysis for the Li_2Te content of the melts. The differences in the values of the molar absorptivities are within the limits of error of the measurements and are probably not an indication of a breakdown of Beer's Law. The average oscillator strength for the transition was calculated to be 0.86 x 10^{-3}. The low oscillator strength of the band implies that it is due to a forbidden transition.

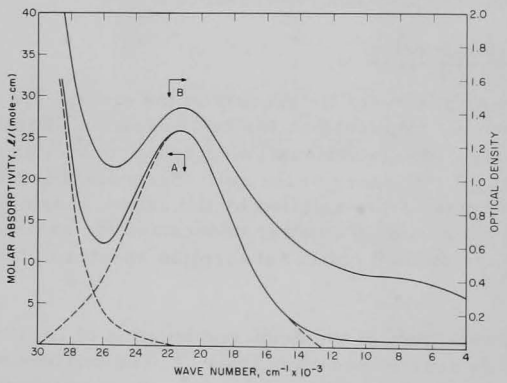

Fig. 80

Absorption Spectrum of Li_2Te in LiCl-LiF (Curve A) and Li_2Te in LiCl (Curve B) at 923°K

120-9941 Rev. 2

Solutions of Cs_2Te in molten CsCl are also red. The absorption spectrum of such a solution at 948°K is characterized by an absorption band with a maximum at 18,200 cm^{-1}, a half-width of 7400 cm^{-1}, and a molar absorptivity of 58.1 at the maximum; the spectrum is shown in Fig. 81. The oscillator strength of the transition was 2.0 x 10^{-2}. The low oscillator

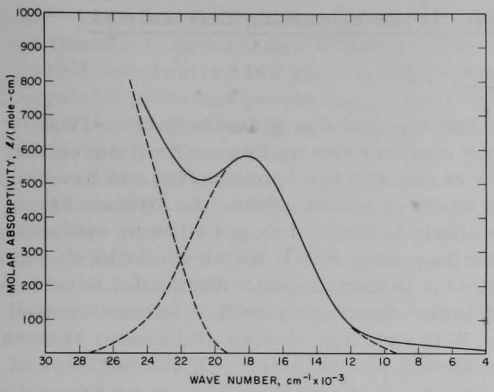

120-9940 Rev. 2

Fig. 81. Absorption Spectrum of Cs_2Te in CsCl at 948°K

strength of the Cs_2Te absorption band indicates that it too originates from a forbidden transition, even though it is about 23 times as intense as the analogous transition in the Li_2Te solutions. The absorption bands of those alkali metal tellurides have been interpreted as arising from 5p-6p atom-like transitions centered on tellurium. The formal charge on the tellurium is approximately -1, corresponding to the species $M\ Te^-$, where M is either lithium or cesium.

The possibility that the alkali metal tellurides do not exchange with solvent cations cannot be ruled out a priori. To test this admittedly remote possibility, we measured spectra of solutions of Li_2Te in CsCl and Cs_2Te in LiCl-LiF eutectic. The spectra were identical with those obtained for solutions of Cs_2Te in CsCl and for Li_2Te in LiCl-LiF, respectively. It was thus demonstrated that the overwhelming concentration of solvent cations causes replacement of the initial alkali metal constituent and ensures that the alkali metal nearest-neighbors surrounding the tellurium are derived from the cations of the solvents.

The spectrum of tellurium dissolved in molten CsCl at 948°K was also observed during this work. The spectrum is characterized by a broad complex absorption band stretching from 27,000 to about 10,000 cm^{-1} and having an oscillator strength of 3.9×10^{-2}. A resolution of this complex band into two overlapping bands with maxima at 15,500 and 20,800 cm^{-1} is a possibility.[126] This spectrum is shown in Fig. 82.

These data suggest several experiments. The nature of dissolved anode metal and intermetallic species might be better defined by studying electrical conductivity, density, optical absorption spectra, Raman spectra, and/or electromigration of colored species. Some of these experiments are now being planned.

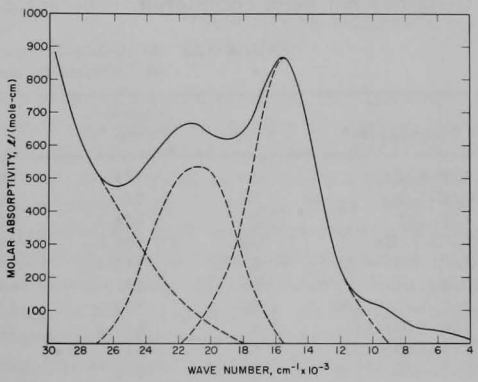

120-9939 Rev. 1

Fig. 82. Absorption Spectrum of Tellurium in CsCl at 948°K

C. Phase Relationships for Lithium Halide-containing Electrolytes

1. Lithium Halide Systems

The selection criteria for electrolytes given in Section IV.C included the desirability of using as electrolytes molten-salt mixtures that are thermodynamically stable with respect to the anode metal and have high electrolytic conductivities and low melting points. Since the lithium halide group is the lowest melting of the alkali halides, it is possible to synthesize an electrolyte of lithium halides melting near 600°K which would be thermodynamically stable in the presence of a lithium anode. Additional advantages in terms of high cell voltages and lower densities result if lithium is used as the anode metal in galvanic cells. With optimum design and proper thermal insulation, it may be possible to maintain the required cell temperature of about 600°K by the resistive heat generated within the cell during its operation.

In addition to the halides, lithium carbonate and lithium hydroxide were considered as possible components for these fused lithium-salt mixtures. The following reactions indicate problem areas that could bring about gross changes in the electrolyte characteristics, thereby casting doubt on the usefulness of the hydroxide or carbonate salts:

$$LiOH + 2Li \rightarrow Li_2O + LiH \qquad \Delta\tilde{G}^{\circ}_{750} = -40 \text{ kcal/mole;} \tag{129}$$

$$LiOH + Li \rightarrow Li_2O + H_2 \qquad \Delta\tilde{G}^{\circ}_{750} = -25 \text{ kcal/mole;} \tag{130}$$

$$Li_2CO_3 + 2Li \rightarrow 2Li_2O + CO \qquad \Delta\tilde{G}^{\circ}_{750} = -35 \text{ kcal/mole.} \tag{131}$$

Consideration of electrolytes was, therefore, limited to only the lithium halide systems; the possible binary and ternary mixtures and their characteristics are listed in Table XXI. Research on all combinations has not been completed. The solid-liquid equilibrium data for the

TABLE XXI. Solid-Liquid Equilibrium Characteristics of Lithium Halide Mixtures

Components[a]	Type[b]	Minimum Temp, °K	Composition	Reference
LiF-LiCl	E	774	30.5 m/o LiF	128
LiF-LiBr	E	726	31.0 m/o LiF	127
LiF-LiI	E	684.1	16.5 m/o LiF	
LiCl-LiBr	SS	795.2	~40 m/o LiCl	127
LiCl-LiI	E	641.4	34.2 m/o LiCl	
LiBr-LiI	SS	~691	~60 m/o LiI	
LiF-LiCl-LiBr	SS	703	22 m/o-31 m/o-47 m/o	129
LiF-LiCl-LiI	E	614.2	11.7 m/o-29.1 m/o-59.2 m/o	
LiF-LiBr-LiI	SS	~640	-	
LiCl-LiBr-LiI	SS	~630	-	

[a]Melting points of the pure lithium halides are as follows: LiF, 1121°K; LiCl, 880.0°K; LiBr, 824.3°K; and LiI, 742.2°K.
[b]E stands for eutectic, and SS stands for solid solution.

LiF-LiBr and LiCl-LiBr systems are the work of Botschwar.[127] The data of Haendler, Sennet, and Wheeler[128] for the LiF-LiCl system were checked in this laboratory, and good agreement was obtained. Figure 83 is a plot of crystallization temperatures for these three binary systems. Ternary systems are of greatest interest as potential electrolytes primarily because of their low melting points. Of the four ternary mixtures listed, only the LiF-LiCl-LiBr system has been investigated to any extent. Bergman and Arabadzhan[129] found that the equilibrium diagram of the LiF-LiCl-LiBr liquidus surface has two crystalline fields: the larger field is composed of pure lithium fluoride, and the smaller is made up of a continuous series of solid solutions of lithium bromide and lithium chloride. Crystallization temperatures for this system are shown in Fig. 84.

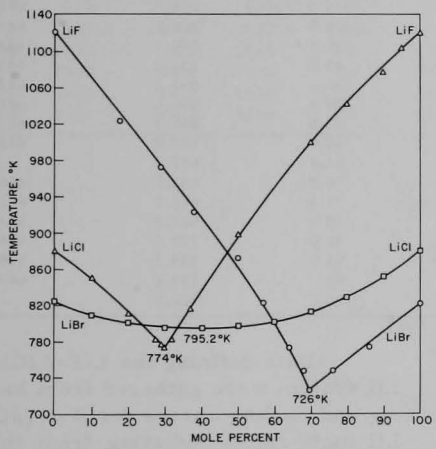

308-611 Rev. 1

Fig. 83. Crystallization Temperatures for the Binary Systems LiF-LiBr,[127] LiCl-LiBr,[127] and LiF-LiCl[128]

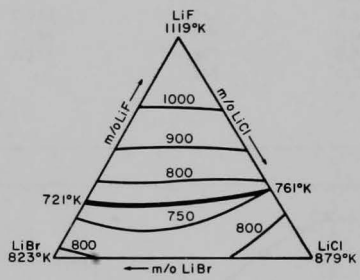

308-633

Fig. 84. Crystallization Temperatures for the Ternary System LiF-LiCl-LiBr[129]

Data describing the solid-liquid equilibrium for the LiF-LiI, LiCl-LiI, and LiF-LiCl-LiI systems were obtained in this laboratory using the same procedures and apparatus as those described previously[110] (see Section IV.C). The LiCl, LiBr, and LiI salts were purified by a modification of the technique described by Laitinen et al.,[107] in which the anhydrous hydrogen halide (gas) was used to remove the last traces of moisture from the molten salt. Preceding the treatment with the gaseous anhydrous halogen acid, the bulk of the water of hydration was removed from finely ground crystals by slow programmed heating of the sample under vacuum. Visual observation of the evolution and condensation of the water served as a guide in the drying process. After drying, the molten, purified salts were filtered through an extra-fine quartz frit. The lithium chloride melting point was 880.0°K, the lithium bromide melting point was 824.3°K, and the lithium iodide melting point 742.2°K. Lithium fluoride was dried in a vacuum for 24 hr at 380°K before use. Its melting point was 1121°K.

The experimental compositions investigated for the LiF-LiI and the LiCl-LiI binary mixtures and the solid-liquid equilibrium temperature data are given in Table XXII and Fig. 85. Both systems are of the eutectic type. The LiF-LiI eutectic composition contains 83.5 m/o LiI melting at 684.1°K, and the LiCl-LiI eutectic composition contains 65.8 m/o LiI melting at 641.4°K.

TABLE XXII. Crystallization Temperatures for the Systems LiF-LiI and LiCl-LiI

LiF-LiI			LiCl-LiI		
m/o LiI	Liquidus Temp, °K	Eutectic Temp, °K	m/o LiI	Liquidus Temp, °K	Eutectic Temp, °K
0.0	1121	-	0.0	880.0	-
10.0	1096.0	684.5	5.0	865.6	640.8
20.0	1071.9	683.4	15.0	833.9	641.1
27.5	1053.1	684.7	25.0	805.2	641.9
35.0	1028.5	684.9	35.0	772.1	642.5
45.0	983.0	684.5	45.0	734.8	642.6
55.0	925.2	684.4	55.0	695.1	642.3
65.0	857.1	684.0	60.0	668.9	642.2
70.0	820.7	684.2	63.5	652.3	641.7
80.0	721.3	684.3	65.0	647.0	642.4
83.5	684.1	-	66.4	642.2	-
84.9	689.4	684.7	70.0	661.5	640.9
90.0	709.8	683.6	74.9	672.5	641.0
95.0	728.4	682.6	80.0	687.9	641.2
100.0	742.2	-	90.0	715.5	638.9
			94.9	729.3	639.9
			95	730.4	640.4
			100	742.2	-

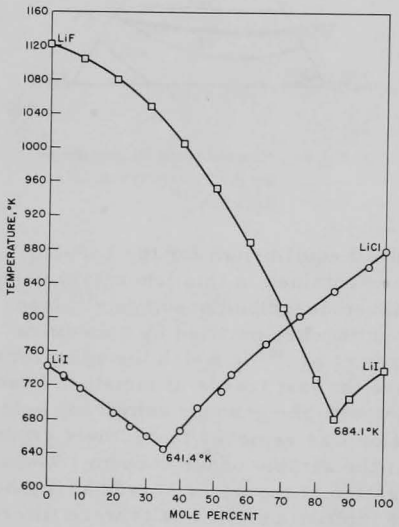

308-666 Rev. 1

Fig. 85. Crystallization Temperatures for the Binary Systems LiF-LiI and LiCl-LiI

Data defining the LiF-LiCl-LiI system were gathered from heating and cooling curves for five LiCl-LiI mole ratios radiating from the LiF corner of the ternary field. Table XXIII gives the experimental compositions investigated and the equilibrium temperatures at which inflections and halts were observed. Figure 86 is a composition-temperature contour diagram for the ternary system constructed from these data and the knowledge of the three binary systems. Inspection of the liquidus surface of the ternary diagram indicates three fields of crystallization, one for each of the pure components in the system. At the intersection of these three fields lies the minimum in the system, a ternary eutectic with a composition of 11.7 m/o LiF-29.1 m/o LiCl-59.2 m/o LiI melting at 614.2°K.

TABLE XXIII. Crystallization Temperatures for the System LiF-LiCl-LiI

Series I		Series II		Series III		Series IV		Series V	
Mole Ratio LiCl:LiI 9:1		Mole Ratio LiCl:LiI 7:3		Mole Ratio LiCl:LiI 1:1		Mole Ratio LiCl:LiI 3:7		Mole Ratio LiCl:LiI 1:9	
m/o LiF	Temp, °K	m/o LiF	Temp, °K	m/o LiF	Temp, °K	m/o LiF	Temp, °K	m/o LiF	Temp, °K
10.0	816.4	10.0	755.7	5.0	701.3	5.0	644.1	10.0	684.2
20.0	781.5	15.0	739.9	10.0	691.0	10.0	653.4	20.0	717.3
25.0	762.3	20.0	727.0	15.0	672.0	15.0	656.4	30.0	815.3
30.0	774.3	25.0	744.8	22.5	732.8	20.0	712.2	48.2	941.1
35.0	817.5	30.0	787.0	30.0	804.4	30.0	806.3	50.0	951.6
40.0	852.8	40.0	862.5	40.0	871.2	40.0	879.6	60.0	1010
50.0	912.1	50.0	924.0	50.0	939.5	50.0	941.9	70.0	1039
60.0	965.0	60.0	973.5	60.0	993.0	60.0	993.7	80.0	1069
70.0	1010	70.0	1018	70.0	1026	70.0	1034	90.0	1095
80.0	1048	80.0	1055	80.0	1059	80.0	1064	100.0	1121
90.0	1085	90.0	1087	90.0	1089	90.0	1091		
100.0	1121	100.0	1121	100.0	1121	100.0	1121		

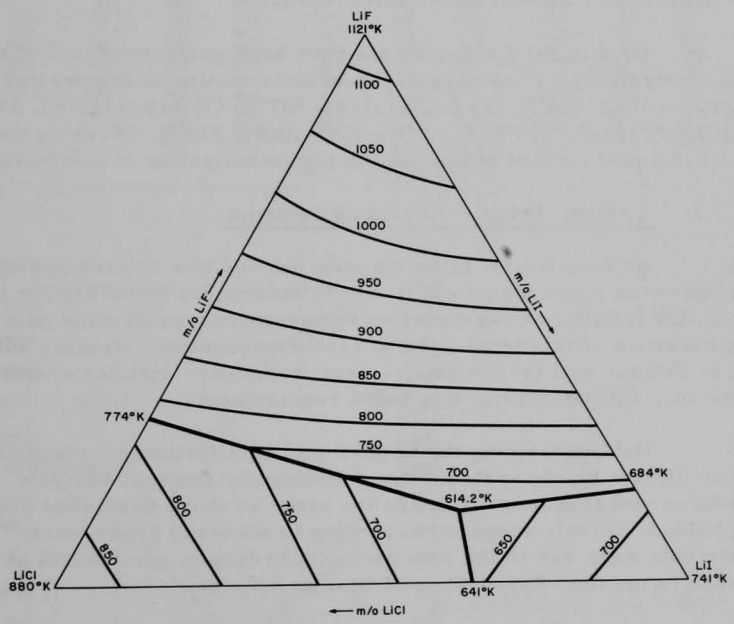

308-641 Rev. 1

Fig. 86. Crystallization Temperatures for the Ternary System LiF-LiCl-LiI

Preliminary experiments for the LiBr-LiI, LiF-LiBr-LiI, and LiCl-LiBr-LiI systems gave the following results: The LiBr-LiI system is a solid-solution mixture with the minimum in the system at about 691°K; the composition at the minimum is about 60 m/o LiI. The minimum temperatures in the LiF-LiBr-LiI and LiCl-LiBr-LiI systems are nearly the same, 640 and 630°K, respectively. Two eutectic binary mixtures and one solid-solution mixture make up the LiF-LiBr-LiI system, whereas the LiCl-LiBr-LiI ternary mixture is composed of one eutectic binary and two solid-solution binary mixtures. Further work on these systems is planned.

Thermodynamic stability data indicate that if the operating temperature of the cell or battery is restricted to below 773°K, it should be possible to use mixed-cation-containing (e.g., lithium, potassium, rubidium, cesium) electrolyte for those cells or batteries using lithium as the anode metal. High-purity lithium is obtained by electrolysis from a LiCl-KCl bath held at 648°K. The very low (0.003 w/o) potassium impurity in lithium metal further establishes the stability of potassium salts in the presence of lithium metal below 773°K.

Preliminary experiments have been performed on five mixed-cation electrolytes. These systems and their minimum temperatures are: (1) LiF-LiCl-KI, 554°K; (2) LiCl-LiI-KI, 537°K; (3) LiBr-LiI-KI, 538°K; (4) LiCl-KCl-RbCl, 538°K; (5) LiBr-KBr-RbBr, 533°K. Work on these systems is planned as part of our continuing investigation of electrolytes.

2. Lithium Hydride-containing Systems

An electrolyte, to be suitable for use in a lithium hydride cell, should have the following properties: (1) reasonable solubility for lithium hydride, (2) stability at regeneration temperatures, preferably with a low vapor pressure at this temperature, (3) thermodynamic stability with respect to lithium, and (4) low anode-metal solubility. Halides of lithium are the only substances meeting these requirements.

Data describing the solid-liquid equilibrium for the lithium hydride-lithium halide systems were obtained by thermal analysis. The procedures and apparatus used are the same as those described previously, using lithium hydride prepared according to standard procedures.[109] All experiments were run in the presence of a hydrogen-gas blanket of 1 atm pressure to prevent dissociation of lithium hydride.

Table XXIV summarizes the pertinent data for the various binary and ternary lithium hydride-lithium halide mixtures of interest. Data for the LiH-LiF system were obtained from the work of Messer and Mellor[130] and are included here for completeness. Table XXV lists the crystallization temperatures for all four binary systems. They are also displayed graphically in Figs. 87-89.

TABLE XXIV. Solid-Liquid Equilibrium Characteristics of Lithium Hydride-Lithium Halide Mixtures

Components[a]	Type[b]	Minimum Temp, °K	Composition	Reference
LiH-LiCl	E	768.8	34.0 m/o LiH	110
LiH-LiBr	E	726.5	29.7 m/o LiH	111
LiH-LiI	E	664.0	23.5 m/o LiH	111
LiH-LiF	SS	957.3	~13 m/o LiH	130
LiH-LiF-LiCl	SS	732	20 m/o-61 m/o-19 m/o	131
LiH-LiCl-LiI	E	606.1	14.5 m/o-27.5 m/o-58.0 m/o	-

[a]Melting points of the pure components are as follows: LiH, 959.5°K; LiF, 1121°K; LiCl, 880.0°K; LiBr, 824.3°K; and LiI, 742.2°K.
[b]E stands for eutectic, and SS stands for solid solution.

TABLE XXV. Crystallization Temperatures for the Binary Systems LiH-LiF, LiH-LiCl, LiH-LiBr, and LiH-LiI

LiH-LiF			LiH-LiCl			LiH-LiBr			LiH-LiI		
m/o LiF	Liquidus, Temp, °K	Solidus, Temp, °K	m/o LiH	Liquidus, Temp, °K	Eutectic Temp, °K	m/o LiH	Liquidus, Temp, °K	Eutectic, Temp, °K	m/o LiH	Liquidus, Temp, °K	Eutectic, Temp, °K
0.00	959.6	-	0.0	880.0	-	0.0	824.3	-	0.0	741.1	-
5.06	958.2	957.0	5.0	866.7	769.0	5.0	809.9	726.3	5.0	728.2	663.2
9.44	957.4	956.3	15.0	835.6	769.4	10.1	794.7	726.7	10.0	714.7	664.3
15.4	957.3	955.8	25.0	805.3	769.9	15.2	779.2	723.6	15.0	698.7	661.5
20.0	958.8	956.3	30.0	783.8	768.4	20.0	763.1	723.8	20.0	678.7	665.0
25.0	961.8	956.7	34.0	768.8	768.8	25.2	746.0	723.6	23.5	664.0	664.0
31.5	966.6	958.2	40.0	791.0	768.5	29.7	726.5	726.5	30.0	712.3	665.0
39.9	971.2	959.9	45.0	809.6	769.7	35.1	758.1	725.7	40.0	777.2	664.6
50.0	977.6	964.9	50.0	834.7	769.0	40.6	787.4	725.6	45.0	801.0	664.1
60.0	995.6	971.6	55.0	841.7	769.0	48.6	821.2	725.4	50.0	825.1	664.2
70.1	1051.7	988.8	60.0	856.6	769.2	55.0	843.5	726.5	60.0	864.2	664.5
80.0	1085.2	1014.2	65.0	870.9	768.4	60.1	861.3	725.4	70.0	894.2	664.0
90.1	1105.6	1059.8	70.0	884.0	768.5	70.0	888.7	726.7	80.0	918.1	661.4
100.0	1121	1121	80.0	906.6	766.9	74.9	902.2	725.4	85.0	929.1	664.0
			94.0	943.5	768.2	79.9	915.8	724.9	90.0	939.3	663.3
			99.0	956.9	766.2	85.0	926.5	726.6	95.0	949.2	663.3
			100.0	959.3	-	89.7	936.9	725.4	100.0	959.5	-
						95.0	948.4	725.4			
						100.0	959.5				

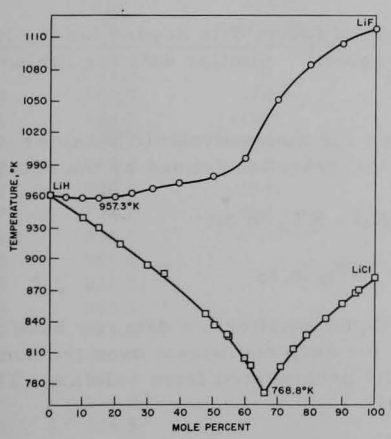

308-664

Fig. 87. Crystallization Temperatures for the Binary Systems LiH-LiF and LiH-LiCl

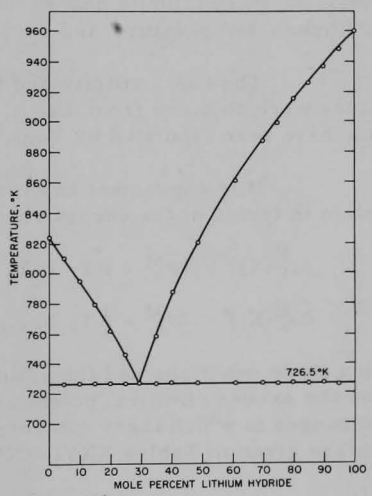

108-8276 Rev. 1

Fig. 88. Crystallization Temperatures for the Binary System LiH-LiBr

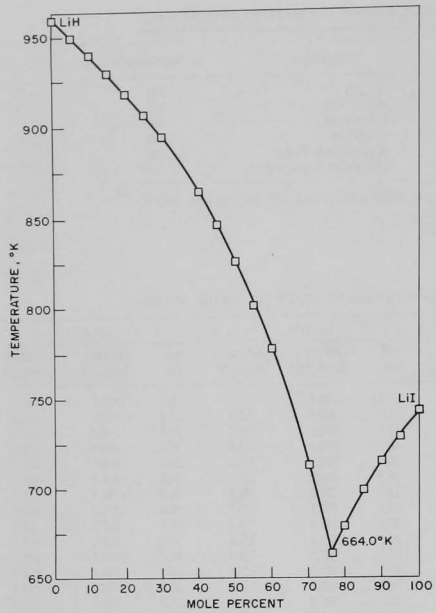

308-665

Fig. 89. Crystallization Temperatures for the Binary System LiH-LiI

A thermodynamic analysis has been made of the solid-liquid equilibrium data for the first three systems of Table XXIV (namely, LiH-LiCl, LiH-LiBr, and LiH-LiI). With no experimental evidence for solid solutions, we assumed that only the pure solid component was precipitating from the mixture. For such a system, the change in the chemical potential on mixing, $\Delta\mu^M$, for the component in solution which is in equilibrium with the pure solid is calculated by use of

$$\Delta\mu_1^M(X_2, T_e) = \Delta\tilde{H}_f \frac{T_e - T_{m1}}{T_{m1}} + T_e \int_{T_{m1}}^{T_e} dT/T^2 \int_{T_{m1}}^{T} \left[\tilde{C}_{p1}(\ell) - \tilde{C}_{p1}(s)\right] dT. \tag{132}$$

In this equation, $\Delta\tilde{H}_f$ is the molar change of enthalpy of the pure component on melting at its melting point, T_m. T_e is the equilibrium temperature of the two-phase system. The standard state of the component in solution is chosen to be the pure supercooled liquid at the equilibrium temperature and at 1 atm.

The heat capacity and heat of fusion data needed for the lithium halides were obtained from JANAF tables.[117] Similar data for lithium hydride have been tabulated by Vogt.[118]

It is convenient to express the thermodynamic behavior of the system in terms of the excess chemical potential defined by the equations

$$\Delta\mu_1^E(X_2) = \Delta\mu_1^M - \underset{\sim}{R}T_e \ln(1 - X_2) - \underset{\sim}{R}T_e \ln \gamma_1; \tag{133}$$

$$\Delta\mu_2^E(X_1) = \Delta\mu_2^M - \underset{\sim}{R}T_e \ln X_2 = \underset{\sim}{R}T_e \ln \gamma_2. \tag{134}$$

Using these equations and the solid-liquid equilibrium data, we have calculated the excess chemical potentials for each component over the composition ranges in which these components precipitated from solution. These data are given in Tables XXVI-XXVIII.

TABLE XXVI. Thermodynamic Properties of the System LiH-LiCl

m/o LiH	T_e, °K	$\Delta\mu^M_{LiCl}$, cal/mole	$\Delta\mu^M_{LiH}$, cal/mole	$\Delta\mu^E_{LiCl}$, cal/mole	$\Delta\mu^E_{LiH}$, cal/mole
0.0	880.0	-		-	
5.0	868.2	-64.3		24.2	
6.1	865.6	-76.8		31.5	
10.1	854.7	-135		45.4	
15.1	840.7	-205		68.7	
21.0	824.8	-295		91.2	
24.9	811.7	-348		114	
28.9	794.9	-454		84.9	
34.0	768.8	-590	-1089	44.3	558
38.2	796.4		-927		597
40.1	802.3		-893		565
44.7	822.7		-773		551
45.1	825.6		-755		543
49.5	834.8		-701		464
52.2	845.5		-648		443
57.6	859.0		-562		380
65.4	889.0		-447		295
69.8	892.9		-368		269
78.6	912.7		-257		179
85.2	929.1		-164		132
90.1	938.3		-114		79.8
100.0	959.3		-		-

TABLE XXVII. Thermodynamic Properties of the System LiH-LiBr

m/o LiH	T_e, °K	$\Delta\mu^M_{LiBr}$, cal/mole	$\Delta\mu^M_{LiH}$, cal/mole	$\Delta\mu^E_{LiBr}$, cal/mole	$\Delta\mu^E_{LiH}$, cal/mole
0.0	824.3	0		0	
5.0	809.9	-74.4		8.2	
10.1	794.7	-152		15.8	
15.2	779.2	-230		23.9	
20.0	763.1	-312		26.0	
25.2	746.0	-398		32.6	
29.7	726.5	-494	-1340	14.7	408
35.1	758.1		-1160		421
40.6	787.4		-983		428
48.6	821.2		-785		393
55.0	843.5		-655		347
60.1	861.3		-552		319
70.0	888.7		-393		237
74.9	902.2		-319		200
79.9	915.8		-242		166
85.0	926.5		-183		117
89.7	936.9		-125		77.4
95.0	948.4		-61.5		35.2
100.0	959.5		0		0

TABLE XXVIII. Thermodynamic Properties of the System LiH-LiI

m/o LiH	T_e, °K	$\Delta\mu^M_{LiI}$, cal/mole	$\Delta\mu^M_{LiH}$, cal/mole	$\Delta\mu^E_{LiI}$, cal/mole	$\Delta\mu^E_{LiH}$, cal/mole
0.0	741.1	0		0	
5.0	728.2	-61.0		13.2	
10.0	714.7	-125		24.7	
15.0	698.7	-201		25.1	
20.0	678.7	-295		5.6	
23.5	664.0	-365	-1715	-11.8	196
30.0	712.3		-1425		278
35.0	747.1		-1220		340
40.0	777.2		-1040		375
45.0	801.0		-900		371
50.0	825.1		-760		378
55.0	845.3		-640		363
60.0	864.2		-532		345
65.0	880.0		-442		312
70.0	894.2		-360		273
75.0	906.3		-293		225
80.0	918.1		-226		181
85.0	929.1		-165		135
90.0	939.3		-108		88.3
95.0	949.2		-53.7		43.1
100.0	959.5		0		0

The deviations from ideality for all systems are large and positive. Such positive deviations are usually caused by dispersion forces or association of one of the components. The thermodynamic behavior of all these binary systems is similar in the dilute regions of the halide in lithium hydride. The differences become more pronounced as the concentration of the halide increases. Figure 90 illustrates these similarities and differences. In Fig. 90, $\Delta\mu^E_{LiH}$ is given as a function of the mole percent of the halide along the saturation curve. The line gives the value of $\Delta\mu^E_{LiH}$ calculated under the assumptions that the halide exists as an ionic aggregate in solution, that lithium hydride is ionized in solution, and that the solutions are ideal.[111,132]

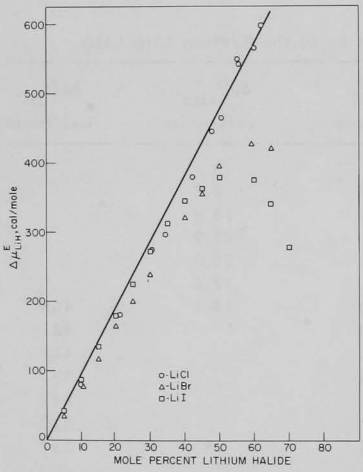

108-8277 Rev. 1

Fig. 90. Comparison of Experimental Data for $\Delta\mu^E_{LiH}$ with Values Calculated Assuming LiX_2^-, Li^+, and H^-. $\Delta\mu^E_{LiH} = -RT_e \ln (X_{LiH} + \frac{1}{2} X_{LiX})$.

The values of $\Delta\mu^E_{LiH}$ for the LiCl-LiH system are surprisingly consistent with the concept that lithium chloride behaves ionically, but probably as an ionic aggregate such as $LiCl_2^-$, over most of the measurable composition range. In the more dilute regions, both the bromide

and the iodide solutes follow the same behavior, but deviate in the more concentrated solutions. The deviations would indicate a change in the (concentrated) solution characteristics progressing from chloride to bromide to iodide. The behavior of the three binary systems is indicative of ordering in the system; it follows closely the behavior calculated for a system in which the existence of ionic aggregates (e.g., $LiX_2^- + Li^+$) is assumed.

Two ternary systems are particularly attractive for use as electrolytes in a lithium hydride galvanic cell. Table XXIX lists the crystallization temperatures for the LiH-LiCl-LiF ternary, and Fig. 91 is the equilibrium diagram. The lateral sides of this system are composed of two binary eutectics (LiH-LiCl and LiCl-LiF) and one binary mixture, which consists of a series of solid solutions. Inspection of the liquidus surface of Fig. 91 indicates two fields of crystallization: that of pure LiCl and that of the solid solutions of LiH-LiF. The intersection of these two fields has a minimum of 732°K.

TABLE XXIX. Crystallization Temperatures for the System LiH-LiCl-LiF

Series I		Series II		Series III		Series IV		Series V		Series VI		Series VII		Series VIII		Series IX		Series X	
Mole Ratio LiH:LiF 1:9		Mole Ratio LiH:LiF 3:7		Mole Ratio LiH:LiF 1:1		Mole Ratio LiH:LiF 7:3		Mole Ratio LiH:LiF 9:1		Mole Ratio LiCl:LiF 7:3		Mole Ratio LiCl:LiF 3:1		Mole Ratio LiCl:LiF 7.75:2.25		Mole Ratio LiCl:LiF 4:1		Mole Ratio LiCl:LiF 8.5:1.5	
m/o LiCl	Temp, °K	m/o LiCl	Temp, °K	m/o LiCl	Temp, °K	m/o LiCl	Temp, °K	m/o LiCl	Temp, °K	m/o LiH	Temp, °K	m/o LiH	Temp, °K	m/o LiH	Temp, °K	m/o LiH	Temp, °K	m/o LiH	Temp, °K
0.0	1105.6	0.0	1051.7	0.0	977.6	0.0	965.2	0.0	957.4	0.0	774.2	0.0	792.7	0.0	801.7	0.0	811.7	0.0	829.2
15.0	1052.2	10.0	1027.6	10.0	962.0	10.0	935.2	10.0	929.8	10.1	767.9	10.0	763.2	10.0	773.5	10.0	784.4	10.0	801.7
30.1	990.8	20.0	987.6	20.0	935.2	20.0	893.4	20.0	902.8	19.6	765.4	15.1	743.5	15.0	757.7	17.5	760.2	18.6	776.3
40.0	936.6	40.0	901.5	30.0	893.5	30.0	868.6	30.0	877.3	22.5	767.5	18.0	734.5	17.5	749.3	20.0	751.6	22.1	764.5
50.0	881.2	45.0	871.3	40.0	850.4	40.0	836.1	40.0	849.3	29.6	789.3	19.0	732.5	20.0	742.0	22.6	741.9	25.0	748.8
55.0	844.4	50.0	844.2	50.0	792.1	50.0	799.4	50.0	817.7	40.8	828.8	20.0	733.6	21.0	735.8	25.0	737.8	27.5	748.5
60.0	817.3	55.0	814.7	55.0	760.9	60.0	756.4	55.0	804.2	49.6	852.0	24.9	756.7	21.6	733.5	27.5	756.0	30.0	762.7
65.0	784.8	60.0	772.1	60.0	735.8	70.0	780.2	60.0	788.3	100.0	959.2	29.9	780.6	22.7	733.7	30.0	767.0	40.0	807.0
75.0	794.3	70.0	773.1	65.0	756.2	80.0	816.4	70.0	783.2			33.5	795.8	25.0	749.1	40.0	809.4	50.0	843.2
80.0	805.4	75.0	793.9	70.0	776.1	90.0	849.7	80.0	819.3			40.0	818.3	35.0	795.0	50.0	843.2	100.0	959.2
85.6	831.9	80.0	811.6	75.0	796.3	100.0	880.0	90.0	854.5			50.0	850.2	45.0	831.4	100.0	959.2		
95.0	865.2	90.0	847.2	80.0	812.6			100.0	880.0			100.0	959.2	100.0	959.2				
100.0	880.0	100.0	880.0	90.0	847.7														
				100.0	880.0														

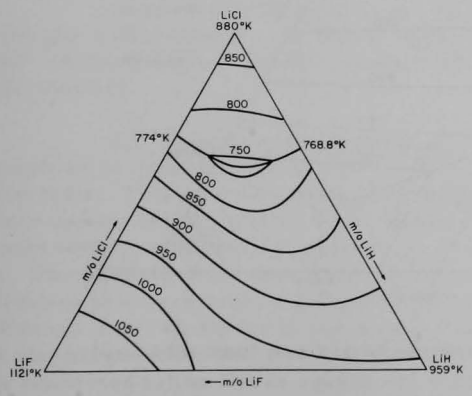

Fig. 91

Crystallization Temperatures for the Ternary System LiH-LiF-LiCl

308-634

Table XXX lists the crystallization temperatures for the LiH-LiCl-LiI system. The lateral sides of this ternary mixture are composed of three binary eutectics: LiH-LiCl, LiH-LiI, and LiCl-LiI. Figure 92 gives the liquidus surface of this mixture, showing three fields of crystallization: those of pure LiH, pure LiCl, and pure LiI. At the intersection of these three fields lies the minimum in the system, the ternary eutectic composed of 14.5 m/o LiH-27.5 m/o LiCl-58.0 m/o LiI melting at 606.1°K. This low-melting eutectic allows the operation of a relatively low-temperature lithium-hydrogen cell, which should result in increased thermal efficiency and higher cell voltage.

TABLE XXX. Crystallization Temperatures for the System LiH-LiCl-LiI

Series I			Series II			Series III			Series IV			Series V			Series VI		
Mole Ratio LiCl:LiI 1:9			Mole Ratio LiCl:LiI 3:7			Mole Ratio LiCl:LiI 1:1			Mole Ratio LiCl:LiI 7:3			Mole Ratio LiCl:LiI 9:1			Mole Ratio LiH:LiCl 34:66		
m/o LiH	Liquidus Temp, °K	Eutectic Temp, °K	m/o LiH	Liquidus Temp, °K	Eutectic Temp, °K	m/o LiH	Liquidus Temp, °K	Eutectic Temp, °K	m/o LiH	Liquidus Temp, °K	Eutectic Temp, °K	m/o LiH	Liquidus Temp, °K	Eutectic Temp, °K	m/o LiI	Liquidus Temp, °K	Eutectic Temp, °K
0.0	715.2	-	0.0	658.3	-	0.0	715.2	-	0.0		-	0.0		-	0.0	768.8	-
10.0	684.3	606.6	5.0	640.6	606.6	5.0	703.4	599.6	10.0	761.9	607.6	10.0	818.0	608.7	22.0	718.4	606.2
20.0	652.8	605.3	10.0	625.9	607.8	10.0	693.6	609.1	20.0	737.8	607.9	20.0	797.5	609.9	30.0	701.2	606.8
25.0	689.1	604.1	20.0	640.2	607.8	15.0	686.1	608.1	30.0	731.1	605.4	30.0	758.4	608.1	40.0	676.4	607.0
30.0	715.9	606.3	25.0	692.3	607.4	20.1	677.2	607.2	35.0	768.4	607.2	40.0	791.6	608.4	50.0	636.2	608.1
35.0	749.1	605.4	30.0	725.1	607.6	25.1	706.7	607.2	40.0	788.9	607.2	50.0	872.6	606.0	54.7	616.4	607.6
45.0	805.3	604.3	40.0	782.9	607.0	35.0	762.2	607.3	50.0	826.0	606.5	60.0	861.0	605.9	56.0	613.4	606.7
55.0	837.6	604.1	50.0	830.0	607.3	45.0	807.7	606.9	60.0	861.7	608.1	70.0	885.7	607.5	65.0	633.0	606.5
65.0	882.5	606.2	60.0	863.7	603.1	55.0	851.7	606.9	70.0	887.4	605.8	75.0	898.8	608.0	77.1	673.4	605.8
75.0	906.3	603.7	70.0	893.3	603.1	65.0	882.6	606.6	80.0	910.4	603.2	85.0	920.5	606.0	100.0	742.2	-
85.0	927.3	601.6	80.0	912.8	605.7	75.0	902.7	606.9	89.4	933.6	603.2	89.6	930.5	606.0			
100.0	959.0	-	90.0	936.4	603.9	85.0	923.6	606.1	100.0	959.0	-	100.0	959.0	-			
			100.0	959.0	-	100.0	959.0	-									

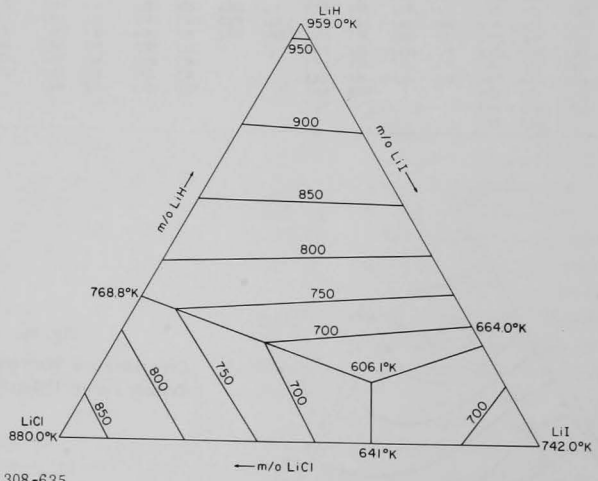

308-635

Fig. 92. Crystallization Temperatures for the Ternary System LiH-LiCl-LiI

D. The Hydrogen Electrode in Lithium Hydride-containing Systems

1. Hydrogen-permeation Studies

Hydrogen has the unique property of diffusing through certain metals at a high rate; attempts have been made to exploit this property in the design of hydrogen cathodes for a thermally regenerative lithium hydride cell system. The use of a suitable permeable-metal diaphragm as an electrode alleviates some of the problems associated with porous metal gas electrodes, namely, concentration overvoltage in the pores and flooding of the electrode with either electrolyte or gas. Thus, with the gas electrode made of a solid thin sheet of metal, hydrogen would diffuse through the diaphragm and be supplied in the atomic state at the metal-fused salt interface, where it can react electrochemically.

Materials that are compatible with a lithium hydride cell environment consisting of liquid lithium, lithium hydride, and a molten alkali halide are somewhat limited. Palladium and silver-palladium alloys, which have a high hydrogen permeability, are not suitable because of their incompatibility with lithium metal; for example, formation of Li_2Pd is possible, which would destroy the diaphragm. Of those materials examined,[133,134] only iron and vanadium are of interest--iron because of its self-cleaning properties, and vanadium because of its high rate of permeation.

The permeation of a diatomic gas through a metal barrier was considered[135] to be a four-step composite rate process: (1) the activated adsorption of the gas on the metal surface, (2) the formation of a gas-metal solution, (3) the diffusion of dissolved gas atoms through the metal crystal lattice, and (4) the recombination of atoms, and the desorption of the gas molecules at the opposite surface.

Of great importance to gas permeation is the solubility constant of the gas-metal system. A metal that possesses a high gas solubility, provided optimum surface conditions exist, will in general exhibit a high rate of permeation.

a. Experimental Procedure. A gas-measuring apparatus was assembled to measure directly the volume of hydrogen permeating through metal foils. This approach was taken because of anticipated high permeation rates and the simplicity of the volume measuring technique under these experimental conditions. Figure 93 is a schematic diagram of this apparatus. The portion of the apparatus comprising the gas-measuring burets, reference pressure tube, mercury U-tube, and reservoirs was constructed of Pyrex. The remainder of the apparatus containing the hydrogen purifier and diaphragm assembly was constructed of Type 304 stainless steel and was connected to the Pyrex system by copper-to-glass seals.

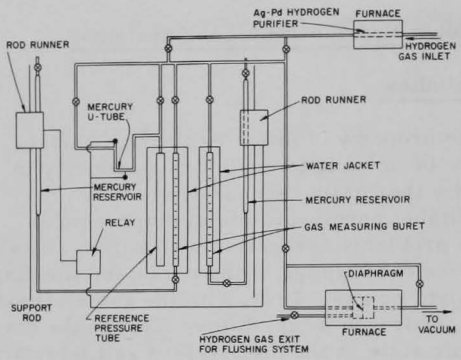

108-7473

Fig. 93. Gas Measuring Apparatus for Hydrogen Permeation Studies

The permeation rates were measured at a constant pressure differential of 1 atm across the diaphragms. This was accomplished by setting and maintaining the pressure in the reference tube at exactly 1 atm. The permeation rate through the diaphragm was measured directly as the change of gas volume in the measuring buret per unit time.

High-purity vanadium metal (99.81%) and Armco iron (99.54%), each of 0.025 cm thickness, were used as diaphragm materials for the gas-permeation studies.

Prior to any measurements, the gas-measuring system was evacuated to about 10^{-4} Torr and then filled with purified hydrogen gas. This process was repeated several times before the pressure was set at 1 atm and a measurement taken. The diaphragm assembly was also evacuated and degassed at ~1100°K for 16 hr prior to any measurements. Leak rates, when the gas-measuring system was filled with helium, were negligible over an 8-hr period. All diaphragm assemblies were leak-checked with a helium mass spectrometer prior to connection with the gas-measuring portion of the system. In addition, a helium-leak check was made at temperature to ensure that neither the diaphragm nor the diaphragm weld opened on heating. After this testing, pure hydrogen was introduced to the assembly and flushed past the diaphragm for several hours to ensure saturation of all the metal system with hydrogen. Reproducibility of successive measurements at temperature was used as an indication that equilibrium had been reached. A constant rate was taken as an indication that little or no surface contamination of the diaphragm by a reactive impurity occurred during an experiment. Overall experimental accuracy was estimated to be ±2%, the maximum uncertainty occurring in the definition of the working area of the diaphragm.

b. Results and Discussion. The general equation for the permeation of a diatomic gas through a metal barrier can be expressed as

$$V = \theta \frac{K_s \mathcal{D}_{A-B^A}}{d} (p_1^{1/2} - p_2^{1/2})\, e^{-\Delta \underset{\sim}{H}^+/\underset{\sim}{R}T}, \qquad (135)$$

where

V = volume of gas permeating the diaphragm, cm^3 (STP);

K_s = solubility constant of the gas-metal system, $atm^{-1/2}$;

p_1 = gas pressure on the upstream side of diaphragm, atm;

and

p_2 = gas pressure on the downstream side of diaphragm, atm.

In the hydrogen-permeation experiments, the downstream side of the diaphragm was continuously evacuated and the upstream hydrogen pressure held constant at 1 atm; this reduces the above equation to

$$V = \theta \frac{K_s \mathcal{D}_{A-B} A}{d} e^{-\Delta H^+/RT}. \tag{136}$$

The results of the experiments are summarized and plotted in Fig. 94 as the logarithm of the rate of permeation versus the reciprocal of the absolute temperature. The solid lines represent smoothing of the experimental data by a least-squares analysis. Current densities given are the equivalent current densities achievable in a cell operating at 100% current efficiency.

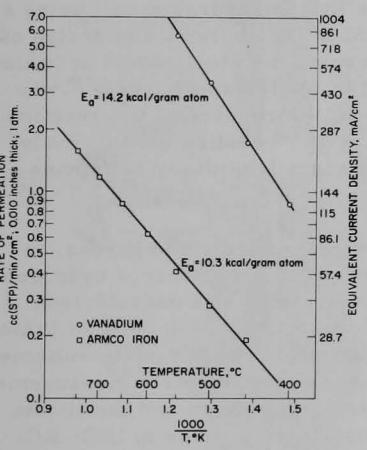

108-8517

Fig. 94. Permeation Isobars for Hydrogen through Vanadium and Armco Iron

Even though the permeation rate of hydrogen through iron is low and for this reason would be capable of supporting about one-tenth the current densities of interest, iron is still somewhat attractive because it is self-cleaning in a hydrogen atmosphere at cell-operating temperatures. The possibility of a special cathode design to increase current density may still be practical in a cell using an iron diaphragm. On the other hand, vanadium appears to be an excellent diaphragm material. It has a high hydrogen permeability at moderate temperatures and is compatible with the cell environment. At a higher cell-operating temperature, a 0.025-cm-thick diaphragm can sustain a theoretical current density in excess of 1000 mA/cm^2 at 870°K. A similar effect can be achieved at lower temperatures by reducing the thickness of the diaphragm.

Because vanadium is not self-cleaning at normal cell temperatures, some preparation of the metal is needed before its maximum hydrogen permeation rate is achieved. This preparation consists of baking the metal in vacuum at 1120°K to remove as much of the volatile surface oxide contamination as possible.

Vanadium is one of a group of metals (V, Nb, Ta) having negative hydrogen absorption coefficients with temperature; that is, the metal absorbs greater quantities of hydrogen at lower temperatures than at higher temperatures. If vanadium metal is cooled in hydrogen, the metal lattice expands, further increasing the permeation rate at low temperatures.

The vanadium diaphragm must be tested more extensively under severe load conditions before it can be used in a practical cell. However, these hydrogen-permeation measurements indicate that the vanadium is an attractive cathode material.

2. Kinetics of the Hydrogen Electrode

A knowledge of the kinetics and mechanism of the electrochemical reaction of hydrogen at the cathode of a lithium-hydrogen cell using a fused lithium halide electrolyte is important in the analysis and design of these cells and systems. Some work concerning the electrolysis of lithium hydride has been reported by Peters[136] and by Potter and Bockris[137] who found that hydrogen was evolved at the anode, the reverse of the reaction in which we are most interested. Johnson *et al.*[110] studied the thermodynamics of this cell (see Section V.A.2), and some laboratory cells have been operated.[138-141]

Only one previous investigation, that of Indig and Snyder, reported on the kinetics or mechanism of cathodic consumption of hydrogen in a lithium-hydrogen cell.[142] They found indications of a one-electron reaction (according to the Nernst equation) in concentration cells of lithium hydride. Because of the lack of kinetic information, steady-state voltametric measurements and nonsteady-state chronopotentiometric measurements were carried out on the cathodic consumption of hydrogen and the anodic production of hydrogen at pure iron and tungsten electrodes in LiCl-KCl electrolytes containing dissolved LiH. These investigations were performed at Argonne by Plambeck and Elder. The paper by Plambeck, Elder, and Laitenen[143] contains complete experimental details and discussion of this work.

a. Experimental Procedure.* The electrochemical cell is shown in Fig. 95. All materials were Type 316 stainless steel, unless otherwise specified. The reactivity of molten lithium and lithium hydride-containing electrolytes is such that no available insulator could withstand prolonged exposure without attack. Because of this, all electrodes were supported by insulators kept above the level of the electrolyte. The liquid lithium was held in a porous stainless steel-fiber disc, which was fitted into the cup electrode holder. Because lithium wetted the fiber disc so

*All experiments were performed in an inert atmosphere of high-purity argon or hydrogen, as specified.

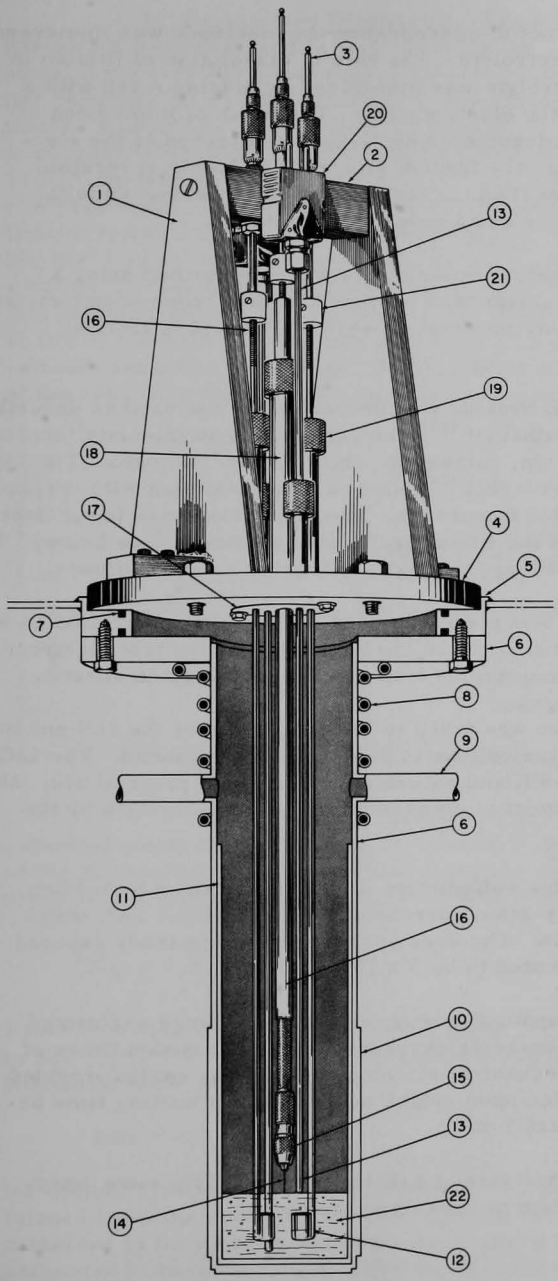

Fig. 95

Schematic Diagram of the Electrochemical Cell

1. Aluminum depth gauge support
2. Micarta insulating bar
3. Micrometer depth gauge
4. Cell head base
5. Base of inert-atmosphere enclosure
6. Furnace well
7. O-ring seal
8. Water-cooling coils
9. Gas inlet
10. Copper sheath
11. Crucible
12. Lithium-cup electrode
13. Thermocouple
14. Wire microelectrode or flag electrode
15. Pin vise
16. Electrode lead rod
17. Insulating disk
18. Nylon-lined brass tube
19. Insulating vacuum coupling
20. Thermocouple connector block
21. Nylon insulating connector
22. Electrolyte

108-8966

tenaciously, the metal was not displaced when the electrode was immersed below the surface of the electrolyte. The rate of dissolution of lithium in the LiCl-KCl eutectic electrolyte was minimized by placing a cap with a small central orifice over the electrode cup. The depth of immersion of the electrodes was set by micrometer depth gauges attached to the electrode support rods. Because the lithium electrode is highly reversible and was of much larger area than the test electrode, it served simultaneously as a counterelectrode and a reference electrode.

The voltametric experiments were performed using a Polarograph; a solid-state galvanostat was used for the chronopotentiometric measurements. The current-time traces were photographed from an oscilloscope.

The lithium hydride was prepared and analyzed as described by Johnson, Wood, and Crouthamel.[110] The lithium had an impurity level of 0.003% with respect to sodium, potassium, chlorine, and nitrogen. The LiCl-KCl eutectic was purified with HCl,[104] followed by a treatment with magnesium to displace heavy-metal impurities. The magnesium was found later to have a deleterious effect on the lithium reference electrode (see below). The hydrogen was purified by passage through a silver-palladium diffuser.

The small test electrode used in the voltametric studies was a 0.023-cm-diam pure iron wire. The chronopotentiometry test electrodes were flags cut from 0.025-cm Armco iron and 0.1-cm tungsten sheets.

Special care was taken to clean all parts of the cell and to reduce all oxide layers on the cell parts before the experiments. The LiCl-KCl eutectic was held at 648°K and saturated with lithium prior to use. At this temperature, displacement of potassium from the electrolyte by the lithium was not noticeable.

Reproducible voltametric data were obtained by holding each potential until a steady-state current was obtained (±0.1 μA), which usually required 3 to 30 min. The area of the working electrode exposed to the electrolyte was estimated to be 5×10^{-3} cm^2.

The chronopotentiometric experiments were performed with the flag electrodes at currents corresponding to transition times of 10 msec to 1 sec. Since mechanical stirring could not be easily provided, natural convection was relied upon, which necessitated a waiting time between experiments of at least 5 min.

All concentrations of LiH in the electrolyte were determined by acidimetric titration of hydrolyzed samples.

b. Results and Discussion. The steady-state voltametric experiments were designed to yield information concerning the rate-limiting steps in the cathodic consumption and anode evolution of hydrogen. Figure 96 shows the results of some of these steady-state voltametric experiments. Curve A is for the electrolyte under a helium atmosphere. The iron-dissolution potential in this electrolyte appeared to be +1.48 V versus Li/Li^+, instead of the expected +2.13 V. This discrepancy is ascribed to the magnesium introduced from the electrolyte onto the surface of the lithium reference electrode during the purification procedure, yielding a Mg/Mg^{++} quasi-reference electrode. The results for the electrolyte under a helium atmosphere were corrected by +0.65 V to bring the iron dissolution potential up to 2.13 V versus Li/Li^+. The small cathodic current shown by Curve A at potentials below 1.2 V is probably caused by the cathodic reduction of hydrogen that had been dissolved in the metal parts of the apparatus during prior heat-treatment in hydrogen.

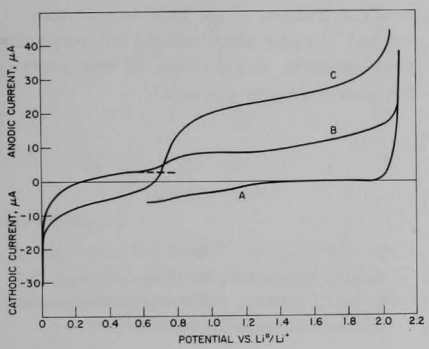

Fig. 96

Voltametric Data for the Lithium Hydride Cell, LiCl-KCl Eutectic, 648°K, Iron Microelectrode

A. Electrolyte alone, helium atmosphere, 1 atm;
B. Lithium-saturated electrolyte, helium atmosphere, 1 atm;
C. Lithium-saturated electrolyte, hydrogen atmosphere, 1 atm.

108-8968 Rev. 1

Curve B is the current-voltage trace for the lithium-saturated electrolyte. The region between 0 and +0.6 V is characteristic of the electrochemical oxidation of dissolved lithium. The region above about +0.6 V was analyzed using the Heyrovsky-Ilkovic equation[144]

$$E_{a-r} = E_{1/2} + \frac{RT}{nF} \ln \frac{i_L - i}{i} . \tag{137}$$

From this equation, the region above about 0.6 V for Curve B corresponded to $E_{1/2}$ = +0.74 V and n = 1.1. This region appears to be characteristic of lithium hydride oxidation:

$$LiH \rightarrow Li^+ + \tfrac{1}{2}H_2 + e^- . \tag{138}$$

No lithium hydride had been added to the cell at this point, but it could have formed from the dissolved lithium metal in the electrolyte and the hydrogen dissolved in the metal parts of the cell. More than enough hydrogen was estimated to have dissolved in the metal parts to produce the concentration of LiH corresponding to the results of Curve B.

Curve C of Fig. 96 was obtained after hydrogen gas was admitted to the system at 1 atm for two days. The additional LiH formed during this period contributed to the larger anodic currents found above 0.6 V as well as the larger cathodic (H_2 reduction) currents below 0.6 V.

Figure 97 shows some current-voltage traces for cells containing added LiH under 1 atm hydrogen pressure. Curve B corresponds to a LiH concentration of 8×10^{-2} m/o LiH in the electrolyte; Curve A corresponds to a saturated LiH solution (about 5 m/o LiH), which did not show an anodic limiting current within the capabilities of the Polarograph. Apparently, activation overvoltages are significant in the cathodic reduction of hydrogen, because no well-defined cathodic limiting currents were obtained at potentials above 0.7 V. The limiting currents for LiH oxidation were measured at several LiH concentrations. Figure 98 shows that a good linear relationship was obtained between the limiting currents and LiH concentration, indicating that the limiting-current (I_L) values did indeed represent mass-transport limited currents. The scatter of the points about the line in Fig. 98 is somewhat larger than might be expected, but the hydrogen-bubble evolution caused random variations of the current, making it difficult to assign accurate time-averaged values.

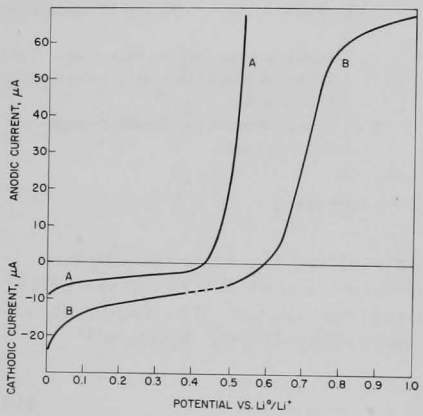

Fig. 97

Voltametric Data for the Lithium Hydride Cell, LiCl-KCl Eutectic, 648°K, Iron Microelectrode; Hydrogen Atmosphere, 1 atm

A. Lithium hydride-saturated electrolyte, about 5 m/o LiH;
B. Unsaturated electrolyte, 8×10^{-2} m/o LiH.

108-8967 Rev. 1

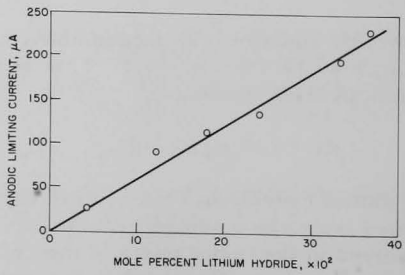

Fig. 98

Effect of Lithium Hydride Concentration on Anodic Limiting Current, LiCl-KCl Eutectic, 648°K, Iron Microelectrode; Hydrogen Atmosphere, 1 atm

108-9094

Since good I_L values were obtained from the anodic portions of the current-voltage curves, it seemed that activation overvoltages were not large, and the curves might be suitable for analysis by the Heyrovsky-Ilkovic equation.[145] This accounts for contributions to the current by both the anodic oxidation of LiH and the cathodic reduction of hydrogen. Figure 99 shows Curve B of Fig. 97 and the corresponding curve (AB) from the Heyrovsky-Ilkovic equation. The value of $I_{L,a}$ used was 73.0 μA; the value of $I_{L,c}$ was taken to be the value of I_c at 0.32 V since there was no well-defined $I_{L,c}$.

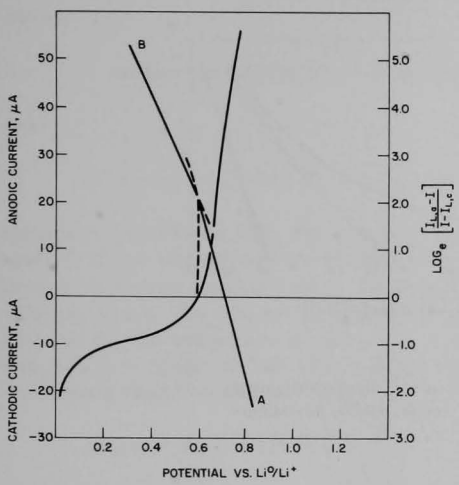

108-9093 Rev. 1

Fig. 99. Heyrovsky-Ilkovic Analysis of Voltametric Curve, LiCl-KCl Eutectic, 648°K, Iron Microelectrode, 8 x 10^{-2} m/o LiH; Hydrogen Atmosphere, 1 atm

Eleven plots were made similar to Curve AB in Fig. 99 using the results of all the experiments performed under several hydrogen pressures and at various LiH concentrations. The mean value of n for the more anodic portion of line AB was 1.079 ± 0.040 e^-/LiH. There was no hydrogen-pressure dependence or LiH concentration dependence of the slope of the anodic branch of line AB. An examination of all the data indicated that the anodic evolution of hydrogen proceeded reversibly, with a value of n = 1 e^-/LiH, while the cathodic consumption of hydrogen proceeded with an appreciable activation overvoltage.

The cathodic portions of the current-voltage data were analyzed using the low-overvoltage portions of the data, avoiding mixed activation-diffusion control regions. The data for cathodic overvoltages of less than 100 mV were used together with the equation

$$\eta = \frac{\underset{\sim}{R}T}{\alpha n F}\left\{\ln I - \ln\left[1 - \exp\left(-\frac{nF}{\underset{\sim}{R}T}\eta\right)\right]\right\} - \frac{\underset{\sim}{R}T}{\alpha n F}\ln I_0 \qquad (139)$$

to determine the values of n and α.

Figure 100 shows the results of a typical experiment, plotted as η versus ln I in Curve A, and as η versus $\left\{\ln I - \ln\left[1 - \exp\left(-\frac{nF}{\underset{\sim}{R}T}\eta\right)\right]\right\}$ in Curves B and C, where n = 2 for Curve B and n = 1 for Curve C. Curve C yields the best straight line, indicating that n = 1. This same result was obtained at several hydrogen pressures. From the slope of Curve C, a value of

0.43 is obtained for α (the fraction of the overvoltage aiding the cathodic reaction). The intercept of Curve C yields an exchange-current density of about 1 mA/cm^2. This is similar to the value obtained on platinum in aqueous acid electrolyte at temperatures below 370°K, but is much lower than the exchange-current densities for Na/Na^+ and Li/Li^+ couples in fused alkali halides.

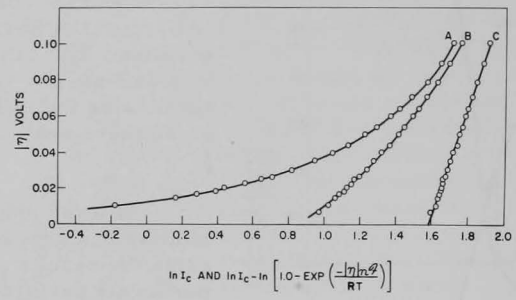

108-9092 Rev. 3

Fig. 100. Overpotential Analysis of Cathodic Voltametric Curve, LiCl-KCl Eutectic, 648°K, Iron Microelectrode, 8 x 10^{-2} m/o LiH; Hydrogen Atmosphere, 1 atm

(A) $|\eta|$ vs. ln I_C;

(B) $|\eta|$ vs. $\ln I_C - \ln\left[1.0 - \exp\left(\frac{-|\eta| n F}{RT}\right)\right]$, $n = 2.0$;

(C) $|\eta|$ vs. $\ln I_C - \ln\left[1.0 - \exp\left(\frac{-|\eta| n F}{RT}\right)\right]$, $n = 1.0$.

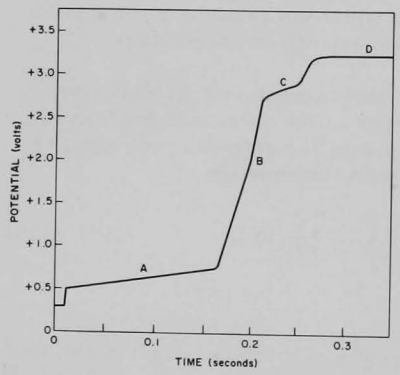

108-9090

Fig. 101. Chronopotentiogram with Tungsten Electrode, LiCl-KCl Eutectic, 648°K; Electrode Area, 0.345 cm^2; Current, 129.7 mA; 25.68 m/o LiH

The diffusion-controlled anodic oxidation of LiH was also studied at constant current using the chronopotentiometric method. Figure 101 is a typical potential-time trace for a tungsten flag electrode of 0.345-cm^2 area; the measurements were obtained at 129.7 mA in 25.68 m/o LiH in LiCl-KCl, at 648°K. Three plateaus were observed. Plateau D corresponds to Cl_2 evolution. Plateau C corresponds to the oxidation of hydrogen to H^+, but the length of the plateau was not treated quantitatively. Plateau A corresponds to LiH oxidation, which starts near 0.5 V (compare to Figs. 97 and 99). The length of plateau A increases with added LiH, as expected, and is independent of the hydrogen pressure.

The time-current relationship at constant current for an electrode process under linear semi-infinite diffusion control is

$$I\tau^{1/2} = \tfrac{1}{2}NFA\mathcal{D}_{i\text{-}m}^{1/2}\pi^{1/2}C, \tag{140}$$

where

τ is the transition time (length of the plateau), sec,

and

C is the concentration of the diffusing species (LiH), moles/cm^3.

Equation 140 shows that the product $I\tau^{1/2}$ is constant for a given concentration if the electrode reaction is diffusion-limited in a semi-infinite linear-diffusion configuration (planar electrode, no convection, no edge effects, etc.). As can be seen from Table XXXI, the product $I\tau^{1/2}$ for plateau A, the oxidation of LiH, was constant over the current density range 0.1-4 Amp/cm^2 at 648°K and for a LiH concentration of 25.68 m/o. Assuming that the overall reaction is

$$2LiH \rightarrow H_2 + 2Li^+ + 2e^-, \tag{141}$$

the mean value of $\mathcal{D}_{LiH\text{-}m}$ from 39 determinations in the range 10-30 m/o LiH was 1.67×10^{-5} cm^2/sec and was independent of hydrogen pressure (over the range 0.5-1.0 atm).

TABLE XXXI. Chronopotentiometric Data, Tungsten Electrode[a]

Current, Amp	Transition Time a, sec	Transition Time c, sec	$I\tau_a^{1/2}$, Amp-sec$^{1/2}$/cm^2	$I\tau_c^{1/2}$, Amp-sec$^{1/2}$/cm^2
0.0817	0.4110	0.0600	0.1525	0.0583
0.1297	0.1690	0.0260	0.1548	0.0580
0.1889	0.0795	0.0150	0.1545	0.0672
0.1889	0.0808	0.0138	0.1557	0.0643
0.2455	0.0480	0 0088	0.1565	0.0670
0.3049	0.0305	0.0046	0.1545	0.0600
0.3636	0.02025	0.00365	0.1501	0.0638
0.4241	0.0155	0.00265	0.1530	0.0632
0.4858	0.01195	0.0025	0.1539	0.0704
0.6093	0.00758	0.0017	0.1536	0.0728
0.7345	0.00526	0.0012	0.1545	0.0736
0.9877	0.00283	0.0008	0.1525	0.0812
1.2425	0.00180	0.00055	0.1528	0.0846

[a]Cell hydrogen pressure, 1 atm; temperature, 648 ± 0.5°K; electrode area, 0.345 cm^2; LiH concentration, 25.68 m/o.

More complex results were obtained using Armco iron flag electrodes. They indicated that interactions of the iron electrode with the melt and with hydrogen caused surface roughening of the electrode, which complicated the interpretation of the results.

We can conclude from the steady-state current-voltage results that the rate of the cathodic reduction of hydrogen on Armco iron in LiCl-KCl at 648°K is determined by the activation overvoltage (or some coupled chemical step) involving a one-electron process, and has a value of α of 0.44, and an exchange current density near 1 mA/cm^2.

The anodic oxidation of LiH to H_2 was diffusion-controlled under all conditions studied and involved one electron per LiH, as might be expected. The diffusion coefficient of LiH in LiCl-KCl eutectic at 648°K from chronopotentiometric measurements with a tungsten flag electrode was 1.67×10^{-5} cm^2/sec.

The results discussed above indicate that a high roughness factor would be desirable on the electrolyte side of the iron foil in LiH cells using an iron diffusion cathode, particularly if current densities in excess of 100 mA/cm^2 are desired.

E. Studies of Cells, Regenerators, and Systems

1. Lithium Hydride Galvanic Cells

a. Cell Studies. Examination of candidate systems for use as energy-conversion devices has shown that the lithium hydride regenerative cell is an attractive choice because it fulfills most of the requirements stipulated for such devices: (1) Lithium hydride readily decomposes below 1300°K, an arbitrary temperature limit that was imposed primarily because, at higher temperatures, strength, physical properties, and corrosion resistance of most materials are seriously affected. (2) Lithium hydride decomposes to give only two products--liquid lithium and gaseous hydrogen-- a feature that makes for ease of separation in the regenerator. (3) The cell-reaction product, LiH, is readily soluble in lithium halide salts and is highly conducting; the latter characteristic provides for a low-resistance overvoltage.

Inherent in the early work on lithium hydride cells were the problems encountered in using porous metal as the hydrogen cathode. Porous-metal electrodes suffer from a variable catalytic activity at the surface of the porous metal and from alternate flooding of the pores by hydrogen gas and fused salt. The use of a hydrogen-permeable membrane as the cathode eliminates these problems. The quantity of hydrogen diffusing through a metal diaphragm is proportional to the difference in the square roots of the hydrogen pressure on each side of the diaphragm.

The quantity of hydrogen diffusing through a 0.025-cm-thick vanadium diaphragm at 773°K is $0.50(p_1^{1/2} - p_2^{1/2})$ Amp/cm^2, where p_1 and p_2 are the hydrogen pressures (in atmospheres) on each side of the diaphragm. The voltage loss for a reversible electrode is

$$\Delta E = -\frac{RT}{2N} \ln \frac{p_1}{p_2} = -\frac{RT}{NF} \ln \frac{p_1^{1/2}}{p_1^{1/2} - \frac{i}{i_L}} \tag{142}$$

where i_L is related to the theoretical current density for a permeable diaphragm and is equal to 0.50 Amp/cm^2 for a 0.025-cm-thick vanadium diaphragm held at 773°K. (At this temperature 3.5 cm^3/min-cm^2 permeates the vanadium diaphragm at a pressure difference of 1 atm to vacuum.) With this relationship, the voltage loss may be as great as 0.1 V for a cell operating at a differential hydrogen pressure of 0.5 atm (to vacuum) and a 100-mA/cm^2 current density. Thus, to maintain a high output voltage from the cell, the cathode should be operated with as high a pressure difference (to vacuum) as practical. Hence, if low regeneration pressures are used, pumps will be needed to bring the hydrogen pressure up to 1 atm or more. Such P-V work could be a severe drain on the cell efficiency, a large fraction of the cell energy conceivably being used for pumping.

To date, practical cell studies have been of a limited nature. A lithium hydride cell with a vanadium diaphragm (see Fig. 102) was operated for 540 hr at 800°K giving current densities that exceeded 200 mA/cm^2 at one-half open-circuit voltage (0.3 V). These data are displayed in Fig. 103 as cell voltage versus current density. Even though this current density is only about one-half the theoretical current density, it was achieved without any high-temperature pretreatment of the metal diaphragm. Most recently, emphasis has been placed on 0.005-cm vanadium diaphragms using the ternary electrolyte LiH-LiCl-LiI, which melts at 614°K.

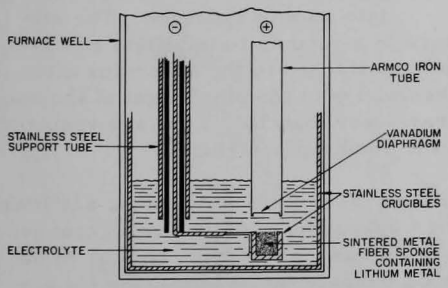

308-613

Fig. 102. Lithium Hydride Cell with a Vanadium-diaphragm Cathode

Data for two cells using thin vanadium diaphragms are shown in Fig. 104, where cell voltage is plotted as a function of current density. The two runs differ significantly in their total internal cell resistance: for experiment 1, the internal resistance was 5.5 ohm-cm^2; for experiment 2, the resistance was 1.42 ohm-cm^2.

The total overvoltage of the cell is made up of (a) the activation overvoltage, (b) the electrolyte ohmic loss, and (c) the concentration

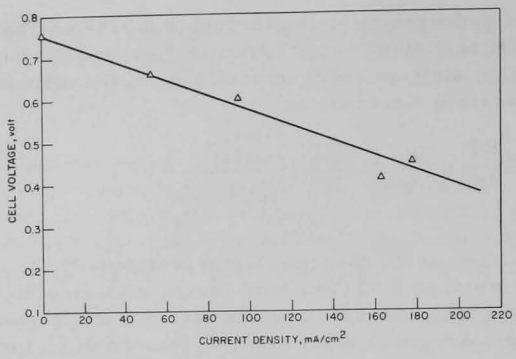

308-615 Rev. 1

Fig. 103. Current Density-Voltage Curve for a Lithium Hydride Cell with a 0.025-cm Vanadium-diaphragm Cathode at 808°K

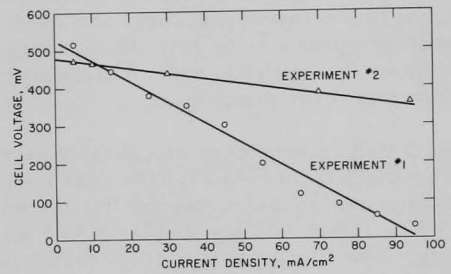

308-528 Rev. 1

Fig. 104. Current Density-Voltage Curve for a Lithium Hydride Cell with a 0.005-cm Vanadium-diaphragm Cathode at 698°K

overvoltage. The greatest voltage losses for the lithium hydride cell are probably due to an overvoltage at the hydrogen electrode associated with the dissociative adsorption of hydrogen. The difference between the two experiments of Fig. 104 is attributed primarily to the technique used for activation of the diaphragm. The activation procedure is designed to remove any oxide layer present on the gas side of the diaphragm, thereby presenting a clean surface for the dissociation of molecular hydrogen into atomic hydrogen. The diaphragm is heated to a high temperature in a vacuum to facilitate removal of the oxide layer. A diffusion pump was attached to the apparatus after the first experiment. The results observed with the diaphragm of the second experiment indicate that pressures lower than 10^{-4} Torr are required for removal of the oxide layer from the diaphragm surface.

Current densities of the order of 300 mA/cm^2 at 620°K are theoretically obtainable for vanadium diaphragms of 0.005-cm thickness. The experimental results are only preliminary, and much remains to be accomplished. However, the results do indicate the possibilities for a lithium-hydrogen cell using a thin vanadium diaphragm.

b. Regeneration Considerations. An attractive feature of the lithium hydride cell system is the apparent ease of regeneration. Literature data[109] indicate that, at 1173°K, pure lithium hydride readily dissociates

to yield an equilibrium hydrogen gas pressure of 1 atm. The relatively low temperature and ease of separation of the gas-liquid metal cell reactants make for convenient operation in a thermally regenerative cell system.

The regenerator dissociates the cell product (lithium hydride) into the reactants (lithium and hydrogen), which may then be returned to their electrode compartments for completion of the cycle. Studies on regeneration conditions should determine the characteristics of the reactions and processes involved in this phase of the lithium hydride cell.

The work on the emf studies of the hydrogen-hydride systems in solutions saturated with lithium hydride was extended to unsaturated solutions. Once the standard emf of the reaction $Li(\ell) + \frac{1}{2}H_2(g) = LiH(s)$ had been determined as a function of temperature, the activity of lithium hydride could be obtained in unsaturated electrolytes of similar cells. After we determined the activity of lithium hydride, we used the Nernst equation,

$$\underset{\sim}{E} = \underset{\sim}{E}^\circ - \frac{\underset{\sim}{R}T}{N\underset{\sim}{F}} \ln \frac{a_{LiH}}{a_{Li}p_{H_2}^{1/2}}, \tag{143}$$

to calculate the hydrogen equilibrium pressure at each temperature and composition. Substituting $a_{Li} = 1$ for pure lithium metal and $\underset{\sim}{E} = 0$, so that the calculations will give the hydrogen equilibrium pressures, Eq. 143 reduces to

$$2\left(\ln a_{LiH} - \frac{N\underset{\sim}{F}\underset{\sim}{E}^\circ}{\underset{\sim}{R}T}\right) = \ln p_{H_2}. \tag{144}$$

The equation relating the standard cell emf to temperature,

$$\underset{\sim}{E}^\circ = 0.9081 - 7.699 \times 10^{-4}\, T, \tag{145}$$

was extrapolated to 1173°K to estimate the hydrogen equilibrium pressure at temperatures near expected regeneration conditions. The data are shown graphically in Fig. 105 where the logarithm of the hydrogen pressure is plotted as a function of the reciprocal of the absolute temperature. For a solution containing 30.2 m/o lithium hydride, a dissociation pressure of 129 Torr H_2 was calculated for 1173°K.

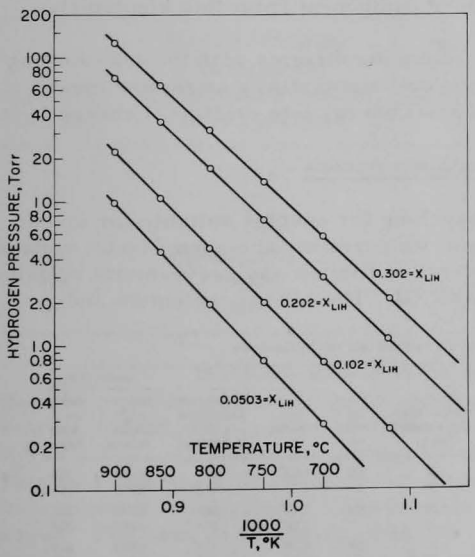

108-8520 Rev. 2

Fig. 105. Calculated Equilibrium Hydrogen Pressure for LiH-LiCl Mixtures

Although no specific design work to define a particular regeneration system has been carried out, some possibilities in equipment design are worth considering. Separation of the hydrogen gas from the liquid metal-electrolyte mixture and separation of the lithium from the electrolyte are required. Both separations can be made[146] using a compact gas-liquid-liquid separator, a cylinder in which the liquid-gas mixture is introduced tangentially at a high velocity. Beneath the cylindrical section is a conical chamber. The gas is removed at the base of the cone, the heavier liquid is removed from the side, and the lighter liquid is removed from the apex.

Using the high permeability of hydrogen gas through certain metals at regeneration temperatures helps to simplify the regenerator problems. A metal diaphragm can be used to separate the hydrogen-gas component from the electrolyte vapor that is present at a finite pressure in the regenerator. Thus, pure hydrogen can be returned to the cathode.

In choosing the LiH-LiCl-LiI electrolyte system (ternary eutectic melting at 614°K), we gained a number of advantages because of the lower cell-operating temperature. Cell voltages will be significantly higher (see Fig. 63). At saturation of the electrolyte with respect to lithium hydride, 625°K, the cell voltage is 0.43 V. Regeneration pressures can be increased significantly by sending to the regenerator a mixture very rich in lithium hydride (90-95 m/o LiH). Such a mixture can be obtained by precipitating lithium hydride as a pure component from this electrolyte.

The use of thin vanadium diaphragms with the low-melting electrolyte makes the lithium hydride cell a potentially attractive means for the continuous conversion of thermal energy into electrical energy.

2. Bimetallic Cells with Lithium Anodes

a. Cell Studies. In searching for couples suitable for use in a bimetallic cell with a lithium anode, we examined the open-circuit voltage characteristics of some binary systems of lithium and heavy-metal systems. The results are presented in Table XXXII. The lithium-selenium and

TABLE XXXII. Calculated Characteristics of Bimetallic Cells with Lithium Anodes

Anode Metal										Specific Energy	
Metal	Atomic Weight	Melting Point, °K	Amp-hr/g	Amp-hr/cm³	Cathode Metal	Cathode Alloy Concentration, a/o Li	Cell Temp, °K	Cell Potential, V	Cathode-metal Requirement, g per g Anode Metal	Watt-hr per g Active Material	Watt-hr per lb Active Material
Li	6.94	381.6	3.89	1.90[a] (at 673°K)	Bi	20	800	0.813[b]	120	0.0316	14.3
						30		0.765	70.9	0.0421	19.1
					Sn	20	800	0.634[c]	68.4	0.0359	16.2
						30		0.580	39.4	0.0558	25.2
					Te	20	798	1.72[d]	73.6	0.0905	41.0
						30		1.68	42.5	0.150	68.0
					Se	10	853	1.91[e]	102.4	0.0718	32.5
						30		1.90[f]	26.6	0.268	122.0

[a]Density data from Liquid Metals Handbook.[86]
[b]Ref. 16.
[c]Ref. 17.
[d]Ref. 64.
[e]Ref. 23.
[f]Estimated.

lithium-tellurium couples are attractive because of the high voltages developed and their high specific energies. The lithium-tin system shows the greatest promise for thermal regeneration since tin has a much lower vapor pressure[38] than any of the other cathode metals. Exploratory studies of the voltage-current density characteristics were made of these and other systems to select the ones most suitable for further study.

The cells used for preliminary voltage-current density measurements contained the molten eutectic mixture of 41 m/o KCl-59 m/o LiCl (melting point 625°K) as the electrolyte. As discussed previously (Section V.A), the voltages obtained from cells with lithium anodes and this electrolyte may be somewhat low, especially above 773°K. Since the cells reported here were operated at 741-766°K, probably the lowering of the cell voltages is negligible. The cathode metals used and the highest-melting intermetallic compounds formed between lithium and the various cathode metals are shown in Table XXXIII. The melting points were taken from Hansen and Anderko.[29] These systems show a large interaction energy as indicated by the large difference between the melting points of the elements and the highest-melting intermetallic compounds. Table XXXIII also indicates the open-circuit cell voltages at essentially the full-charge condition (very little lithium in the cathode alloy).

TABLE XXXIII. Discharge Voltage-Current Characteristics of Lithium-anode Bimetallic Cells

Cathode Material	Highest Melting Intermetallic Compound Formed with Lithium	Melting Point of Compound, °K	Open-circuit Cell Voltage, V	Cell Temp, °K
Te	Li_2Te	Unknown	1.93	769 ± 5
Bi	Li_3Bi	1418	0.93	762 ± 2
Sn	Li_7Sn_2	1056	0.73	723 ± 10
Pb	$Li_{10}Pb_3$	999	0.69	756 ± 9
Zn	Li_2Zn_3	793	0.67	741 ± 6
Cd	LiCd	822	0.66	766 ± 20

In the cell experiments, a 4.60-cm-diam tantalum crucible was used to contain the cathode metal and the electrolyte when the cathode metal was Bi, Cd, Pb, Sn, or Zn. The interelectrode distance was varied from 1.5 to 3.3 cm. The molten-lithium anode was contained in an Armco iron ring as a floating disk on the top of the electrolyte. Figure 106 shows the experimental arrangement. These cells were operated under a blanket of argon. The area of the anode, 4.46 cm^2, was used to calculate the current densities shown in Fig. 106. For the tellurium cathode, the tantalum container was not satisfactory and was replaced with one of Vycor. Electrical contact with the tellurium was made using a platinum wire. The Vycor

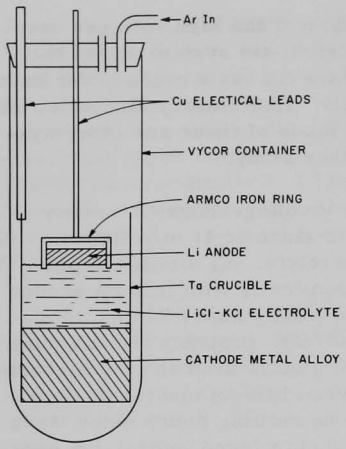

308-508

Fig. 106. Schematic Diagram of the Lithium-containing Bimetallic Cell Used in Voltage-Current Density Measurements

container was satisfactory for only about two days, after which it cracked during operation, probably because of lithium attack.

Figure 107 shows the discharge voltage-current density characteristics of Li-Sn, Li-Bi, Li-Cd, Li-Pb, Li-Te, and Li-Zn cells. These curves indicate the high current densities available from bimetallic cells.

On the basis of these preliminary experiments, the lithium-tellurium cell was selected for further study because it exhibited high voltage and excellent current-density capabilities.[116] Before constructing cells for more detailed studies, however, we had to resolve some problems. The corrosive qualities of tellurium and its alloys pose containment difficulties; because of the low conductance of tellurium, the cathode area must be maximized; there is a possible hazard due to the toxicity of tellurium.

From the rather sparse data on solubilities of metals in tellurium, it was discovered that pure iron has a low solubility in tellurium, while nickel is soluble to a considerable extent.[29] Also, preliminary results of corrosion tests at 728°K showed that iron was only slightly attacked in tellurium, while Type 304 stainless steel, which contained nickel, was readily attacked.[147]

Using this information, we constructed[148] the lithium-tellurium secondary cell shown in Fig. 108. The cathode cup, 3.7-cm ID by 2.2 cm high, was fabricated from Armco iron. To compensate for the low electrical conductance of tellurium, the cathode was designed with an annular fin, which served as a current collector. Two anode-metal retainer-current collectors, having geometric areas of 3.9 and 10 cm^2, were made from Type 316 stainless steel. The quantities of lithium and tellurium used in the cell were varied, but the maximum Li:Te ratio corresponded to 30 a/o lithium in tellurium in the cathode alloy at complete discharge. The maximum theoretical capacity of the cell was 9.55 Amp-hr. Although the electrolyte, LiF-LiCl-LiI eutectic, has a melting point of 614°K, the melting point of tellurium (723°K) determined the minimum operating temperature of the cell. Usually the cell was operated in the range 740-773°K. All experiments were performed in a high-purity helium atmosphere.

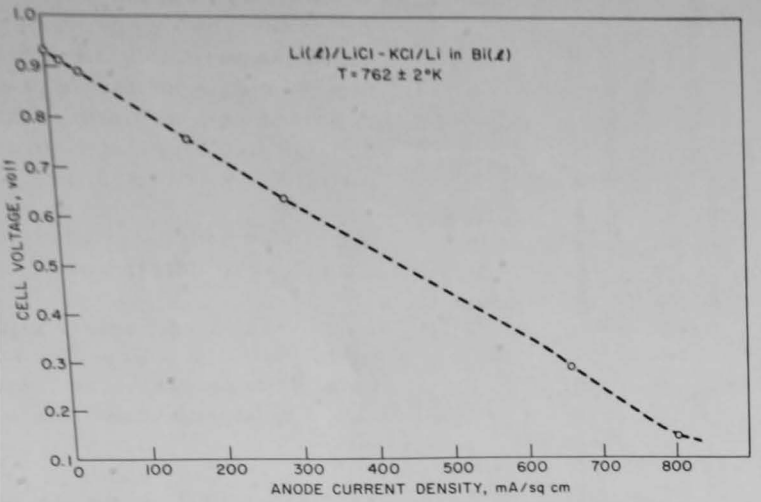

108-9869 Rev. 2

(a) Lithium-Bismuth, T = 762 ± 2°K

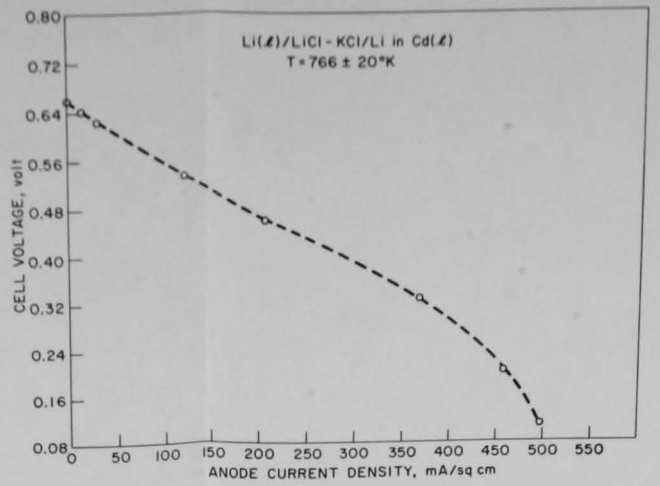

108-9870 Rev. 1

(b) Lithium-Cadmium, T = 766 ± 20°K

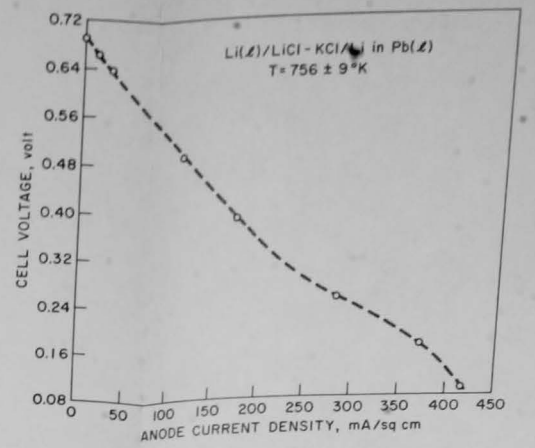

108-9871 Rev. 1

(c) Lithium-Lead, T = 756 ± 9°K

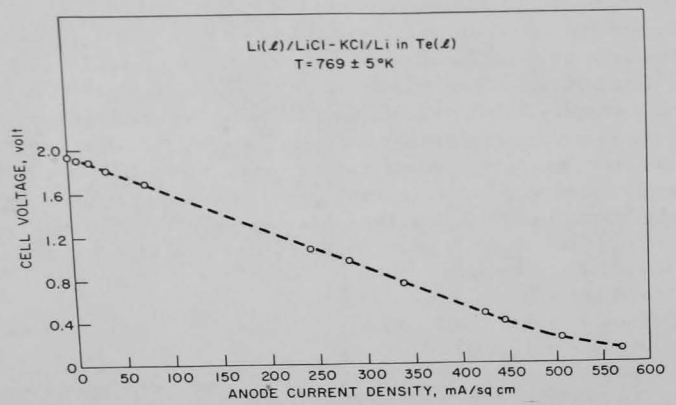

108-9872 Rev. 1

(d) Lithium-Tellurium, T = 769 ± 5°K

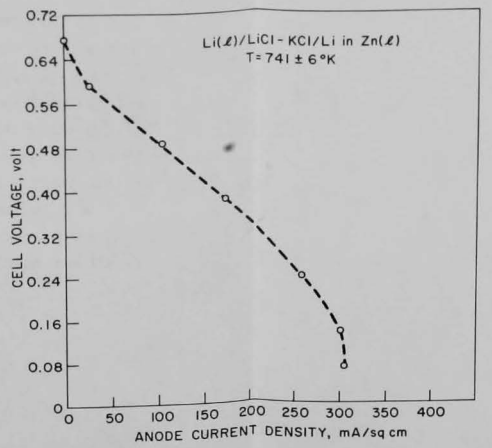

108-9873 Rev. 1

(e) Lithium-Zinc, T = 741 ± 6°K

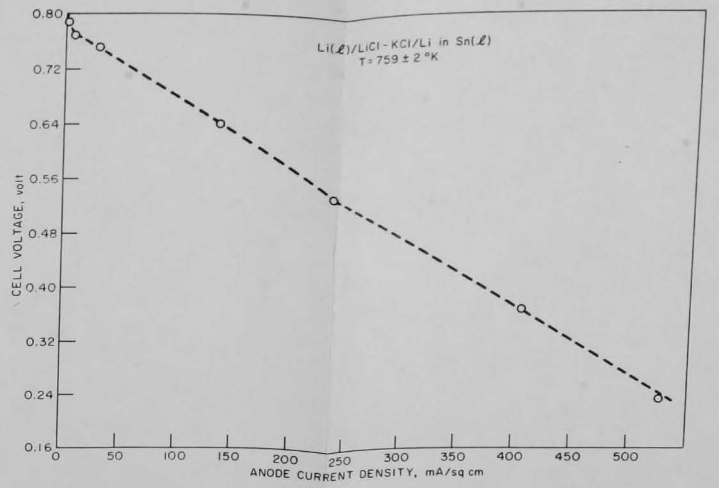

108-9886 Rev. 1

(f) Lithium-Tin, T = 759 ± 2°K

Fig. 107. Voltage of Lithium-containing Bimetallic Cells as a Function of Current Density; Electrolyte: LiCl-KCl

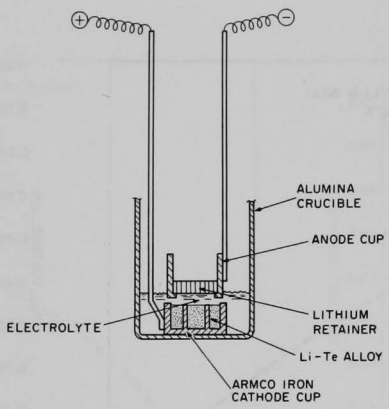

308-584 Rev. 1

Fig. 108. Experimental Lithium-Tellurium Cell (Schematic Representation)

The current-voltage measurements were carried out with the aid of a dc power supply, precision ammeters and voltmeters (0.25%), and a set of heavy-duty variable resistors. All results are reported on a resistance-included basis. Separate voltage- and current-measuring terminals were used.

Two kinds of current-voltage curves were determined:

(1) Steady-state curves, starting in the fully charged condition for the discharge curve, and starting in the fully discharged condition for the charge curve.

(2) Short-time discharge curves. These data were taken a few seconds after the start of current flow from the fully charged condition, and represent nearly maximum performance, corresponding to a low concentration of anode metal in the cathode alloy (about 5 a/o lithium in tellurium).

Figure 109 shows typical current-voltage curves for lithium-tellurium cells operated at 743°K. These data correspond to steady-state curves at a cathode alloy composition of 20 a/o lithium in tellurium. Current densities in excess of 7 Amp/cm^2 were obtained on both charge and discharge. This indicated that practical cells based on this system could be charged in 15 min or less. Similar results were obtained with both anodes (3.9 and 10 cm^2), which indicated that there was no significant difference in behavior at the cathode between these two runs. Since both the charge and discharge curves are straight lines, only small concentration and activation overvoltages are expected to be present; the largest losses are resistive in nature.

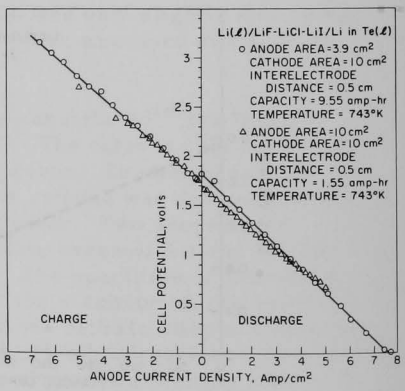

308-621 Rev. 1

Fig. 109. Steady-state Voltage-Current Density Curves for a Lithium-Tellurium Cell at 743°K

The slopes of the discharge curves of Fig. 109 correspond to 0.021 ohm for the cell with the 10-cm^2 anode, and 0.061 ohm for the cell with the 3.9-cm^2 anode, both with interelectrode distances of approximately 0.5 cm. The calculated resistances

of the electrolyte were 0.013 and 0.033 ohm for the 10- and 3.9-cm^2 anode cells, respectively, based on an estimated resistivity of 0.26 ohm-cm for the lithium halide electrolyte. The discrepancy between the calculated electrolyte resistance and the observed cell resistance is attributed to the resistance of the cathode alloy and the current collectors.

The cell design was modified to improve performance in a lithium-tellurium cell with a 10-cm^2-area anode. The cathode cup now had a three-turn spiral-fin current collector made from a strip of 6-mm-high, 1-mm-thick Armco iron. Also, the anode current collector was provided with lower-resistance leads. This cell had a theoretical capacity of 1.55 Amp-hr.

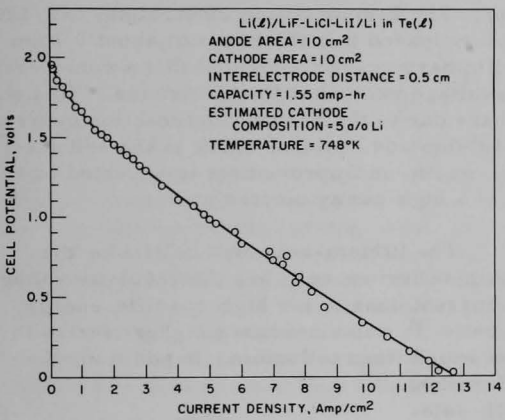

308-622 Rev. 1

Fig. 110. Short-time Voltage-Current Density Curve for a Lithium-Tellurium Cell at 748°K

Figure 110 is a typical discharge curve for this improved cell. The cell was charged between data points, and the data were taken within several seconds after discharge started. Because of this procedure, the lithium content of the cathode was kept low--about 5 a/o lithium in tellurium. A current density of 7 Amp/cm^2 was obtained at 0.7 V, corresponding to a power density of 4.9 W/cm^2, including resistance losses. The maximum current density observed was 12.7 Amp/cm^2. The maximum temperature rise observed during the high current-density discharges was 30 Kelvin degrees.

Figure 111 shows the constant-current charge and discharge voltage-capacity curves for this cell at 753°K. The curve marked "0 Amp" shows the open-circuit voltage as a function of time (upper abscissa); the other curves show the terminal voltage of the cell as a function of charge accepted or delivered at various constant charge and discharge rates. The plateau voltages of Fig. 111 correspond to some of the points on the curve shown in Fig. 109; the initial voltages at the ordinate of Fig. 111 correspond approximately to the voltages shown in Fig. 110.

The constancy of the voltages in Fig 111 is a unique characteristic of the lithium-tellurium cell. This behavior is in contrast to that of the sodium-bismuth cell, where a more distinct decrease of cell voltage with discharge was observed, particularly at high current densities.[7]

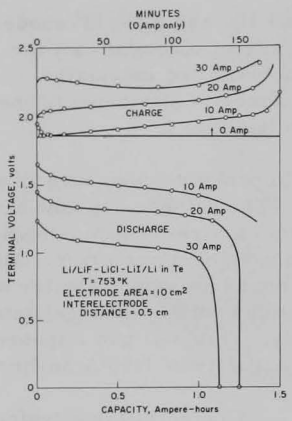

308-623 Rev. 1

Fig. 111

Constant-current Voltage-Capacity Curves for a Lithium-Tellurium Cell at 753°K

After test periods of up to 300 hr at 723-773°K, the electrolyte showed no degradation.

In addition to the open-cell experiments, a closed lithium-tellurium cell has been operated. The cell proper, a diagram of which appears in Fig. 112, was made of stainless steel in which Armco iron cups were inserted for the tellurium and the lithium. The iron lithium retainer was prewetted with lithium at 820°K before installation. The lithium halide electrolyte, LiF-LiCl-LiI, was loaded to a thickness of about 0.7 cm. Preliminary results indicated that a considerable overvoltage existed at the electrodes. This was perhaps due to the result of interaction between the lithium and residual water in the salt electrolyte. Again, an improvement is expected by the use of a high-purity electrolyte.

The lithium-selenium cell, like the lithium-tellurium cell, has the requisite voltage and current density for high-specific-energy, high-specific-power secondary cells.[149] Selenium has a higher electronegativity and a lower equivalent weight than tellurium. In addition, the melting point of selenium, 490°K, makes it possible to operate cells with selenium cathodes at temperatures below 570°K. A problem is posed, however, by the low electrical conductance of selenium, but provision of a metallic network for current collection from the lithium-selenium alloy cathode seems to have overcome this difficulty.

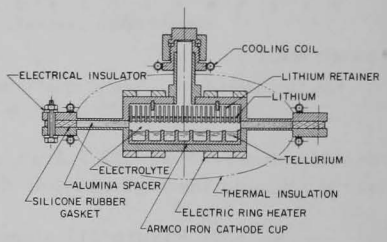

308-603

Fig. 112. Cross Section of Lithium-Tellurium Cell

An experimental lithium-selenium cell, similar in design to the lithium-tellurium cell shown in Fig. 108 was constructed. The cathode cup, 3.5-cm ID x 0.48 cm high (geometrical area = 10 cm^2), was built using Armco iron, a material found adequately resistant to corrosion by selenium under the conditions of these experiments. The anode-metal retainer-current collector was made of 1-mm Type 316 stainless steel sheet wound in a spiral (geometrical area = 3.9 cm^2). The amounts of lithium and selenium in the cell were varied with a maximum of 60 a/o lithium in selenium in the cathode alloy at complete discharge. The LiF-LiCl-LiI eutectic, which melts at 614°K, was used as the electrolyte for most of the experiments. Other electrolytes tested include the eutectic of LiCl-LiI-KI (m.p. = ~538°K) and that of

LiCl-KCl-CsCl (m.p. = ~538°K). The minimum cell-operating temperature was set by the melting point of the electrolyte. The current-voltage measurements were carried out in the same manner as those described for the lithium-tellurium cell above, and again all results are reported on a resistance-included basis. The experiments were performed in a high-purity helium atmosphere.

Because of the low electrical conductance of selenium, an Armco iron network was provided in the cathode to aid in current collection. Three types of networks have been tested; these networks are formed by the addition of iron filings, iron turnings, or iron wires to the cathode alloy. The ratio of the filings to the selenium was varied from 24.4 to 60 w/o iron. Only one weight ratio, 30 w/o iron, was tried with the turnings. The 0.0338-cm-diam x ~2-in.-long iron wires were inserted in the cathode as bundles; the ratio of iron to selenium was about 30 w/o when the wires were used. Figure 113 shows typical voltage-current density curves for cells with and without an iron network in the cathode. Considerable improvement was observed when iron was added to the cathode, the cell containing turnings giving better performance than the cell with filings. The best cell performance, however, was obtained when iron wires formed the current-collecting network. For the cell containing iron wires, an open-circuit voltage of 2.08 V and a short-circuit current density of 8.7 Amp/cm^2 were obtained; the maximum power density was 3.4 W/cm^2 at 0.8 V. Furthermore, less iron was required to achieve the same performance improvement when wires rather than filings or turnings were used.

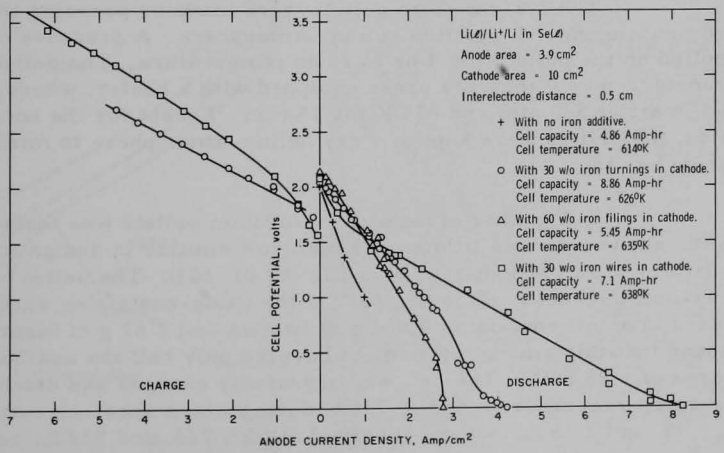

308-959

Fig. 113. Current Density-Voltage Characteristics of Lithium-Selenium Cells with and without Iron Additives in the Cathode

The performance of the lithium-selenium cell is similar to that of the lithium-tellurium cell. Also, since selenium has a lower atomic weight than tellurium (78.96 versus 127.6), a lithium-selenium secondary cell may weigh significantly less than a lithium-tellurium secondary cell of the same power and energy rating.

An outstanding potential advantage of this cell, low operating temperature, has not been fully realized because the electrolyte showing the best performance in the lithium-selenium cell thus far is the eutectic mixture of LiF-LiCl-LiI. Further work will be done using lower melting electrolytes.

b. Cells and Batteries with Immobilized Electrolytes. Because of the advantages of immobilized electrolytes over the liquid electrolyte pointed out in Section IV.D.1.b, paste electrolytes containing LiF-LiCl-LiI eutectic and an inert filler have been studied.

To prepare the paste electrolyte, a 50 w/o-50 w/o mixture of LiF-LiCl-LiI eutectic (m.p. = 614°K) and inert ceramic filler was held at 773°K for 17 hr in a dry helium atmosphere. The product was then crushed at room temperature in a hermetically sealed ball mill and sieved to obtain a fine powder with an average particle diameter of less than 88 μ. This powder was pressed into paste electrolyte pellets; two sizes of cylindrical pellets, 2.5 and 1.9 cm in diameter, were made.

The 1.9-cm-diam pellets were made by pressing the powder mixture in a die under a purified helium atmosphere. A pressure of 700 atm was applied on the pellets for 3 hr at room temperature. The pellets were then transferred to a separate press equipped with a heater, where they were pressed in air at 550 atm and 673°K for 15 min. Except for the hot-pressing operation, the pellets were kept in a dry helium atmosphere to minimize contamination by air.

The quality of these 1.9-cm-diam pellets was tested by using one as the electrolyte in a lithium-bismuth cell similar in design to one cell of the battery shown schematically in Fig. 58 (p. 103). The pellet was filed to a 3.43-mm thickness, removing part of the oxide-containing surface zones, and placed in a cell containing 0.064 g of lithium and 2.67 g of bismuth. (We later found that this amount of bismuth covered only half the available electrode area of 1.98 cm^2.) The cell was repeatedly charged and discharged at temperatures ranging from 653 to 758°K during which short-circuit currents of 1.7, 1.85, and 2.15 Amp were observed at 653, 726, and 758°K, respectively. An electrolyte resistance of approximately 0.88 ohm, corresponding to a specific resistance of 5.8 ohm-cm at 726°K, was estimated from the results. Although these results are preliminary, the resistivity is much higher than anticipated.

The 2.5-cm-diam pellets were pressed in a manner similar to that for the 1.9-cm-diam pellets, except that the final hot-pressing operation was not performed. Instead, the pellets were sintered at 673°K for 1 hr in an inert atmosphere. A lithium-tellurium cell was assembled to test a 2.5-cm-diam pellet which had been filed to a 3-mm thickness. The cell was loaded with 0.20 g of lithium and 5.44 g of tellurium. To facilitate current collection, we placed 3.65 g of iron wires in the cathode compartment. The effective electrode area was 3.25 cm^2, which was completely wetted by both lithium and tellurium. The cell was repeatedly charged and discharged at temperatures ranging from 460 to 475°C, during which short-circuit currents up to 7 Amp (current densities of up to 2.1 Amp/cm^2) were observed. A paste resistance of approximately 0.244 ohm or a specific resistance of 2.6 ohm-cm was estimated from the results over the temperature range 733-748°K. The cell developed a short circuit after approximately 50 hr of operation. Examination of the cell on disassembly disclosed that the seal area of the pellet had developed hairline cracks through which the liquid metal had penetrated, causing the short circuit. It was concluded, therefore, that the hot pressure method, which yields stronger pellets, would be more suitable for paste electrolyte preparation. Further efforts on the minimization of air contamination are expected to yield electrolytes of much lower specific resistance.

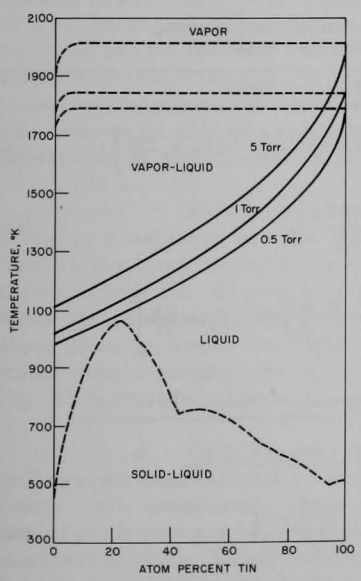

308-629 Rev. 1

Fig. 114. Estimated Vapor-Liquid Equilibrium Relationships for the Lithium-Tin System

c. Regeneration Systems.

General design considerations for bimetallic cell systems were discussed in Section IV.D. The equations derived for mass and heat balances, cathode-metal circulation, and mass and heat transfer also apply to bimetallic cell systems with lithium anodes. Because of the low vapor pressure of lithium, the regenerator must be designed to perform at low pressures. The lithium-tin system illustrates this problem. The liquid-vapor phase relationships, calculated from thermodynamic data of Foster[150] were used to estimate system pressures; Fig. 114 shows the results. As was pointed out in Section IV.A, eliminating overlap of the liquid-vapor loop and liquid-solid hump is essential. Therefore, the lowest practical regeneration temperature for a composition of about 30 a/o Li in Sn is approximately 1400°K with an estimated system pressure of 0.5 Torr or less. This may be compared with 5 Torr at 1043°K for a 30 a/o Na-70 a/o Pb system (see Section IV.A).

In a flow system such as the regenerator-condenser section of a thermally regenerative bimetallic cell system, energy must be dissipated to overcome the viscous frictional loss. The energy so dissipated is, in general, manifested as a pressure drop in the direction of the vapor flow. Equations describing the pressure and temperature changes of the vapor flow in a straight regenerator tube have been derived for a variety of cases. These include:

(1) Isothermal, with frictional loss and heat transfer without phase change.

(2) Adiabatic, with frictional loss without phase change.

(3) Nonisothermal with friction, heat transfer, and phase change.

Table XXXIV summarizes these equations. They were derived under the assumptions that: (1) the vapor obeys the ideal-gas law, (2) the flow is in the continuum regime, and (3) the flow is laminar. In addition, the absence of entrainment (i.e., carryover of liquid droplets by the vapor) and the absence of inert gas in the vapor are assumed. Since the vapor temperature will be high (>1100°K) while the pressure is low (<1 atm), the application of the ideal-gas law is justified. As far as flow regimes are concerned,

TABLE XXXIV. Pressure and Temperature Changes of the Vapor Flow in a Straight Regenerator Tube

	Pressure Drop	
1. Isothermal, with friction and heat transfer; no phase change	$P_2^2 - P_1^2 = -8\,\frac{G\underset{\sim}{R}}{Dg_c}\left[\frac{h(\zeta - 1)}{\zeta\underset{\sim}{R}}(T_w - T_v) + T_v\,\frac{8\nu\rho}{D}\right]\Delta L$	(146)
2. Adiabatic, with friction; no phase change	$P_2^2 - P_1^2 = -64\,\frac{\nu\rho G\underset{\sim}{R}\overline{T}_v}{D^2 g_c}\,\Delta L$	(147)
3. Temperature change, with friction and heat transfer; with phase change	$P_2^2 - P_1^2 = -\frac{8G\underset{\sim}{R}\overline{T}_v}{Dg_c}\left[\left(\frac{2h}{\Delta\underset{\sim}{H}_v}\right)(\overline{T}_w - \overline{T}_v) + \frac{8\nu\rho}{D}\right]\Delta L$	(148)
	Temperature Change	
1. Isothermal, with friction and heat transfer; no phase change	No change	
2. Adiabatic, with friction; no phase change	$\frac{1}{T_2^2} - \frac{1}{T_1^2} = 64\,\frac{\zeta - 1}{\zeta}\cdot\frac{G^3\underset{\sim}{R}^2\nu\rho\Delta L}{\overline{P}^4 D^2 g_c^2}$	(149)
3. Temperature change, with friction and heat transfer; with phase change	$\int_1^2 \frac{dT_v}{(T_w - T_v)\,T_v^2} = -\frac{4(\zeta - 1)\,G\underset{\sim}{R}h\Delta L}{\Delta\underset{\sim}{H}_v\zeta\overline{P}^2 Dg_c}$	(150)

the criteria are not clearly established. However, the fact that the smallest dimension of the equipment is larger than the mean free path of molecules justifies the assumption of continuum flow. For example, in the lithium-tin system with a system pressure of 0.5 Torr, the mean free path of a lithium vapor molecule is 7.2×10^{-3} cm at 1320°K, which is considerably less than the smallest dimension of the regenerator. To verify the assumption of laminar flow, the Reynolds number was calculated as follows: If the regeneration rate is equivalent to a current density of 10 Amp/cm^2, a lithium vapor flow rate of 2.57 g/(cm^2-hr) is required. Taking 7.5×10^{-5} g/(cm-sec)* as the viscosity of lithium vapor at 1320°K and 5 cm as a regenerator diameter, we obtain a Reynolds number of 47.6. This value indicates that the flow is well under the critical Reynolds number of 2000 and in the laminar regime.

In an ideal regenerator-condenser system, heat from the vapor is removed only in the condenser and not at the regenerator wall. Therefore, the regenerator vapor section, which should be well insulated, can be considered to be an adiabatic system. Thus, Eqs. 147 and 149 apply. For a typical lithium bimetallic cell regenerator with 5-cm ID and 30-cm length, the pressure at the condenser becomes 0.466 Torr with an average vapor temperature of 1320°K and with a vapor pressure at the evaporation surface of 0.5 Torr. For isothermal flow, the pressure drops can be more or less dependent upon the heat transfer, as can be seen from Eq. 146. In practice, the temperature of a vapor drops as it flows, and partial condensation may take place in the regenerator vapor section; this is undesirable from the viewpoint of corrosion and energy losses. Additional heat sources may have to be placed around the regenerator vapor section to prevent condensation. In such a case, Eqs. 148 and 150 must be solved simultaneously.

Several regenerator designs have been suggested and three of these, illustrated in Figs. 57-59, were discussed in Section IV.D. In contrast to the linear arrangement of the condenser section of the regenerator shown in Fig. 56, the regenerator in Fig. 57 has a very short distance between the evaporating surface and the condenser area and provides a large vapor passage area. Currently, a study to determine mass, heat, and momentum-transport characteristics in a system such as that shown in Fig. 57 is underway.

d. Cell-regenerator Systems. The lithium-metal bimetallic cell system represented schematically in Fig. 54 consists of four components: cell, regenerator, heat exchanger, and vapor condenser. The function of each component and the flow of liquid and vapor in this system are identical to those in the sodium cell system. However, the regenerator temperature will probably be higher, about 1500°K, while the cell temperature may be as low as 614°K, the melting point of the LiF-LiCl-LiI eutectic electrolyte. The system pressure will also be low, in the range of 0.5 Torr.

*Calculated from the Hirshfelder's equation using the Lennard-Jones (6-12) potential and corrected for variable molecular weight of lithium vapor.

The exact operating temperatures and pressures would depend upon the properties of the cathode alloy and the fused-salt electrolytes, and upon the corrosion resistance of the container materials. Several auxiliary components, such as those discussed in Section IV.D, are also needed for the laboratory-model system.

Requirements for ideal cell systems include low irreversible losses, optimum rate processes, and high reliability. Because of the low solubility of lithium in lithium halide electrolytes, a much lower self-discharge rate is expected for lithium cells than for other cells with alkali-metal anodes. Reasonable goals for thermally regenerative bimetallic cells with lithium anodes are as follows:

Cell current density	500 mA/cm^2
Single-cell open-circuit voltage	0.8 V
Current efficiency	90%
Voltage efficiency	50-70%
Overall thermal efficiency	15-21%
Dependable operating life	$1\frac{1}{2}$ yr
Specific power	10 W/lb

The lithium anode bimetallic system may present unique problems in terms of heat, mass, and momentum transfer because of low system pressure, in addition to the problems already discussed in Section IV.D. These transport processes are strongly influenced by the flow regime in which the system is operating. The most commonly adopted way of defining the flow regime uses the ratio of the Mach number and the square root of the Reynolds number, i.e., $Ma/\sqrt{Re}$.

Ordinary gas dynamics prevails for $Ma/\sqrt{Re} \ll 1$ and $Re \gg 1$. For flows in which the value of $Ma/\sqrt{Re}$ is small but not negligible, the layer of gas immediately adjacent to a solid wall is no longer at rest but has a finite velocity. This flow regime is called slip flow. The regime is defined by the following limits:[151]

$$0.01 < \frac{Ma}{\sqrt{Re}} < 0.1, \qquad Re > 1; \tag{151}$$

$$0.01 < \frac{Ma}{Re} < 0.1, \qquad Re < 1. \tag{152}$$

It has been recognized since the time of Smoluchowski[152] and Knudsen[153] that there is a temperature discontinuity as well as a slip velocity at the interface between a solid and a gas at low pressures.

These result in reduced skin friction and reduced heat transfer. However, because of the complexity of phenomena in the slip-flow regime, there are few, if any, analytical guidelines available for designing equipment.

The two concepts of cell system designs (linear combination and composite), which have been discussed in Section IV.D, also apply to the bimetallic cell systems with lithium anodes. Again, an immobilized electrolyte is an attractive possibility in system design. Among the designs discussed, the composite designs with and without immobilized electrolyte, as shown in Figs. 57-59 are particularly attractive for lithium anode systems because of their low-pressure-drop characteristics. Systems of composite design will be tested in connection with the lithium-tin system.

VI. MATERIALS STABILITY

A. Introduction

In thermally regenerative galvanic cell systems with fused-salt electrolytes and liquid-metal electrodes, cell operating temperatures of up to 870°K and regenerator temperatures considerably above 1070°K may be encountered. The fused-salt electrolytes are usually binary and ternary mixtures of alkali fluoride, chloride, bromide, and iodide salts. The liquid-metal electrodes may consist of bismuth, lead, tin, tellurium, or selenium cathodes and lithium, sodium, or potassium anodes.

The corrosion problems in such systems arise from various sources. Fused salts, liquid metals, and liquid-metal alloys are extremely corrosive under static conditions, as well as under dynamic conditions where large temperature differences are present. Particularly severe corrosion problems can occur at the liquid metal-vapor metal and liquid metal-fused salt interfaces. Superimposed on all these is the corrosion caused in the cell portion of the system by the electrochemical reactions occurring there.

B. Heavy-metals Compatibility

1. Literature Survey

Liquid-metal corrosion generally depends on the rate of solution and the solubility of the solid test material in the liquid metal, although it may be complicated by the formation of surface intermetallic compounds and oxide films, and by the effects of impurities in the liquid metals. In spite of these complicating factors, much information can be obtained by studying the phase diagram of the solid material and the liquid metal. Good compilations of phase diagrams for binary metal systems are available.[29, 154] However, published data on heavy liquid metals at elevated temperatures are still very limited, especially at temperatures above 1073°K. Table XXXV summarizes available data on corrosion by heavy liquid metals published from 1950 to 1965. Corrosion data before 1950 have been collected in the Liquid Metals Handbook.[86] Detailed discussions of some of the data are available elsewhere.[24]

2. Static-corrosion Tests Using Heavy Metals

Because of the lack of information on the corrosion of construction materials by heavy metals above 1073°K, a series of static-corrosion tests was conducted.[22]

TABLE XXXV. Summary of Experimental Data in Literature (1950-1965) on Corrosion of Container Materials by Heavy Metals

Container Materials	Static Tests								Dynamic Tests							
	Bi		Pb		Sn		Bi, Pb, Sn Alloys		Bi		Pb		Sn		Bi, Pb, Sn Alloys	
	Temp, °K[a]	Ref. No.	Temp, °K[a]	Ref. No.	Temp, °K[a]	Ref. No.	Temp, °K[a]	Ref. No.	Temp, °K	Ref. No.	Temp, °K	Ref. No.	Temp, °K	Ref. No.	Temp, °K	Ref. No.
Steels (low-carbon alloy steel, etc.)	773	155	773	155	673	189	473	159	773	158, 175, 211	923	205			723	172, 173
	823	157, 169	823	177	1273	22	823	169	823	174	973	164, 165			923	205
	1073	177	1173	189			1033	167	873	160	1073	199			1073	156
	1123	160	1253	200			1073	215	898	187	1078	163				
	1223	203	1273	22, 216					923	205	1123	64				
	1253	189-192							973	176, 178, 179	1173	193				
	1273	208							1123	64						
	1473	22, 166, 209							1143	170						
									1173	193						
									1223	210						
Ag			823	177												
Al	823	161	823	177	773	171										
	893	214														
Be	1073	214					1073	215	761	207						
	1273	188														
Co	1173	214	823	177			801	214								
							1373	184								
Cr	823	177	923	177	823	177	1373	184								
	1123	203	1273	216												
Cu	733	212, 213	733	212, 213					773	183						
Fe	998	195	823	177	673	189	1073	215			1073	199				
	1123	203	1273	216			1373	184								
	1273	209														
Ni	903	195	823	177	1373	162	1373	184			1073	199			1073	156
			1273	216												
			1373	162												
Ti	903	214	1253	200			1373	184								
			1273	216												
V	1073	214					1373	184								
	1173	198														
Y	1003	206	1373	162	1373	162										
Zr	973	206	1253	200			1373	184								
			1273	216												
Refractory Metals	1071	206	1253	200	823	177	1073	215	761	207	1073	199				
	1073	214	1273	177, 180, 216	1073	196	1373	184,	813	202						
	1253	170, 208	1373	162, 185	1253	170		185	823	181						
	1273	188, 197, 201,			1273	209			873	201						
		204, 209			1373	162			1098	197						
	1473	166							1323	64						
									1373	182						
Nonmetals																
Graphite	973	194			1253	170	973	194	973	217						
	1253	170					1373	184	1673	186						
	1273	204														
Oxides	1253	170	1273	216	1253	170	1373	184	813	202						
	1273	204, 209			1273	209										
Glasses	1253	170	1273	216	1253	170	1373	184								
	1273	204														
Borides			1089	168												
Nitrides			1089	168												
Carbides	1253	170	1089	168	1253	170	1373	184								
Silicides			1089	168	1253	170										

[a]Maximum temperature of the experiment.

The materials under study were usually cut from sheet stock in the form of coupons, 1.5 x 2.5 x 0.3 cm. The liquid metal and a coupon were contained in a crucible fabricated of Mo-30 w/o W, an alloy considered to be nearly inert to attack by bismuth, tin, or lead. The loaded crucible

was placed under an argon atmosphere in a stainless steel bomb located in a resistance-heated furnace and was held at the test temperature for a predetermined period of time. The results are summarized in Tables XXXVI and XXXVII.

Some of the refractory-metal coupons were studied by use of an electron-probe X-ray microanalyzer after the corrosion tests. These results are included in Table XXXVII. No intermetallic compound formation was perceptible between any of the refractory metals tested and bismuth, tin, or lead, except for the niobium that formed Nb_3Sn in the presence of tin. A very thin layer ($<4\,\mu$) of $NbFe_3$ formed at the niobium-lead interface. This layer was due to iron present as an impurity in the lead ($<$10 ppm Fe). The corrosion of molybdenum and tantalum by liquid tin at 1273°K occurs intergranularly, i.e., through dissolution along the grain

TABLE XXXVI. Static Corrosion of Nonrefractory Metals and Alumina by Bismuth, Tin, and Lead

	Bismuth			Tin			Lead		
Test Material	Temp, °K	Time, hr	Results	Temp, °K	Time, hr	Results	Temp, °K	Time, hr	Results
Nonrefractory Metals									
Armco Iron	1123 1273	24 50	Slight attack. Complete dissolution.	a	-	-	-	-	-
1040 Steel	1273	22	Intermetallic layer, <80 μ thick. Cr preferentially segregated.	a	-	-	-	-	-
304 Stainless Steel	1123	97	Intergranular, <100 μ depth. No attacks found in vapor phase.	a	-	-	-	-	-
316 Stainless Steel	973	97	Slight dissolution. Decarburization, <5 μ depth in both liquid and vapor phases.	a	-	-	1123	112	Slight dissolution. Wetted.
2-1/4 w/o Cr-1 w/o Mo Steel	1123	100	Slight dissolution, <14 μ. Very little wetting.	a	-	-	1273	100	Wetted. Dissolution, 300 μ thickness.
	1273	163	Intergranular, <200 μ. Completely wetted.						
Co-20 w/o Cr-15 w/o W-10 w/o Ni-3 w/o Fe	-	-	-	-	-	-	1123	142	Slightly wetted. No corrosion.
							1273	119	Very slight attack. 50% surface wetted.
405 Stainless Steel	1123	94.5	Slightly wetted. Intergranular, <40 μ thickness.	a	-	-	1123	99	No attack. 40% surface wetted.
440 Stainless Steel	1123	100.5	Wetted. Intergranular, <150 μ thickness.	a	-	-	1123	100.5	No corrosion. Completely wetted.
Insulation Materials									
High-purity Alumina	873	99	No attack. No wetting.	873	77.5	No attack. No wetting.	-	-	-
	1123	52	Partly wetted and grayed.	1123	29	Slightly wetted.	-	-	-
	1273	72	Partly wetted and grayed, not electrically conducting.	1273	74	Completely wetted. Slightly conducting.	-	-	-

[a]In view of the high solubility of this material in tin, no test was made.

TABLE XXXVII. Static Corrosion of Refractory Metals by Bismuth, Tin, and Lead at 1273°K

Test Material	Bismuth		Tin		Lead	
	Time, hr	Results	Time, hr	Results	Time, hr	Results
Refractory Metals						
Molybdenum	95	No intermetallic formation. Very small solubility. No wetting. No corrosion.[a]	97	No intermetallic formation. Intergranular corrosion layer 90-100 μ.[a]	-	-
Niobium	137	No intermetallic formation. Some solubility of Nb in Bi. Traces of Nb found in grain boundaries of Bi.	160	A 70 μ layer of Nb_3Sn found at Nb-Sn interface.[a]	95	A 3 μ layer of $NbFe_3$ found at Nb-Pb interface. No corrosion by lead.[a]
	137	Severe intergranular attack. Specimen became brittle.	96	Severely attacked. Became brittle.		
Tantalum	100	No intermetallic formation. No corrosion.[a]	100	No intermetallic formation. Intergranular penetration of Sn.[a]	100	No intermetallic formation. Localized intergranular attack to a depth of less than 10 μ.[a]
Tungsten	115	No intermetallic formation. Very minute solubility. No corrosion. Good wetting.[a]	96	No intermetallic formation. Very minute solubility. No corrosion.[a]	96	No corrosion. Partly wetted.
Mo-30 w/o W	143	No intermetallic formation. Very minute solubility. No corrosion. Good wetting.	90	No intermetallic formation. Very minute solubility. No corrosion. No wetting.[a]	135	No corrosion.
	>2300	No visible attack. Intermetallic, 100 μ thickness.	>1200	No visible deterioration. Intermetallic, ~100 μ thickness.		
Mo-50 w/o Re	91	No apparent attack. Intermetallic, <12 μ. Wetted.	63.5	No apparent attack. Wetted.	-	-
Nb-1 w/o Zr	167	Severe intergranular attack, <250 μ depth. Specimen became brittle.	160	Intergranular attack, <100 μ depth. Completely wetted.	-	-
Nb-10 w/o W-2.5 w/o Zr	71.5	Slight dissolution and pittings.	87.5	Slight dissolution and pittings. Completely wetted.	-	-
Nb-28 w/o Ta-10 w/o W-1 w/o Zr	137	Completely wetted. Became brittle.	97.5	Wetted. Intermetallic, ~100 μ thickness.	99	No corrosion. Wetted.

[a]Analysis by electron-probe X-ray analyzer.

boundaries in the refractory metals. Minute solubilities of niobium in bismuth, tungsten in bismuth, and tungsten in tin at 1273°K were also detected by the electron-probe microanalyzer, although for practical purposes, the rate of corrosion was negligible.

The static-corrosion test results indicated that although steels or stainless steels may be suitable for the cell portion of sodium-lead, sodium-bismuth, and lithium-tin systems, the only promising container materials for regenerators for these three systems are some refractory metals and their alloys. Niobium and its alloys, which became brittle after exposure to either bismuth or tin at 1273°K, do not appear to be promising. Neither does alumina, which was wetted after exposure to either bismuth or tin at 1273°K. At present, tantalum, Mo-30 w/o W, and Ta-10 w/o W alloys are attractive possibilities for use in the construction

of regenerators because of their ease of fabrication. Tungsten and rhenium should become good possibilities as fabrication methods are developed.

There are fewer limitations on construction materials for secondary cells than for thermally regenerative systems. Generally, inexpensive and readily obtainable materials can be utilized. The 300-series stainless steels have been used to construct sodium-bismuth and sodium-lead cells operating near 825°K. Type 304 stainless steel was resistant to sodium and bismuth after 17 months of cell operation at 825°K.[22] The Type 304 stainless steel cell portion of a sodium-lead regenerative system was operated for 1000 hr at about 825°K with less than 5 μ corrosion.

Armco iron has been used for the cathode-current collectors in lithium-tellurium and lithium-selenium cells. During cell operation of over 400 hr for each type of cell, the integrity of the current collectors was maintained. Experiments have been performed to determine the corrosion of Armco iron by tellurium and selenium. An Armco-iron crucible was contacted with tellurium for 74.1 hr at 743-758°K; in another test, an Armco-iron coupon was immersed in a tellurium bath for 100 hr at 728°K. The corrosion rates in these tests were 21 mm/yr for the crucible and 11 mm/yr for the coupon. Another Armco-iron crucible was contacted with selenium for 172 hr at 773°K; the corrosion rate was 1 mm/yr. Corrosion of iron by tellurium and by selenium is of the dissolutive rather than the intergranular type. Further corrosion experiments must be performed on Armco iron before its suitability for use in tellurium and selenium can be adequately evaluated.

Other metals have been exposed to tellurium and selenium with mixed results. Molybdenum and tantalum were both attacked by molten tellurium, but tungsten showed no attack after exposure to tellurium for 7 days at 823°K. On the other hand, tungsten completely disintegrated after being exposed to selenium for 6 days, but molybdenum was unattacked after contacting selenium for 18 hr at 770°K. The corrosion resistance of tantalum to selenium has not been tested.

Type 304 stainless steel was readily attacked by tellurium at 730°K and a high-melting alloy formed. Nickel and chromium form high-melting intermetallic compounds, such as $NiTe_2$, with tellurium.[29] No tests have been performed to determine the corrosion of Type 304 stainless steel by selenium.

3. Dynamic-corrosion Tests

In a thermally regenerative cell system, the circulation of the cathode-metal alloy between the cell and regenerator sections depends upon the thermal convection induced by the temperature difference between the cell and the regenerator. Since, in general, the materials of construction have higher solubilities in the cathode alloys at high temperatures, the circulating liquid metal tends to dissolve the container material at the regenerator section, where the temperature is highest, and deposit it in the cell section, where the temperature is lowest. This type of corrosion is called dynamic corrosion. Dynamic-corrosion tests were conducted using thermal-convection loops, fabricated of the test material, as shown in Fig. 115. The loops were constructed in the form of parallelograms about 25-cm high and 15-cm wide, using test-metal pipe (1.37-cm OD and 0.92-cm ID). Electric heaters were used to maintain the sections of the loop at different selected temperatures, causing thermal convection of the liquid metal around the loop. At the end of each experiment, the loop was dissected radially and the internal cross-sectional areas of loop sections that had been exposed to the liquid metal were determined by means of enlarged photographs and a planimeter. Minimum thicknesses of the pipe walls were also measured. The flow rates of liquid metal in the loop were calculated from heat balances around the hot leg of the loop. Flow rates were also determined by application of a heat pulse as follows: A gas torch was applied to a small area at a point in the loop for a short period of time, after which the induced high-temperature liquid slug was sensed at a downstream position by a thermocouple. The two methods showed fair agreement.

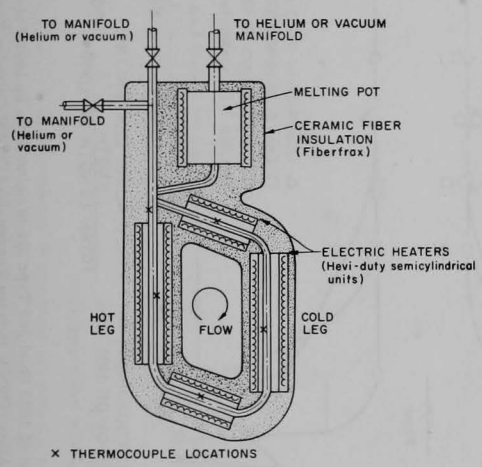

108-8721 Rev. 1

Fig. 115. Thermal-convection Loop (Schematic Representation) for Dynamic-corrosion Studies

The cross-sectional area changes after the corrosion tests of 1020 steel and Type 316 stainless steel (loops 4 through 9) are plotted in Figs. 116 and 117. The most severe dissolution of steel, resulting in as much as a 60% increase in the inside cross-sectional area of the pipe, is at the entrance of the hot leg, which is the 35 to 45% axial coordinate in Figs. 116 and 117. There is much less corrosion in the 35 to 25%

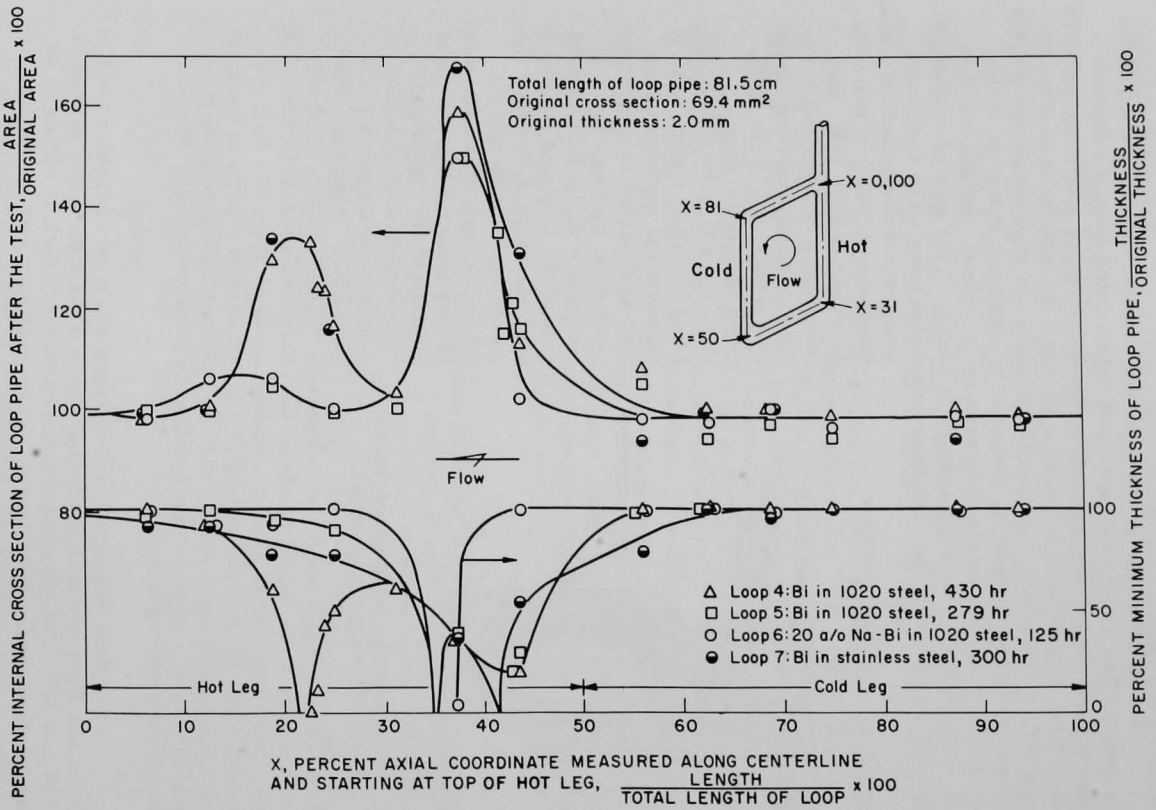

108-9474 Rev. 2

Fig. 116. Dynamic Corrosion of 1020 Steel and Type 316 Stainless Steel by Liquid Bismuth and Sodium-Bismuth Alloy (1123°K Hot-leg Temperature, 723°K Cold-leg Temperature)

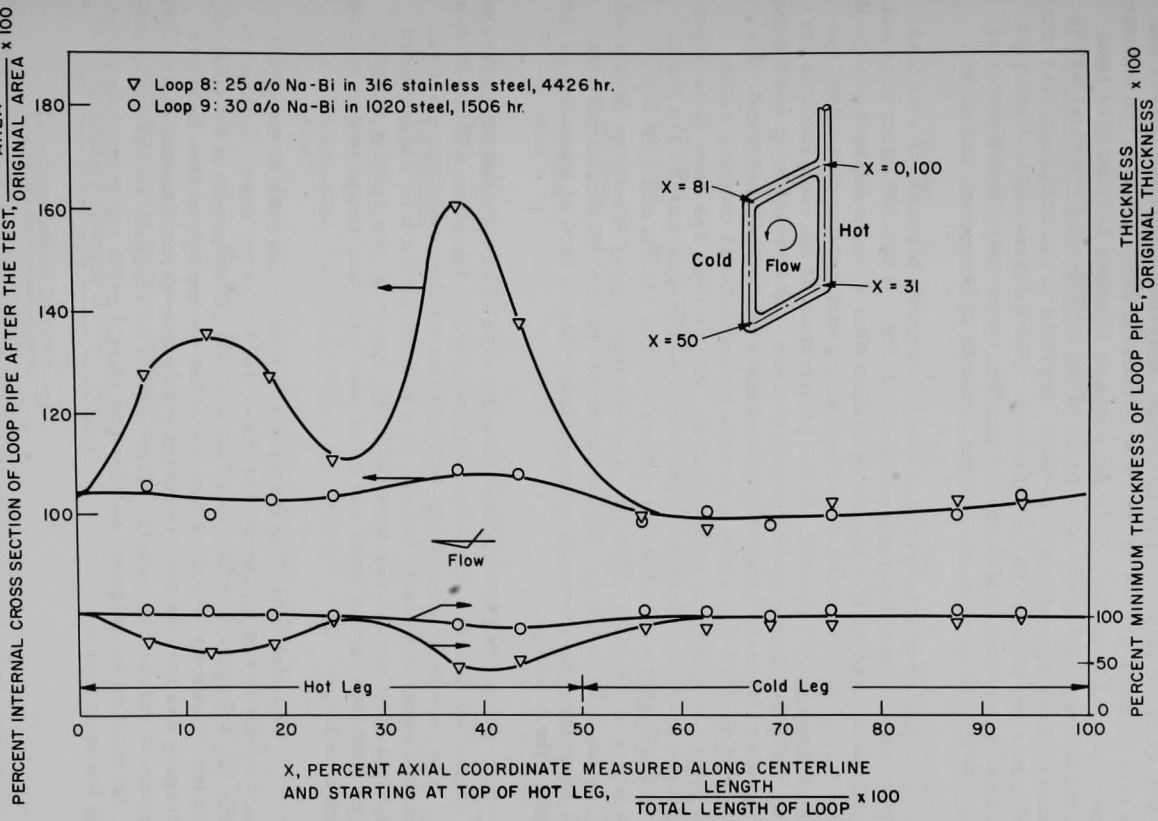

108-9475 Rev. 1

Fig. 117. Dynamic Corrosion of 1020 Steel and Type 316 Stainless Steel by Sodium-Bismuth Alloys (923°K Hot-leg Temperature, 823°K Cold-leg Temperature)

coordinate. A second severe dissolution takes place at the region of the 10 to 25% axial coordinate. The graphical integration of these curves has shown that as much as 70% of the total corrosion takes place in the entrance section of the hot leg. No significant changes in cross section have been observed in the cold-leg section. Most of the transferred material was in the form of loose aggregates of metallic crystals in the cold leg. No transferred materials adhered to the tube wall. The spectrochemical analyses of the low-carbon steel loops showed that the mass-transferred material was essentially iron, containing slight amounts of chromium and nickel.

Some refractory-metal loops containing bismuth, tin, or lead have been studied at temperatures above 1273°K. A Mo-30% alloy loop was constructed by welding five pieces of drilled tube 1.59-cm OD by 0.635-cm ID. Because of the relative difficulty of machining and welding this alloy, special techniques were required. In the preparation of the loop sections for welding, cold-machining techniques were used. After machining and before welding, all parts were vapor-degreased and ultrasonically cleaned. The loop was assembled in a semiclean area by assemblers wearing clean cotton gloves to minimize contamination. All welding was done in an argon-atmosphere pressure chamber. The loop was charged with 30 a/o Na-Bi alloy and operated with a hot-leg temperature of 1323°K and a cold-leg temperature of 973°K for 2488 hr, at which time linear fractures developed along the axis of the tubing. No corrosion of the loop by the bismuth was found; therefore the fractures were probably due to lack of annealing of the loop after the welding.

Table XXXVIII summarizes the results of all dynamic corrosion tests conducted to date using steel, stainless steel, tantalum, and Mo-30 w/o W loops. The results of these tests indicate that neither stainless steel nor low-carbon steel is suitable for use in a sodium-bismuth or sodium-lead cell system at temperatures above 1073°K; however, the results support the view that low-carbon steel can be of use in the low-temperature section of such a cell.

The task of finding materials to contain bismuth or tin under dynamic conditions at temperatures above 1273°K is not easy. It involves not only the selection of materials, but also the development of fabrication techniques. However, recent advances of the technology in this field are encouraging and include such techniques as vapor deposition and electrolytic deposition of refractory metals. Combination of adequate refractory materials, fabrication techniques, and designs should solve the materials problem in the near future.

TABLE XXXVIII. Dynamic Corrosion of Various Materials by Bismuth, Lead, and Sodium-Bismuth and Sodium-Lead Alloys

Loop Number	Test Material	Liquid Metal	Max Hot-leg Temp °K	Max Hot-leg Temp °C	Min Cold-leg Temp °K	Min Cold-leg Temp °C	Time, hr	Results
2	1020 Steel	Bi	823	550	723	450	1000	Dissolution, up to 250 μ depth.
3	1020 Steel	Bi	1073	800	973	700	24	Slight dissolution. Plugs formed, stopping circulation.
4	1020 Steel	Bi	1123	850	723	450	430	Leak developed.[a] Dissolution of up to 60% of the loop metal at the hot leg.
5	1020 Steel	Bi	1123	850	723	450	279	Leak developed.[a] Dissolution of up to 50% of the loop metal at the hot leg. Slight intergranular penetration.
6	1020 Steel	Bi-20 a/o Na	1123	850	723	450	125	Leak developed.[a] Dissolution of up to 50% of the loop metal at the hot leg.
9	1020 Steel	Bi-30 a/o Na	923	650	823	550	1506[b]	Slight mass transfer.
12	1020 Steel	Pb	1123	850	923	650	690	Plugs formed, stopping circulation.
17	1020 Steel	Pb-30 a/o Na	1073	800	873	600	345	Plugs formed, stopping circulation.
7	316 Stainless Steel	Bi	1123	850	723	450	300	Leak developed.[a] Extensive mass transfer. Intergranular penetration.
8	316 Stainless Steel	Bi-25 a/o Na	923	650	823	550	4426[b]	Dissolution of up to 65% of the loop metal at the hot leg.
11	316 Stainless Steel	Pb	1123	850	923	650	706	Plugs formed, stopping circulation.
13	316 Stainless Steel	Pb-30 a/o Na	1123	850	923	650	1224	Plugs formed, stopping circulation.
15	316 Stainless Steel	Pb-30 a/o Na	1073	800	873	600	348	Plugs formed, stopping circulation.
10	Mo-30 w/o W	Bi	1323	1050	973	700	2488	Fractures developed in loop. No corrosion.
16	Ta	Pb-30 a/o Na	1323	1050	1023	750	932	Leak developed in stainless steel sheath.

[a]The leak developed at the entrance section of the hot leg.
[b]No leaks were found at the end of experiment.

C. Electrolyte Compatibility Studies

1. Literature Survey

The corrosion of materials by fused salts has long been an important problem in electrochemistry and metallurgy. Even so, only limited data were available in the open literature until fused salts began to receive

attention as nuclear-fuel carriers and reprocessing media. Corrosion results have been published on the alkali-metal fluorides,[218-234] chlorides,[235-254] and hydroxides.[227, 255-275] These references are discussed elsewhere.[24]

Extensive corrosion studies were conducted at Oak Ridge National Laboratory[218,229, 230] on nickel and on chromium-iron alloys in fluoride salts used as nuclear-fuel carriers. The chromium was selectively leached from the surface of the alloys by the fluoride salts. In addition, diffusion of chromium from the subsurface regions was also observed, causing the formation of voids in the metal.[221] Grimes et al.[224] have discussed the mechanism of the chromium removal from the surface in terms of the following factors:

a. Impurities in the melt

Example: $FeF_2 + Cr \rightarrow CrF_2 + Fe$ (153)

Other impurities: NiF_2, CrF_3, CrF_4, FeF_3, HF and UF_5

b. Oxide films on metal surfaces:

Example: $2Fe_2O_3 + 3CrF_4 \rightarrow 3CrO_2 + 4FeF_3$ (154)

FeF_3 now reacts with chromium as indicated by Eq. 153.

c. Constituents in the nuclear fuel

Example: $Cr + 2UF_4 \rightarrow 2UF_3 + CrF_2$ (155)

Dynamic-corrosion studies using loops demonstrated that a rapid attack takes place initially by the reaction of chromium with impurities, oxide films, and the UF_4 as indicated in Eqs. 153-155. As quasi-equilibrium amounts of CrF_2 are accumulated in the salt, the attack proceeds linearly with time. Since at low temperatures the equilibrium is shifted to the left in Eq. 155, chromium precipitates in the cooler regions of the loop. In liquid metals, the driving force for dynamic corrosion is the difference in solubility of solid-metal constituents in the liquid metal at the different temperature levels, whereas in fused fluoride systems, the driving force for mass transfer results from a temperature dependence of the equilibrium constants for the chemical reactions.[224] As a result of extensive studies at Oak Ridge National Laboratory, a Ni-Cr-Mo-Fe alloy (approximately 74 w/o Ni-6 w/o Cr-15 w/o Mo-5 w/o Fe) designated as INOR-8[232] was developed, which is highly resistant to 11.2 m/o NaF-46.0 m/o LiF-41.3 m/o KF-2.5 w/o UF_4 and its variations.

Although the corrosion-mechanism studies of the fused-salt systems are still in their early stages, several important contributions in this field have appeared recently, particularly for the chloride systems.

Electrochemical considerations were given for a system containing nickel and NaCl-KCl by Littlewood et al.[246-248] The corrosion effects of even slight contamination of the melt by materials such as water and oxygen were pointed out;[236, 248] thus, purity of the salt is important.

Friend[265] summarized corrosion reactions of metals in NaOH at 1073-1273°K. The high-temperature decomposition,

$$2NaOH = Na_2O + H_2O, \tag{156}$$

is followed by

$$Na_2O + M = MO + 2Na \tag{157}$$

and

$$Na_2O + MO = Na_2MO_2. \tag{158}$$

Also,

$$H_2O + M = MO + H_2. \tag{159}$$

Thus, the overall reaction would be

$$2NaOH + M = Na_2MO_2 + H_2. \tag{160}$$

Because of this reaction, several authors[256, 263, 267, 268, 274, 275] suggested that any additives causing an increase in the hydrogen overvoltage or an increase in the difficulty with which hydrogen is evolved should retard the corrosion process. Some investigators[256, 263, 275] have demonstrated the inhibition of nickel corrosion in fused NaOH by the use of a hydrogen atmosphere. Although the low melting points of hydroxides are attractive for cell applications, chemical instability of the salt and high self-discharge rates must be overcome for use in a practical cell.

2. Experimental Results of Fused-salt Corrosion Tests

Austenitic stainless steels, including Types 304, 316, and 347, have been used to contain reagent-grade sodium halide mixtures at temperatures up to 973°K. No visual deterioration of the container materials has been observed. A ferritic stainless steel, Type 440, was tested in a mixture of 15.2 m/o NaF-31.6 m/o NaCl-53.2 m/o NaI at 973°K for 100 hr. Metallographic examination indicated that the specimen had been attacked along the grain boundaries; however, this test was conducted using commercially available reagent-grade sodium iodide, which contained some residual moisture. Therefore, the result requires confirmation by further studies.

D. Alkali-metal Compatibility Studies

1. Literature Survey

Considerable interest is currently centered on the use of alkali metals as heat-transfer media in power-generation systems, particularly in space and nuclear applications. These liquid metals are used for coolants in nuclear reactors and for working fluids in turbines. The literature contains extensive corrosion studies, and several reviews are available;[276-286] only a partial list of recent references is presented here. The literature survey indicates that, in general, more materials are resistant to attack by alkali metals than to attack by heavy metals. Some alloys such as TZM (Mo-0.5 w/o Ti-0.08 w/o Zr) and Mo-50 w/o Re were resistant under static conditions to liquid lithium at a temperature as high as 1873°K.[276] Pure iron, ferritic and austenitic stainless steels, and refractory metals are resistant to liquid sodium under static and dynamic conditions up to 1033°K.[277] These same container materials, except for the refractory metals, are stable in liquid lithium under static and dynamic conditions up to 873°K; refractory metals are expected to be resistant up to above 1073°K.[277] In the alkali metals, effects of impurities on corrosion rates become significant. One effect of oxygen in sodium is that it increases the amount of mass transfer observed in the cold sections of systems made of metal-base alloys and austenitic stainless steels.[278] Lithium nitride has been found to be the most harmful contaminant.[277]

2. Results of Alkali-metal Corrosion Tests

Because alkali metals are less corrosive than heavy metals, experimental studies on the alkali metals have been limited to qualitative evaluations.

The sodium-lead regenerator made of Type 316 stainless steel (see Section IV.D.2) which had run for a total operating time of over 150 hr (including preliminary runs) at 1023-1103°K was dissected for internal corrosion examination. Intergranular attack of 20 μ depth due to liquid sodium was found in the condensing section, but no corrosion was observed in the vapor section. A slight pitting was found in the vapor-liquid interface region of the regenerator.

The corrosion by sodium in the anode compartment of the sodium-bismuth cell (see Section IV.D) was minor.

E. Insulators for Bimetallic Cells

To build compact bimetallic cells, insulators are required to achieve effective space utilization. This is true not only for single cells, but is especially important when multiple-cell (battery) design is considered.

For cells or batteries containing sodium and sodium-alloys, the answer to the insulator problem is relatively simple. Both Al_2O_3 and BeO have the required corrosion resistance. In addition, Al_2O_3 has the added advantage that it can be plasma-sprayed to fabricate a wide variety of configurations having relatively nonporous walls.

Insulators that may be used in cells containing lithium and lithium-alloys are much more difficult to find. At present, only the frozen salt can be recommended, without qualification, from a chemical standpoint. For efficient space utilization, this insulator is not very desirable; it is quite bulky and requires cooling to remain solid.

In the study of the open-circuit emf characteristics of lithium-containing cells, porous BeO crucibles were used successfully. Immersed in the electrolyte of molten LiCl-LiF and containing liquid lithium metal, these crucibles showed no signs of attack after temperature cycling in the region between 773 and 1073°K for 2 weeks. However, in tests with lithium alone, BeO was attacked and fell apart after only 25 hr at 623°K. The mechanism of the protective action of the cell environment is not understood at present. Possibly the wetting ability of the molten salt provides the protection against lithium attack. Until this is understood, BeO cannot be recommended without qualification as an insulator in lithium-containing cells.

Both fused silica and Vycor are embrittled and fall apart in melts containing lithium in solution. Similarly, polycrystalline and single-crystal Al_2O_3 break up, the latter with complete disintegration in lithium at 723°K after 24-36 hr. However, single-crystal Al_2O_3 appears unattacked when contacted with lithium for 24 hr at 573°K. Hot-pressed BN was tested in lithium and showed no attack after 24 hr at 573°K. However, when contacted with lithium for 24-36 hr at 723°K, BN showed signs of fracture. The solid BN used contained 2.4% boric oxide, B_2O_3, which may have contributed to the reaction observed. Boron carbide was tested at 723°K and after 24 hr showed some attack by lithium.

After due consideration of the above information, we decided to defer, for the present, further consideration of the nitrides and carbides. In some cases, these refractory materials are semiconductors and not useful as insulators. In the other cases, lithium will probably react with the material, at least to some extent, and again a poor insulator will result.

The materials of primary interest as insulators are those that contain a cation identical with the anode metal in the cell. The use of such a material will reduce possible detrimental redox reactions between the anode and the insulator. Thus those insulators to be given first consideration are the oxides and double oxides containing lithium. The stable oxide, Li_2O,

which might serve as an insulator, is difficult to handle because of its hygroscopic nature. The lithium oxide must be stabilized in a double oxide to remove this undesirable feature.

Table XXXIX lists various oxides that may have the requisite chemical stability as double oxides. Their stability is indicated by their free energies of formation from the elements at 1000°K (per gram atom of oxygen) as taken from Glassner.[287] Note that those appearing below Li_2O are themselves stable with respect to the reaction

$$2yLi + M_xO_y \rightarrow yLi_2O + xM. \tag{161}$$

TABLE XXXIX. Relative Stabilities of Some Metal Oxides at 1000°K

Compound	ΔG_f°, Free Energy of Formation, kcal/per g atom oxygen	Compound	ΔG_f°, Free Energy of Formation, kcal/per g atom oxygen
SiO_2	- 83	Sc_2O_3	-115
TiO_2	- 92	SrO	-117
Al_2O_3	-108	MgO	-118
CeO_2	-108	BeO	-118
ZrO_2	-108	Y_2O_3	-119
UO_2	-109	La_2O_3	-122
Li_2O	-110	$(R.E.)_2O_3$[a]	-122
HfO_2	-110	ThO_2	-123
BaO	-111	CaO	-127

[a]R.E. = rare-earth element.

Beryllium oxide was eliminated previously and will not be discussed further. Probably the alkaline-earth oxides, MgO, CaO, BaO and SrO, will not form a stable double oxide with Li_2O because of the extreme basicity of both the alkaline-earth oxides and lithium oxide. Further, the general hygroscopic nature of the alkaline-earth oxides probably precludes their direct use as insulators. Radioactivity and sensitivity to thermal shock have tentatively eliminated UO_2 and ThO_2 from consideration.

A literature survey was made of the double oxides between Li_2O and SiO_2, TiO_2, Al_2O_3, Ce_2O_3, CeO_2, ZrO_2, Y_2O_3, La_2O_3, and CaO. The oxide HfO_2 is not included as it was considered similar to ZrO_2. The oxides of yttrium, lanthanum, and cerium were chosen to be representative of the rare-earth oxides.

The survey showed that either the stable double oxides of Ce_2O_3, CeO_2, Y_2O_3, La_2O_3, or CaO with Li_2O are not formed, or, if formed, apparently do not have increased stability over the single oxides. The compounds

showing increased stability in double-oxide formation with Li_2O are listed in Table XL and are discussed below.

TABLE XL. Properties of Some Double Oxides with Li_2O

Oxide	$\Delta \tilde{G}^{\circ}_{f,298}$, kcal/mole	Double Oxide	$\Delta \tilde{G}^{\circ}_{f,298}$, kcal/mole	$\Delta \tilde{G}^{\circ}_{298}$ (Reaction with Lithium) Oxide, kcal/mole	Double Oxide, kcal/mole
SiO_2	-198	Li_2SiO_3	-361	-70	-41
TiO_2	-212	Li_2TiO_3	-377	-56	-25
Al_2O_3	-375	$LiAlO_2$	-269	-27	+1.5
ZrO_2	-248	Li_2ZrO_3	-396[a]	-20	-6
Li_2O	-134	-	-	-	-

[a]Estimated, $\Delta \tilde{H}^{\circ}_{f,298}$ = -417.2 kcal/mole from the elements;

$\Delta \tilde{H}^{\circ}_{f,298}$ = -15.2 kcal/mole from the oxides.

Silica, SiO_2, is not stable at 298°K (by -70 kcal) with respect to reaction with lithium:

$$SiO_2 + 4\,Li \rightarrow 2\,Li_2O + Si. \tag{162}$$

Double oxides of Li_2O and SiO_2 form a series of compounds, which tend to occur as glasses. For the 1:1 compound, Li_2SiO_3, the stability with respect to lithium is enhanced to -41 kcal for the reaction

$$Li_2SiO_3 + 4\,Li \rightarrow 3\,Li_2O + Si. \tag{163}$$

This increased stability is not sufficient; SiO_2 and lithium still react with ease. Compounds such as $Li_2O \cdot xSiO_2$ are not suitable as insulators.

Similarly, TiO_2 is unstable with respect to reaction with lithium, the free-energy change for the reaction

$$TiO_2 + 4\,Li \rightarrow 2\,Li_2O + Ti \tag{164}$$

being -56 kcal at 298°K. The double oxide, Li_2TiO_3 is more stable; the reaction

$$Li_2TiO_3 + 4\,Li \rightarrow 3\,Li_2O + Ti \tag{165}$$

has a free-energy change of -25 kcal at 298°K. Again, there is potential instability in the reaction of the double oxide with lithium; therefore $Li_2O \cdot xTiO_2$ compounds were not considered further.

The compound $LiAlO_2$ exists in two crystal forms with a transition temperature somewhere between 873-1173°K. The low-temperature form reportedly will not hydrolyze in boiling water. As indicated previously, alumina reacts with lithium, having a free-energy change of -27 kcal at 298°K for the reaction

$$Al_2O_3 + 5\ Li \rightarrow 3\ Li_2O + 2\ Al. \tag{166}$$

The double oxide, $LiAlO_2$, is more stable. The reaction with lithium,

$$LiAlO_2 + 3\ Li \rightarrow 2\ Li_2O + Al, \tag{167}$$

is not spontaneous by about +1.5 kcal at 298°K. Though the free-energy change is only slightly positive, there is indication of compound stability in the cell environment. Therefore, lithium meta-aluminate, Li_2AlO_2, will be examined further as an insulator.

The compound Li_2ZrO_3 is resistant to hydrolysis. The free-energy change for the reaction

$$Li_2O + ZrO_2 \rightarrow Li_2ZrO_3 \tag{168}$$

can be estimated as -14 kcal at 298°K from the reported ΔH_{298} of -15.2 kcal. Zirconia, ZrO_2, apparently reacts with lithium; at 298°K, the free-energy change is -20 kcal for the reaction

$$ZrO_2 + 4\ Li \rightarrow 2\ Li_2O + Zr. \tag{169}$$

The free-energy change for the reaction of the double oxide with lithium,

$$Li_2ZrO_3 + 4\ Li \rightarrow 3\ Li_2O + Zr, \tag{170}$$

has been estimated to be -6 kcal at 298°K. Even with the uncertainties in the calculations, these values are of the proper magnitude to indicate that Li_2ZrO_3 is a possible insulator for the lithium anode bimetallic cells. Because of the great similarity in the chemistry of zirconium and hafnium, the double oxide, Li_2HfO_3, is also being considered further for use as an insulator.

Any oxide or refractory material that might be used as an insulator could also be used in powder form to make a paste electrolyte, thus immobilizing the fused halide. We will continue to examine the compounds $LiAlO_2$, Li_2ZrO_3, and Li_2HfO_3 to test their effectiveness as insulators.

F. Guidelines for the Selection of Cell and Regenerator Materials

Liquid-metal corrosion depends for the most part simply on the dissolution rate and the extent of solubility of the solid metal in the liquid metal. Many complicating factors can influence the dissolution rate or the solution limit. The formation of surface intermetallic compounds, oxides, or nitrides are good examples of such factors. In addition, temperature gradients and impurities in the liquid metals have an important role. Therefore, it is nearly impossible to set up universal guidelines for liquid metal corrosion. Figure 118 summarizes literature data and the results of present investigations on static-corrosion resistances of materials to liquid bismuth, lead, and tin.

Some materials that are suitable construction materials for one type of liquid, such as heavy liquid metal, are not necessarily adequate for containing other liquids, such as fused salts. For example, ferritic stainless steel is adequately resistant to liquid lead at 1123°K under dynamic conditions, but stainless steel of this type may be inadequate for containing halide electrolytes. Therefore, when two different liquids are contained in one place, the selection of container materials requires care.

Austenitic stainless steels have been adequate for the cell and condenser sections of thermally regenerative sodium-lead and sodium-bismuth cell systems. Austenitic stainless steels, particularly Types 347 and 316, have also been used with lithium cells up to 973°K without visible corrosion of the container materials. Armco iron has been found resistant to tellurium up to 773°K. In the sections containing circulating cathode alloy and in the regenerator, which operate above 1073°K, refractory metals must be used. Among the refractory metals, tantalum, Mo-30 w/o W, and Ta-10 w/o W alloys are attractive because of their ease of fabrication. Other refractory metals, especially tungsten and rhenium, may become more attractive as advanced fabrication techniques such as vapor deposition, electrolytic deposition, and plasma spray methods become refined. Therefore, it is just as important to find a suitable design and fabrication technique as to find a suitable container material.

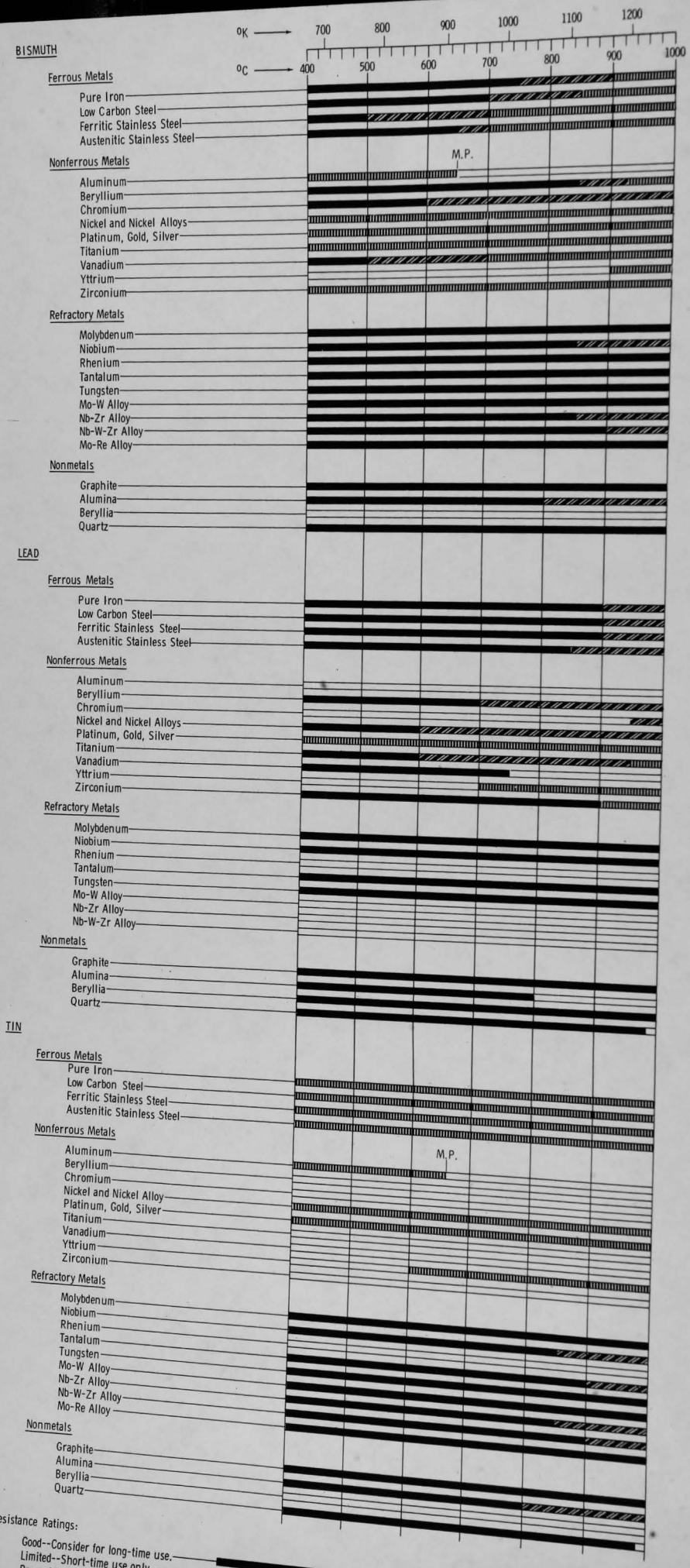

Fig. 118

Summary of Published Data for the Static-corrosion Resistance

APPENDIX A

Purification of Gases for Inert-atmosphere Enclosures

Inert-gas atmospheres are required when working with reactive molten metals and molten salts, when welding refractory metals, or when doing other experimental work using materials that are extremely sensitive to the chemically reactive gases. The principal contaminants are oxygen, nitrogen, water vapor, and, less frequently, hydrogen, organic vapors, and acid vapors.

There are two methods of maintaining high purity in an inert atmosphere in a working enclosure, i.e., an enclosure fitted with gloves for manual manipulations inside the enclosure. One can continually flush at a high flow rate with a pure gas. A less wasteful and more practical approach is to cycle the inert gas through a purification unit.

The problem, then, concerns not only the absolute purity of the original charge of gas, but the maintenance of the purity of the box atmosphere in the face of continuing contamination. For example, water vapor continually diffuses into the box through the gloves; it also enters with in-leaking air and on new equipment brought into the box. Keeping the pressure inside the enclosure slightly higher than ambient reduces in-leakage, but when radioactive materials are handled, in-leakage is preferable to the release of hazardous materials to the surroundings.

Both argon and helium are commonly used in these enclosures. Argon is more available, economical, and easier to pump. The lower boiling point of helium makes cryogenic purification more convenient.

The most useful purification processes fall into two general categories:

1. Chemical
   a. Gas-solid chemical reactions, such as those using "getters" for removing oxygen or nitrogen.
   b. Combination of hydrogen and oxygen over a palladium catalyst to form water, which is then removed physically.
2. Physical
   a. Adsorption of moisture on activated alumina or Molecular Sieves and of impurities on activated charcoal.
   b. Refrigeration for removing water vapor.

The choice of any process for a purification system will be influenced by factors such as the scale of operations, regeneration or disposal of spent reactants, availability of suitable forms of reactants for use on a plant scale, etc.

The inherent difficulties involved in the use of argon in inert-gas systems, e.g., kinetics of the gettering reaction, suitable pumps, etc., often prompts the use of helium as the inert gas. Cryogenic adsorption techniques can maintain helium at a very high purity and permit easy repetitive regeneration of the absorber.

Published information on helium purification systems is scarce. Foster, Johnson, and Crouthamel[44] describe an operating system in some detail. White and Smith[288] and Walton[289] discuss the general approaches that may be followed. However, one should not overlook the information given by Dushman[290] on the adsorption coefficients for various gases on charcoal at cryogenic temperatures. A general review on glovebox techniques is given by Barton.[291]

Figure A.1 is a schematic diagram of a helium-purification system. The contaminated gas from the working enclosure first passes through a

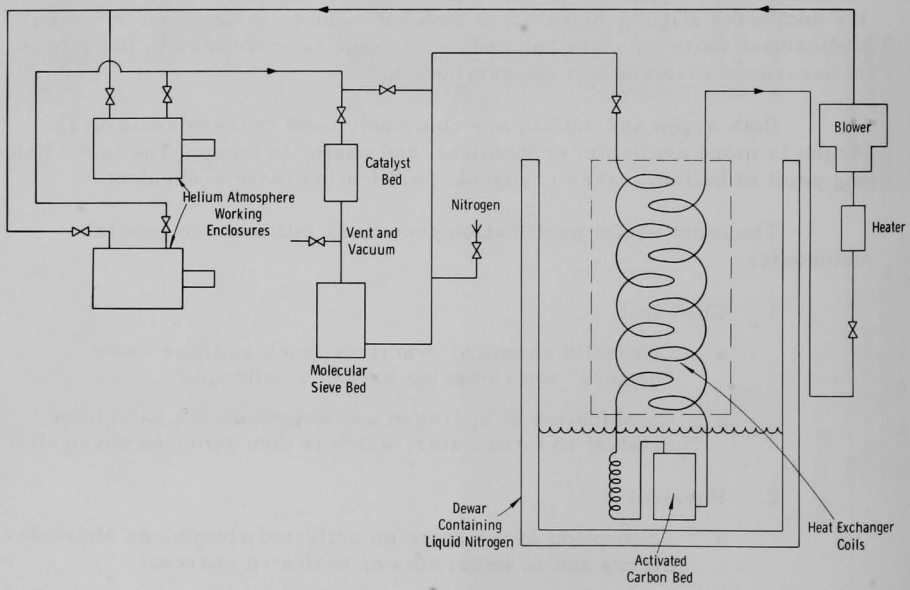

308-229

Fig. A.1. Schematic Diagram of Helium-purification System

palladium catalyst. This unit* reduces the hydrogen content to <1 ppm by the catalytic combination with oxygen to form water. (An excess of oxygen in the incoming gas stream is assumed.)

Depending on the amount of the hydrogen-gas contaminant in the inert gas, one may reject the use of the palladium catalyst in the system. We have operated systems both ways with equally good performance. Although adsorption capacity for hydrogen on the carbon bed is not as great as for oxygen or nitrogen, it is sufficient for the low hydrogen content of the gas normally encountered.

After leaving the catalyst bed, the helium gas passes through a dryer unit consisting of a bed of Molecular Sieves. This bed collects moisture, minimizing ice or snow formation in the subzero sections of the purification system. The dryer bed is 20 cm in diameter and 30 cm deep. Linde Type 5A Molecular Sieve pellets (3 mm) are used in this bed. Next, the gas is precooled by passing through one side of the heat exchanger located in a large Dewar. This Dewar is sufficiently deep so that the heat exchanger is suspended in the nitrogen vapor above the liquid nitrogen.

The first heat-exchanger design consisted of a coil of copper tubing, sections of which were separated from one another by short stainless steel nipples. Copper fins connected the coil for the incoming gas stream to the coil for the exiting gas stream. This system operated satisfactorily; however, improvements could be made. More recently, the heat-exchanger design has used two concentric coils in parallel. The concentric coils consist of 2.2-cm-OD tubing inside 3.5-cm-OD tubing, formed into a compact coil. The incoming gas flows in the annular section, where it is cooled by the nitrogen vapor surrounding the coil and by the cold helium gas exiting from the inner tube.

From the heat exchanger, the helium passes through a coil immersed in liquid nitrogen and then through an activated-charcoal adsorber bed. This bed is 20 cm in diameter and 30.5 cm high. Activated coconut charcoal (8-14 mesh) for the bed was obtained from Barneby-Cheney** and was contained in an all-copper vessel to promote heat transfer. This adsorber removes oxygen, nitrogen, and any traces of water vapor remaining in the gas. To be most effective, the activated charcoal and the incoming gas stream should be at liquid-nitrogen temperatures. The gas then passes to the other side of the heat exchanger and, by means of a "canned" blower, is pumped back to the working enclosure.

One problem faced in setting up a purification system for helium gas was finding a blower capable of giving the required flow rate against

* Dexo Model D-300-200, Englehard Industries, Inc., Newark, New Jersey.

** Barneby-Cheney Co., Columbus, Ohio.

the pressure drops in the system. The density of helium (about one-seventh that of air) places a restriction on the types of blowers that can be used. An eight-stage centrifugal blower,* completely enclosed in a steel container, has been used successfully in these helium systems. Operating times in excess of 12,000 hr have been noted, even though the blowers are required to operate in extremely dry atmospheres.

During regeneration of the dryer bed and adsorber bed, the boxes and the blower chamber are isolated from the system. The carbon bed is regenerated by heating to approximately 423°K and evacuating. Because the boxes are normally shut down during the weekend, regeneration takes place at that time. The dryer is regenerated by passing a hot stream of 1-2 cfm of dry nitrogen in reverse direction to the normal flow while the dryer is heated to 573°K. The dryer is evacuated to about 10 μ pressure before being put back into service.

For operation of the purification unit at a recirculation rate of about 10 cfm, oxygen and nitrogen levels of less than 5 ppm and a moisture level of less than 1 ppm were obtained routinely in two 850-liter-volume working enclosures connected in parallel with the system.

Helium-purification systems have been designed for two different enclosure volumes: a small system for enclosure volumes up to approximately 2830 liters, and a larger system for enclosures greater than 2830 liters. Both systems use the same dryer and adsorber, but differ in the size of the heat exchanger and blower. The blower in the larger system is the Rotron Spiral Blower.** This blower will pump approximately 900 liters/min of air at a static pressure of 35 cm water, as opposed to only 280 liters/min for the same static pressure with the centrifugal blower mentioned earlier.

*Rotron Blower, Model MLPM, Type A8-701, Rotron Mfg. Co., Woodstock, New York.
**Rotron Blower Model SL2E2.

APPENDIX B

Quasi-thermodynamic Analysis of Self-discharge Sodium Transfer in Cells with Electrolytes Having Electronic and Ionic Conductivity

1. Assumptions

a. All calculations are for cells in which the electrode-electrolyte interfaces are parallel planes.

b. The quantity of cathode alloy is sufficiently large and the alloy sufficiently agitated so that concentration gradients do not exist at any time. The composition of the cathode alloy is constant.

c. Steady-state conditions apply at any fixed current; i.e.,

(1) The current through any plane through the electrolyte and parallel to the electrode-electrolyte interface is constant.

(2) The total number of sodium nuclei in the electrolyte is constant.

d. The electrodes are in thermodynamic equilibrium with the electrolyte immediately adjacent to them (the anolyte and catholyte), and the sodium atoms dissolved in the electrolyte are in equilibrium with sodium ions and dissolved electrons.

e. The partial sodium-ion conductivity is constant throughout the electrolyte.

f. The partial electronic conductivity of the electrolyte is directly proportional to the concentration of dissolved sodium metal; i.e.,

$$\kappa_e = K_e X_{Na}. \tag{B.1}$$

g. The atoms and ions in the electrolyte migrate independently.

h. No convection currents occur in the cell.

i. The activity coefficient of sodium metal dissolved in the electrolyte, γ_{Na}, is constant and is defined by the equation

$$\mu_{Na} = \mu^{\circ}_{Na} + \underset{\sim}{R}T \ln \gamma_{Na} X_{Na}. \tag{B.2}$$

j. The effective diffusion coefficient of sodium atoms in the electrolyte, $\mathcal{D}_{Na-m}$, is constant.

k. The chemical potential of sodium ions, defined as

$$\mu_i = \mu_i^\circ + \underset{\sim}{R}T \ln \gamma_i X_i, \tag{B.3}$$

is constant through the electrolyte.

l. The standard state of sodium is the liquid metal in the cell environment.

2. Derivation

Consider the concentration cell

$$\underset{\text{(anode)}}{\text{Na}} \Big/ \text{Na}, \text{Na}^+, e^-, X^- \;\overset{(1)}{\vdots}\; \overset{(2)}{\vdots}\; \text{Na}, \text{Na}^+, e^-, X^- \Big/ \underset{\text{(cathode)}}{\text{Na-alloy}} \tag{B.4}$$

where all composition changes occur between the imaginary boundaries, (1) and (2). The equivalent current density for sodium atoms through the electrolyte toward the cathode, i_{Na} (Amp/cm^2), will be

$$i_{Na} = \frac{F\mathcal{D}_{Na\text{-}m}\rho X_{Na}}{M\underset{\sim}{R}T} \frac{d\mu_{Na}}{dx}. \tag{B.5}$$

The partial current density of the sodium ions, i_{Na^+}, is

$$i_{Na^+} = -\frac{\kappa_i}{F}\frac{d\mu_i}{dx} - \kappa_i \frac{d\psi}{dx}, \tag{B.6}$$

where ψ is the local electrical potential in the electrolyte. The partial electrical current density due to electrons in the electrolyte, i_e, is

$$i_e = \frac{\kappa_e}{F}\frac{d\mu_e}{dx} - \kappa_e \frac{d\psi}{dx}, \tag{B.7}$$

where μ_e is the chemical potential of the electrons. Note that the current carried by electrons is considered to be positive when the electrons themselves flow toward the anode. The total electrical current density, i, is the sum of the partial current densities (Eqs. B.6 and B.7):

$$i = i_{Na^+} + i_e = \frac{1}{F}\left(\kappa_e \frac{d\mu_e}{dx} - \kappa_i \frac{d\mu_i}{dx}\right) - (\kappa_i + \kappa_e)\frac{d\psi}{dx}. \tag{B.8}$$

The apparent self-discharge transfer rate of sodium is

$$J_{Na} = i_{Na} - i_e = (i_{Na} + i_{Na^+}) - i. \tag{B.9}$$

Using assumption c above, Eq. B.9 shows that J_{Na} must be independent of the position, x, in the electrolyte and thus is constant for a given i. From assumption d, we can write

$$\mu_{Na} = \mu_i + \mu_e. \tag{B.10}$$

Using this result, we may write

$$J_{Na} = -\left(\frac{F\mathcal{D}_{Na-m^\rho} X_{Na}}{M\underset{\sim}{R}T} + \frac{1}{F}\cdot\frac{\kappa_i\kappa_e}{\kappa_i+\kappa_e}\right)\frac{d\mu_{Na}}{dx} - \frac{\kappa_e i}{\kappa_i+\kappa_e}. \tag{B.11}$$

From assumption g

$$\frac{d\mu_{Na}}{dx} = \underset{\sim}{R}T\frac{d\ln X_{Na}}{dx}; \tag{B.12}$$

substituting this in Eq. B.11, we have

$$J_{Na} = -\left[\frac{F\mathcal{D}_{Na-m^\rho}}{M} + \frac{K_e\,\underset{\sim}{R}T\,\kappa_i}{F(\kappa_i+\kappa_e)}\right]\frac{dX_{Na}}{dx} - \frac{\kappa_e i}{\kappa_i+\kappa_e}. \tag{B.13}$$

Integrating this equation for the boundary conditions,

(1) At the anode, $x = 0$, $X_{Na} = X_{an}$; (B.14)

(2) At the cathode, $x = L$, $X_{Na} = X_{ca}$; (B.15)

we obtain

$$J_{Na} + i = \left[\frac{\kappa_i\,\underset{\sim}{R}T}{FL} + \frac{F\mathcal{D}_{Na-m^\rho}\kappa_i i}{LMK_e(i+J_{Na})}\right]\ln\left[\frac{J_{Na}\kappa_i + (J_{Na}+i)\,K_eX_{an}}{J_{Na}\kappa_i + (J_{Na}+i)\,K_eX_{ca}}\right]$$

$$+ \frac{F\mathcal{D}_{Na-m^{-\rho}}(X_{an} - X_{ca})}{LM}. \tag{B.16}$$

The cell reaction producing current in the external circuit is

$$Na_A + Na^+_{ca} + e^-_C \rightarrow Na^+_{an} + Na_C + e^-_A, \tag{B.17}$$

where the subscripts A and C refer to the anode and cathode themselves, and an and ca to the anolyte and catholyte, respectively. The Gibbs free-energy change, $\Delta\underset{\sim}{G}$, for this reaction is

$$\Delta\underset{\sim}{G} = (\mu_{Na,C} - \mu_{Na,A}) + (\mu_{i,an} - \mu_{i,ca}) + F(\psi_{an} - \psi_{ca})$$

$$+ (\mu_{e,A} - \mu_{e,C}) - F(\psi_A - \psi_C). \tag{B.18}$$

If this were an ordinary cell without transference,[39] we would have

$$\mu_{e,A} = \mu_{e,C}, \tag{B.19}$$

$$\mu_{i,an} = \mu_{i,ca}, \tag{B.20}$$

and

$$\psi_{an} = \psi_{ca}, \tag{B.21}$$

so that

$$\Delta \underset{\sim}{G} = \mu_{Na,A} - \mu_{Na,C} + F(\psi_C - \psi_A). \tag{B.22}$$

By definition,[292] the open-circuit cell potential is

$$E_{oc} = \psi_C - \psi_A, \tag{B.23}$$

and if only equilibrium processes take place, $\Delta \underset{\sim}{G} = 0$; then Eq. B.22 becomes

$$-FE_{oc} = -F\underset{\sim}{E} = \mu_{Na,C} - \mu_{Na,A}, \tag{B.24}$$

where $\underset{\sim}{E}$ is the theoretical thermodynamic open-circuit potential.

For the cell with ionic and electronic conductivity, the conditions given by Eqs. B.19, B.20, and B.21 reduce to

$$\mu_{e,A} = \mu_{e,C} \tag{B.25}$$

and

$$\mu_{i,an} = \mu_{i,ca}, \tag{B.26}$$

and Eq. B.18 reduces to

$$\Delta \underset{\sim}{G} = -F\underset{\sim}{E} - F\Delta E + FE = 0 \tag{B.27}$$

if only equilibrium processes take place, where

$$\Delta E = \psi_{ca} - \psi_{an}. \tag{B.28}$$

To calculate this quantity, we combine Eqs. B.8 and B.10 to obtain

$$d\mu_i = \frac{\kappa_e}{\kappa_i + \kappa_e} d\mu_{Na} - F d\psi - \frac{F_i}{\kappa_i + \kappa_e} dx. \tag{B.29}$$

Substituting Eq. B.11 in Eq. B.29 yields

$$d\mu_i = -\frac{F}{\kappa_i}\left[J_{Na}\,dx + \frac{F\mathcal{D}_{Na-m^\rho}}{M}\,dX_{Na} + i\,dx\right] - F\,d\psi. \tag{B.30}$$

By assumption k, $d\mu_i = 0$ and Eq. 30 becomes

$$d\psi = -\frac{1}{\kappa_i}\left[(J_{Na}+i)\,dx + \frac{F\mathcal{D}_{Na-m^\rho}}{M}\,dX_{Na}\right], \tag{B.31}$$

which is integrated to yield

$$\psi_{ca} - \psi_{an} = -\frac{1}{\kappa_i}\left[(J_{Na}+i)\,L + \frac{F\mathcal{D}_{Na-m^\rho}}{MK_e}(\kappa_{e,ca} - \kappa_{e,an})\right]. \tag{B.32}$$

Substituting this in Eq. B.27, we obtain

$$E = \underset{\sim}{E} - \frac{F\mathcal{D}_{Na-m^\rho}}{MK_e\kappa_i}(\kappa_{e,ca} - \kappa_{e,an}) - \frac{(J_{Na}+i)\,L}{\kappa_i}, \tag{B.33}$$

or, if i = 0 and using Eq. B.16 in Eq. B.33,[21]

$$E\big|_{i=0} = \underset{\sim}{E} - \frac{\underset{\sim}{R}T}{F}\ln\frac{\kappa_i + \kappa_{e,an}}{\kappa_i + \kappa_{e,ca}}. \tag{B.34}$$

APPENDIX C

Methods for the Study of Liquid-Vapor Equilibria

1. Total Vapor-pressure Measurements

a. The Quasi-static Method

The quasi-static method of measuring vapor pressure was introduced by Rodebush and Dixon[293] in 1925 and analyzed more recently by Beusman.[50] The principle of the method is explained in terms of Fig. C.1. The sample is held in a closed vessel, which has tubes F and G extending up from it. Tube G is closed at the upper end and a differential manometer (E) connects F and G. Manometer D measures the absolute pressure in F. The stopcock system represented by A and B connects F to a vacuum source (I) and permits pressure decrements to be made in the sample system by allowing gas to expand into volume C. The sample chamber is uniform in temperature, but the temperature drops along F and G outside the chamber. At the start of an experiment, both tubes and the chamber contain inert gas at a pressure higher than the vapor pressure of the sample. As a quantity of inert gas is drawn into C, a brief pressure fluctuation is noted on the differential manometer as the front of the reduced-pressure region moves down F and up G. This rapid equalization of pressure proceeds at a rate controlled by the frictional resistance to the flow of the inert gas through the tubes and the chamber. In this analysis, the tube diameter is assumed to be large enough and the pressure high enough so that only viscous flow is to be considered. The contribution from molecular flow is negligible. This condition, it will be found, places a lower pressure limit (about 5 Torr) on the method. As long as the system pressure is higher than the vapor pressure, no condensation occurs in the tubes. This means that there is effectively no continuous net movement of vapor up the tubes. Under these conditions, each pressure reduction results in a brief deflection of the differential manometer.

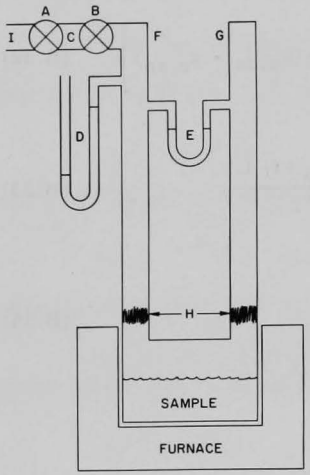

308-626

Fig. C.1. Schematic Diagram of the Classical Form of the Quasi-static Method for Measuring Vapor Pressures

The first pressure decrement that makes the inert gas pressure equal to or slightly less than the vapor pressure also results in the establishment of a condensation zone (H). Vapor streams up the tubes to the condensation sites, and condensate returns by running down the tube walls. The pressure decrement causing this condition also results in a deflection

of the differential manometer. Now, however, the pressure difference is not brief, but persists markedly longer, and is sometimes termed a "semi-permanent deflection." The condensation zone in tube F does not hinder pressure reduction into the chamber since the ascending vapor in tube F is moving in the same direction as inert gas flows under the influence of the pressure reduction. But, in tube G, the vapor ascending to the condensation zone constitutes a counterstream or barrier to the inert gas trapped in the upper part of tube G. This situation makes pressure equalization in the differential manometer a slow process. Given enough time, of course, the inert gas trapped in G will diffuse through the rising vapor and equalize the pressure. (Pressure equalization during the preliminary decremental steps takes about 2 to 8 sec, depending on the pressure. When the vapor pressure was reached, the differential manometer deflections lasted 30 to 60 sec, and sometimes longer.) Once it is established that the system has been evacuated to the vapor pressure of the sample, the pressure is read on the absolute manometer (D).

A lower limit to the vapor pressures may be measured by the quasi-static method. This limit occurs when diffusive flow makes a significant contribution to the overall flow rate. At pressures lower than this limit, the flow is inherently slow and a long-lived pressure fluctuation may be observed in the differential manometer. Such an indication would not be distinguished easily from the kind that genuinely signals the end point of the pressure reductions. For the apparatus used in these investigations, this lower limit of operation is conservatively about 5 Torr, but may be extended to about 1 to 2 Torr. Errors arising from the pressure gradient across the condensation zone would be expected to arise only if the pressure went down to about 0.1 Torr. Therefore, this second limitation is not encountered in practice.

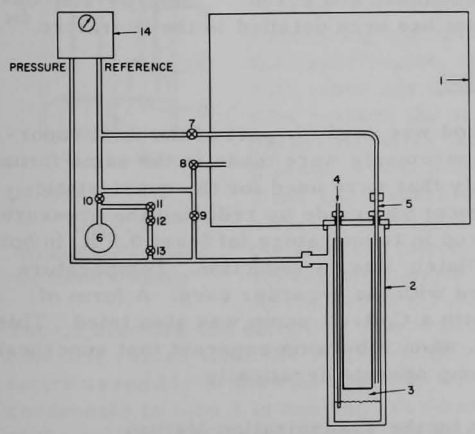

108-9319

Fig. C.2. Schematic Diagram of the Apparatus Used in an Adaptation of the Rodebush-Dixon (Quasi-static) Technique for Measuring Vapor Pressures

With this background on the principle of operation of the quasi-static method, the design and operation of the apparatus actually used may be understood, using the schematic diagram in Fig. C.2. Since air and moisture-sensitive alkali-metal systems are being studied, the apparatus was assembled as part of an inert atmosphere (helium) glovebox (1). A double flange in the floor of the box permits a furnace well (2) to be sealed to the outside of the box. A furnace

fits around this well. The sample cell assembly (3) is loaded with sample and placed inside the well from inside the box. Through one of the tubes on 3, a thermocouple well (4) is inserted and dips below the surface of the sample. Through the other tube on 3, an open-ended 5-6-mm tube (5) is inserted with the lower end positioned in the vapor space of the cell. After the cell is loaded and in position, the interior of the well is isolated from the glovebox by means of a cover plate, which is sealed to the upper side of the flange. Both the thermocouple well (4) and the tube (5) are held in position by means of O-ring-sealed vacuum couplings, which also complete the seal that isolates the well from the glovebox. Tube 5 connects with the pressure measuring and control system outside the box. The well is constructed with a side arm to which the pressure measuring and control system is also connected. This system consists of a vacuum pump (6), piping, valves (7-13), and a pressure gauge (14).

The gauge used is a Texas Instruments fused-quartz, precision pressure gauge; it covers the range 0-1000 Torr with a sensitivity of 0.01 Torr, a reproducibility of 0.02 Torr, and a calibration accuracy of 0.015%. In the measurements, the gauge is used both as a differential-pressure detector and as an absolute-pressure gauge, depending on the setting of the valves. The reference and pressure sides of the gauge are shown in the figure. "Zero" pressure (10^{-3} Torr) is the reference pressure. The expansion volume ratios fixed by the valves are such that the finest reduction is four parts per thousand.

Effectively, our apparatus is a single-tube adaptation of the double-tube method described by Rodebush and Dixon.[293] Step-by-step operating procedure for our equipment has been detailed in the literature.[294]

b. The Boiling-point Method

The boiling-point method was used for part of the total vapor-pressure determinations, and measurements were made in the same furnace well and sample container assembly that were used for the quasi-static method. A boiling-point measurement was made by reducing the pressure in decrements until there was a drop in temperature (at least 0.5°K) in both the liquid and vapor phases immediately after a reduction. Temperature changes of 0.2°K could be perceived with the recorder used. A form of ebulliometry using an apparatus with a Cottrell pump was also tried. This technique was discarded, however, when it became apparent that superheating problems made the Cottrell pump operate erratically.

2. Vapor Density and Composition by the Transpiration Method

The transpiration method was used to obtain data on the overall composition and density of the vapor above a series of molten alloys at a given temperature. This method consists of saturating a known volume of inert

gas with metal vapor as the carrier gas streams over the sample, and then by condensing the vapor at a convenient downstream location. Knowledge of the volume of carrier gas used to transport the vapor and analysis of the condensate allow one to calculate the vapor composition and the partial pressures of the components (subject to certain limitations discussed below).

The transpiration apparatus is shown in Fig. C.3. The largest component is the sample container, a cylinder about 6 cm in diameter and 40 cm long, which is surrounded at its lower half by a tube furnace. A cover plate is bolted to a flange in the sample tube; an O ring in the flange provides a tight seal. In the cover plate are four vacuum couplings which allow four small (6-mm) tubes to be introduced into the sample tube and to be moved up or down without leakage of gas into or out of the sample tube. One of the small tubes (not shown in Fig. C.3) is closed at the lower end and is a thermocouple well for measuring the temperature of the gas phase. In the preliminary part of the experiment, while the apparatus and sample are attaining temperature equilibrium, a slow stream of carrier gas is passed into tube 3 and out of tube 2. Both tubes are closed at the bottom except for 0.4-mm orifices for gas flow. This direction of flow is opposite to that in effect during the run proper. At time zero, when the run starts, the flow direction is reversed. The main function of tube 2 is as a carrier-gas (argon) inlet. Tube 3 is the vapor-sample condensing and collecting tube. In its passage through the vapor region, the carrier gas becomes saturated with vapor and carries it up into the cool region of tube 3 where the vapor condenses. The carrier gas passes on; after leaving tube 3, its gas volume is measured with a wet test meter (0.5% accuracy). Tube 1 is a thermocouple well and stirrer. During a run, it is rotated occasionally to stir the melt with the attached paddle, 4. The drip deflector, 7, prevents condensed material outside tube 3 from entering tube 3. At the end of a run, all tubes are raised several inches. Tube 1 also has the sampling cup, 6, attached to the splash shield, 5. When tube 1 is raised after the run, a sample of the melt is held in the cup. The entire assembly is then quenched by withdrawing it from the furnace. The condensate in tube 3 is analyzed to determine the masses of the components of the melt that were vaporized, transported, and condensed. These results yield the vapor composition.

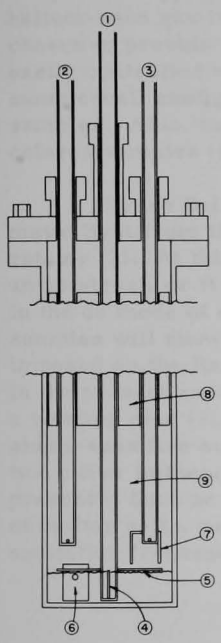

108-9112

Fig. C.3

Transpiration Apparatus (Schematic Diagram)

The question of vapor saturation of the carrier gas requires special attention. If the carrier gas flows too rapidly, it will be unsaturated.

If it flows extremely slowly, diffusion of vapor into the collector tube will give spuriously high values for the vapor density. Several experiments must be done at different carrier-gas flow rates to determine whether saturation has been achieved. If over a range of flow rates the calculated partial pressure (or vapor density) of a species remains constant, then it is assumed that equilibrium vapor has been sampled. This is the so-called "plateau test," which has been discussed by Alcock and Hooper[295] as well as others.

APPENDIX D

Description of Laser-excited Raman Spectrophotometer
(by E. L. Gasner)

A laser-excited Raman spectrophotometer for use with molten-salt samples has been designed and constructed utilizing many commercially available components. The 4358 Å line from a low-pressure mercury-arc lamp has been the traditional light source for Raman experimentation. For the present apparatus, however, a Spectra Physics Model 125 continuous helium-neon gas laser with a nominal power output of 50 mW at 6328 Å was chosen to provide the excitation light. The path of the laser beam can be easily controlled without serious loss of intensity for use with the unusual sample-cell configurations required for handling corrosive molten-salt samples. Also, the red 6328 Å radiation can be used to study blue-absorbing colored samples (such as solutions of Li_3Bi in molten LiCl).

Figure D.1 is a schematic illustration of the apparatus. Monochromatic light from the laser source (1) passes through a plane of polarization rotator (2). At this point, the light can be mechanically chopped to provide an ac signal, or it can pass unimpeded to generate a dc signal. However, in the dc mode of operation, black-body radiation from the molten-salt samples will show up as large, somewhat noisy background curves superimposed on the Raman spectrum. For this reason, provision has been made in the present apparatus to mechanically chop the laser beam at 400 cps with a rotating disc (3), and to amplify the signal from the photomultiplier with a phase-sensitive ac amplifier (4). The average value of the back-body radiation curve is thereby reduced to zero (although the noise contribution is still present). Such ac operation is virtually essential for Raman investigations of molten salts, particularly when red 6328 Å radiation is used as the excitation frequency.

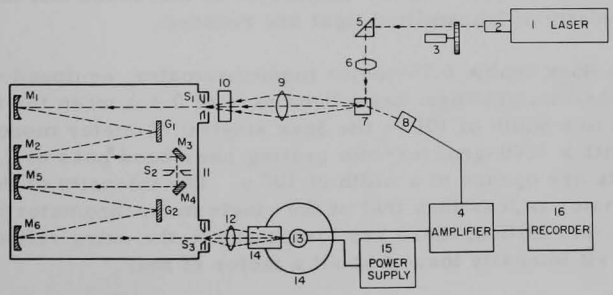

308-637

Fig. D.1. Laser-excited Raman Spectrophotometer (Schematic Diagram)

The 400-cps beam is reflected by a prism (5) and then passes vertically through a focusing lens (6) to the sample (7). About 4% of the beam is

reflected from the front surface of the uncoated prism to a photo-resistive detector (8), which provides a reference signal for the ac amplifier. A portion of the Raman light scattered upward by the sample is reflected by a mirror to a lens (9) and focused through optical filters (10) (optional) onto the entrance slit (S_1) of a 0.75-meter f/6.8 Spex Model 1400 scanning double monochromator (11), equipped with a pair of 103-mm-square, 1200-grooves/mm gratings blazed for 7500 Å. Light that has entered the double monochromator through the entrance slit is reflected from a collimating mirror (M_1), a plane-dispersing grating (G_1), a condensing mirror (M_2), and a plane-transfer mirror (M_3) before passing out through the exit slit (S_2). The exit slit also serves as the entrance slit for the second half of the double monochromator. The optical path of the second half is similar to the path in the first half. The light is reflected from a second plane-transfer mirror (M_4), a collimating mirror (M_5), a plane dispersing grating (G_2), and a condensing mirror (M_6) before passing out through the final exit slit (S_3).

The double monochromator is, in effect, two monochromators operated in series. This series operation greatly reduces stray light and grating-ghost intensity, and permits the study of weak Raman lines in the presence of large amounts of directly reflected exciting light. When two monochromators are operated in series, they can be arranged so that their dispersion is additive or subtractive. Consider, for example, operation with all three slits open the same amount. If white light enters the entrance slit of the first monochromator, the light leaving the second slit will not be monochromatic but will consist of a small, but nevertheless real and finite, range of frequencies, regularly increasing from one edge of the slit to the other. This variation in frequency can be increased or simply inverted in direction as a result of passing through the second monochromator. Inspection of the various reflections in the optical path of the Spex 1400 double monochromator reveals that the dispersion is increased and the band pass and the intensity of transmitted light are reduced.

The Spex double 0.75-meter monochromator, equipped with 1200 grooves/mm gratings, has a band pass of 0.5 Å when the three slits are opened to a width of 100 μ; the Spex single 0.75-meter monochromator, equipped with a 1200-grooves/mm grating, has a band pass of 1.0 Å when the two slits are opened to a width of 100 μ. The intensity of the double monochromator is less than that of the single monochromator by a factor of two, and, in addition, there are losses due to the extra reflections (~50%) for an overall intensity loss of about a factor of four.

The two instruments should be compared at the same band pass. Opening the three slits of the double instrument to a width of 200 μ increases the band pass to 1.0 Å, and (assuming that the wider entrance slit can still be filled with light) increases the intensity by a factor of four. Contrary to many widely held opinions, a double monochromator can produce the same intensity as that produced by a single instrument.

Referring once again to Fig. D.1, light from the final exit slit is focused by a condensing lens (12) onto the photosensitive cathode of a specially selected photomultiplier tube (13). The photomultiplier tube is surrounded by a cryostat (14) to permit cooling of the tube. The photomultiplier cryostat incorporates an evacuated cylinder with quartz windows at each end to provide an optically transparent thermal barrier in front of the photo-cathode. A high-voltage power supply (15) activates the photomultiplier. The signal from the photomultiplier is amplified by a phase-sensitive ac amplifier, and the amplified signal is recorded by a conventional strip-chart recorder (16).

ACKNOWLEDGMENTS

We are grateful to R. C. Vogel for encouragement and support of this program. S. E. Wood has given valuable advice, particularly in the area of thermodynamics. The contributions of J. P. Elder, J. A. Plambeck, and R. R. Heinrich are appreciated. Expert technical assistance has been provided by J. W. Allen, R. Eppley, S. A. Johnson, G. H. Kucera, J. L. Peck, G. L. Rogers, M. B. Silverman, and J. Tralmer. Both technical and painstaking editorial assistance have been provided by E. J. Hathaway.

REFERENCES

1. B. C. Almaula, in *Proc. 17th Annual Power Sources Conference*, p. 82, PSC Publications Committee, Red Bank, N. J. (1963).

2. G. R. Frysinger, in *Engineering Developments in Energy Conversion*, p. 266, Amer. Soc. Mech. Eng., New York (1965).

3. A. Leonard, in *Proc. Intersociety Energy Conversion Engineering Conference*, p. 322, Amer. Inst. Aeronautics and Astronautics, New York (1966).

4. B. I. Leefer, in *Proc. 20th Annual Power Sources Conference*, p. 172, PSC Publications Committee, Red Bank, N. J. (1966).

5. S. F. Bauer, in *Proc. 20th Annual Power Sources Conference*, p. 162, PSC Publications Committee, Red Bank, N. J. (1966).

6. R. W. Fritts, in *Proc. Intersociety Energy Conversion Engineering Conference*, p. 148, Amer. Inst. Aeronautics and Astronautics, New York (1966).

7. H. Shimotake and E. J. Cairns, *Performance Characteristics of a Sodium-Bismuth Cell*, presented at the Dallas meeting of the Electrochemical Society (May 1967).

8. C. E. Crouthamel, M. S. Foster, and D. Anthes, "Thermally Regenerative Emf Cell," *Chemical Engineering Division Summary Report, April, May, June 1961*, ANL-6379, pp. 229-242 (Oct 1961).

9. C. E. Crouthamel, M. S. Foster, R. R. Heinrich, and R. Eppley, "Thermally Regenerative Emf Cell," *Chemical Engineering Division Summary Report, July, August, September 1961*, ANL-6413, pp. 199-201.

10. C. E. Crouthamel, M. S. Foster, R. R. Heinrich, R. Eppley, and M. Jones, "Regenerative Emf Cell," *Chemical Engineering Division Summary Report, October, November, December 1961*, ANL-6477, pp. 204-213 (March 1962).

11. C. E. Crouthamel, M. S. Foster, C. E. Johnson, R. R. Heinrich, R. Eppley, and S. F. Banazek, "Regenerative Emf Cell," *Chemical Engineering Division Summary Report, January, February, March 1962*, ANL-6543, pp. 195-203 (June 1962).

12. C. E. Crouthamel, M. S. Foster, C. E. Johnson, R. R. Heinrich, R. Eppley, and S. F. Banazek, "Regenerative Emf Cell," *Chemical Engineering Division Summary Report, April, May, June 1962*, ANL-6569, p. 156 (Aug 1962).

13. C. E. Crouthamel, M. S. Foster, C. E. Johnson, R. R. Heinrich, R. Eppley, and S. F. Banazek, "Regenerative Emf Cell," *Chemical Engineering Division Summary Report, July, August, September 1962*, ANL-6596, pp. 201-207.

14. C. E. Crouthamel, M. S. Foster, C. E. Johnson, R. R. Heinrich, R. Eppley, J. Allen, and G. H. McCloud, "Regenerative Emf Cell," *Chemical Engineering Division Summary Report, October, November, December 1962*, ANL-6648, pp. 213-216 (May 1963).

15. C. E. Crouthamel, M. S. Foster, C. E. Johnson, R. R. Heinrich, R. Eppley, J. Allen, and G. H. McCloud, "Regenerative Emf Cell," *Chemical Engineering Division Summary Report, January, February, March 1963*, ANL-6687, pp. 188-198.

16. C. E. Crouthamel, M. S. Foster, C. E. Johnson, A. K. Fischer, R. Eppley, J. Allen, and S. A. Johnson, "Regenerative Emf Cell," *Chemical Engineering Division Summary Report, April, May, June 1963*, ANL-6725, pp. 224-234.

17. C. E. Crouthamel, M. S. Foster, C. E. Johnson, A. K. Fischer, R. Eppley, J. Allen, and S. A. Johnson, "Regenerative Emf Cell, *Chemical Engineering Division Semiannual Report, July-December 1963*, ANL-6800, pp. 403-420 (May 1964).

18. C. E. Crouthamel, M. S. Foster, C. E. Johnson, A. K. Fischer, R. Eppley, J. Allen, R. R. Heinrich, J. C. Hesson, and H. Shimotake, "Energy Conversion," *Chemical Engineering Division Semiannual Report, January-June 1964*, ANL-6900, pp. 304-329 (Aug 1964).

19. C. E. Crouthamel, J. C. Hesson, A. D. Tevebaugh, C. E. Johnson, R. R. Heinrich, J. Elder, J. Plambeck, M. S. Foster, R. Eppley, H. Shimotake, G. H. McCloud, A. K. Fischer, and S. A. Johnson, "Energy Conversion," *Chemical Engineering Division Semiannual Report, July-December 1964*, ANL-6925, pp. 235-247 (May 1965).

20. C. E. Crouthamel, J. C. Hesson, A. D. Tevebaugh, C. E. Johnson, R. R. Heinrich, J. Elder, J. Plambeck, M. S. Foster, R. Eppley, G. H. McCloud, A. K. Fischer, S. A. Johnson, H. Shimotake, J. Tralmer, G. Rogers, and J. Allen, "Energy Conversion," *Chemical Engineering Division Semiannual Report, January-June 1965*, ANL-7055, pp. 213-229 (Oct 1965).

21. C. E. Crouthamel, J. C. Hesson, A. D. Tevebaugh, J. D. Bingle, C. E. Johnson, R. R. Heinrich, E. J. Hathaway, M. S. Foster, G. H. McCloud, A. K. Fischer, S. A. Johnson, H. Shimotake, J. Tralmer, G. Rogers, J. Allen, and M. Silverman, "Energy Conversion," *Chemical Engineering Division Semiannual Report, July-December 1965*, ANL-7125, pp. 200-236 (May 1966).

22. A. D. Tevebaugh, J. D. Bingle, M. S. Foster, G. H. McCloud, C. E. Johnson, E. J. Hathaway, N. Quattropani, A. K. Fischer, S. A. Johnson, E. L. Gasner, J. C. Hesson, H. Shimotake, G. Rogers, and M. Silverman, "Energy Conversion," *Chemical Engineering Division Semiannual Report, January-June 1966*, ANL-7225, pp. 214-225 (Nov 1966).

23. E. J. Cairns, A. D. Tevebaugh, J. D. Bingle, C. E. Johnson, M. S. Foster, E. J. Hathaway, J. Peck, E. L. Gasner, T. F. Young, G. H. McCloud, A. K. Fischer, S. A. Johnson, S. E. Wood, H. Shimotake, G. Rogers, and J. Kargol, "Energy Conversion," *Chemical Engineering Division Semiannual Report, July-December 1966*, ANL-7325, pp. 179-196 (April 1967).

24. J. C. Hesson and H. Shimotake, in *Regenerative Emf Cells*, C. E. Crouthamel and H. L. Recht, Eds., Advances in Chemistry Series *64*, p. 82, Amer. Chem. Soc., Washington, D. C. (1967).

25. H. A. Liebhafsky and E. J. Cairns, *Fuel Cells and Fuel Batteries*, John Wiley and Sons, New York, in press (1968).

26. H. A. Liebhafsky and E. J. Cairns, in *Fuel Cells, a CEP Technical Manual*, p. 50, Amer. Inst. of Chem. Engrs., New York (1963).

27. A. K. Fischer, in *Regenerative Emf Cells*, C. E. Crouthamel and H. L. Recht, Eds., Advances in Chemistry Series *64*, p. 121, Amer. Chem. Soc., Washington, D. C. (1967).

28. I. I. Kornilov, *The Chemistry of the Metallides*, J. W. Loweberg, translator, p. 17, Consultants Bureau, New York (1966).

29. M. Hansen and K. Anderko, *Constitution of Binary Alloys*, McGraw-Hill, New York (1958).

30. E. M. Levin, C. R. Robbins, and H. F. McMurdie, *Phase Diagrams for Ceramists*, Amer. Ceramic Soc., Columbus, Ohio (1964).

31. A. S. Dworkin, H. R. Bronstein, and M. A. Bredig, J. Phys. Chem. *66*, 572 (1962).

32. M. A. Bredig and H. R. Bronstein, J. Phys. Chem. *64*, 65 (1960).

33. J. W. Johnson and M. A. Bredig, J. Phys. Chem. *62*, 606 (1958).

34. M. A. Bredig and J. W. Johnson, J. Phys. Chem. *64*, 1900 (1960).

35. C. E. Johnson and E. J. Hathaway, *Solid-Liquid Phase Equilibria for the Ternary Sodium Fluoride-Sodium Chloride-Sodium Iodide System*, J. Chem. Eng. Data (to be published).

36. C. E. Johnson and E. J. Cairns, *Solid-Liquid Phase Equilibria for the Ternary Lithium Fluoride-Lithium Chloride-Lithium Iodide System*, J. Chem. Eng. Data (to be published).

37. C. E. Johnson and R. R. Heinrich, in *Regenerative Emf Cells*, C. E. Crouthamel and H. L. Recht, Eds., Advances in Chemistry Series *64*, p. 105, Amer. Chem. Soc., Washington, D. C. (1967).

38. M. S. Foster, in *Regenerative Emf Cells*, C. E. Crouthamel and H. L. Recht, Eds., Advances in Chemistry Series *64*, p. 136, Amer. Chem. Soc., Washington, D. C. (1967).

39. E. A. Guggenheim, *Thermodynamics*, p. 391, Interscience Publishers, Inc., New York (1957).

40. K. Hauffe and A. L. Vierk, Z. Elektrochem. *53*, 151 (1949).

41. M. F. Lantratov, Russian J. Inorg. Chem. *4*, 927 (1959).

42. M. S. Foster, G. H. McCloud, and E. J. Cairns, *Electrochemical Studies of the Sodium-Bismuth System*, presented at the Symposium on Electrode Processes, Miami Beach Meeting of American Chemical Society (April 1967).

43. W. E. Garner, *Chemistry of the Solid State*, p. 31, Academic Press, Inc., New York (1955).

44. M. S. Foster, C. E. Johnson, and C. E. Crouthamel, *Helium-purification Unit for High-purity Inert-atmosphere Boxes*, ANL-6652 (Dec 1962).

45. C. E. Johnson, M. S. Foster, and M. L. Kyle, Nucl. Applications *3*, 563 (1967).

46. B. Porter and M. Feinleib, J. Electrochem. Soc. *103*, 300 (1956).

47. N. S. Kurnakow and A. N. Kusnetzow, Z. Anorg. Chem. *23*, 455 (1900).

48. A. K. Fischer, J. Chem. Phys. *45*, 375 (1966).

49. J. Egan and J. Bracker, in *Nuclear Engineering Department Progress Report, May 1-August 31, 1960*, BNL-646, p. 6, Brookhaven National Laboratory.

50. C. Beusman, *Activities in the KCl-$FeCl_2$ and LiCl-$FeCl_2$ Systems*, ORNL-2323, Oak Ridge National Laboratory (May 1957).

51. J. Berkowitz, W. A. Chupka, and A. K. Fischer, Argonne National Laboratory, unpublished data.

52. R. Hultgren, R. L. Orr, P. D. Anderson, and K. K. Kelley, *Selected Values of Thermodynamic Properties of Metals and Alloys*, John Wiley and Sons, Inc., New York (1963).

53. D. R. Stull and G. C. Sinke, *Thermodynamic Properties of the Elements*, Advances in Chemistry Series *18*, Amer. Chem. Soc., Washington, D. C., (1956).

54. M. Sittig, *Sodium, Its Manufacture, Properties and Uses*, Reinhold Publishing Corp., New York (1956).

55. R. G. Ward and J. R. Wilson, Nature *182*, 334 (1958).

56. E. F. W. Seymour and G. A. Styles, Proc. Phys. Soc. *87*, 473 (1966).

57. F. A. Vetter and O. Kubaschewski, Z. Elektrochem. *57*, 243 (1953).

58. N. G. Schmal and P. Sieben, *Physical Chemistry of Metallic Solutions and Intermetallic Compounds*, Vol. 1, National Physics Laboratory Symposium No. 9, Her Majesty's Stationery Office, London (1959).

59. E. Högfeldt, Arkiv för Kemi *7*, 315 (1954).

60. E. Högfeldt, Rec. Trav. Chim. *75*, 790 (1956).

61. *Metals Handbook*, 8th Edition, American Society for Metals, Metals Park, Ohio (1964).

62. W. D. Harkins and H. F. Jordan, J. Amer. Chem. Soc. *52*, 1751 (1930).

63. R. C. Vogel, M. Levenson, and F. R. Masten, *Chemical Engineering Division Research Highlights, May 1964-April 1965*, ANL-7020, pp. 198-225.

64. R. C. Vogel, M. Levenson, J. Schraidt, and J. Royal, *Chemical Engineering Division Research Highlights, May 1965-April 1966*, ANL-7175, pp. 184-211.

65. E. Heymann, Australian Chem. Inst. J. and Proc. *4*, 38 (1937).

66. E. Heymann, R. J. L. Martin, and M. F. R. Mulcahy, J. Phys. Chem. *47*, 473 (1943).

67. E. Heymann and H. P. Weber, Nature *141*, 1059 (1938).

68. E. Heymann and H. P. Weber, Trans. Faraday Soc. *34*, 1492 (1938).

69. M. F. R. Mulcahy and E. Heymann, J. Phys. Chem. *47*, 485 (1943).

70. Yu. K. Delimarskii, O. G. Zarubitskii, and I. G. Pavlenko, Ukr. Khim. Zh. *30*, 1289 (1964).

71. Yu. K. Delimarskii, I. G. Pavlenko, O. G. Zarubitskii, and Y. A. Oleinik, Zh. Prikl. Khim. *38*, 816 (1965).

72. Yu. K. Delimarskii and O. G. Zarubitskii, Dopovidi Akad. Nauk RSR 1965, 619.

73. Yu. K. Delimarskii, O. G. Zarubitskii, and I. G. Pavlenko, Ukr. Khim. Zh. *31*, 469 (1965).

74. Yu. K. Delimarskii, O. G. Zarubitskii, and I. G. Pavlenko, Ukr. Khim. Zh. *31*, 573 (1965).

75. I. G. Pavlenko, O. G. Zarubitskii, and V. A. Oleinik, Dopovidi Akad. Nauk Ukr. RST 1963, 1222.

76. R. D. Weaver, S. W. Smith, and N. L. Willman, J. Electrochem Soc. *109*, 653 (1962).

77. C. S. Smith, Trans. A.I.M.E. *137*, 236 (1940).

78. W. Plato, Z. physik. Chem., *58*, 350 (1907).

79. N. S. Rassonskaya and A. G. Bergman, J. Gen. Chem., USSR, *23*, 11 (1953).

80. M. A. Kuvakin and P. S. Kusakin, Russian J. Inorg. Chem. *4*, 1188 (1959).

81. M. Amadori, Atti della reale accademia nazionale dei Lincei *21I*, 467 (1912).

82. I. I. Ilyasov and A. K. Bostandzhiyan, J. Gen. Chem., USSR, *26*, 2673 (1956).

83. O. Ruff and W. Plato, Ber. Deutsch. chem. Ges. *36*, 2357 (1903).

84. N. S. Dombrovskaya, Isvest. Sektora. Fiz. Khim. Anal., Inst. Obshcheî Neorg. Khim. Akad. Nauk SSSR *20*, 127 (1950).

85. B. Agruss, J. Electrochem. Soc. *110*, 1097 (1963).

86. R. N. Lyon, *Liquid Metals Handbook*, NAVEXOS P-773 (Rev), Office of Naval Research (1954).

87. J. C. Hesson, Argonne National Laboratory, private communication.

88. G. H. J. Broers, thesis, University of Amsterdam, Amsterdam (1958).

89. G. H. J. Broers and M. Schenke, in *Fuel Cells*, Vol. 2, Reinhold Publishing Company, New York (1963).

90. G. H. J. Broers and M. Schenke, *High Temperature Galvanic Fuel Cells*, AD-234912, U. S. Army Procurement Center (Jan 1960).

91. G. H. J. Broers, in *Fuel Cells, a CEP Technical Manual*, p. 90, Amer. Inst. of Chem. Engrs., New York (1963).

92. S. Yoshizawa, Z. Takehara, and Y. Nakanishi, Denki Kagaku *35*, 294 (1967).

93. S. C. Hyman, C. F. Bonilla and S. W. Ehrlich, Chem. Eng. Progr. *49*, No. 5, Heat Transfer, 21 (1953).

94. D. Dropkin and E. Somerscales, J. Heat Transfer *87*, 77 (1965).

95. A. Emery and N. C. Chu, J. Heat Transfer *87*, 110 (1965).

96. R. P. Stein in *Advances in Heat Transfer*, Vol. 3, T. Irvine, Jr., and J. P. Hartnett, Eds., p. 101, Academic Press, New York (1966).

97. *Proceedings of the 1963 High-Temperature Liquid-Metal Heat Transfer Technology Meeting*, Vol. 1 and 2, ORNL-3605 (1964).

98. S. Hatta, Technol. Repts. Tohoku Imp. Univ. *8*, 1 (1929).

99. J. Crank, *The Mathematics of Diffusion*, p. 34, Oxford University Press, London (1956).

100. W. D. Weatherford, Jr., J. C. Tyler, and P. M. Ku, *Properties of Inorganic Energy Conversion and Heat Transfer Fluids for Space Applications*, WADD-TR-61-96, Wright Air Development Division (1961).

101. P. J. Martro and W. M. Rohsenow, Report No. 5219-33, Heat Transfer Laboratory, MIT (1965).

102. E. R. G. Eckert, E. M. Sparrow, W. E. Ibele, and R. J. Goldstein, J. Heat Mass Transfer *9*, 599 (1966).

103. W. M. Rohsenow, Ind. Eng. Chem. *58*, 40 (1966).

104. Y. S. Tang, Nuclear Applications *1*, 521 (1965).

105. S. R. Gunn and L. G. Green, J. Amer. Chem. Soc. *80*, 4482 (1958).

106. C. E. Messer, L. G. Fasolino, and C. E. Thalmayer, J. Amer. Chem. Soc. *77*, 4524 (1955).

107. H. A. Laitinen, W. S. Ferguson, and R. A. Osteryoung, J. Electrochem. Soc. *104*, 516 (1957).

108. D. L. Maricle and D. N. Hume, J. Electrochem. Soc. *107*, 354 (1960).

109. C. E. Messer, *A Survey Report on Lithium Hydride*, NYO-9470, Tufts University (Oct 1960).

110. C. E. Johnson, S. E. Wood, and C. E. Crouthamel, Inorg. Chem. *3*, 1487 (1964).

111. C. E. Johnson, S. E. Wood, and C. E. Crouthamel, J. Chem. Phys. *44*, 884 (1966).

112. C. Wagner and A. Werner, J. Electrochem. Soc. *110*, 326 (1963).

113. E. Elchardus and P. Laffitte, Bull. Soc. Chem. France *51*, 1572 (1932).

114. M. S. Foster, S. E. Wood, and C. E. Crouthamel, Inorg. Chem. *3*, 1428 (1964).

115. M. S. Foster, C. E. Crouthamel, and S. E. Wood, J. Phys. Chem. *70*, 3042 (1966).

116. M. S. Foster and C. C. Liu, J. Phys. Chem. *70*, 950 (1966).

117. *JANAF Thermochemical Tables*, Dow Chemical Company (1962).

118. J. W. Vogt, *Measurements of Thermal Properties of LiH and LiH-Li Mixtures: Enthalpy, Heat of Fusion, Conductivity*, TAPCO Report NP-11888, Thompson Ramo Wooldridge, Inc. (Oct 1961).

119. K. K. Kelley and E. G. King, *Entropies of the Elements and Inorganic Compounds*, Bulletin 592, Bureau of Mines (1961).

120. J. King, F. A. Ludwig, and J. J. Rowlette, in *Energy Conversion for Space Power*, Vol. 3, p. 387, N. W. Snyder, Ed., Academic Press, New York (1961).

121. E. R. Van Artsdalen and I. S. Yaffee, J. Phys. Chem. *59*, 118 (1955).

122. M. S. Foster, C. E. Crouthamel, D. M. Gruen, and R. L. McBeth, J. Phys. Chem. *68*, 980 (1964).

123. J. Fischer, Argonne National Laboratory, private communication.

124. E. L. Gasner and H. H. Claasen, *Raman Spectrum of XeF_6*, presented at the Miami Beach Meeting of the American Chemical Society (April 1967).

125. G. J. Janz and D. W. James, J. Chem. Phys. *35*, 739 (1961).

126. D. M. Gruen, R. L. McBeth, M. S. Foster, and C. E. Crouthamel, J. Phys. Chem. *70*, 472 (1966).

127. A. A. Botschwar, Z. anorg. u. allgem. Chem. *210*, 163 (1933).

128. H. M. Haendler, P. S. Sennet, and C. M. Wheeler, J. Electrochem. Soc. *106*, 264 (1959).

129. A. G. Bergman and A. S. Arabadzhan, Zh. Neorgan. Khim *8*, 1228 (1963).

130. C. E. Messer and J. Mellor, J. Phys. Chem. *64*, 503 (1960).

131. C. E. Johnson, E. J. Hathaway, and C. E. Crouthamel, J. Chem. Eng. Data *11*, 372 (1966).

132. C. E. Johnson, S. E. Wood, and E. J. Cairns, *Reply to the Comments of Bredig*, J. Chem. Phys. *46*, 4168 (1967).

133. R. R. Heinrich, C. E. Johnson, and C. E. Crouthamel, J. Electrochem. Soc. *112*, 1067 (1965).

134. R. R. Heinrich, C. E. Johnson, and C. E. Crouthamel, J. Electrochem. Soc. *112*, 1071 (1965).

135. C. J. Smithels, *Gases and Metals*, John Wiley and Sons, Inc., New York (1937).

136. K. Peters, Z. anorg. u. allgem. Chem. *131*, 140 (1923).

137. E. C. Potter and J. O'M. Bockris, in Colloques Intern. Centre Natl. Rech. Sci. (Paris) *39*, Electrolyse, C3-C6 (1952).

138. R. E. Shearer and R. C. Werner, J. Electrochem. Soc. *105*, 693 (1958).

139. R. C. Werner, R. E. Shearer, and T. A. Ciarlariello, in *Proc. 13th Annual Power Sources Conference*, p. 122, PSC Publications Committee, Red Bank, N. J. (1959).

140. R. E. Shearer, J. W. Mausteller, T. A. Ciarlariello, and R. C. Werner, in *Proc. 14th Annual Power Sources Conference*, p. 76, PSC Publications Committee, Red Bank, N. J. (1959).

141. T. A. Ciarlariello and R. C. Werner, Chem. Engr. Progr. *57*, 42 (1961).

142. M. E. Indig and R. N. Snyder, J. Electrochem. Soc. *109*, 757 (1962).

143. J. A. Plambeck, J. P. Elder, and H. A. Laitenen, J. Electrochem. Soc. *113*, 931 (1966).

144. C. H. Liu, K. E. Johnson, and H. A. Laitenen, in *Molten Salt Chemistry*, M. Blander, Ed., p. 695, Interscience, New York (1964).

145. J. J. Lingane, *Electroanalytical Chemistry*, 2nd ed., p. 260, Interscience, New York (1958).

146. D. R. Snoke, *Zero Gravity Separator Development for Regenerative Fuel Cell*, TAPCO Report ASD-TDR-62-240, Thompson Ramo Wooldridge, Inc., Cleveland, Ohio (1962).

147. H. Shimotake and E. J. Cairns, *Bimetallic Galvanic Cells with Fused Salt Electrolytes*, in Advances in Energy Conversion Engineering 1967, p. 951, American Society of Mechanical Engineers.

148. H. Shimotake, G. Rogers, and E. J. Cairns, *Performance Characteristics of the Lithium-Tellurium Cell*, presented at the Chicago Meeting of the Electrochemical Society (Oct 1967).

149. E. J. Cairns and H. Shimotake, *Recent Advances in Fuel Cells and Their Application to New Hybrid Systems*, Fifth Biennial Fuel Cell Symposium, Vol. 11, No. 3, p. 321, American Chemical Society Meeting, Chicago, Ill., Sept. 10-15, 1967.

150. M. S. Foster, C. E. Crouthamel, and S. E. Wood, J. Phys. Chem. *70*, 3042 (1966).

151. S. A. Schaaf and P. L. Chambré, *Flow of Rarefied Gases*, p. 5, Princeton University Press, Princeton, New Jersey (1961).

152. M. V. Smoluchowski, Ann. Physik. *33*, 1559 (1910).

153. M. Knudsen, Ann. Physik. *34*, 593 (1911).

154. R. P. Elliott, *Constitution of Binary Alloys*, First Supplement, McGraw Hill, Inc., New York, 1965.

155. B. C. Agrawal, Trans. Indian Inst. Metals *16*, 184 (Sept 1963).

156. T. Akutagawa and K. Ogawa, J. Japan Inst. Metals *24*, 256 (1960).

157. J. E. Atherton, Jr., O. F. Kammerer, C. J. Klamut, and J. Sodofsky, *Static Corrosion Behavior of Materials in Bi and U-Bi Solution at 550°C*, BNL-395, Brookhaven National Laboratory (Aug 1954).

158. *Liquid Metal Fuel Reactor Experiment Quarterly Technical Report, July-September 1958*, BAW-1125, Babcock and Wiscox Co.

159. B. Blumenthal, L. R. Kelman, and H. V. Rhude, *Some Metallurgical Considerations in the Design and Operation of the Top Seal of EBR-II*, ANL-6837 (April 1964).

160. *Nuclear Engineering Department Progress Report*, BNL-418, November 15, 1955-February 15, 1956; BNL-434, February 15-December 31, 1956; BNL-472, January 3-April 30, 1957; BNL-477, May 1-September 30, 1957; BNL-491, October 1-December 31, 1957; BNL-506, January 1-March 31, 1958; BNL-516, April 1-June 30, 1958; BNL-536, July 1-September 30, 1958; BNL-554, October 1-December 31, 1958; BNL-583, May 1-August 31, 1959; BNL-595, September 1-December 31, 1959; BNL-646, May 1-August 31, 1960; BNL-659, September 1-December 31, 1960; Brookhaven National Laboratory.

161. D. Buttinelli, G. deGregorio, and G. Signorelli, Ric. Sci. Rend. *1*, 127 (1961).

162. R. J. Cash, R. M. Fisher, and M. R. Core, *Compatibility Studies of Several Molten Uranium and Thorium Alloys in Niobium, Tantalum, and Yttrium*, IS-888, Ames Laboratory (Feb 1964).

163. J. V. Cathcart and W. D. Manly, Corrosion *12*, 87t (1956); Corrosion *10*, 432 (1954).

164. J. C. Clifford, *A Loop for Circulating Liquid Lead-Bismuth Mixtures: Corrosion and Equipment Studies*, M. S. thesis, Iowa State University of Science and Technology (1958).

165. J. C. Clifford, *A Loop for Circulating Liquid Lead-Bismuth Mixtures: Corrosion Studies and Operation*, Ph.D. thesis, Iowa State University of Science and Technology (1960).

166. J. F. Collins, *Summary Report on the Solubility of Metals and Alloys in Pure Bismuth Eutectic at Temperatures up to 2200°F*, NEPA-1800, NEPA Division, Fairchild Engine and Airplane Corporation (April 1951).

167. J. F. Collins and H. R. Stephan, *The Solubility of Metals and Alloys in Lead-Bismuth Eutectic at Temperatures up to 2200°F*, NEPA-1803, NEPA Division, Fairchild Engine and Airplane Corporation (April 1951).

168. W. H. Cook, *Corrosion Resistance of Various Ceramics and Cermets to Liquid Metals*, ORNL-2391, Oak Ridge National Laboratory (June 1960).

169. M. A. Cordovi, *Static Corrosion Behavior of Construction Materials in an Environment of Liquid Bismuth Base Metals at 500°C*, BNL-179, Brookhaven National Laboratory (March 1952).

170. T. A. Coultas, *Corrosion of Refractories by Tin and Bismuth*, NASA-SR-192, North American Aviation, Inc. (Sept 1952).

171. A. K. Covington and A. A. Woolf, J. Nucl. Energy, Pt. B: Reactor Technology *1*, 35 (1959).

172. R. Cygan, *Circulation of Pb-Bi Eutectic at Intermediate Temperatures*, NAA-SR-253, North American Aviation, Inc. (Oct 1953).

173. R. Cygan, *Lead-Bismuth Eutectic Thermal Convection Loop*, NAA-SR-1060, North American Aviation, Inc. (Oct 1954).

174. D. W. Dawe, G. W. Parry, and G. W. Wilson, J. Brit. Nuclear Energy Conf. *5*, 24 (Jan 1960).

175. R. E. Deville and W. R. Foley, *Liquid Metal Fuel Reactor Experiment: Liquid Bismuth Dynamic Corrosion Tests*, BAW-1253, Babcock and Wilcox Company (June 1960).

176. C. J. Egan, *Dynamic Corrosion and Mass Transfer of Chrome Steel by Bismuth*, AECD-3733, California Research Corporation (Dec 1951).

177. V. W. Eldred, *Interactions Between Solid and Liquid Metals and Alloys*, AERE-X/R 1806, Atomic Energy Research Establishment (1953).

178. O. J. Elgert and C. J. Egan, *Dynamic Corrosion of Steel by Liquid Bismuth*, CRD-T1-74, California Research and Development Company (Aug 1952).

179. O. J. Elgert and C. J. Egan, *Dynamic Corrosion of Steel by Liquid Bismuth*, MTA-12, California Research and Development Company (Jan 1953).

180. A. deS. Brasunas, *Interim Report on Static Liquid Metal Corrosion*, ORNL-1647, Oak Ridge National Laboratory (May 1954).

181. H. M. Finniston, in *Australian Atomic Energy Symposium Proc. 1958*, 189.

182. R. W. Fisher and C. B. Fullhart, in *Proceedings of the Second United Nations International Conference on the Peaceful Uses of Atomic Energy, Geneva, 1958, 7*, 216, United Nations, New York.

183. W. D. Forgeng, Jr., *Corrosion of Copper by Liquid Lead in an Isothermal Loop*, Ph.D. thesis, Purdue University (1962).

184. J. J. Gangler, J. Am. Ceram. Soc. *37*, 312 (July 1954).

185. R. C. Grassi, D. W. Bainbridge, and J. W. Harman, *Final Report on Metallurgical Investigation of Materials Subjected to Liquid Lead-Bismuth Alloy Environment*, AECU-2201, University of California (July 1952).

186. W. J. Hallett and T. A. Coultas, *Dynamic Corrosion of Graphite by Liquid Bismuth*, NAA-SR-188, North American Aviation, Inc. (Sept 1952).

187. G. W. Horsley and J. T. Maskrey, J. Iron Steel Inst. (London) *189*, 139 (June 1958).

188. G. W. Horsley and J. T. Maskrey, J. Inst. Metals *86*, 401 (1957/1958).

189. Y. Imai and T. Ishizaki, Nippon Genshiryoku Gakkaishi *2*, 96 (1960).

190. Y. Imai, T. Ishizaki, K. Nishino, and T. Matumoto, in *Corrosion of Reactor Materials, Volume II*, International Atomic Energy Agency, Vienna (1962).

191. Y. Imai and K. Nishino, Sci. Rept. Res. Inst., Tohoku Univ., Ser. A, *15(4)* 186 (1963).

192. Y. Imai and K. Nishino, Sci. Rept. Res. Inst., Tohoku Univ., Ser. A, *15(4)* 197 (1963).

193. J. A. James and J. Trotman, J. Iron Steel Inst. (London) *194*, 319 (March 1960).

194. Y. Kamemoto, Y. Takahashi, and S. Yamaguchi, Nippon Genshiryoku Gakkaishi *6*, 71 (Feb 1964).

195. C. J. Klamut, D. G. Schweitzer, Y. G. Y. Chow, R. A. Meyer, O. F. Kammerer, J. R. Weeks, and D. H. Gurinsky, in *Proceedings of the Second United Nations International Conference on the Peaceful Uses of Atomic Energy, Geneva, 1958, 7*, 173, United Nations, New York.

196. J. R. Lance, G. A. Kemeny, Am. Soc. Metals, Trans. Quart. *56*, 204 (1963).

197. E. D. Lloyd, in *Plansee Proc. 3rd Seminar, Reutte/Tyrol, 1958*, 249 (1959).

198. *Technical Progress Report for the Period of April-September 1955*, NMI-1139, Nuclear Metals, Inc. (Feb 1956).

199. *Aircraft Nuclear Propulsion Project, Quarterly Progress Report for Period Ending June 10, 1953*, ORNL-1556, Oak Ridge National Laboratory (July 1953).

200. R. Parkman and O. C. Shepard, *Investigation of Materials for Use in Heat Transfer System Containing Liquid Lead Alloys, Report No. XII, Final Report*, ORO-45, Stanford University (June 1951).

201. G. W. Parry and L. W. Graham, J. Inst. Metals *87*, 125 (Dec 1958).

202. R. Potter, R. Wingard, and R. Boggild, *Preliminary Handling Tests of Liquid Bismuth*, NEPA-1482, NEPA Division, Fairchild Engine and Airplane Corporation (June 1950).

203. H. A. Pray, R. S. Peoples, and W. K. Boyd, *Corrosion by Molten Bismuth*, BMI-773, Battelle Memorial Institute, October 1952.

204. E. L. Reed, J. Amer. Ceramic Soc. *37*, 146 (1954).

205. A. J. Romano, C. J. Klamut, and D. H. Gurinsky, *The Investigation of Container Materials for Bi and Pb Alloys. Part I. Thermal Convection Loops*, BNL-811, Brookhaven National Laboratory (July 1963).

206. D. G. Schweitzer and J. R. Weeks, Am. Soc. Metals, Trans. Quart. *54*, 185 (1961).

207. J. W. Seifert and A. L. Lowe, Jr., Corrosion *17*, 475t (1961).

208. O. C. Shepard, J. R. Morgan, R. Parkman, K. L. Keating, and R. D. Seibel, *Investigation of Materials for Use in a Heat Transfer System Containing Liquid Lead or Bismuth, Report No. 14*, AECU-2549, Stanford University (April 1953).

209. H. Shimotake and J. C. Hesson, Trans. Am. Nucl. Soc. *8*(2), 413 (1965).

210. H. R. Stephan and W. J. Koshuba, "Circulation of Bismuth at Elevated Temperatures," *Progress Report on Project 2-01, NEPA-1675*, NEPA Division, Fairchild Engine and Airplane Corporation (Dec 1950).

211. C. H. Waide, L. E. Kukacka, R. A. Meyer, J. Milau, J. H. Klein, J. G. Y. Chow, C. J. Klamut, and D. H. Gurinsky, *Uranium-Bismuth In-Pile Corrosion Test Loop, Radiation Loop No. 1*, BNL-736 (T-265), Brookhaven National Laboratory (May 1961).

212. A. G. Ward and J. W. Taylor, J. Inst. Metals *86*, 36 (1957/1958).

213. A. G. Ward and J. W. Taylor, J. Inst. Metals *85*, 145 (1956/1957).

214. J. R. Weeks, Am. Soc. Metals, Trans. Quart. *58*, 302 (1965).

215. W. D. Wilkinson, *Attack on Metals by Bismuth-Lead-Tin Alloy at Elevated Temperatures*, ANL-5262 (Jan. 15, 1954).

216. W. D. Wilkinson, E. W. Hoyt, and H. V. Rhude, *Attack on Materials by Lead at 1000°C*, ANL-5449 (Oct 1955).

217. S. Yajima, Y. Kamemoto, and Y. Takahaski, Nippon Genshiryoku Gakkaishi *5*, 672 (1963).

218. G. M. Adamson, W. D. Manly, and R. S. Crouse, in *ANP Materials Meeting, November 16-18, 1954*, ORNL-2685, p. 127, Oak Ridge National Laboratory (March 1959).

219. L. Hays and W. Seefeldt, "Fluorination Corrosion," *Chemical Engineering Division Summary Report, July, August, September, 1959*, ANL-6068, pp. 107-109.

220. *Progress Relating to Civilian Applications During May 1963*, BMI-1632, Battelle Memorial Institute (May 1963).

221. A. deS. Brasunas, Metal Prog. *62*(6), 88 (1952).

222. J. H. DeVan, *Examinations of Pump Impellers from Sodium and Fused Salt Pump Endurance Tests*, ORNL-CF-61-4-77, Oak Ridge National Laboratory (April 1961).

223. J. H. DeVan and R. B. Evans, III, in *Corrosion of Reactor Materials, Volume II*, p. 557, International Atomic Energy Agency, Vienna (1962).

224. W. R. Grimes, F. F. Blankenship, G. W. Keilholtz, H. F. Poppendiek, and M. T. Robinson, in *Proceedings of the Second United Nations International Conference on Peaceful Uses of Atomic Energy, Geneva, 1958, 28*, 99, United Nations, New York.

225. E. E. Hoffman, P. Patriarca, C. F. Leitten, Jr., and G. M. Slaughter, *An Evaluation of the Corrosion and Oxydation Resistance of High Temperature Brazing Alloys. Period Covered: July 1954-September 1955*, ORNL-1934, Oak Ridge National Laboratory (Nov 1956).

226. A. P. Litman, *Corrosion of Volatility Pilot Plant Mark I INOR-8 Hydrofluorinator and Mark III L Nickel Fluorinator After Fourteen Dissolution Runs*, ORNL-3253, Oak Ridge National Laboratory (Feb 1962).

227. A. P. Litman and A. E. Goldman, *Corrosion Associated with Fluoridation in the Oak Ridge National Laboratory Fluoride Volatility Process*, ORNL-2832, Oak Ridge National Laboratory (June 1961).

228. M. B. McDonald, J. L. Crowley, and D. L. Clark, Trans. Am. Nucl. Soc. *2*(1), 174 (1959).

229. W. D. Manly, G. M. Adamson, Jr., J. H. Coobs, J. H. DeVan, D. A. Douglas, E. E. Hoffman, and P. Patriarca, *Aircraft Reactor Experiment-Metallurgical Aspects*, ORNL-2349, Oak Ridge National Laboratory (Jan 1958).

230. W. D. Manly, J. H. Coobs, J. H. DeVan, D. A. Douglas, H. Inouye, P. Patriarca, T. K. Roche, and J. L. Scott, in *Proceedings of the Second United Nations International Conference on Peaceful Uses of Atomic Energy, Geneva, 1958, 7*, 223, United Nations, New York.

231. R. A. Meyer and J. C. Bokros, in *Nuclear Graphite*, R. E. Nightingale, Ed., p. 445, Academic Press, New York (1962).

232. *Molten-Salt Reactor Program Semiannual Progress Report for Period Ending July 31, 1964*, ORNL-3708, Oak Ridge National Laboratory (Nov 1964).

233. G. P. Smith, J. H. DeVan, and A. G. Grindell, J. Basic Eng. *85*, 329 (Sept 1963).

234. A. Taboada, W. H. Cook, and P. Patriarca, Trans. Am. Nucl. Soc. *7*, 438 (Nov 1964).

235. H. R. Copson, J. Electrochem. Soc. *100*, 257 (1953).

236. C. Edeleanu and R. Littlewood, Electrochem. Acta *3*, 195 (1960).

237. C. B. Gill, M. E. Straumanis, and W. B. Schlechten, J. Electrochem. Soc. *102*, 42 (1955).

238. J. H. Jackson and M. H. LaChance, Trans. Am. Soc. Metals *46*, 157 (1954).

239. D. H. Jansen, *Dynamic Corrosion Screening Tests on Inconel and Nickel in $NaCl$-$MgCl_2$-UCl_3 Bath*, ORNL-CF-57-6-72, Oak Ridge National Laboratory (June 1957).

240. V. P. Kochergin and N. E. Bogatereva, Nauchn. Dokl. Vysshei Shkoly, Khim. i. Khim. Tekhnol. *1959*, No. 1, 206.

241. V. P. Kochergin, E. P. Druzhinina, G. V. Men'shenina, and E. P. Asanova, Zh. Prikl, Khim. *33*, 1580 (1960).

242. V. P. Kochergin, A. V. Kabirov, and O. N. Skornyakova, J. Appl. Chem. USSR *27*, 883 (1954).

243. V. P. Kochergin, L. G. Khaibullina, and O. G. Potapova, Zh. Neorgan. Khim. *1*, 2617 (1956).

244. V. P. Kochergin and O. G. Potapova, Izv. Vysshikh Uchebn. Zavedenii Khim. i. Khim. Teknol. *2*, 406 (1959).

245. V. P. Kochergin and G. I. Stolyarova, J. Appl. Chem., USSR, *29*, 789 (1956).

246. R. Littlewood, Electrochim. Acta. *3*, 270 (1961).

247. R. Littlewood and E. J. Argent, Electrochim. Acta. *4*, 114 (1961).

248. R. Littlewood and E. J. Argent, Electrochim. Acta. *4*, 155 (1961).

249. P. A. Nelson, M. L. Kyle, G. A. Bennett, and L. Burris, Jr., Electrochem. Technol. *3*, 263 (1965).

250. C. J. Raseman, H. Susskind, G. Farber, W. E. McNulty, and F. J. Salzano, *Engineering Experience at Brookhaven National Laboratory in Handling Fused Chloride Salts*, BNL-627, Brookhaven National Laboratory (June 1960).

251. A. W. Schlechten, M. E. Straumanis, and C. B. Gill, J. Electrochem. Soc. *102*, 81 (1955).

252. M. V. Smirnov, V. P. Volodin, and I. N. Ozeryanaya, Dokl. Akad. Nauk USSR *115*, 418 (1964).

253. H. Susskind, F. B. Hill, L. Green, S. Kalish, L. Kukacka, W. E. McNulty, and E. Wirsing, Jr., Chem. Eng. Prog. *56*, No. 3, 57 (1960).

254. H. Susskind, F. B. Hill, L. Green, S. Kalish, L. E. Kukacka, W. E. McNulty, and E. Wirsing, Jr., *Corrosion Studies for a Fused Salt-Liquid Metal Extraction Process for the Liquid Metal Fuel Reactor*, BNL-585, Brookhaven National Laboratory (June 1950).

255. C. M. Craighead, L. A. Smith, and R. I. Jaffee, *Screening Tests on Metals and Alloys in Contact with Sodium Hydroxide at 1000 and 1500°F*, BMI-706, Battelle Memorial Institute (Nov 1951).

256. C. M. Craighead, L. A. Smith, E. C. Phillips, and R. I. Jaffee, *Continued Studies of Corrosion by Fused Caustic*, AECD-3704, Battelle Memorial Institute (Dec 1952).

257. A. F. Forestieri, *Effects of Additives on Corrosion and Mass Transfer in Sodium Hydroxide-Nickel Systems Under Free-Convection Conditions*, NACA-RM-E54E19, Lewis Flight Propulsion Laboratory (Aug 1954).

258. J. N. Gregory, N. Hodge, and J. V. G. Iredale, *The Corrosion and Erosion of Nickel by Molten Caustic Soda and Sodium Uranate Suspensions Under Dynamic Conditions*, AERE-C/M-273, Atomic Energy Research Establishment (March 1956).

259. J. N. Gregory, N. Hodge, and J. V. G. Iredale, *The Static Corrosion of Nickel and Other Materials in Molten Caustic Soda*, AERE-C/M-272, Atomic Energy Research Establishment (March 1956).

260. E. I. Gurowich, Zh. Prikl. Khim. *32*, 817 (1959).

261. W. E. Manly, *Operation of a Ni-NaOH Thermal Convection Loop*, ORNL-CF-51-11-186, Oak Ridge National Laboratory (Nov 1951).

262. N. E. Miller and E. M. Simmons, Chem. Eng. Prog. *52*, No. 19, Part IV, 113 (1956).

263. R. R. Miller, *Thermal Properties of Sodium Hydroxide and Lithium Metal: Fourth Progress Report, November 1, 1952 to January 31, 1953, NRL-Memo-130; Progress Report No. 4,* Naval Research Laboratory.

264. D. R. Mosher and R. A. Lad, *Kinetic Study of Mass Transfer by Sodium Hydroxide in Nickel under Free-convection Conditions,* NACA-RM-E53K24, Lewis Flight Propulsion Laboratory (March 1954).

265. *Proceedings of the First Information Meeting on Hydroxide and Metal Interaction,* ORNL-CF-51-11-204, Oak Ridge National Laboratory, (Aug 1953).

266. E. M. Simmons, N. E. Miller, J. H. Stand, and C. V. Weaver, *Corrosion and Component Studies on Systems Containing Fused NaOH,* BMI-1118, Battelle Memorial Institute (July 1956).

267. G. P. Smith, *Corrosion of Materials in Fused Hydroxides,* Am. Inst. Mining Met. Engrs., Inst. Metals Div., Spec. Publ. No. 2, 71 (1956).

268. G. P. Smith, *Corrosion of Materials in Fused Hydroxides,* ORNL-2048, Oak Ridge National Laboratory (March 1956).

269. G. P. Smith, E. E. Hoffman, *Corrosion Products Formed in the Reaction Between Fused Sodium Hydroxide and Iron-rich Alloys of Iron, Chromium, and Nickel,* ORNL-2156, Oak Ridge National Laboratory (May 1957).

270. G. P. Smith and E. E. Hoffman, Corrosion *13,* 627t (1957).

271. G. P. Smith, E. E. Hoffman, and M. E. Steidlitz, Corrosion *13,* 561t (1957).

272. G. P. Smith, M. E. Steidlitz, and E. E. Hoffman, Corrosion *14,* 47t (1958).

273. G. P. Smith, M. E. Steidlitz, and E. E. Hoffman, *Experimental Procedures Used for the Measurement of Corrosion and Metal Transport in Fused Sodium Hydroxide,* ORNL-2125, Oak Ridge National Laboratory (Oct 1956).

274. W. J. Smothers, *Progress Report for the Period January 1, 1953 through March 31, 1953,* AECU-2872, University of Arkansas (April 1953).

275. D. D. Williams, C. T. Ewing, *Thermal and Related Physical Properties of Molten Materials: Progress Report, Period February 1, 1953 to May 1, 1953,* NRL-Memo-170, Progress Report 5, Naval Research Laboratory (June 1953).

276. J. A. DeMastry, J. Nucl. Appl. *3,* 127 (1967).

277. J. R. DiStepano and E. E. Hoffman, *Corrosion Mechanisms in Refractory Metal-Alkali Metal Systems,* ORNL-3424, Oak Ridge National Laboratory (Sept 1963).

278. E. G. Brush, Corrosion *11,* 299t (1955).

279. M. F. Amateau, *Effects of Molten Alkali Metals on Containment Metals and Alloys at High Temperatures,* DMIC-169, Battelle Memorial Institute (May 1964).

280. J. R. DiStepano, *Corrosion of Refractory Metals by Lithium,* ORNL-3551, Oak Ridge National Laboratory (March 1964).

281. H. W. Leavenworth and R. E. Cleary, Acta Met. *9,* 519 (1961).

282. A. P. Litman, *The Effect of Oxygen on the Corrosion of Niobium by Liquid Potassium*, ORNL-3751, Oak Ridge National Laboratory (July 1965).

283. E. E. Hoffman, *Corrosion of Materials by Lithium at Elevated Temperatures*, ORNL-2074, Oak Ridge National Laboratory (March 1956).

284. J. H. Stand, C. M. Simmons, J. A. DeMastry and J. M. Ginco, *Compatibility of Liquid and Vapor Alkali Metals with Construction Materials*, DMIC-227, Battelle Memorial Institute (April 1966).

285. J. R. Weeks, Mater. Sci. Technol. Advan. Appl. *1962*, 709.

286. C. A. Zimmerman, *Corrosion of Type 316 Stainless Steel in NaK Service--A Literature Survey*, IDO-14651, Phillips Petroleum, Idaho Falls, Idaho (Feb 1965).

287. A. Glassner, *The Thermochemical Properties of the Oxides, Fluorides, and Chlorides to 2500°K*, ANL-5750 (1957).

288. P. A. F. White and S. E. Smith, *Inert Atmospheres*, Butterworths Publications, Washington, D. C. (1962).

289. G. N. Walton, Ed., *Glove Boxes and Shielded Cells*, Butterworths Publications, London (1958).

290. S. Dushman, *Scientific Foundations of Vacuum Techniques*, J. M. Lafferty, Ed., 2nd ed., John Wiley and Sons, New York (1962).

291. C. J. Barton, in *Technique in Inorganic Chemistry*, H. B. Jonassen and A. Weissberger, Eds., p. 259, Interscience Publishers, New York (1963).

292. J. G. Kirkwood and I. Oppenheim, *Chemical Thermodynamics*, p. 206, McGraw-Hill Book Company, Inc., New York (1961).

293. W. H. Rodebush and A. L. Dixon, Phy. Rev. *26*, 851 (1925).

294. A. K. Fischer, Rev. Sci. Instr. *37*, 717 (1966).

295. C. B. Alcock and G. W. Hooper, in *Physical Chemistry of Process Metallurgy, Part 1*, Georg R. St. Pierre, Ed., Interscience, New York (1961).

X

ARGONNE NATIONAL LAB WEST
3 4444 00011574 1

B